PHYSICAL MODELING OF LANDSLIDE GENERATED TSUNAMIS IN VARIOUS SCENARIOS FROM FJORDS TO CONICAL ISLANDS

A Dissertation
Presented to
The Academic Faculty

by

Brian C. McFall

In Partial Fulfillment
of the Requirements for the Degree
Doctor of Philosophy in the
School of Civil and Environmental Engineering

Georgia Institute of Technology
August 2014

PHYSICAL MODELING OF LANDSLIDE GENERATED TSUNAMIS IN VARIOUS SCENARIOS FROM FJORDS TO CONICAL ISLANDS

Approved by:

Dr. Hermann M. Fritz, Advisor
School of Civil and Environmental Engineering
Georgia Institute of Technology

Dr. Donald R. Webster
School of Civil and Environmental Engineering
Georgia Institute of Technology

Dr. Kevin A. Haas
School of Civil and Environmental Engineering
Georgia Institute of Technology

Dr. Paul A. Work
Estuarine Hydrodynamics and Sediment Transport
U.S. Geological Survey

Dr. Josef D. Dufek
School of Earth and Atmospheric Sciences
Georgia Institute of Technology

Date Approved: June 23, 2014

ACKNOWLEDGEMENTS

It has truly been an honor to pursue a doctoral degree at the Georgia Institute of Technology, but I could not have accomplished this degree without the guidance and encouragement of several people.

I would like to thank my family, whose never ending love and encouragement has made this academic endeavor possible. I would like to express my deepest gratitude to my advisor, Dr. Hermann Fritz, for his support and guidance throughout this project. I am also grateful to Dr. Paul Work, Dr. Kevin Haas, Dr. Donald Webster and Dr. Josef Dufek for serving on my committee. Their comments and suggestions greatly improved this dissertation. Last but not least, I would like to thank my fellow graduate students especially, Xiufeng Yang, Brittany Bruder, Stephanie Smallegan, Chatchawin Srisuwan and David Young for their help and support throughout my tenure at Georgia Tech.

This work was supported by National Science Foundation, Division of Civil, Mechanical and Manufacturing Innovation through grant numbers CMMI-0936603, CMMI-0927178, CMMI-0421090 and CMMI-0402490. Additionally, this work was supported by the Department of Defense through the Science, Mathematics & Research for Transformation (SMART) fellowship. The scientific and technical support Network for Earthquake Engineering and Simulation (NEES) and the O.H. Hindsdale wave research facility is acknowledged.

TABLE OF CONTENTS

Page

LIST OF TABLES

Page

LIST OF FIGURES

Page

SUMMARY

Tsunamis generated by landslides and volcanic island collapses account for some of the most catastrophic events in recorded history. The highest recorded tsunami runup of 524 m was produced by a landslide in a fjord in Lituya Bay, Alaska (1958). Unfortunately field data from these types of events is very limited, consisting of rare field measurements of landslide scarp, landslide deposit, tsunami runup and eyewitness accounts. Critically important data related to the landslide motion and both spatial and temporal tsunami evolution are lacking.

Source and runup scenarios based on real world events are physically modeled in the three dimensional NEES tsunami wave basin (TWB) at Oregon State University in Corvallis, Oregon. Topographical and bathymetric features can greatly affect wave characteristics and runup heights. Landslide generated tsunamis were studied in different topographic and bathymetric configurations: basin-wide propagation and runup, a narrow fjord, curved headland and conical island scenarios.

A unique pneumatic landslide tsunami generator (LTG) was deployed to simulate landslides with varying geometry and kinematics. The LTG consists of a 0.756 m^3 slide box filled with naturally rounded river gravel or cobbles which is accelerated by means of four pneumatic pistons down the 2H:1V slope, launching the granular landslide towards the water surface. The wave profiles were measured using an array of resistance wave gauges. The granular landslide width, thickness and front velocity were measured using above and underwater cameras. Wave runup was measured with a combination of resistance wave gauges and overlapping video recordings calibrated along the slope.

The effects from lateral hill slope curvature are analyzed by comparing the wave properties generated on the planar hill slope of the basin-wide propagation scenario and the convex conical hill slope of the conical island scenario. The leading wave crest amplitude

generated on a planar hill slope is 3% larger on average than the leading wave crest generated on a convex conical hill slope, while the leading wave trough and second wave crest amplitudes are smaller. Between 0.5-16% of the landslide kinetic energy is transferred into the leading wave crest and 1-24% is converted into the wave train. Cobble landslides transfer on average 43% more kinetic energy into the wave train than the gravel landslide.

The fjord scenario traps the wave energy resulting in the average maximum runup being 10% larger than in the curved headland scenario, which allows some wave energy to leak into the open basin. Predictive equations for the offshore and laterally propagating wave and runup amplitudes, periods, celerities and lengths are derived, which allow an initial rapid tsunami hazard assessment. Finally, the predictive wave and runup equations are applied to the 2007 landslide generated tsunami in Chehalis Lake, Canada. The experimental data provides high precision benchmark scenarios to advance and validate fully 3D numerical models of complex landslide generated tsunamis.

CHAPTER I

INTRODUCTION

Tsunami waves are a series of gravity waves generated by impulsively displacing a large volume of water. The word "tsunami" is derived from the Japanese two character word with "tsu" meaning harbor and "nami" meaning wave. Historically tsunamis have sometimes been called "tidal waves", which is a misleading term because they are not related to the tides. Tsunami waves typically have very long periods and wave lengths. Consequently they are barely noticeable in the deep ocean with wave heights less than a few meters, while the wave height can drastically increase as the wave approaches shallower water and coastal regions. Bathymetric and topographic features can cause the wave to refract, diffract, shoal and break. Tsunamis can be generated by seismic activity, landslides, volcanic eruptions or extreme events such as an asteroid impact or underwater explosion. Herein only tsunamis generated by landslides will be considered.

Landslide generated tsunamis may account for 10% of the recorded tsunamis (Kajiura, 1990). A landslide is a movement of rock, debris or earth down an incline (Cruden, 1991). Mass flows can be categorized as high density rock and soil movements or low density glacier falls and snow avalanches. Landslides with an initial position above, at and below the waterline are called subaerial, partially submerged and submarine landslides respectively. Often landslides are triggered by seismic events. Subaerial landslides are not affected by variations of the water surface. Submarine and partially submerged landslides can be triggered by fluctuations in the water elevation such as the filling or draining of a reservoir or oceanic tides.

Landslide generated tsunamis can occur in confined bays, fjords and reservoirs, or in the open ocean mainly at continental shelf breaks and volcanic islands. The impulse wave can be broken into three phases: wave generation, wave propagation and wave runup. The wave generation begins with the inception of slide motion or impact with the water surface and continues through the slide runout. The wave propagation includes radial spreading and dispersion. The wave runup consists of the wave propagating into shallower water and up a shoreline (Müller, 1995).

The largest recorded tsunami was generated by a landslide and occurred in Lituya Bay, Alaska in 1958 (Miller, 1960). The wave height exceeded 100 m in Gilbert Inlet resulting in a runup of 524 m on the opposing headland (Fritz et al., 2001; Fritz et al., 2009). The landslide was triggered by an earthquake on the Fairweather fault with a Richter scale magnitude of 8 (Tocher and Miller, 1959). Table 1 lists some of the important landslide generated tsunamis from the last few centuries. The table includes some of the generation parameters such as the landslide volume, V_s, hill slope angle, α, and the water depth, h. The effects of the event such as the wave runup, R, and the number of fatalities are included in the table.

Data from field events is only available for a few cases and is limited to the landslide scarp, landslide deposit, the trimline of destroyed vegetation and farfield tide gauge recordings. Near field and time-resolved data from these events is not available. Physical and numerical models are required to improve the understanding of this multi-phase and interdisciplinary hazard. Numerical models can be validated and improved by comparing results to experimental data. Physical models can be used to produce predictive equations for assisting in rapid hazard assessment and mitigation.

Table 1: Selected landslide generated tsunamis with generation parameters and tsunami effects.

Date	Location	Parameters			Effects		Reference
		V_s (10^6 m^3)	α (°)	h (m)	R (m)	Fatalities	
1741	Oshima-Oshima (JP)	2500	-	2000	13	2,000	Satake (2007)
1792	Unzen Volcano (JP)	500	10	64	10-30	>15,000	Ogawa (1924)
1883	Krakatau (ID)	-	-	20	35	36,000	Simkin and Fiske (1983) , Yokoyama (1981)
1888	Ritter Island (PNG)	5000	10-15	1000	20	<100	Ward and Day (2003)
1934	Tafjord (NO)	2-3	60	>200	62	41	Jørstad (1968), Slingerland and Voight (1979)
1946	Aleutian Islands (USA)	200,000	4.3	4000	42	167	Fryer et al. (2004)
1958	Lituya Bay (USA)	31	40	122	524	2	Miller (1960), Fritz et al. (2001), Fritz et al. (2009),
1963	Vajont Reservoir (IT)	240	0-40	240	270	~2000	Müller (1964)
1971	Yanahuin Lake (PE)	0.1	45	38	30	400-600	Plafker and Eyzaguirre (1979), Slingerland and Voight (1979)
1980	Spirit Lake (USA)	430	-	-	200	0	Voight et al. (1981), Voight et al. (1983)
1998	Papau New Guinea	4-6	-	-	15	>2000	Synolakis et al. (2002)
1999	Fatu Hiva (FP)	20-50	>45	<50	8	0	Okal et al. (2002)
2002	Stromboli (IT)	20-30	-	800	10	0	Tinti et al. (2005), Romano et al., (2013)
2003	Montserrat (WI)	200	-	1000	15	0	Watt et al. (2012)
2006	Java	-	-	-	21	600	Fritz et al. (2007)
2010	Haiti	~ 0.4	-	1750	2	3	Fritz et al.(2013), Hornbach et al. (2010), McHugh et al., (2011)

CHAPTER II

LITERATURE REVIEW

2.1 Introduction

Landslide generated tsunamis account for some of the most catastrophic events recorded. Field data from these events is mostly limited to the slide scarp, submarine deposit, tree trimline from the tsunami runup and far field tide gauge recordings. Landslide generated tsunamis can be produced by subaerial, partially submerged and submarine landslides. The study of landslide generated tsunamis consists of complex multi-phase and multi-material processes. **Figure 1** defines some parameters noted in the study of landslide generated tsunamis.

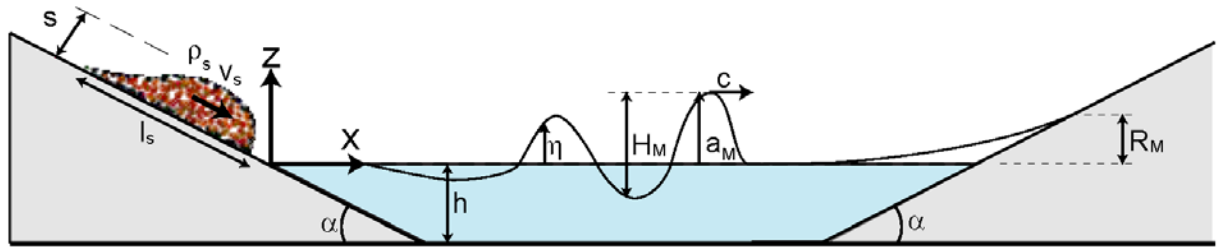

a)

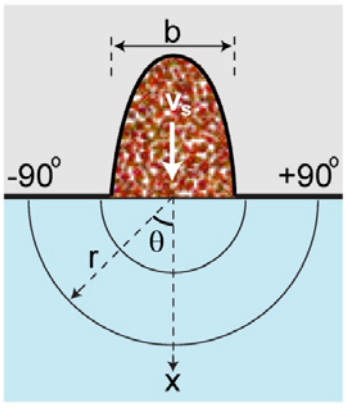

b)

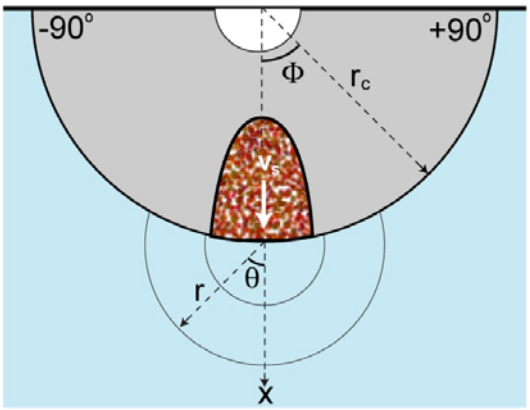

c)

Figure 1: Definition parameters and coordinate systems: (a) vertical profile, (b) plan view of a straight, plane hill slope, (c) plan view of conical island scenario.

The study of landslide generated tsunamis can be broken into the following four categories:

- Tsunami generating landslide
- Tsunami wave generation
- Tsunami wave propagation
- Tsunami wave runup and coastal impact

Each category has been studied independently and some categories have been studied simultaneously. The entire process should be studied as a whole to better understand the risks associated with near field hazards. It is adequate to study each category separately for far field hazard analysis.

This chapter discusses relevant studies previously performed on topics related to landslide generated tsunamis. Analytical, physical and numerical modeling efforts on landslide generated tsunamis will be reviewed. Conclusions are drawn from the literature review and current research gaps identified at the end of the chapter.

2.2 Landslides

2.2.1 Landslide Dynamics

Landslide dynamics are influenced by many parameters. One of the important parameters controlling landslide dynamics is the coefficient of friction. Heim (1932) observed that the slope of the landslide energy line is approximately the same as the coefficient of friction for sliding masses. Shreve (1968) referred to the observed friction coefficient as the equivalent

coefficient, which is dependent on the size of the landslide volume, unlike the material dependent typical friction coefficient. Fritz (2002) compared equivalent friction coefficients as a function of slide volume for subaerial, submarine and Martian landslides. The subaerial landslide data represents Alpine dry rock, nonvolcanic avalanches (Scheidegger, 1973). The submarine landslide data was compiled by Hampton et al. (1996) and the Martian landslide data was estimated by McEwen (1989). The equivalent friction coefficient was measured from the top of the landslide scarp to the toe of the landslide deposit, rather than the initial to end landslide centroid. All the cases highlight a decay in the equivalent friction coefficient with an increase in slide volume.

Fritz (2002) determined from subaerial landslides with volumes, V_s, exceeding 100,000 m^3 that the equivalent friction coefficient, f, as a function of slide volume in m^3 is given by

$$\log f = 0.15666 \log V_s + 0.62419 \qquad (1)$$

with a correlation coefficient of $r^2 = 0.82$. The relationship between the equivalent friction coefficient and slide volume varies with different landslide materials, and may not be applicable for clays. The equivalent coefficient of friction could be calculated with Equation 1 if the slide volume is estimated and then the slide velocity, v_s, could be predicted using Newtonian laws of motion as:

$$v_s = \sqrt{2g\,\Delta z(1 - f\cot\alpha)} \qquad (2)$$

where g is the gravitational constant, Δz is the vertical drop height of the landslide and α is the hill slope angle. Subaerial landslides have reached estimated velocities up to 150 m/s in recorded history (Körner, 1976).

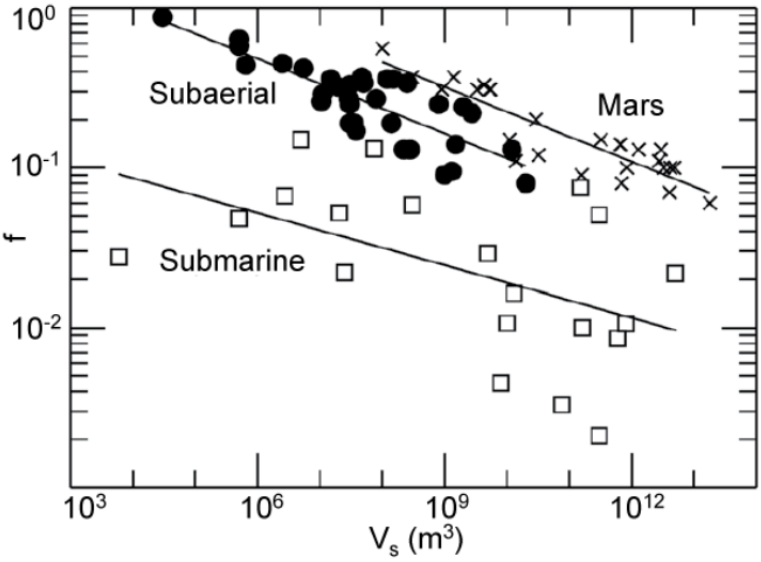

Figure 2: Equivalent coefficient of friction, f, as function of landslide volume, V_s, for subaerial landslides (Scheidegger, 1973), submarine landslides (Hampton et al., 1996) and Martian landslides (McEwen, 1989) compiled by Fritz (2002).

Submarine landslides can occur on relatively shallow slopes and can travel long distances because of the small friction coefficients compared to subaerial slides. Submarine landslides can have volumes two orders of magnitude larger than the largest known subaerial landslide. The scatter in submarine data in **Figure 2** indicates that other parameters than the slide volume may be necessary to describe the equivalent coefficient of friction for submarine landslides. Drag forces induced by the surrounding fluid may be an important parameter in submarine landslides.

Landslides naturally behave in a fluid-like manner and deposit in a very long, thin layer. Hypotheses explaining the fluidization of granular landslides include an upward flow of air by Kent (1966), a hovercraft action by Shreve (1966; 1968) and Hsü (1975), generation of high pressure steam by Habib (1975) and Goguel (1978), lubrication by molten rock by Erismann (1986), and development of a thin, rapidly shearing layer of fluctuating particles beneath a densely packed overburden by Kent (1966) and Melosh (1986).

2.2.2 Granular Landslide Experiments

Physical modeling of granular landslides generally consists of releasing granular material from rest on an incline. Huber (1980) conducted 2D experiments on impulse generated waves produced by granular landslides. Details on the impulse generated waves are discussed in Section 2.3.4 Granular Slide Models, but the details of the slide will be mentioned here. The granular slide material consisted of rounded river gravel with d_{50} =20 mm and grain diameter distribution ranging from 8 to 30 mm. The gravel was placed on the ramp behind an initially vertical gate. The gate was suddenly rotated to allow the gravel to slide down the ramp. To increase the slide impact velocity, the gate was placed higher on the ramp. Plüss (1987) conducted similar landslide experiments to Huber (1980), but only the granular slide was studied. A horizontal runout section was installed at the toe of the ramp. The slope of the ramp in Plüss (1987) ranged from 45˚- 60˚. Koch (1989) performed 2D experiments and released the landslide on a ramp with a varying gradient curving from 60˚ to horizontal at the bottom.

The Savage and Hutter (1989; 1991) model uses a Coulomb-type basal friction law to characterize avalanche and debris flow. Iverson (1997) conducted large scale chute experiments in an inclined flume to study the momentum transfer in debris flow and measured the basal fluid pressure. In the physical model approximately 10 m^3 of saturated sand and gravel was released by a gate at the top of the flume. The experiments extended the Savage and Hutter model by including the effects of pore fluid (Denlinger and Iverson, 2001).

Koch et al. (1994) conducted three-dimensional granular landslide experiments on a partly curved surface. A pile of granular material was released to run down a 5 m long, 3 m wide slide with an initial slope ranged 20˚- 60˚. Seven different granular materials were tested including glass beads, quartz and marble granules. Gray et al. (1999) expanded the experiments

by modeling three-dimensional landslides in a complex basal topography. The landslides were modeled with quartz chips with a mean diameter of 2 – 4 mm on a parabolic incline with an initial slope of 40˚.

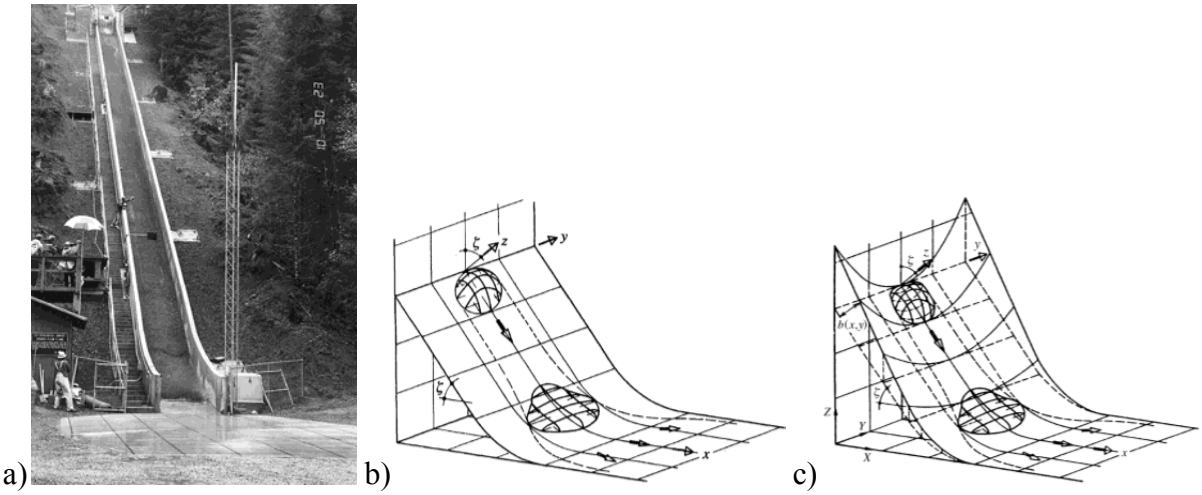

Figure 3: Debris flow and 3D granular landslide experiments: (a) basal pressure in debris flow study (Iverson, 1997), (b) 3D landslides on a partly curved surface (Koch et al., 1994) and (c) 3D landslides in a complex basal topography (Gray et al., 1999).

Iverson et al. (2004) conducted experiments with granular landslides on irregular terrain. The landslides were modeled with two different types of quartz sand. The first sand type was angular with a grain diameter between 0.5 – 1 mm and the second type consisted of rounded grains 0.25 – 0.5 mm in diameter. The experiment results calibrated and validated the Coulomb continuum model, which extended previous Coulomb point mass models.

Pudasaini et al. (2008) conducted several series of experiments on granular landslides in curved and twisted channels to study the transverse shearing and cross-stream momentum transport from the topography obstructing or redirecting the landslide motion. Three different landslide materials were used: silicon dioxide, brown quartz and crystal sand. The experimental channels extended up to 6 m long along the thalweg.

a) 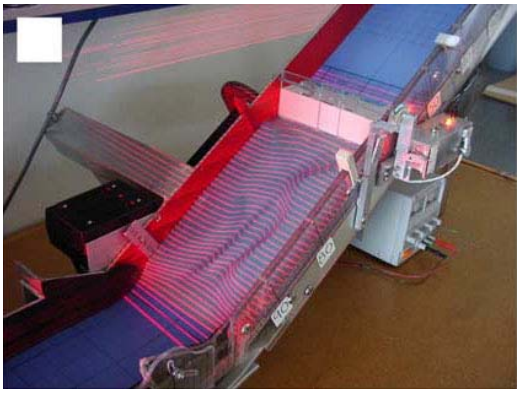 b) 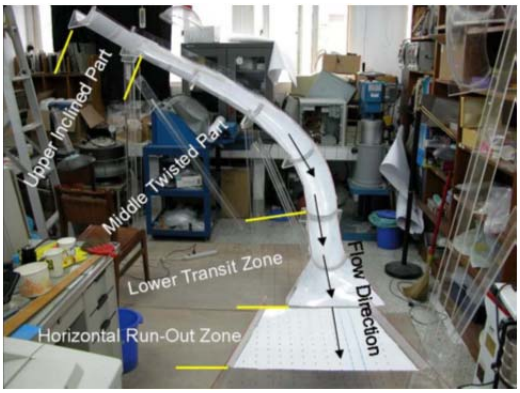

Figure 4: Granular landslide experiments: (a) on irregular terrain (Iverson et al., 2004) and (b) in curved and twisted channels (Pudasaini et al., 2008).

2.3 Modeling of Landslide Generated Tsunamis

2.3.1 2D Block Slide Models

Impulse wave generation can be modeled with a block sliding into the water. One of the first block experiments was conducted by Russell (1837; 1844) to model a solitary wave. This plunger configuration consisted of heavy block positioned on the water surface at the beginning of a trial. The plunging block is dropped and sinks vertically into the water at the end of a channel. Impulse waves are generated and propagate down the channel. Russell found that the volume of water displaced equaled the volume of water in the wave, and the wave propagated at a constant celerity given by $c = \sqrt{g(h + a)}$ where c is the celerity, h is the water depth and a is the wave amplitude. Monaghan and Kos (2000) extensively studied the vertically plunging box at the end of a channel using experiments and numerical simulations.

Experiments showed that the water under the plunging box is forced out horizontally with enough velocity to form a reverse separation vortex in front of the block while producing a solitary wave. The reverse vortex propagates behind the solitary wave down the tank. The PIV vector field of the vortex generation, shape and propagation is similar to an infinitesimal segment of a vortex ring produced by an impulsively started jet engine (Gharib et al., 1998; Shusser and Gharib, 2000). The numerical model results exceeded the experimental values by 3-18%. This is most likely caused by the gap between the sinking box and the sidewalls, which may reduce the wave height by approximately the same amount. Monaghan and Kos (2000) determined the leading wave crest amplitude to be

$$a_{c1} = 3h \left(\frac{m_s}{40\,\rho_w shb}\right)^{2/3} \left(\frac{s}{h}\right) \qquad (3)$$

where m_s is the box mass, ρ_w is the water density, s is the box thickness, h is the water depth and b is the box width. The impulse wave runup was studied by Monaghan and Kos (1999) using smooth particle hydrodynamics (SPH) simulations.

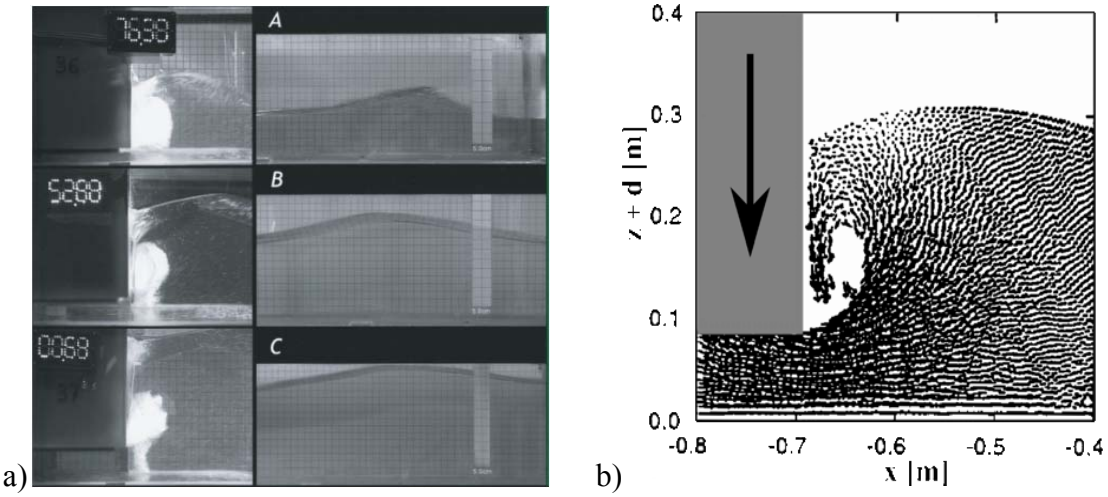

a) b)

Figure 5: Plunging block models: (a) Near field recording of reverse vortex and (b) SPH simulation of the near field by Monaghan and Kos (2000).

Wiegel (1955) and Noda (1970) described the wave profiles generated by a submerged rigid box dropping vertically or sliding down a slope. Wiegel (1955) determined that underwater landslides produced dispersive waves and only 1-2% of the landslide energy is converted into wave energy. Noda (1970) studied wave generation from a falling submerged box both experimentally and theoretically using linear theory. Using the theoretical results and experimental results from Wiegel et al. (1970), the generated waves were classified by Froude number, $F = v_s/\sqrt{gh}$, and normalized slide thickness, $S = s/h$. The wave classifications are: oscillatory waves, nonlinear transition wave, solitary wave and bore.

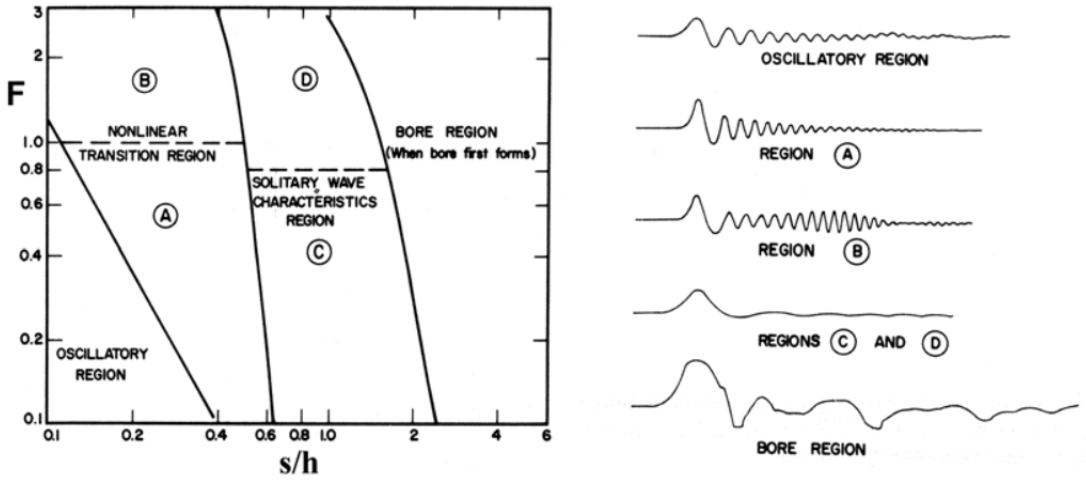

Figure 6: Wave classifications and profiles for a vertically sinking block model based on slide Froude number, $\boldsymbol{F = v_s/\sqrt{gh}}$, and normalized slide thickness, $\boldsymbol{S = s/h}$, given by Noda (1970).

Wiegel et al. (1970) compared his experimental results with the theoretical models of Kranzer and Keller (1959). The experimental waves produced by a falling block at various heights produced a wave height relationship described by $H(x)/h \propto x^{-1/5}$, while the Kranzer and Keller (1959) mathematical model inferred a wave height relationship $H(x)/h \propto x^{-1/3}$.

Sinking block experiments were performed by Bukreev and Guseev (1996) in extremely small water depths of 0.04 and 0.08 m prone to scale effects due to viscous wave attenuation. Panizzo et al. (2002) used plunging block experiments as a preliminary study for three-dimensional model experiments.

Fritz (2002) performed preliminary experiments with a falling block and a wedge block with rollers to reduce friction on a 10˚ incline plane. The wave generation between the two methods differs because the sliding wedge does not produce the previously noted reverse separation vortex. Law and Brebner (1968) conducted experiments using blocks of various lengths, heights and weights sliding down a roller ramp with an 18˚-25˚ incline. The wave height attenuation for these experiments was described by $H(x)/h \propto x^{-1/2}$. According to Brebner in Slingerland and Voight (1979), the Kamphius and Bowering (1970) study produced better and more useful correlations.

Kamphuis and Bowering (1970) performed experiments on a roller ramp using a weighted tray and the ramp inclination ranged from 20˚-90˚. The experiments were conducted in a 45 m long and 1 m wide flume with water depths at 0.23 m and 0.46 m. The wave heights decayed with increasing slope angle, but the effect was minor between 20˚-60˚. The far field wave height was dependent on landslide Froude number, $F = v_s/\sqrt{gh}$, and the slide volume per unit width, $q = l_s/h \times s/h$ with slide length l_s, slide thickness s and water depth h. The far field wave height at x/h = 37 for relatively thick slides with $s/h \geq 0.5$ is given by

$$\frac{H\,(x=37h)}{h} = F^{0.7}\left(0.31 + 0.2\log q\right) \qquad (4)$$

The wave height decreased exponentially with distance from the source as given by

$$\frac{H}{h} = \frac{H\,(x=37h)}{h} + 0.35\,e^{-0.08\,(x/h)} \qquad (5)$$

for $0.1 < q < 1$ and $10 \leq x/h \leq 48$. The wave period increased linearly with x/h. The wave height and velocity reached asymptotic values, but the wave length did not. The energy conversion from the slide to the wave train varied from 10 – 50%.

Heinrich (1992) performed numerical and experimental modeling of a wedge sliding down a ramp. The nonlinear Eulerian code, NASA-VOF2D, uses the finite difference method to numerically solve the complete Navier Stokes equations. Subaerial and submarine slides were modeled. The numerical model matched the first wave crest and trough very well, but discrepancies in the amplitude and phase occurred in the trailing waves. Heinrich (1992) also describes a three-dimensional version of the code, NASA-VOF3D.

Watts (1997; 1998; 2000) modeled submarine landslides with triangular blocks sliding down a ramp with an incline of 45˚. The right triangle prism produced a trough above the block due to the horizontal top face of the block, while the vertical front face produced a crest in front of the block (Watts, 1998). The Hammack number, $Ha = t_{sd}\sqrt{gh}/(l_s \cos\alpha)$, was identified as the dimensionless wave maker time. The Hammack number describes the ratio between the time of slide-water interaction, t_{sd}, and the linear, long wave celerity to the horizontal projection of the slide length, l_s (Hammack, 1973). Most submarine solid block experiments convert 3-7% of the maximum block energy into wave energy, with the energy conversion decreasing with initial submergence.

Watts et al. (2003) performed experiments on submarine landslides using a semi-ellipsoid and compared the experimental results to the depth-averaged nonlinear shallow water wave equations. The equations underestimated the wave amplitude. The depth-averaged nonlinear shallow water wave equations have been applied to landslide generated impulse waves by Raney and Butler (1975), Chiang et al. (1981), Chaudhry et al. (1983), Townson and Kaya (1988), Mader (1988; 1999), Harbitz (1993), Jiang and LeBlond (1992; 1993; 1994), Johnson and Mader

(1994), Imamura and Gica (1996) and Tinti and Bortolucci (2000). Neglecting the vertical velocities is inaccurate for the impulse wave generation and the near field areas.

Walder et al. (2003) performed experiments with a solid block sliding down a ramp in a smoothly curving flume with water depths of h = 0.051, 0.09 and 0.13 m. The ramp incline ranged 11.2˚to 19.5˚. Scaling analysis of the Euler equations produced the following nondimensional parameters: vertical slide Froude number, $F \sin\alpha = \left[v_s/\sqrt{gh}\right] \sin\alpha$, relative slide volume, $V = V_s/(bh^2)$, and the relative time of underwater motion, $T_s = t_s(g/h)^{1/2}$. The maximum amplitude was determined with a correlation coefficient of r^2 = 0.66 and is given by

$$\frac{a_{max}}{h} = 1.32\left(\frac{T_s}{V}\right)^{-0.68} \tag{6}$$

when $a_{max}/h < 0.85$. The effect of the vertical Froude number was found to be negligible. The relative time of underwater motion could be described as $T_s = 4.8(l_s/h)^{0.4}$ and is solely dependent on the relative slide length, l_s/h.

Ataie-Ashtiani and Najafi-Jilani (2008), Ataie-Ashtiani and Nik-Khah (2008) and Najafi-Jilani and Ataie-Ashtiani (2008) performed experiments in a 2.5m wide, 1.8 m deep and 25 m long wave flume using solid steel blocks with different shapes and granular material. Both the landslide width and the 15˚-60˚ incline were narrower than the flume width. The maximum crest amplitude was given by

$$\frac{a_{cmax}}{h} = (0.405 + 0.078(VF^2)^{1.28})\left(\frac{T_s}{V}\right)^{-0.278}\left(\frac{l_s}{t_s}\right)^{-0.12}\left(\frac{r}{h}\right)^{-0.48} \tag{7}$$

with relative slide volume $V = V_s/(bh^2)$, slide Froude number $F = v_s/\sqrt{gh}$, relative time of underwater motion $T_s = t_s/\sqrt{g/h}$, t_s is the dimensional time of underwater motion, l_s is the slide length, r is the distance away from the impact source and h is the water depth. The energy conversion from the slide to the water wave ranged from 5% to 50%. The highest energy

conversion was from the solid blocks and the lowest was from the granular slides. Ataie-Ashtiani and Yavari-Ramshe (2011) used these experimental results to validate a 3D Boussinesq-type numerical model.

Sælevik et al. (2009) used several box modules which were connected and accelerated by a conveyor belt. The waves generated by the train of box modules produced nonlinear oscillatory waves. Sælevik et al. concluded that the landslide volume was the governing parameter for the leading wave amplitude and the landslide length is more important for trailing waves. The PIV measurements of the velocity field demonstrated the applicability of higher order Boussinesq equations to describe the generated waves.

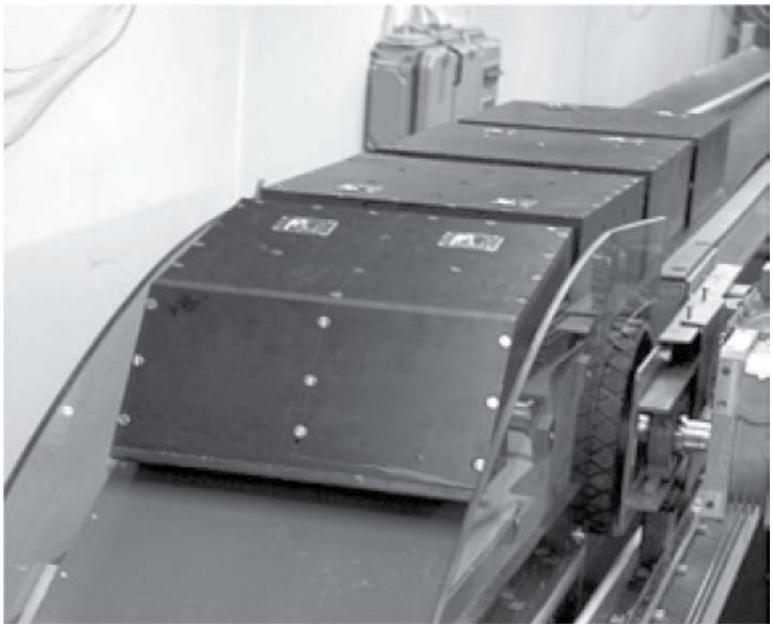

Figure 7: Box modules connected and accelerated by a conveyor belt (Sælevik et al., 2009).

Sue et al. (2011) studied submarine landslides by sliding a rigid semi-ellipsoid down a 15˚ incline in a 14.67 m long, 0.25 m wide and 0.505 m deep basin. A smooth transition was formed between the incline and the floor of the basin. The sliding block had a major axis length

of 0.500 m and a height of 0.026 m. The specific gravity of the rigid landslide was adjustable. A particle tracking velocimetry (PTV) technique was used to measure the landslide kinematics. Numerical simulations using a solved boundary element method based on linear, inviscid and irrotational wave theory were compared with the physical experiments.

2.3.2 3D Block Slide Models

Wave properties from two-dimensional block slide models are functions of the distance from the source, but wave properties in three-dimensional block models are functions of the radial distance from the source and the angular direction from the source as described in **Figure 1**. Johnson and Bermel (1949) performed experiments using metal discs impacting the water surface in a basin to study the waves generated by a nuclear explosion. Two tests from these experiments are presented in Slingerland and Voight (1979) and the wave amplitude decay was determined to be proportional to $1/r$.

Panizzo et al. (2005) performed 3D block slide experiments in a 6 m wide, 12 m long and 0.8 m deep wave basin. The rectangular block slide was released at the end of the basin adjacent to the side wall assuming symmetry of the wave propagation. The water depths were h = 0.4 m and 0.8 m. The block ramp incline angles tested were $\alpha = 16^{\circ}$, 26° and 36°. The waves were characterized using wavelet analysis (Panizzo et al., 2002). The relative time of underwater motion was given by

$$t_s^* = t_s \sqrt{\frac{g}{d}} = 0.43 \left(\frac{bs}{h^2}\right)^{-0.27} F^{-0.66} (\sin\alpha)^{-1.32} \qquad (8)$$

with the slide width b, slide thickness s, and slide Froude number F. The maximum wave height in the near field is described by

$$\frac{H_{max}}{h} = 0.07\left(\frac{t_S^*}{A_S^*}\right)^{-0.3136}(\sin\alpha)^{-0.88}\exp(0.6\cos\theta)\left(\frac{r}{h}\right)^{-0.44} \quad (9)$$

with the dimensionless slide front surface $A_w^* = (bs)/h^2$, angular direction from the slide propagation direction θ, and the radial distance from the source *r*. The dimensionless wave height increases with slide velocity and decreases with radial distance from the source. Predictive equations for wave period and surface elevation were also determined.

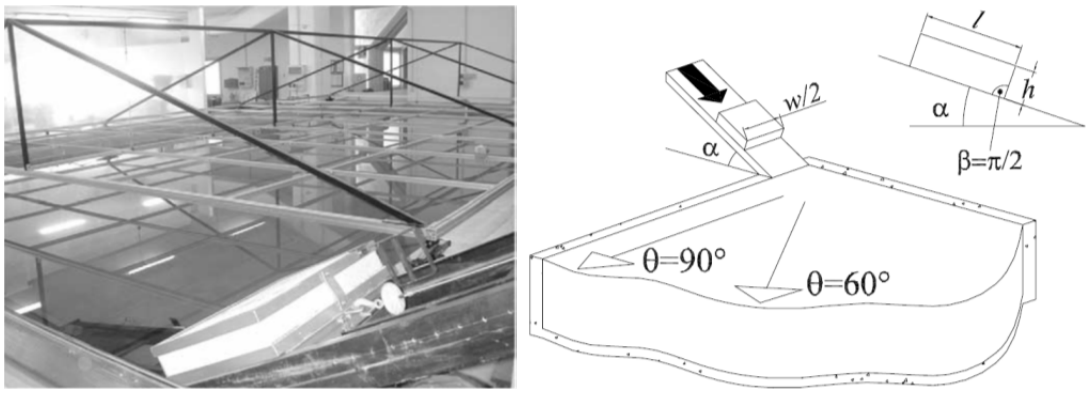

Figure 8: Experimental setup by Panizzo et al. (2005)

Panizzo et al. (2005) compared the data from their 3D block slide experiments with the 3D predictive equation of Huber and Hager (1997) and the predictive equation from the 2D data of Fritz et al. (2004). The data sets from Huber and Hager (1997) and Fritz et al. (2004) modeled the landslide with granular material. The Huber and Hager (1997) equation over predicted the measured wave height by a factor of 2-3. The Fritz et al. (2004) equation predicted the maximum wave height to be 5-10 times larger than the 3D experimental data. The directional wave energy distribution accounts for some of the difference between the Panizzo et al. (2005) data and the Fritz et al. (2004) equation. The slide impacting the basin floor in Panizzo et al. (2005) would dissipate some of the slide energy resulting in less wave energy.

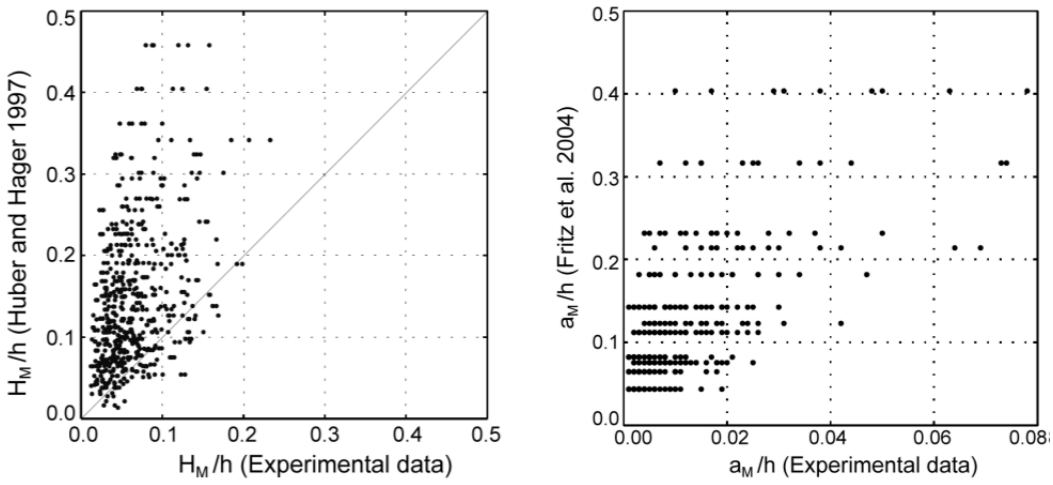

Figure 9: Comparison of Panizzo et al. (2005) experimental 3D data with (a) the maximum wave height 3D predictive equation (Huber and Hager, 1997) and (b) the maximum wave amplitude 2D predictive equation (Fritz et al., 2004).

Enet and Grilli (2005), Grilli and Watts (2005) and Enet and Grilli (2007) used a solid block with an approximate Gaussian cross-section in a 3.7 m wide, 1.8 m deep and 30 m long wave tank. The block shape was chosen to compare with the numerical simulations from the fully nonlinear potential flow model in Grilli et al. (2002). The lateral runup from a subaerial landslide is larger than from a comparable submarine landslide based on the analysis of video runup recordings.

Di Risio et al. (2009a) used half an ellipsoid shaped block to model a landslide in a 5.5 m wide, 1.8 m deep and10.8 m long wave tank. Subaerial and partially submerged landslides are simulated on a 1V:3H inclined plane. The lateral runup initially grows from the generation site and reached a maximum approximately two landslide widths away, then the runup decays as it continues to propagate. It was also observed that the crests propagated laterally faster than the troughs and the wave period increased with lateral wave propagation. Di Risio et al. (2009b) performed similar experiments on a conical island which is described in Section 2.5 Edge Waves.

Heller et al. (2012) performed 2D and 3D block landslide experiments to compare the wave characteristics. The 2D experiment trials were conducted in a 1.7 m long, 0.25 m wide and a still water depth h=0.10 m basin, and a 2.1 m long, 2.0 m wide and 0.2-0.4 m deep basin for the 3D trials. The wave height was approximately 20% larger in the 2D scenario at five water depths from the impact than the 3D scenario. Scale effects from the small-scale physical model could have contaminated the results.

Bruggemann (2012) used a larger physical 2D and 3D block model than Heller et al. (2012) to analyze effects on the wave characteristics. The 2D experimental trials were performed in a 24.5 m long, 0.60 m wide and 1.0 m high flume with water depths of h = 0.25 and 0.50. The 3D basin was 20 m long and 12 m wide with water depths of h = 0.25 and 0.50. In both cases a 57.3 kg block with a density of 1550 kg/m^3 slid down a 45˚ incline. The 3D waves were found to decay much faster than the in 2D. The wave height and amplitude were seen to be functions of the distance from the source, but a function to characterize the behavior was not found.

2.3.3 Piston Slide Models

The landslide water body interaction may be approximated by a vertical wall horizontally penetrating the water body as the landslide thickness approaches the water depth. Extreme examples of such events occurred at Vajont dam in Italy and Spirit Lake at Mount St. Helens (Müller, 1964; Voight et al., 1983). A typical horizontal motion piston wave maker was used by Miller (1970) to study coastal landslides and Hammack(1973) used a vertically penetrating piston from the channel bottom to study tsunami generation. The disadvantage to piston slide models is that two assumptions have to be made: the boundary condition at the wave maker's face panel and the forced piston motion of the wave maker. The wave height to piston stroke

ratios over the relative water depths is referred to by Madsen (1971), Dean and Dalrymple (1991), Synolakis (1991) and Hughes (1993). When plate motion is small, the classic study by Ursell (1960) is applicable. In shallow water, Galvin (1964) reasoned the volume of water displaced by the lavender (plunger) is equal to the volume of water under the crest of a propagating wave.

The theoretical solution for the case of a vertical wall moving horizontally into a body of water was derived by Noda (1970). The problem was linearized by assuming the wall displacement was much less than the water depth. With this solution the maximum water elevation occurred at x/h~2 and was predicted by

$$\frac{a}{h} = 1.32 \left(\frac{v_s}{\sqrt{gh}}\right) \qquad (10)$$

for a displacement at constant horizontal velocity, v_s. This linear solution was compared to the nonlinear data collected by Miller and White (1966). The linear solution matched the trend of the data, but typically under predicted the normalized wave amplitude. The data from Das and Wiegel (1972) confirmed the linear solution of Noda (1970).

Hunt (1988) produced a solution for water waves generated by distant landslides modeled by injecting a volume of fluid at a point source through the bottom of a reservoir. Gozali and Hunt (1989) used the method of characteristics to compute numerical solutions for water waves generated by a close landslide which was modeled with a moving vertical wall.

Sander (1990) investigated unidirectional shallow water waves generated by a rigid moving boundary representing a partially submerged landslide penetrating slowly compared to the wave propagation celerity. A piston type wave maker was used to produce waves within the range: Froude number, $F = v_s/\sqrt{gh}$, from 0.01 to 0.4, amplitude to water depth ratios from a/h = 0.01 to 0.4 and water depth from h =0.05 to 0.15 m. Most of the waves were weakly

nonlinear. The boundary motion may have been similar to the Vajont landslide, but relatively slower. Estimates for the Vajont landslide Froude number approach $F = 0.6 – 1$ (Müller, 1964).

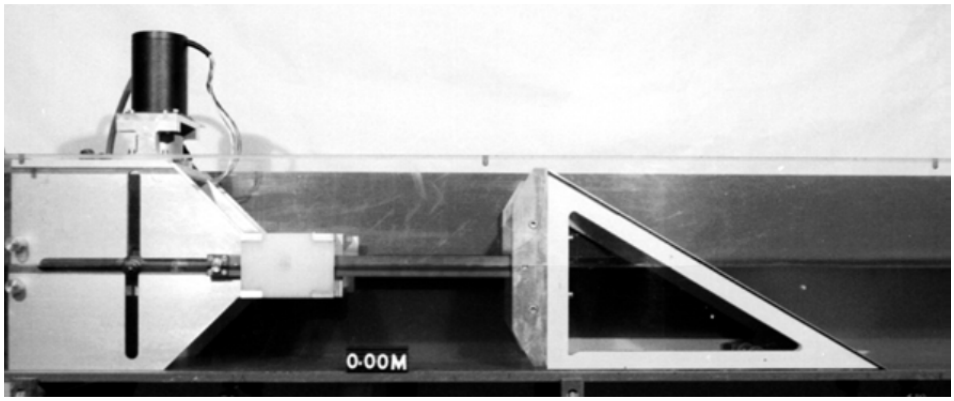

Figure 10: Piston wave generator with wedge cross-section by Sander (1990).

The Sander (1990) experiments show that wave height and wave length are related to the piston or landslide Froude number for wedge shaped piston wave generators. Small Froude numbers resulted in smaller wave crests and deeper troughs, and larger Froude numbers resulted in larger wave crests and shallower troughs. Wu (1981) and Villeneuve and Savage (1993) presented a numerical solution of Boussinesq type equations reproducing the weakly nonlinear shallow water waves.

2.3.4 Granular Slide Models

Slingerland and Voight (1982) used empirical regression analysis to produce prediction equations of the dimensionless first wave amplitude based on the dimensionless slide kinetic energy. The data used in the regression analysis was from three-dimensional, site specific,

experiments performed at a 1:120 and 1:300 scale by Ball (1970), Davidson and Whalin (1974) and Davidson and McCartney (1975). The slides were tabular or triangular in shape and initially positioned above the water surface. The slides consisted of gravel, iron or lead bags. The data consisted of 20 experiments with 3 slide types and 3 water levels. The slide Froude number ranged F=0.5-5. The dimensionless slide thickness was in the range: $0.37 < s/h < 0.8$ and the prototype slide volume ranged 0.7-39 x10^6 m^3. The maximum wave amplitude at x/h=4 for a semi-circular impulse wave propagating in the slide axial direction is given by

$$\log\left({}^{a_m}/_{h}\right) = -1.25 + 0.75 \log E_{sk} \tag{11}$$

with water depth h and dimensionless kinetic energy E_{sk}:

$$E_{sk} = \frac{1}{2} \frac{\rho_s}{\rho_w} \frac{V_s}{h^3} \frac{v_s^2}{gh} \tag{12}$$

where ρ_s and ρ_w are the respective slide and water densities, V_s is the slide volume, v_s is the slide front impact velocity and g is the gravitational constant.

Huber (1980) conducted 2D and 3D experiments on impulse generated waves produced by granular landslides, performing over 1000 experimental trials. The granular slide material consisted of rounded river gravel with d_{50} =20 mm and a grain diameter distribution ranging from 8 to 30 mm. The grain density was ρ_g = 2,700 kg/m^3. The gravel was placed on the ramp behind a vertical gate, forming a triangular prism. The gate was suddenly rotated to allow the gravel to slide down the ramp. To increase the slide impact velocity, the gate was placed higher on the ramp. This configuration results in long, thin landslides with the front moving much faster than the back of the slide. The experiment parameters covered the following ranges: slide mass 5-50 kg, slide front impact velocity 1-5 m/s, water depths h = 0.12-0.36 m, ramp angle α = 28-60˚ and energy conversion from the slide to the water wave 1-40%. The experimental

results of Huber (1980) were described by Huber and Hager (1997). The wave height from 2D impulse waves was given by

$$H = 0.88 \sin\alpha \left(\frac{\rho_s}{\rho_w}\right)^{1/4} \left(\frac{V_s}{b}\right)^{1/2} \left(\frac{x}{h}\right)^{-1/4} \quad (13)$$

with ramp angle α, slide and water density ρ_s and ρ_w, slide volume V_s, slide width b, location x, and water depth h.

The three-dimensional experiments conducted by Huber (1980) produced radial waves. The wave height showed a strong dependence on radial distance from the source, r, and the angular distance from the landslide direction, γ. The dimensionless wave height from 3D experiments is given by

$$\frac{H}{h} = 2 \cdot 0.88 \sin\alpha \cos^2\left(\frac{2\gamma}{3}\right) \left(\frac{\rho_s}{\rho_w}\right)^{1/4} \left(\frac{V_s}{b\,h^2}\right)^{1/2} \left(\frac{r}{h}\right)^{-2/3} \quad (14)$$

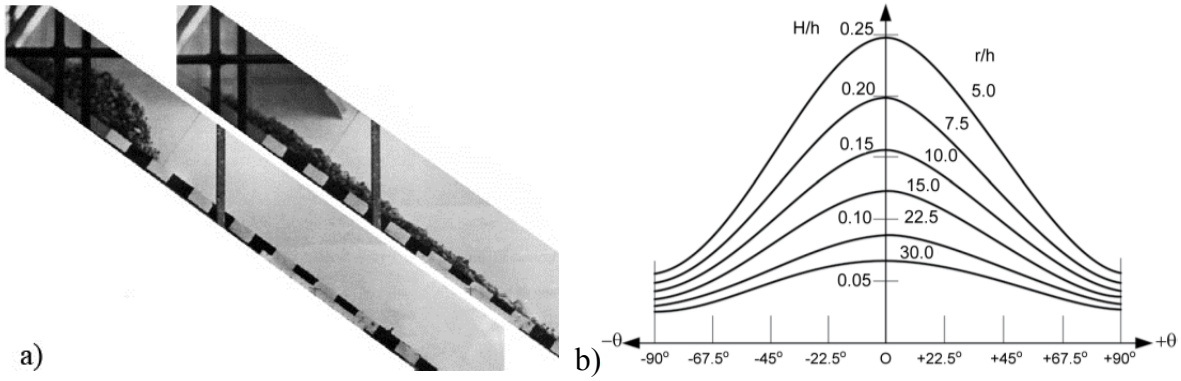

Figure 11: (a) Granular flow from the 2D experiment with ramp incline angle α = 32˚, slide mass m=30 kg at t = 0.1 s and t = 0.6 s after the gate opening (Huber, 1980); (b) Dimensionless wave height attenuation as function of angular direction and radial distance from a 3D experiment (Huber and Hager, 1997).

Huber and Hager (1997) determined the wave amplitude attenuation to be proportional to $(r/h)^{-2/3}$ and be angularly dependent. The largest wave heights occur along the landslide axis as shown in **Figure 11b**. Kranzer and Keller (1959) produced an analytical solution for the circular decay of wave amplitude to be proportional to 1/*r*. Van Dorn (1961) found the radial tsunami divergence from the four Redwing nuclear blasts at the Bikini Islands to be proportional to $r^{-5/6}$, while noting the experimental uncertainties encompass the 1/*r* spreading law.

The thin granular slides from Huber (1980) may not adequately model typical landslides initially moving as a solid block, and then disintegrating into debris flows. Fritz and Moser (2003) designed a pneumatic machine to better model this transitional phenomenon. Fritz (2002) conducted an extensive series experiments on granular impulse generated waves in a flume. The experiments are summarized in Fritz et al. (2001; 2003a; 2003b; 2004) and Fritz et al. (2009). The two-dimensional experiments were conducted in a 0.5 m wide, 1 m deep and 10 m long flume. The pneumatic landslide generator was capable of independently controlling landslide parameters. The 137 experimental trials covered the following parameter ranges: water depth h = 0.3- 0.675 m, hill incline angle α = 30 - 90˚, landslide mass 27 -108 kg, relative slide thickness: $0.07 \leq s/h \leq 0.6$, relative slide volume 0.07-1.6, slide impact velocity 2.7- 8.4 m/s and the slide Froude number F =1-4.8. The landslide material consisted of artificial granular material (PP-$BaSO_4$) with the grain density of $\rho_g = 2640\ kg/m^3$ and a bulk density of $\rho_s = 1620\ kg/m^3$. The generated waves were categorized as weakly nonlinear oscillatory waves, nonlinear transition waves, solitary-like waves and dissipative transient bores.

Particle image velocimetry (PIV) analysis was used to study the near field flow dynamics. These measurements serve the calibration and validation of numerical models (Mader and Gittings, 2002; Quecedo et al., 2004; Weiss and Wünnemann, 2007) The impact flow regimes were categorized based on the slide Froude number F as no flow separation, local flow

separation, backward collapsing impact crater and outward collapsing impact crater. High slide velocity impacts generate an impact leading to a water displacement significantly exceeding the slide volume. The criterion for flow separation is given by

$$F > \left({}^{5}/_{3} + {}^{1}/_{2}\, S\right) \tag{15}$$

with slide Froude number $F = v_s/\sqrt{gh}$, and dimensionless slide thickness $S = s/h$. The maximum wave amplitude is given by

$$\frac{a_c}{h} = 0.25\, F^{1.4}\, S^{0.8} \tag{16}$$

with maximum wave crest amplitude a_c and water depth h. The energy conversion from the slide to the first wave was found to be between 2-30%.

Zweifel (2004) extended the physical model of Fritz (2002) to study the effects of the slide bulk density ρ_s. The granular density ranged from $\rho_g = 955\ kg/m^3$ to $2640\ kg/m^3$. The maximum wave amplitude from Zweifel et al. (2006) is given by

$$\frac{a_m}{h} = \frac{1}{3}\, F\, S^{1/2}\, M^{1/4} \tag{17}$$

with dimensionless slide mass, $M = m_s/(\rho_s b h^2)$ and slide width b. The wave amplitude attenuation was found to be given by

$$\frac{a(x)}{h} = 2\, S^{1/2} \tanh 0.25\, F^{3/2}\, (M/X)^{1/2} \tag{18}$$

with dimensionless distance from the source $X = x/h$. In addition to granular slides, Zweifel (2004) conducted experiments with a block in the same flume. The wave amplitude was similar for the block experiments compared to the granular slides for slide Froude numbers greater than 3. For smaller Froude numbers the maximum wave amplitude predictive equation for the

granular slide over predicts the measured wave amplitude produced by the box. The relationship between the box amplitude and the granular amplitude is given by

$$\frac{\frac{a_{M\,box}}{h} - \frac{a_M}{h}}{\frac{a_{M\,box}}{h}} = 1 - 0.26F \qquad \text{for} \quad 0.5 \leq F \leq 2.8 \tag{19}$$

with a correlation coefficient of $r^2 = 0.97$.

Heller (2008) and Heller and Hager (2010) extended the physical modeling of Fritz (2002) and Zweifel (2004) to study scale effects and effects of slide granulate characteristics on the generated tsunami waves. The maximum wave amplitude height and period were found to be given by the following equations:

$$\frac{a_m}{h} = \frac{4}{9} P^{4/5} \tag{20}$$

$$\frac{H_m}{h} = \frac{5}{9} P^{4/5} \tag{21}$$

$$T_m (g/h)^{1/2} = 9\, P^{1/2} \tag{22}$$

$$P = F\, S^{1/2}\, M^{1/4} (\cos\beta)^{1/2} \tag{23}$$

$$\beta = (6/7)\, \alpha \tag{24}$$

where α is the hill angle and β accounts for the effect of the hill slope angle on the wave amplitude up to $\alpha = 90°$. The wave amplitude and wave height attenuation beyond the maximum was found to be given by

$$\frac{a(x)}{h} = \frac{3}{5} \left(P\, X^{-1/3}\right)^{4/5} \tag{25}$$

$$\frac{H(x)}{h} = \frac{3}{4} \left(P\, X^{-1/3}\right)^{4/5} \tag{26}$$

Heller and Hager (2011) analyzed the data from Heller (2008), Fritz (2002) and Zweifel (2004) to classify the waves based on the slide parameters. Heller et al. (2009) identified the relevant wave type parameter, T, as

$$T = S^{1/3} M \cos(\beta) \tag{27}$$

Plotting the relevant wave type parameter, T, versus the slide Froude number produced the following relationships:

$$T < {}^{4}/_{5}\, F^{-7/5} \qquad \text{Stokes-like wave} \tag{28}$$

$${}^{4}/_{5}\, F^{-7/5} \leq T \leq 11\, F^{-5/2} \qquad \text{cnoidal- or solitary-like wave} \tag{29}$$

$$T > 11\, F^{-5/2} \qquad \text{bore-like wave.} \tag{30}$$

Heller and Spinneken (2013) compared the wave characteristics generated from granular landslides described in Heller and Hager (2010) and a block landslides with matching slide Froude number F, relative slide thickness S, relative mass M and hill slope incline α. The relationship between the two landslide models is given by

$$\frac{a_{m,block}}{a_{m,granular}} = \frac{27}{16}\, P^{1/10} \left(B\Phi T_s^{1/2}\right)^{9/10} \tag{31}$$

$$\frac{H_{m,block}}{H_{m,granular}} = \frac{9}{5}\, P^{1/10} \left(B\Phi T_s^{1/4}\right)^{9/10} \tag{32}$$

$$\frac{T_{m,block}}{T_{m,granular}} = \frac{19}{18}\, P^{-1/4}\, T_s^{1/8} \tag{33}$$

$$\frac{a(x)_{block}}{a(x)_{granular}} = \frac{11}{6}\, P^{1/10}\, X^{-1/30} \left(B\Phi T_s^{3/4}\right)^{9/10} \tag{34}$$

$$\frac{H(x)_{block}}{H(x)_{granular}} = 2\,P^{1/10}\,X^{-1/30}\left(B\Phi T_s^{1/2}\right)^{9/10} \quad (35)$$

$$\frac{T(x)_{block}}{T(x)_{granular}} = \frac{13}{18}\,T_s^{1/12} \quad (36)$$

$$T_s = \frac{t_s}{[h+l]/V_s} \quad (37)$$

with the slide width to flume width ratio $B = b_s/b$, the relative front angle of the landslide $\Phi = \sin^{1/2}\phi$, time of underwater slide motion t_s, water depth h, slide length l, and mean slide velocity V_s. It was found that block slides can produce larger, identical or even smaller waves based on the expressions for B, Φ and T_s.

Rzadkiewicz et al. (1997) performed experiments on tsunamis generated by submarine granular landslides by releasing a mass of sand on a hill slope with an angle of 30˚ or 45˚ in a flume 0.3 m wide, 2 m deep and 4 m long. The grain diameter distribution of the three sand types used to model the submarine landslides were: 50 – 250 μm, 0.8 – 2 mm and 2 – 7 mm. The experimental results were modeled numerically with the 2D Navier Stokes model - NASA-VOF2D and a 2D diffusion model was applied to describe the sediment rheology by a Bingham law. The numerical parameters were calibrated with the results of the experiments. The simulations showed that the Bingham diffusion model is not the appropriate model for the study of granular flows, but it reproduced the experimental profiles with acceptable accuracy. Capone et al. (2010) modeled the experiment results using a smooth particle hydrodynamics (SPH) code to simulate the landslide deformation, its water interaction and wave propagation. Variations between the numerical model and the experimental results were attributed to different boundary conditions.

Antunes do Carmo and Carvalho (2011) performed experiment on subaerial landslide generated tsunamis by releasing masses of different materials on a 30˚ to 45˚ hill slope from in a

flume 1 m wide, 1.5 m deep and 40 m long. An opposing sloping headland, simulating a dam, was placed approximately 12 m from the sloping headland. The sliding masses were simulated with several calcareous blocks measuring 0.10 m x 0.08 m x 0.07 m (L x H x W) with a relative density $\rho_s/\rho = 2.38$ and porosity of 0.40. The results from the physical model were compared with two numerical models. The first model was based on the Reynolds-averaged Navier-Stokes (RANS) equations with the free surface described by a volume of fluid (VOF) method. The second numerical model was based on the modified Boussinesq equations. Both models were highly dependent on the inflow boundary condition based on the sliding mass velocity.

Mohammed (2010) conducted a series of experiments on subaerial landslide generated tsunamis in a 3D wave basin measuring 26.5 m wide, 2.1 m deep and 48.8 m long. The granular landslides were generated with a novel pneumatic landslide tsunami generator (LTG) on a 1V:2H slope. The LTG was also used this current phase of experiments and additional details on the LTG can found in the Experimental Setup Chapter. Mohammed modeled the landslide with naturally rounded river gravel with $d_{50} = 13.71$ and a grain size distribution of 12.7 mm to 19 mm. Mohammed and Fritz (2012) produced predictive equations using regression analysis for the leading wave crest amplitude, leading wave trough amplitude and second wave crest amplitude. The predictive wave amplitudes are given by

$$\frac{a_{c1}}{h} = 0.31\, F^{2.1} S^{0.6} \left(\frac{r}{h}\right)^{-1.2F^{0.25}S^{-0.02}B^{-0.33}} \cos\theta \qquad (38)$$

$$\frac{a_{t1}}{h} = 0.7\, F^{0.96} S^{0.43} L^{-0.5} \left(\frac{r}{h}\right)^{-1.6F^{-0.41}B^{-0.02}L^{-0.14}} \cos\theta \qquad (39)$$

$$\frac{a_{c2}}{h} = 1.0\, F^{0.25} B^{-0.4} L^{-0.5} \left(\frac{r}{h}\right)^{-1.5F^{-0.5}B^{-0.07}L^{-0.3}} \cos^2\theta \qquad (40)$$

where a_{c1}, a_{t1} and a_{c2} are the respective leading wave crest, trough and second crest amplitudes, h is the water depth, F is the landslide Froude number, S is dimensionless slide thickness, $S=s/h$,

B is the dimensionless slide width, $B=b/h$, L is the dimensionless slide length, $L=V_s/(sbh)$, and θ is the angular distance from the slide axial direction.

2.3.5 Numerical Modeling of Landslide Generated Tsunamis

Ward (2001) studied tsunamis generated by complex landslides by using a pseudo-Green's function method which sums the tsunamis produced by many smaller slides of various thickness, width, length, orientation and initiation time. The potential collapse of Cubmre Vieja volcano and tsunami generation at La Palma, Canary Islands was modeled by Ward and Day (2001) using this method. Tinti et al. (2011) used this technique to model a historical landslide generated tsunami from the volcanic island of Ischia, Italy. Abadie et al.(2012) modeled the potential Cumbre Vieja volcanic flank collapse and tsumani using a 3D Navier-Stokes model at the source and a 2D Boussinesq to simulate the propagation. Ward and Day (2008) developed a tsunami modeling technique using tsunami balls or packets of tsunami energy. The balls of tsunami energy behave similar to debris avalanche, but without the underlying basal friction. The tsunami ball acceleration allows for a smooth transition from deep water waves through breaking waves and final runup. The tsunami balls behave according to long wave theory in the deep ocean and like a water landslide flooding on land. The 1958 Lituya Bay Tsunami and the 1963 Vajont dam event were modeled using the tsunami ball technique (Ward and Day, 2010; Ward and Day, 2011).

Lynett and Liu (2002) modeled the generation and propagation of submarine landslide generated tsunamis by solving the depth integrated continuity and momentum equations with a high order finite difference model. The model is capable of simulating weakly nonlinear effects or non-dispersive wave systems. The model solutions were compared with experimental data from Hammack (1973) and Watts (1997). Watts et al. (2003) showed that nonlinear and

dispersive propagation models may be necessary for modeling landslide generated tsunamis. Watts et al. (2003) used GEOWAVE, which utilizes the TOPICS (Tsunami Open and Progressive Initial Condition Systems) model for wave generation and the nonlinear Boussinesq wave model, FUNWAVE, for surface wave propagation. Huang et al. (2012) used GEOWAVE to simulate the 2008 Gongjiafang landslide generated tsunami, and the model results matched the field data and witness videos of the event.

Grilli and Watts (1999) developed a 2D fully nonlinear potential flow solver, 2D-FNPF, to model tsunamis generated by submarine landslides in a numerical tank developed by Grilli et al. (1989). The submarine landslide was modeled with a submerged semi-elliptoid on a plane slope. Grilli and Watts (2005) modeled tsunamis generated by submarine slides and slumps. The model was extended to a 3D wave tank by Grilli et al. (2002) to model three-dimensional tsunamis generated by submarine landslides. The underwater slide was modeled by specifying a shape and velocity along the slide boundary. Slide deformation is not incorporated into this model.

Ma et al. (2012) developed a nonhydrostatic wave model, NHWAVE, based on a Godunov-type scheme that solves the incompressible Navier-Stokes equations to simulate wave refraction, diffraction, shoaling, breaking and landslide generated tsunamis in a finite water depth. The model was tested against experimental data and could predict wave shoaling with only three to five vertical layers. The water surface profile and evolution from a landslide generated tsunami was predicted and matched the experimental results.

Multi-phase models can describe the slide rheology and fluid properties of a water body. Multi-phase models generally solve the Navier-Stokes equations in an Eulerian grid for the landslide, air and water. Mader and Gitting (2002) used the SAGE model to obtain the near field wave characteristics of impulse waves generated by subaerial landslide generated tsunamis. The model uses an adaptive mesh refinement (AMR) scheme to simulate the different phases in the

solution. The SAGE model solves the compressible Navier-Stokes equations with a high resolution Godunov differencing scheme. Mader and Gittings (2006) used the model to simulate the 1883 Krakatoa volcanic eruption and tsunami. Queccedo et al. (2004) differentiated and defined the different phases in the landslide generated tsunami process by implementing the level set formulation of the Navier-Stokes equation (Sethian, 1996; Fedkiw et al., 1999). The landslide is modeled as a generalized viscoplastic fluid as proposed by Chen and Ling (1996).

Abadie et al. (2008; 2010) used a volume of fluid (VOF) method to model the landslide and water interaction. The model was validated with solitary waves produced by a Russell-type plunger and impulse waves generated by block and granular landslides. Horrillo (2006) developed a 2D numerical model using the VOF technique to study tsunami wave generation, propagation and runup. Montagna et al. (2011) used the fully three-dimensional commercial code FLOW-3D, based on a VOF technique to simulate the wave generation and inundation from a landslide generated tsunami on a conical island. In contrast, Schwaiger and Higman (2007) used a mesh free Lagrangian hydrocode based on Smooth Particle Hydrodynamics (SPH) to reduce numerical dissipation and improve material interface tracking. Mazzanti and Bozzano (2011) used a SPH code to simulate subaerial and partially submerged landslide propagation coupled with a linear shallow water wave model to simulate the tsunami.

Weiss et al. (2009) modeled the 1958 Lituya Bay, Alaska landslide generated tsunami by adapting the multi-material model, iSALE (Wünnemann et al., 2006). This finite difference hydro code models fluid flows and solid body deformations at subsonic and supersonic speeds (Amsden et al., 1980). Basu et al. (2010) used FLOW-3D to model the Lituya Bay event. Both numerical models matched the experimental results of Fritz et al. (2001) and the measured field runup. Beget and Kowalik (2006) compared tsunami height and inundation from numerical models with field data and historic accounts of the 1883 Augustine tsunami. Calibrating numerical models with field cases can improve model accuracy and validate the models.

Didenkulova et al. (2010) derived analytical solutions for wave generation by submarine landslides on the convex bottom profiles of $h \sim x^{4/3}$ and $h \sim x^4$ using shallow water wave theory. The solutions are expressed in the form of the Duhamel integral. Wang et al. (2011) derived equations to describe the wave generation by a slender, solid subaerial landslide. The solid friction between the beach slope and the bottom of the solid landslide, the fluid viscous (lubrication) friction and the pressure on the wetted surface of the slide were included in the slide motion formulation and wave generation.

2.4 Runup and Rundown

The wave runup is an important parameter for hazard mitigation and design of shoreline structures. Maximum runup predictive equations have been derived analytically and empirically. Hall and Watts (1953) empirically derived a predictive maximum runup equation based on physical experiments conducted at the Waterways Experiment Station (WES) of the U.S. Army Corps of Engineers (USACE), Vicksburg, Mississippi. The experiments produced a solitary wave with a piston-type wavemaker and measured the wave runup on an impermeable beach set to various slope angles. The equation derived by Hall and Watts for the maximum runup on slopes 12˚- 45˚ is

$$\frac{R}{d} = 3.05\, S^{-0.13} \left(\frac{H}{d}\right)^{1.15\, S^{0.02}} \tag{41}$$

with runup height R, slope S, wave height H and still water depth d.

Similar empirical equations for the relationship between the normalized wave runup and the normalized solitary wave height were produced by Camfield and Street (1969) and Kishi and Saeki (1966) using laboratory investigations. No analytical relationship was established between wave theory and these predictive equations.

Carrier and Greenspan (1958) derived a linear analytical solution for wave runup on a sloping beach using a nonlinear transformation and solved several initial value problems. The transformation later became known as the Carrier and Greenspan transformation or CG transformation. Keller and Keller (1964) solved the runup for linear periodic wave propagating along a flat bottom and then up a plane beach. Guza and Thornton (1982) and Holman (1986) analyzed the periodic wave swash or runup on natural beaches.

Synolakis (1987) used the CG transformation to produce the linear and nonlinear solutions for a solitary wave propagating over a flat bottom and then up a plane beach. Synolakis also showed that the linear and nonlinear solutions produced the same equation for the maximum runup. The equation for the maximum runup is referred to as the *runup law* and is

$$\frac{R}{d} = 2.831\,(\cot\beta)^{1/2}\left(\frac{H}{d}\right)^{5/4} \tag{42}$$

with runup height R, runup slope angle β, wave height H and still water depth d.

Sælevik et al. (2013) studied solitary wave runup on a plane and composite beach in a 25 m long, 0.5 m wide and 1 m deep wave tank. The plane beach had an inclination of 10˚ and the composite beach had a 10˚ slope connected to a 4˚ slope above the still water level. The water surface was measured with acoustic wave gauges and the velocity field was measured with particle image velocimetry (PIV). The Synolakis (1987) maximum runup equation consistently over predicted the maximum runup on the plane beach. The discrepancy may be due to scaling effects and the breaking wave assumption used in the equation was not valid in the experiment. Experimental results were compared to numerical simulations using an incompressible Navier-Stokes solver, and the water surface was described with a volume of fluid (VOF) technique. The runup process was very similar between the plane and composite beach.

Madsen and Schäffer (2010) produced analytical solutions for a tsunami wave propagating along a constant depth and running up a plane beach. Solutions for a single wave, N-

wave and transient waves were produced. The maximum runup height and maximum rundown elevation for a single wave condition is given by

$$\frac{R_{up}}{d} = 2.831\ (\cot\beta)^{1/2}\ \left(\frac{H}{d}\right)^{5/4} \tag{43}$$

$$\frac{R_{down}}{d} = -1.125\ (\cot\beta)^{1/2}\ \left(\frac{H}{d}\right)^{5/4} \tag{44}$$

with the maximum runup and rundown elevation R_{up} and R_{down} respectively, runup slope β, wave height H and still water depth d. Clearly, the maximum runup equation produced by Madsen and Schäffer (2010) equals Synolakis (1987). Özeren and Postacioglu (2012) used a CG transformation to derive a numerical solution for the nonlinear wave runup and rundown, but an asymptotic maximum and minimum were not established.

Cnoidal wave runup was studied by Synolakis et al. (1988) with the water surface described by

$$\eta(x,t) = y_t - 1 + H\ cn^2[2K\left(\frac{x}{L} + \frac{t}{T}\right)\Big| m] \tag{45}$$

where y_t is the distance from the trough to the bottom. H, L and T are the dimensionless wave height, length and period, respectively. $K(m)$ is the first elliptical integral with m as the elliptical parameter. The function $cn\ (z|m)$ is the Jacobian elliptic function. Using the linear theory described by Keller and Keller (1964), Synolakis obtained the maximum runup height as

$$\frac{R_{up}}{h_o} = 2\,\zeta_2 + \frac{4\,\pi^2}{m\,K^2}\,\frac{H}{h_o}\,\max\left\{\sum_{i=0}^{\infty}\frac{q^{2i+1}}{(1+q^{2i+1})^2} + \sum_{i=0}^{\infty}\sum_{j=0}^{\infty}\frac{q^{i+j+1}\,(M_{ij}+N_{ij})}{(1+q^{2i+1})(1+q^{2j+1})}\right\} \tag{46}$$

where $q = \exp(-\frac{\pi K'}{K})$ with $K' = K(1-m)$. M_{ij} and N_{ij} are described as

$$M_{ij} = \sqrt{\hat{k}_{ij}\pi\, X_o}\cos\left(\hat{k}_{ij}(X_o - ct) - \frac{\pi}{4}\right) \quad (47)$$

$$N_{ij} = \sqrt{\hat{k}_{ij}\pi\, X_o}\cos\left(\tilde{k}_{ij}(X_o - ct) - \frac{\pi}{4}\right) \quad (48)$$

where $\hat{k}_{ij} = \frac{2\pi(i+j+1)}{\lambda}$ and $\tilde{k}_{ij} = \frac{2\pi|i-j|}{\lambda}$. Equation 46 varies slightly from the equation given by Synolakis et al. (1988) to account for possible typos addressed in Chan and Liu (2012).

Whittaker and Watson (1927) described the cnoidal wave water surface in terms of a series of sinusoidal progressive waves given by as

$$\zeta(x,t) = \sum_{n=1}^{\infty} \tilde{A}_n \cos(\tilde{\Omega}_n(t-\tilde{t})) \quad (49)$$

where $\tilde{A}_n = H\,\frac{2\,\pi^2}{m\,K^2}\,\frac{n\,q^n}{1-q^{2n}}$, $\tilde{\Omega}_n = \frac{2\,n\,\pi}{T}$ and $\tilde{t} = -\frac{x}{c}$. Chan and Liu (2012) applied the methods described by Madsen and Schäffer (2010) to this surface profile to derive the cnoidal runup solution for the moving shoreline (*U, R*) as

$$U(\tau) = \sum_{n=1}^{\infty} \frac{2\,\tilde{A}_n}{s}\sqrt{\pi\,\tilde{\Omega}_n^3\,t_o}\sin\left(\tilde{\theta}_n + \frac{\pi}{4}\right) \quad (50)$$

$$R(\tau) = \sum_{n=1}^{\infty} 2\,\tilde{A}_n\sqrt{\pi\,\tilde{\Omega}_n\,t_o}\cos\left(\tilde{\theta}_n + \frac{\pi}{4}\right) - \frac{U^2}{2\,g} \quad (51)$$

where $\tilde{\theta}_n = \left(\tilde{\Omega}_n\,\tau - 2\,t_o + \frac{X_o}{c}\right)$, $\tau = t - \frac{U(\tau)}{s\,g}$ and s is the slope of the beach.

2.5 Edge Waves

Stokes (1846) described the trapped edge wave phenomenon on a plane beach and Ursell (1952) derived the first full edge wave solution with the fundamental zeroth mode resulting the Stokes' edge wave solution. Ursell (1952) derived the edge wave dispersion relationship as

$$\omega^2 = gk_y \sin(2n+1)\,\alpha \qquad (52)$$

with n=0, the wave frequency ω, the lateral wave number k_y and the hill slope angle α.

Eckart (1951) derived the solution for the shallow water wave edge wave on a plane slope. Smith and Sprinks (1975) used a similar technique and Eckhart (1951) and obtained the asymptotic zeroth mode edge wave dispersion relationship on a curvilinear shoreline as

$$\omega^2 \approx gk_y \tan\,\alpha\,\left[1-\frac{1}{4}\left(k_y r_c\right)^{-1}\right]^2 \qquad (53)$$

where ω is the wave frequency, k_y is the lateral wave number, α is the slope angle and r_c is the island radius at the undisturbed waterline. Seo and Liu (2013) compared the profiles of the shallow water edge wave theory to the full linear edge wave theory on a plane slope and found that when the bottom slope was less than or equal to 0.01, the shallow water solution was a suitable approximation for the full linear solution.

Longuet-Higgins (1967) studied the effect of the trapped shallow water edge waves on planar slopes and around conical islands. Longuet-Higgins determined that the perfect wave trapping on typical conical islands was impossible because the average angular velocity is given by $(gh)^{1/2}/r$ and in order for the wave energy to be refracted inwards the angular velocity must remain constant or increase, requiring the water depth, *h*, to increase proportionally to r^2. Lautenbacher (1970) used shallow water wave theory to numerically study refractive influence of conical island bottom topography on normally incident waves and observed that maximum inundation

could occur on directly in line with the wave, on the side of the island or on the lee side of the island.

Gonzales et al. (1995) noted that edge waves from coastal disturbances such as tsunamis can be discriminated. Shore trapped edge waves produced by the oblique energy from subaerial landslide generated tsunamis have been observed in experimental testing by Chang (1995), Liu and Yeh (1996), Liu et al. (1998), Liu et al. (2005), Lynett and Liu (2005) and Di Risio et al. (2009a). Sammarco and Renzi (2008) derived an analytical model to study transient edge waves traveling along the shoreline and compare the model to experimental data described by Di Risio et al. (2009a). Renzi and Sammarco (2012) extended the study to analyze the effects of the slide shape and continental shelf on the generated waves. Renzi and Sammarco (2010) derived another analytical model for the edge waves propagating around a conical island and the results were compared to the plane beach model.

Lynett and Liu (2005) used a series of depth integrated numerical model simulations to analyze the lateral runup and rundown produced by subaerial and submarine landslide motion. Predictive equations were produced to describe the lateral wave propagation. The near field was described as the shoreline, adjacent to the landslide projection, where the source-specific dominate the wave field. Source-specific waves decay rapidly from the source due to amplitude spreading. Far field is defined as the shoreline, displaced from the landslide projection, where the edge waves become important. Lynett and Liu (2005) estimated the near-far field division for subaerial landslides to be given by

$$\frac{y}{W} \approx 5 \tag{54}$$

where y is lateral distance and W is width of the slide. The runup at the near-far field division is given by

$$\frac{R}{\Delta h} \approx 0.1\,\epsilon^{-1/4}\gamma \qquad (55)$$

where R is the runup height, Δh is the maximum vertical slide thickness, ϵ is the ratio of Δh to the vertical distance from the water level to the landslide starting position and γ is the ratio of the slide density to the water density.

Edge wave propagating along a curved coastline such as an island have been studied. Yeh et al. (1994), Briggs et al. (1995) and Liu et al. (1995) performed physical experiments to simulate the tsunami wave which impacted Babi Island, Indonesia on 12 December 1992 as a result of the Flores M_w 7.5 earthquake. During the event the original tsunami was split into two waves, with one wave propagating around each side of the island. The two trapped edge waves collided on the lee side of the island and created an amplification of the wave runup. A concrete conical island was built with a base diameter of 7.2 m and height of 0.625 m with side slopes of 1V:4H in a basin that was 30 m wide and 25 m long. A solitary wave was generated with a directional piston wave maker. The solitary waves had wave height to depth ratios ranging from 0.05 to 0.20. The experiments produced results similar to the field case where the runup was amplified on the lee side of the island.

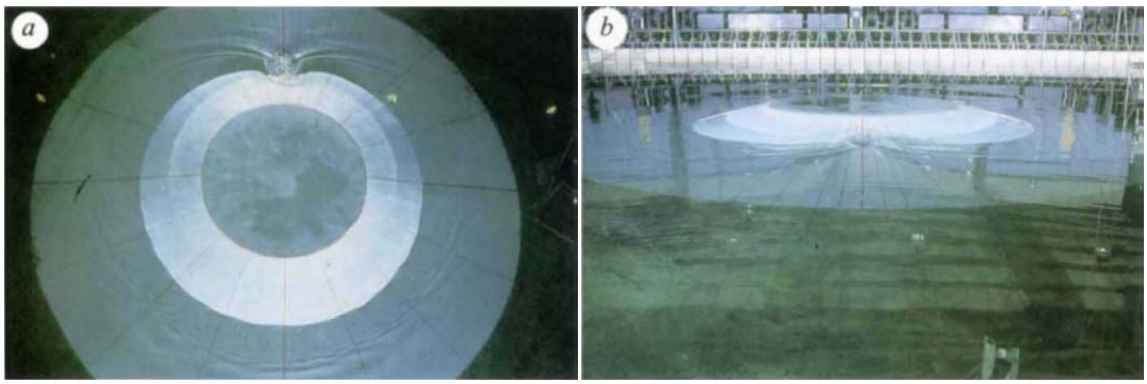

Figure 12: Views of the wave runup on the rear side of the island from the laboratory model of Yeh et al. (1994) (a) top view; the wave struck the island from the bottom of the photo, (b) profile view of the rear of the island.

Di Risio et al. (2009b) physically modeled scenarios similar to the tsunamigenic volcano flank collapse at Stromboli, Italy on 30 December 2002. A conical island 8.9 m in diameter and 1.2 m tall with a 1V:3H side slope was constructed in a basin that was 50 m long, 30 m wide and 3 m deep. A block in the shape of half an elliptoid with a major axis dimension of 0.8 m was slid down the side of the island. Runup gauges were installed in the conical island to measure the runup around the island. The reference origin was the center of the island and the reference angle, θ, was the angular distance from the slide trajectory.

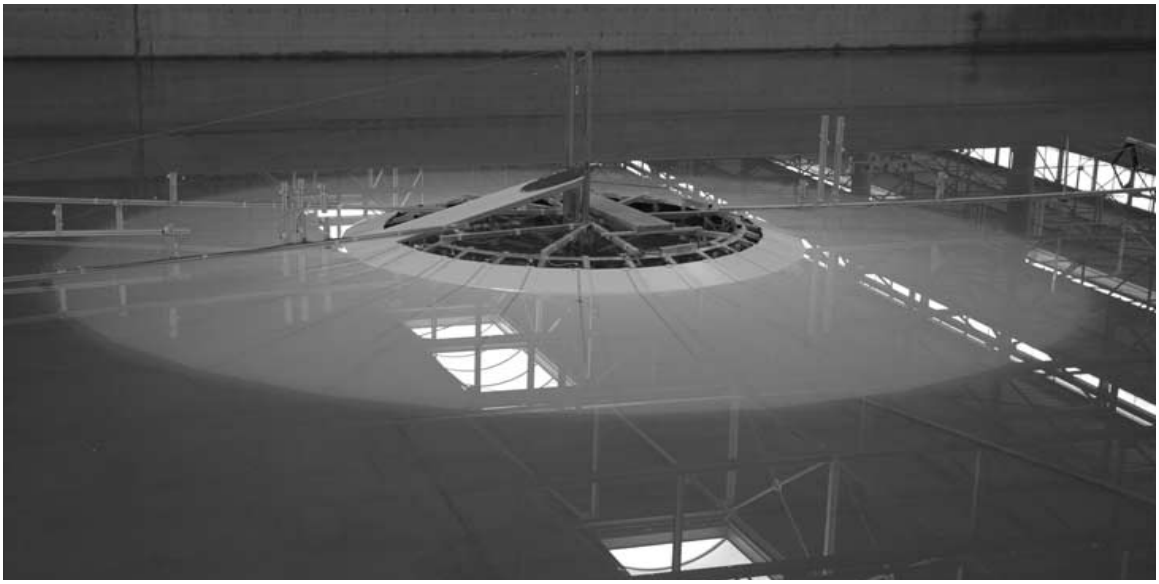

Figure 13: Conical island setup of Di Risio et al. (2009b).

Di Risio et al. (2009b) determined that the first wave produced the maximum runup and rundown for the first 90˚, then the second wave produced the largest runup, followed by the third wave and sometimes the fourth wave would produce the largest wave before the two trapped waves wrapping around both sides of the island would collide at the θ=180˚ mark. This behavior

is typical of frequency dispersive waves with the wave energy travels at the group velocity, which is slower than the wave celerity. The maximum runup increases from the slide impact location to a distance approximately two slide widths away, then begins to decay as it propagates around the island until the two waves collide on the lee side of the island creating a localized amplification of the runup.

2.6 Conclusions from Previous Studies

The following conclusions are drawn from the literature review:

- Landslide generated tsunamis are generally smaller in length and period than tectonically generated tsunamis and are typically in the intermediate water depth wave regime.
- Solid block landslide models dissipate kinetic energy when a block abruptly impacts the tank bottom or is stopped by another type of braking mechanisms during experiments, thereby reducing conversion into wave energy.
- Solid block landslide models do not incorporate slide deformation and do not produce long subaqueous run-out lengths.
- Predictive equations produced by solid block landslide models may overestimate the maximum wave height compared to granular slide models.
- The first wave from landslide generated waves may not be the largest.
- The lateral wave runup adjacent to the landslide can be very hazardous.
- The first wave could initially produce the largest lateral runup adjacent to the landslide impact, but subsequent waves could produce the largest runup as propagation distance increases.
- The governing parameters of landslide generated wave generation are: the landslide impact velocity v_s, landslide width b, landslide thickness s, landslide volume V_s,

landslide density ρ_s, landslide porosity n, landslide hill slope angle α, water density ρ_w and still water depth h.

- Three-dimensional wave height attenuation parameters are the dimensionless radial distance from the source *r/h*, the propagation direction θ and the wave generation parameters.
- The maximum wave height in three-dimensional models is in the axial landslide direction.
- Not all conclusions derived for subaerial, partially submerged and submarine landslides are universally applicable.
- Data from physical models can be used to calibrate and validate numerical models.
- Depth integrated wave models are not appropriate for modeling impulsively generated waves because the vertical velocities cannot be neglected in the near field.
- Complete Navier-Stokes solving models simulate the tsunami wave generation by landslides well.
- Predictive empirical equations produced from physical models are difficult to apply to real world scenarios because of bathymetric effects.

2.7 Identified Research Gaps

The following research gaps are observed in the literature review:

- Physical modeling of landslides generated tsunamis with granular landslide material has not been tested in a conical island configuration.
- Surface reconstruction of 3D deformable landslides has not been performed with modern instrumentation, i.e. stereo particle image velocimetry setup.
- Predictive equations for the lateral runup height and amplitude attenuation from subaerial landslide generated waves have not been produced.

- The effects of complicated bathymetric geometry like fjords or conical islands have not been studied with granular landslide material.
- Physical data to validate three-dimensional numerical models is insufficient and does not incorporate wave runup.
- The understanding of the landslide generated tsunami hazard is not adequate enough to be incorporated in FEMA hazard maps and mitigation plans.

CHAPTER III

EXPERIMENTAL SETUP

3.1 Introduction

Physical experiments on tsunamis generated by subaerial unconfined deformable granular landslides were executed at the O.H. Hinsdale Wave Research Laboratory at Oregon State University in Corvallis, Oregon. A novel Landslide Tsunami Generator (LTG) was deployed in the tsunami wave basin (TWB) of the George E. Brown Network of Earthquake Engineering Simulation (NEES) at Oregon State University. The initial deployment of the LTG is described by Mohammed (2010). An overview of the physical model and instrumentation deployed is provided in this chapter.

3.2 Dimensional Analysis

Dimensional analysis applied to fluid mechanics is described in detail in Hughes (1993), Dalrymple (1985) and Yalin (1971) among others. Dimensional analysis alone cannot obtain a complete solution or reveal the inner mechanism of a phenomenon. The Π theory subtracts the number of fundamental dimensions, o, such as mass, length and time, from the number of governing independent parameters, n, to determine the number of dimensionless parameters, m (Buckingham, 1914). The equation $m = n - o$ produces the governing dimensionless parameters $\Pi_1, \Pi_2, \ldots, \Pi_m$. Arbitrariness in the determination of the conditions of similitude occurs when the number of dimensionless parameters exceeds six (Birkhoff, 1950). The governing independent parameters are listed in **Table 2**.

Table 2: Governing parameters for tsunamis generated by granular landslides

Symbol	Description	Dimension	Fundamental Dimension
b	Slide width	[m]	[L]
s	Slide thickness	[m]	[L]
l_s	Slide length	[m]	[L]
V_s	Slide volume	[m^3]	[L^3]
v_s	Slide velocity	[m/s]	[LT^{-1}]
h	Water depth	[m]	[L]
ρ_s	Slide density	[kg/m^3]	[ML^{-3}]
ϕ'	Slide internal friction angle	[°]	[-]
d_{50}	Median grain diameter	[m]	[L]
δ	Basal friction angle	[°]	[-]
ρ_w	Water density	[kg/m^3]	[ML^{-3}]
α	Hill slope angle	[°]	[-]
r	Radial propagation distance	[m]	[L]
θ	Propagation direction	[°]	[-]
t	Time	[s]	[T]
g	Gravitational acceleration	[m/s^2]	[LT^{-2}]
Φ	Angular direction of lateral propagation around conical island	[°]	[-]
r_c	Conical island shoreline radius	[m]	[L]

A total of 18 independent parameters governing the tsunami generation by granular landslides and subsequent wave propagation have been identified. The last two independent parameters, Φ and r_c, only apply to the conical island configuration discussed in the subsequent section. Water viscosity is not included in the list of parameters. Both the landslide and water waves are driven by gravity. The physical model is designed to minimize the scale effects of the water viscosity, and the viscous dampening of the wave attenuation due to the bottom boundary layer is approximately 1% per 10 m of propagation distance according to Keulegan (1948). The drag forces applied to the submerged landslide consist of skin friction drag, which is dependent on the water viscosity, and form drag. Froude similarity models are scaled to minimize the skin friction drag compared to the form drag, thereby minimizing the effects of water viscosity (Hughes, 1993). The gravitational acceleration, g, hill slope angle, α, water density, ρ_w, internal friction angle, ϕ', and basal fiction angle, δ, remain constant in this study. The slide width, thickness and length dimensions are considered at water impact. The slide length at impact is included and defined as $l_s = V_s/(bs)$ in terms of the slide width and thickness at impact. The mass of the slide is not redundantly listed because it is a function of the bulk slide density and the slide volume given by the equation $m_s = \rho_s V_s$. The bulk slide density is defined as

$$\rho_s = (1-n)\,\rho_g \tag{56}$$

in terms of granulate density, ρ_g, and the slide porosity, n. The slide porosity includes the effects of the granulate size distribution and shape. The granulate shape would additionally affect the landslide internal friction angle. Further description of the landslide granulate size and shape is discussed in Section 3.5 Granular Landslide Material. The time of underwater slide motion, t_s, is not considered in this study because of the poorly defined end of slide motion compared to a solid block abruptly stopping on a basin floor (Fritz, 2002). The governing nondimensional parameters for tsunami generation and propagation by granular landslides are listed in **Table 3**.

Table 3: Nondimensional governing parameters for tsunamis generated by granular landslides

Dimensionless Parameter	Description
$\Pi_1 = F = v_s/\sqrt{(gh)}$	Slide Froude Number
$\Pi_2 = B = b/h$	Relative slide width
$\Pi_3 = S = s/h$	Relative slide thickness
$\Pi_4 = V = V_s/h^3$	Relative slide volume
$\Pi_5 = D = \rho_s/\rho_w$	Relative slide density
$\Pi_6 = D_g = d_{50}/h$	Relative slide grain size
$\Pi_7 = \phi'$	Slide internal friction angle
$\Pi_8 = \delta$	Basal friction angle
$\Pi_9 = \alpha$	Hill slope angle
$\Pi_{10} = R = r/h$	Relative propagation distance
$\Pi_{11} = \theta$	Propagation direction
$\Pi_{12} = R_c = r_c/h$	Relative conical island radius
$\Pi_{13} = \Phi$	Angular direction around conical island
$\Pi_{14} = T_r = t\,(g/h)^{1/2}$	Relative time

A total of 14 dimensionless parameters which govern the tsunami generation and propagation by granular landslides have been identified. The hill slope angle, relative slide density, slide internal friction angle and basal friction angle are the only dimensionless parameters which are constant in this study. The predictive equations are derived in this study using a multi-variable regression analysis of the dimensionless parameters. The predictive equations were simplified by excluding the dimensionless parameters with minor effects.

3.3 Physical Model

The physical experiments were performed at the George E. Brown Network of Earthquake Engineering and Simulation (NEES) tsunami wave basin (TWB) at Oregon State University in Corvallis, Oregon. The concrete tsunami wave basin is 48.8 m long, 26.5 m wide and 2.1 m deep. The east wall of the TWB is equipped with a long stroke, directional wave maker which was not used and remained static during these experiments. The landslide tsunami generator (LTG) was placed at the opposite end of the wave basin from the wave maker. A moveable instrumentation bridge spans across the entire 26.5 m width of the TWB. The bridge measures 1.4 m wide between the outside of the bridge frame where the wave gauges can be attached.

The previous phase of experiments described by Mohammed (2010) used the LTG to study the wave generated by a landslide off a ramp into an open basin. This series of experiments used the LTG in several more complex topographic and bathymetric configurations. The current set of experimental scenarios was conducted in two phases. The first phase was performed in 2010 and tested scenarios in **Figure 14** and **Figure 15**. The second phase was performed in 2011and tested the conical island scenario in **Figure 16**. The instrumentation was consistent in both phases except for the particle image velocimetry (PIV) setup. A planar PIV setup was used in the first phase and a stereo PIV setup was used in the second phase. Details of the PIV setup are discussed in Section 3.6.3 Particle Image Velocimetry.

The first topographic setting is the fjord scenario. The fjord configuration consists of the LTG mounted to a ramp with an opposing headland ramp 5.52 m from the toe of the landslide ramp. Both the landslide ramp and the opposing headland ramp were built at a slope of 1:2 (vertical:horizontal) or $\alpha = 27.1^{\circ}$. Wave gauges were strategically placed in the basin along rays at various angles from the landslide source to describe the tsunami wave angular dependence. In

repeated experimental trials the movable instrumentation bridge was placed at two alternating positions: the center of the fjord and adjacent to the opposing headland ramp.

The next scenario tested in this phase of experiments is the curved headland setting. This configuration is inspired by the opposing headland in the Gilbert Inlet of the Lituya Bay, Alaska (1958) event (Miller, 1960; Fritz et al., 2001; Fritz et al., 2009). The LTG was mounted to the same landslide ramp as noted in the previous scenario, but in contrast a 90˚ bend is introduced in the opposing headland ramp. Half of the opposing headland faced the landslide ramp and the other half is rotated 90˚. The two ramps are connected with a 90˚ conical section. The distance between the two opposing ramp sections is 5.52 m between the ramp toes, corresponding to the fjord scenario.

The third scenario was the basin-wide propagation and runup configuration. In this setting the LTG was attached to the same ramp and a plane opposing headland ramp was placed 23.0 m from the toe of the landslide ramp. The curved headland and the basin-wide propagation and runup scenarios are shown in **Figure 15**.

The final scenario tested is the conical island setting. This configuration was tested in the second phase of experiments, and simulates a landslide off an island or a volcano flank collapse. The conical island had a diameter of 10 m at the base and a slope of 27.1˚, corresponding to the ramp slope in previous scenarios.

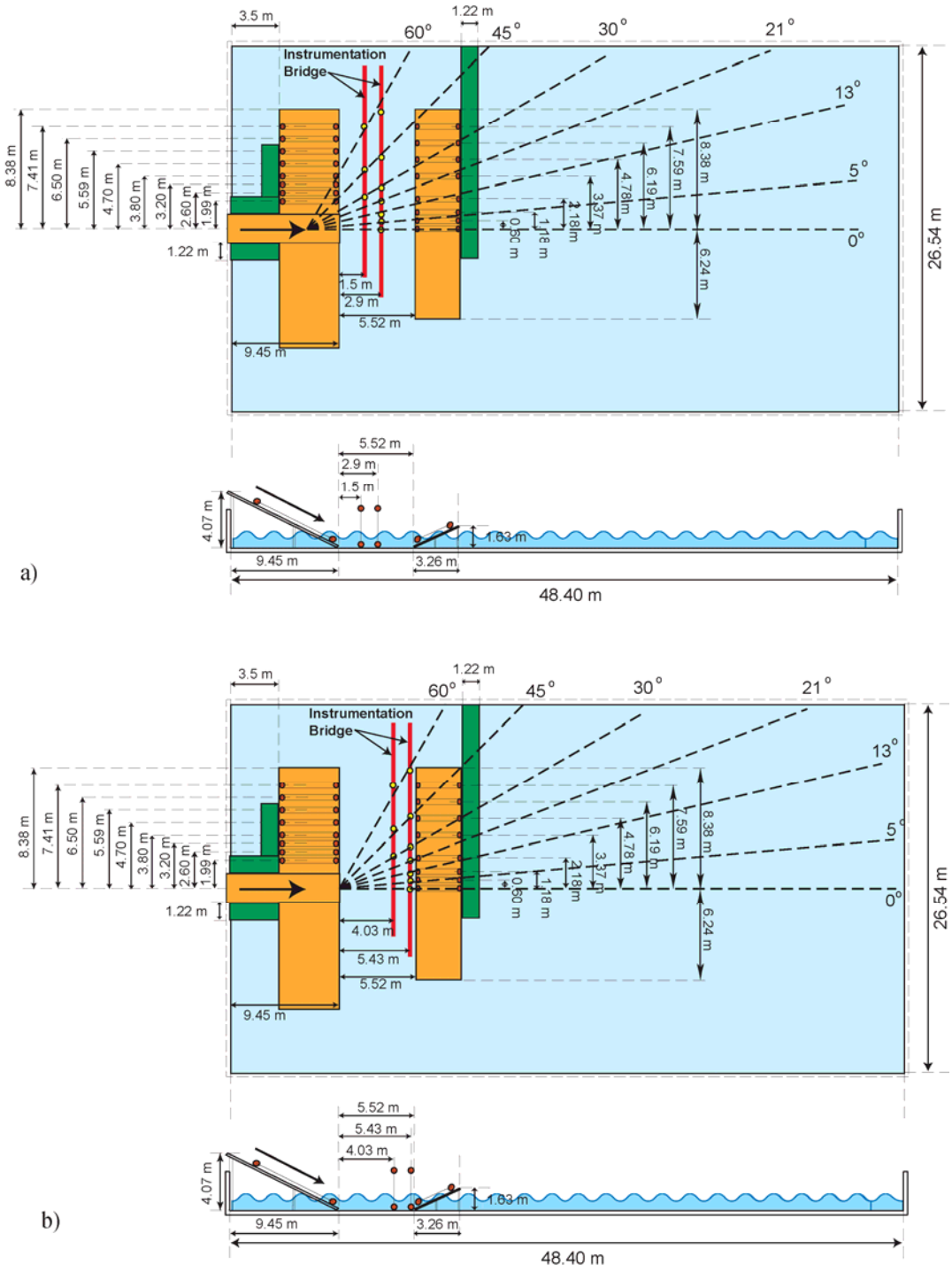

Figure 14: Fjord scenario from the 2010 phase of experiments: (a) with instrumentation bridge 1.5 m from landslide ramp toe and (b) instrumentation bridge position 4.03 m from landslide ramp toe. Resistance wave gauges and runup wave gauges are shown with yellow and red circles.

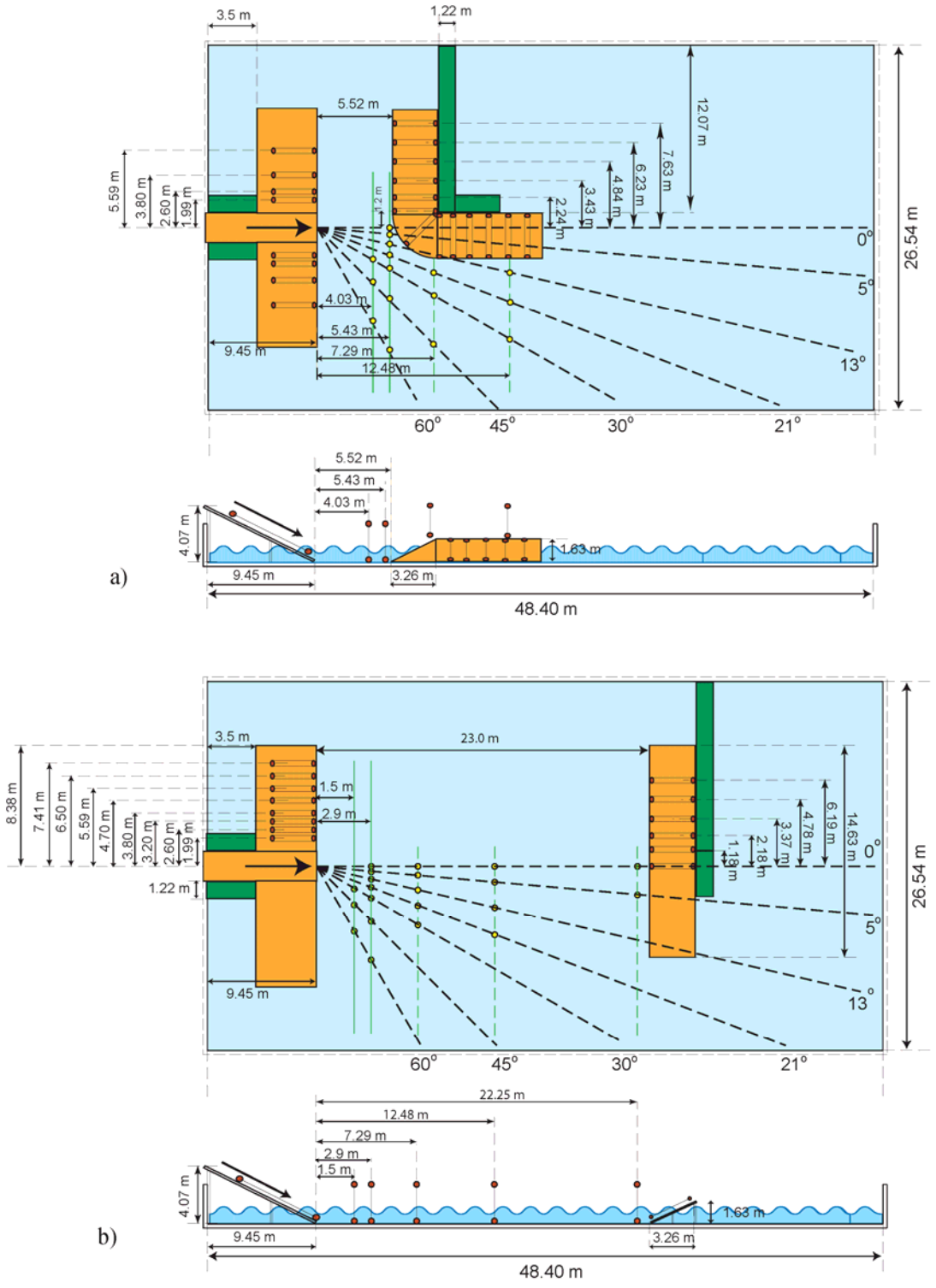

Figure 15: Additional scenarios from the 2010 phase of experiments: (a) curved headland and (b) basin-wide propagation and runup. Resistance wave gauges and runup wave gauges are shown with yellow and red circles.

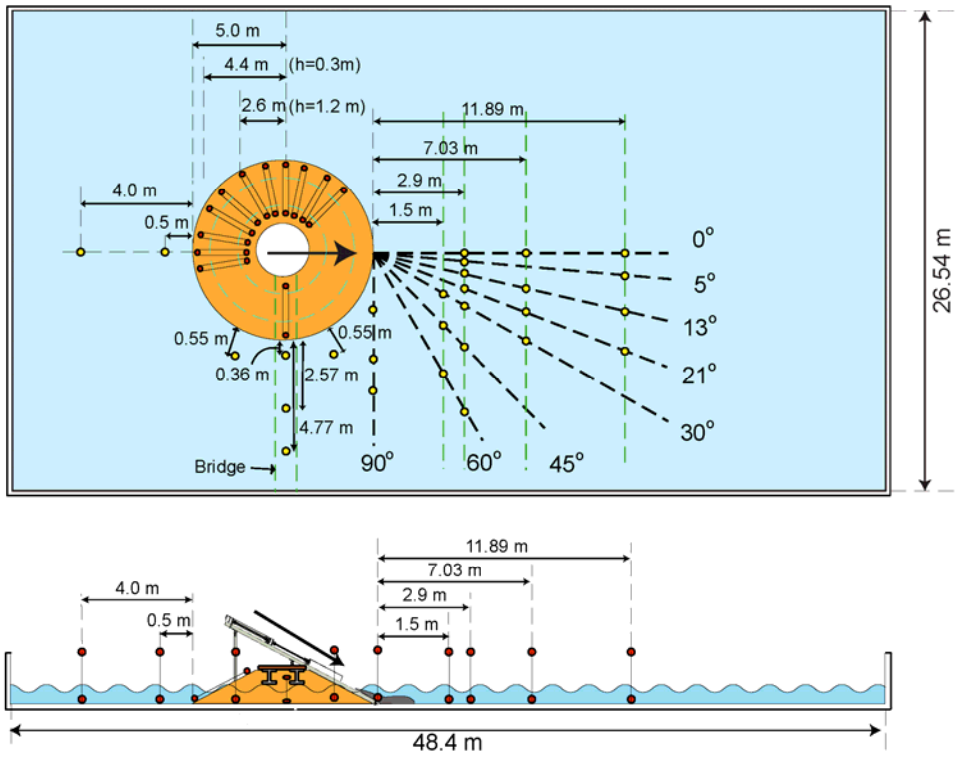

Figure 16: The conical island scenario from the 2011 phase of experiments. Resistance wave gauges and runup wave gauges are shown with yellow and red circles.

The fjord scenario and the conical island scenario were scanned using light detection and ranging (LiDAR) equipment to create a three dimensional point cloud of the basin, instrumentation and constructed scenario surfaces. The point cloud allows for three dimensional surface reconstruction of the basin and experimental setup. The LiDAR scanner used was a RIEGL VZ-400 (http://www.riegl.com/nc/products/terrestrial-scanning/produktdetail/product/scanner/5/). An image from the LiDAR scan of the conical island scenario is shown in **Figure 17**.

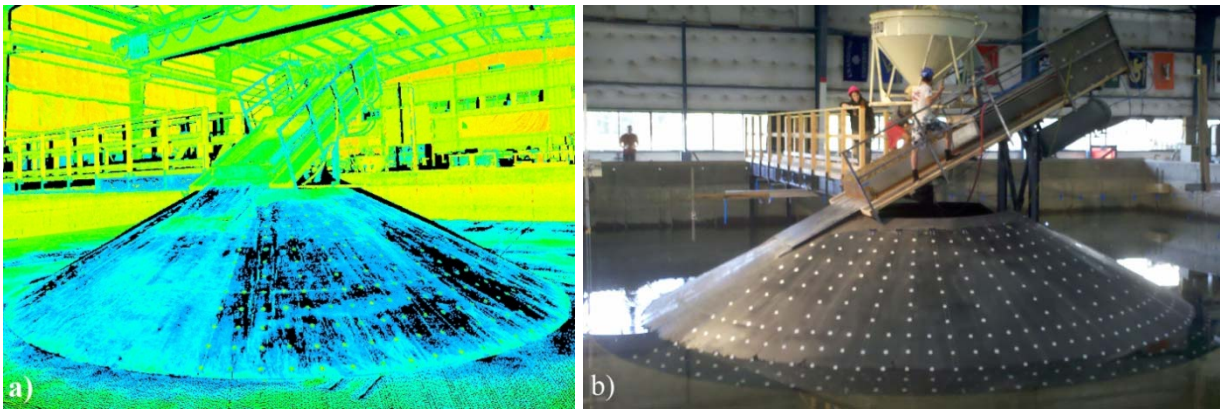

Figure 17: Conical island setup: (a) reflectance image from the LiDAR scan of the conical island scenario and (b) photo of the conical island scenario taken from a similar perspective as the LiDAR scan image.

3.4 Pneumatic Landslide Tsunami Generator

The initial landslide accelerations and shapes were controlled by a pneumatic landslide tsunami generator (LTG). The design of the LTG is an extension of the two dimensional pneumatic tsunami generator designed by Fritz and Moser (2003). The initial deployment of the LTG in the tsunami wave basin in 2006 is discussed by Mohammed (2010). The LTG can simulate landslides with varying geometry and kinematics. The landslide material is loaded into a 2.1m x 1.2m x 0.3m aluminum slide box riding on UHMWPE-plastic gliders with lateral rail guides and accelerated by four pneumatic pistons as shown in **Figure 18**. The landslide volume can be reduced with the installation of a vertical divider plate in the slide box.

The four pneumatic pistons consist of a standard double-acting stainless steel cylinder with rods and have a piston diameter of 0.1 m with a stroke length of 2 m. The pneumatic circuit for the box motion consisted of separate branches for the forward and backward thrusts. A 2-stage stationary air compressor with an integrated 0.303 m^3 air reservoir supplies the compressed air to a pressure regulated 0.303 m^3 air reservoir connected directly to the solenoid valves at the piston ends. A precision proportional pressure regulator adjusts the reservoir air pressure

between 4 and 10 bar prior to the launch. The pneumatic system was controlled with preset trigger signals, while proximity switches served as safety. Prior to each experiment the trigger settings were determined and programmed to the integrated controller. The slide box is launched by ventilation resulting in an initial acceleration larger than gravity, g. The flap initially containing the granular material in the slide box opens mechanically with the initiation of downhill box motion. The maximum box velocity v_B was reached approximately at half stroke and the landslide material was released from the confined box motion into a purely gravity driven landslide. The valves at both cylinder ends were switched to decelerate the slide box pneumatically. The design of the LTG mimics natural landslide motion on the hill slope, where some landslides initially move as a solid block, followed by disintegration under the influence of basal friction, internal friction and gravity to collapse into a debris avalanche on a hill slope.

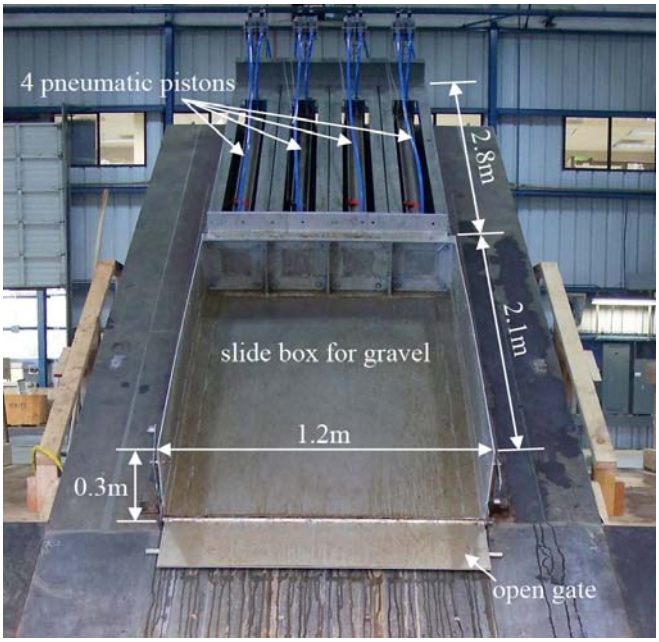

Figure 18: Pneumatic landslide tsunami generator (LTG) mounted on the hill slope ramp with the slide box retracted and the gate open.

The slide box position along the piston stroke was measured with cable extension transducers. **Figure 19** shows the box position for the four tested initial pneumatic pressure settings: 4, 6, 8 and 10 bar. A wavelet filter denoised the position data and the box velocity was determined by the derivative of the box position. The box acceleration was determined by the second derivative of the box position. The measured peak box velocity exceeded 4 m/s.

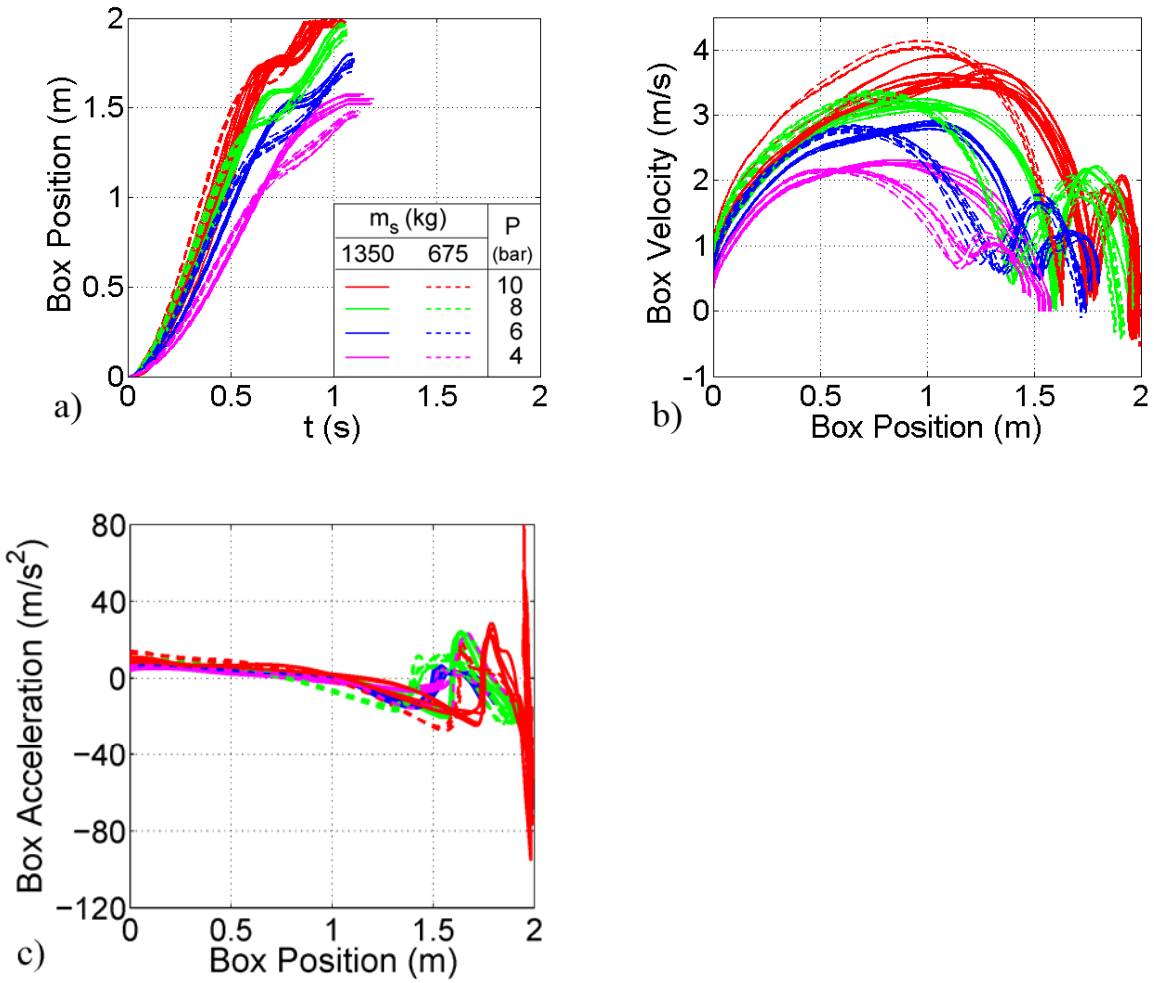

Figure 19: Measured LTG (a) box position, (b) box velocity and (c) box acceleration for various initial pneumatic settings.

3.5 Granular Landslide Material

The landslides were predominantly modeled with naturally rounded river gravel with $d_{50} = 13.71$ mm within a sieve size range of 12.7 mm to 19.05 mm. The naturally rounded river gravel is shown in **Figure 20a**. Larger naturally rounded river cobbles were also used in the conical island scenario to study any variation in the landslide and wave characteristics. The cobbles were larger than the 19 mm sieve size and had a gradation much larger than the gravel. Some of the cobbles were larger than 100 mm in all dimensions. The naturally rounded river cobbles are shown in **Figure 20b**. Both the naturally rounded river gravel and cobbles were acquired from Green and White Rock Products Inc. in Corvallis, Oregon out of the Willamette River. The following slide properties are applicable to both the naturally rounded river gravel and cobbles:

- Slide grain density, $\rho_g = 2.6$ t/m^3
- Bulk slide density, $\rho_s = 1.76$ t/m^3
- Porosity, $n = 0.31$
- Internal friction angle, $\phi' = 41^\circ$
- Basal friction angle on steel, $\delta = 23^\circ$

Experiments were conducted with two landslide volumes, V_s, of 0.756 and 0.378 m^3 corresponding to landslide masses m of 1350 kg and 675 kg.

Figure 20: Landslide granulate: (a) Naturally rounded river gravel predominately used to the model three-dimensional deformable landslides and (b) naturally rounded river cobbles used as a second landslide material in the conical island scenario.

3.6 Instrumentation Deployed in the Tsunami Wave Basin

3.6.1 Wave Gauges

An array of resistance wave gauges were strategically placed in the wave basin for each scenario to measure wave and runup profiles. Two different types of resistance wave gauges were installed in the TWB: cantilever and wire wave gauges. Both gauges have a similar design, but the cantilever resistance wave gauges use two stainless steel rods as conductor probes and the wire gauges use two stainless steel wires as conductor probes. The cantilever gauges can be attached to the movable instrumentation bridge, but the wire gauges have to be fixed to a structure or the basin floor.

The wave gauge consists of two equally spaced conductor probes immersed in water. The conductivity of the water is used to determine the water surface elevation. When a constant voltage is applied across the conductors, the resistance is varied by the water surface elevation

and by Ohm's Law the current drawn between the conductors is varied. The resistance wave gauges used in the experiment consists of an oscillator that produces a constant amplitude 20 volt peak-to-peak 10 kHz sine wave and the circuit is based on the Wein bridge oscillator. The output of the oscillator is AC coupled to a differential probe drive. A high speed 100 milliamp current booster is used to produce the current required to drive the probe. The current sensing is performed by measuring the voltage drop across a 1 Ohm resistor placed in series with the probe. The sensed 10 kHz voltage is AC coupled to an instrumentation amplifier with an output of a single 10 kHz signal which is amplitude modulated by the change in current in probe induced by changes in the water surface elevation. The signal is demodulated with a full wave precision rectifier which also acts as a low-pass filter. The output of the rectifier filter combination is an analog voltage signal proportional to the wave height. A diagram of the resistance wave gauge is seen in **Figure 21b**. The voltage is converted to a physical elevation by multiplying the voltage by a calibration coefficient.

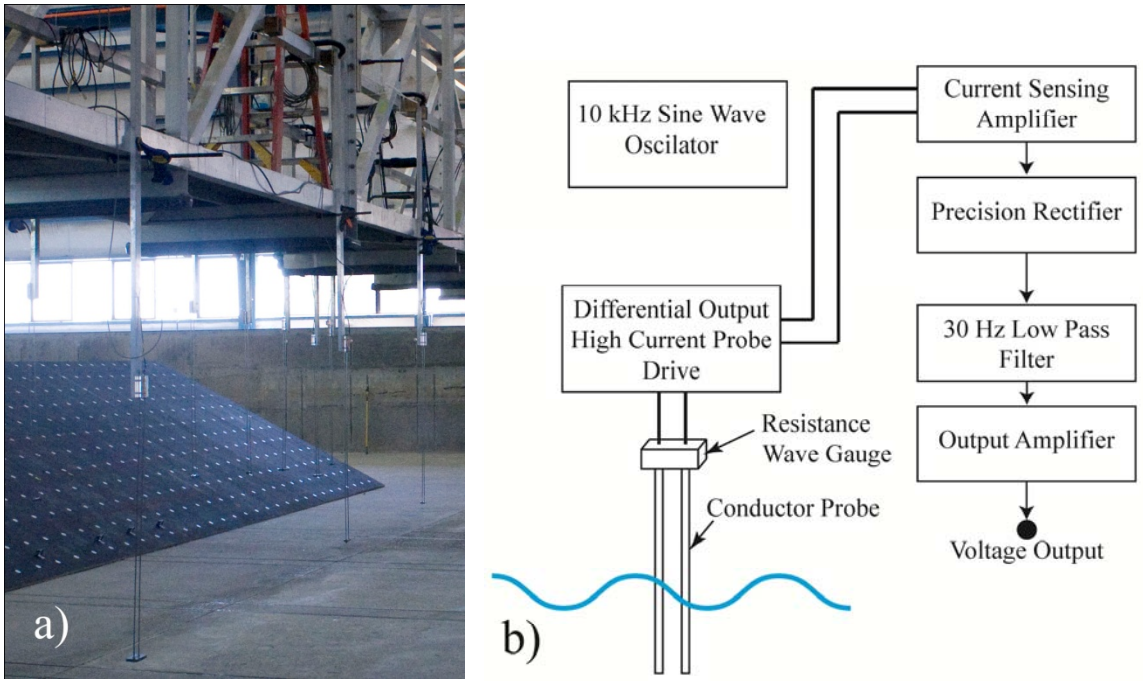

Figure 21: Resistance wave gauges: (a) Cantilever types mounted to the instrumentation bridge, (b) diagram of the circuit configuration.

Calibration coefficients were determined during the filling and draining of the basin. An ultrasonic transmitter-receiver measured the water surface elevation and the calibration coefficients were determined by simultaneously comparing the analog voltage recorded for each gauge. The gauges generally exhibit a nominal sensitivity of 0.2 V/cm and the calibration has proven them to be very linear over a 0.5 m range with a 0.7% error over the length of a cantilever gauge probe.

The cantilever wave gauges consists of two 3.2 mm diameter stainless steel rods which are 0.72 m long. The rods are spaced 254 mm apart with plastic lucite plates. The probes are connected to the circuit with 20 gage wire. The runup was measured using a hybrid system consisting of wire resistance gauges and overlapping camera recordings. The runup gauges are validated with image processing of the camera recordings. The wire gauges are also connected to the circuit using 20 gauge wires.

Between 26 and 40 wave gauges were used in the wave gauge array in the TWB. Ten cantilever wave gauges were used in the basin-wide, fjord and curved headland scenarios. Thirteen cantilever wave gauges were used in the conical island scenario. All cantilever wave gauges were attached to the instrumentation bridge. The remaining wave gauges used in the wave gauge array were wire gauges attached to slopes to measure runup or attached to the basin floor to measure the water surface elevation at that location. The wave gauge locations can be seen in **Figure 14 - 16**.

3.6.2 Camera Setup

Multiple above and underwater cameras were installed to measure landslide properties and wave runup. A total of 12 cameras were used including a stereo particle image velocimetry

(PIV) camera setup and a high-speed camera. Two cameras were mounted on the landslide hill slope: One was above and one was below the water surface. Another camera was mounted underwater facing the landslide slope. The multiple camera positions allow above and underwater measurements to be taken of the landslide mass during the multi-phase landslide process, from the initial box movement to the end of the runout deposit. **Figure 22** shows nine typical camera views used to measure landslide properties and wave runup in the curved headland scenario.

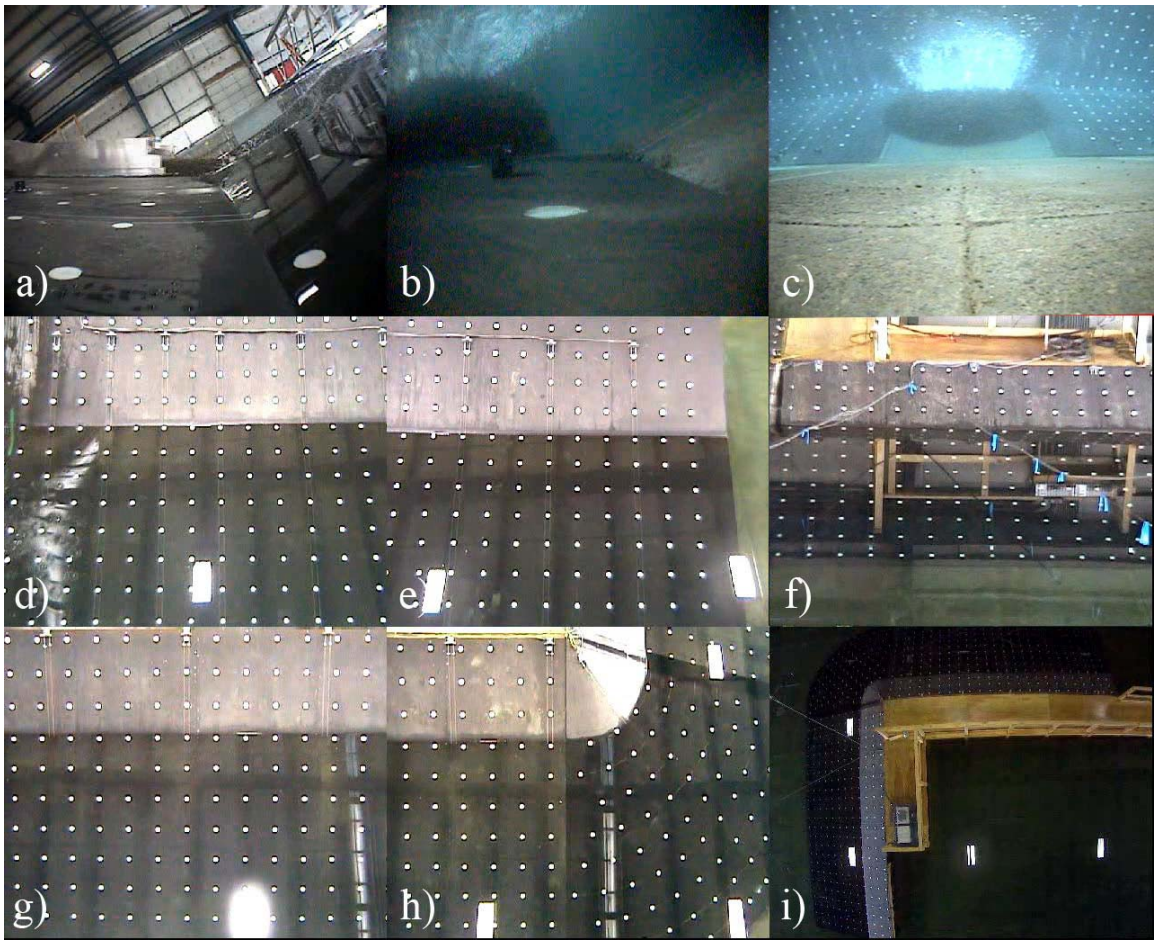

Figure 22: Typical camera recordings in the curved headland scenario with water depth, h = 1.2 m: (a) side view of the landslide impacting the water, (b) underwater side view of the landslide, (c) underwater front view of the landslide, (d) lateral slope adjacent to the landslide, (e) lateral slope adjacent to the view in (d), (f) opposing headland parallel to landslide motion, (g) opposing

headland perpendicular to the landslide motion, (h) conical section of the opposing headland, (i) overall view of the opposing headland.

In addition a high-speed camera was deployed to capture temporally resolved details of the landslide kinematics, particularly the landslide front velocity. The high-speed camera was focused on the landslide motion region and impact location. It was set to record at a frame rate of 100 fps. A PIV camera set up was similarly positioned to capture the landslide motion and water impact. Further discussion of the PIV camera setup is described in the subsequent section. **Figure 23** shows the camera views from the high speed camera and the high-resolution PIV camera setup.

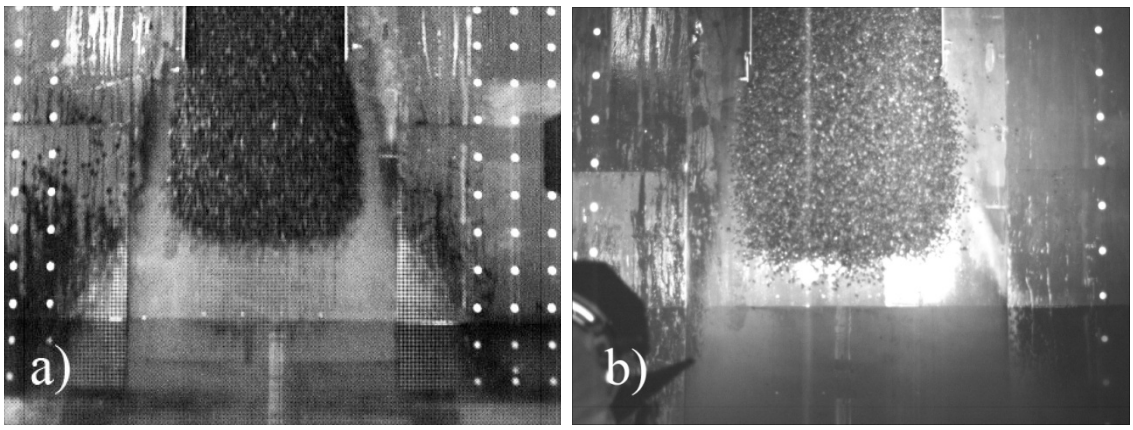

Figure 23: Landslide overhead cameras views: (a) high-speed camera, (b) PIV camera.

Cameras focused on the runup slopes were used as part of a hybrid system to validate the runup gauge recordings. The images from the cameras focused on the slopes were rectified using the dot pattern on the slopes. The dots were 44 mm in diameter and spaced 300 mm apart. Calibration boards were used for in-situ image rectification of camera recordings focusing on the

landslide region. The dot pattern on the calibration boards matched the dot pattern on the slopes. **Figure 24** shows the placement of a calibration board for a side camera.

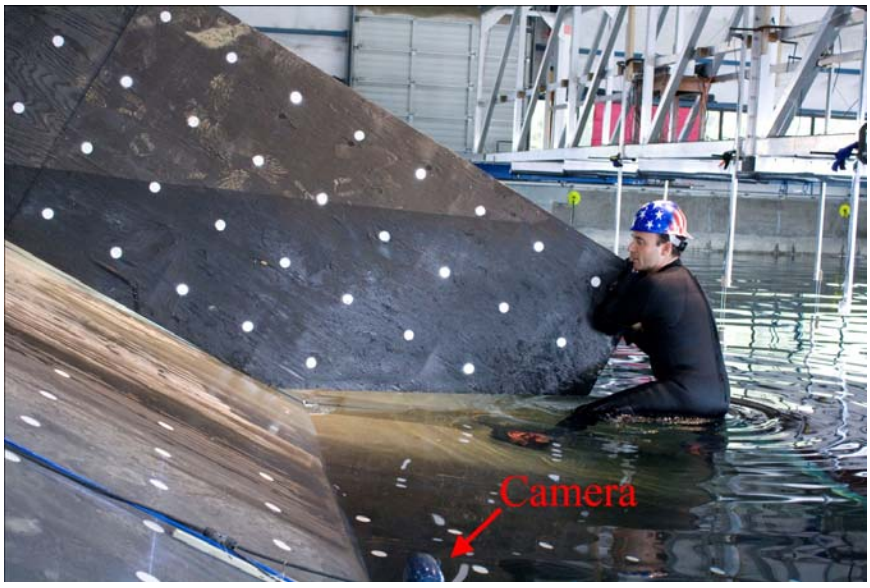

Figure 24: Calibration board placed in front of a side camera for in-situ image rectification.

3.6.3 Particle Image Velocimetry

Two different particle image velocimetry (PIV) configurations were used. A planar PIV configuration was used in the 2010 experiments to measure the landslide surface kinematics in the basin-wide, fjord and curved headland experimental configurations. The increased lateral spreading of the landslide in the conical island configuration required a stereo PIV configuration to better analyze the landslide kinematics. Planar PIV uses one CCD camera. The stereo PIV configuration uses two CCD cameras and can perform surface reconstruction. The speckled pattern of the gravel is used for correlation analysis in the PIV analysis. The water surface in the impact region was seeded with naturally buoyant high density polyethylene (HDPE) particles

with a density of 953 kg/m3for correlation analysis. The seeding material is shown in **Figure 25b**.

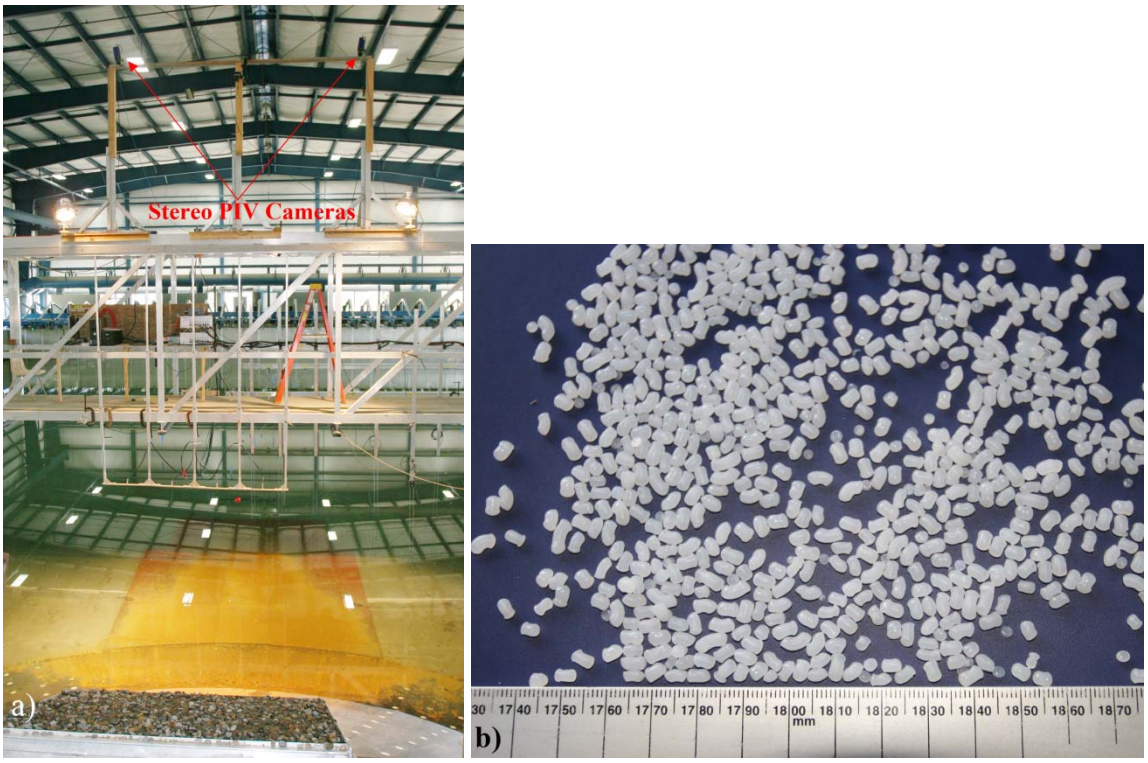

Figure 25: (a) Stereo PIV configuration with CCD cameras, (b) HDPE seeding material for the PIV analysis.

The CCD cameras used were Image Pro Plus 2M CCD progressive-scan-camera with dual frame capabilities for correlation purposes. The CCD camera can record at a frame rate of 30 fps with a resolution of 1600x1200 pixels. The CCD camera was placed 6.9 m normal to the landslide hill slope for the planar PIV configuration. The viewing area for this configuration is approximately 15.4 m^2 (4.57 m x 3.43 m). The viewing area for this configuration can be seen in **Figure 23b** in the previous section. The two CCD cameras in the stereo PIV configuration were

spaced 3.3 m apart creating a 26˚ angle between the two cameras and the center of landslide. The cameras were both placed 7.35 m normal to the island slope with an approximate viewing area of approximately 16.4 m^2 (4.86 m x 3.65 m). Sample viewing areas for the two cameras in the stereo PIV configuration is shown in **Figure 26**.

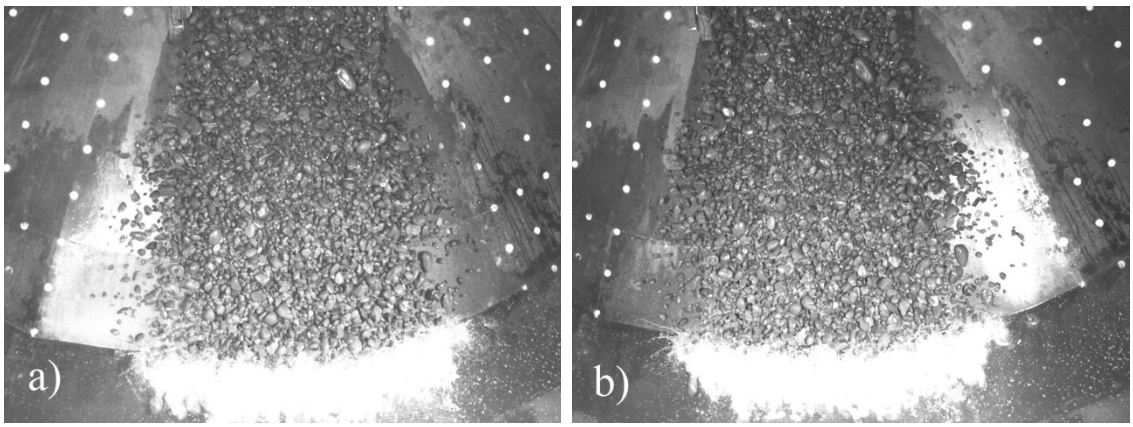

Figure 26: Viewing area from the (a) south CCD camera and the (b) north CCD camera.

The image acquisition and PIV analysis is performed with Da Vis software by La Vision, Inc. The image acquisition was activated by a programmable timing unit (PTU) which is controlled by a triggering mechanism from the LTG. The CCD cameras recorded 341 single exposure images at a frame rate of 28.59 fps. The speckled pattern of the gravel is used to measure the surface velocities of the landslide using PIV correlation analysis. Velocities can be validated with the front velocity measured by the side camera and the high-speed camera. The seeding material on the water surface is used for measuring water surface kinematics using PIV

correlation analysis and can be used for water surface reconstruction in the stereo PIV configuration.

3.6.4 Multi-transducer Acoustic Array

The landslide deposit was scanned with a multi-transducer acoustic (MTA) array. The transducers measure the vertical distance from the transducer to the landslide deposit surface. The MTA consists of four arrays of eight transducers which are aligned to produce a total of 32 transducers spanning 2.56 m. Each array is contained in a stainless steel housing and the transducers are spaced 0.08 m on center. The transducers have a diameter of 0.02 m and operate at 2 MHz with a half-beam angle of 1.1˚. The measurement range of the acoustic transducers is 0.05 m to 4.20 m. **Figure 27** shows the MTA and the full 32 transducer array.

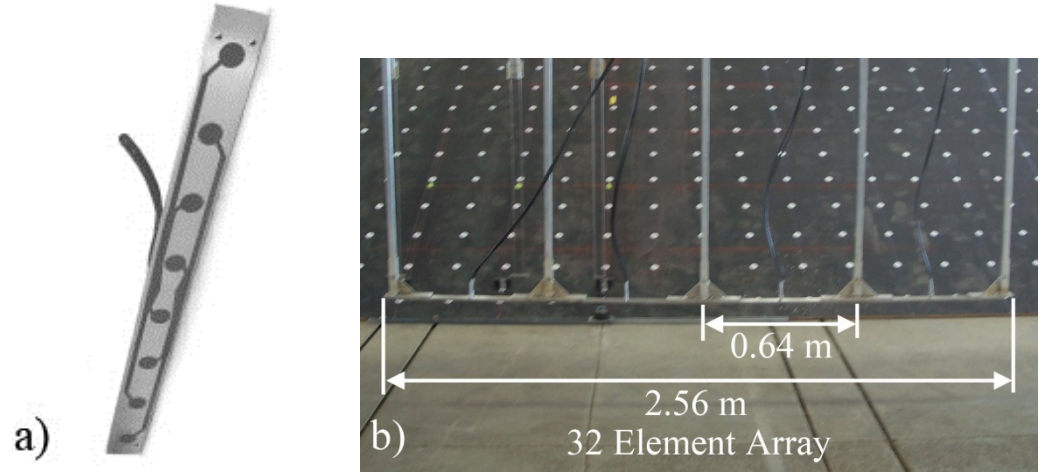

Figure 27: (a) Multi-transducer acoustic (MTA) array with eight transducers, (b) MTA with a total of 32 transducers.

The MTA is mounted on the bridge face closest to the landslide. The MTA is not centered on the slide deposit because of the deposit width. The symmetry of the deposit allows the MTA to be shifted 320 mm from center for the basin-wide, fjord and curved headland configurations to scan both the center and edge of the deposit. The increased lateral spreading in the conical island required the MTA to be shifted 920 mm from centered on the slide deposit. The horizontal position of the MTA is measured with a laser range finder (LRF). The LRF is attached to the instrumentation bridge and measures the distance to a target on the back wall of the basin. Both the MTA and LRF record independently and the two data sets are interpolated with their time stamp.

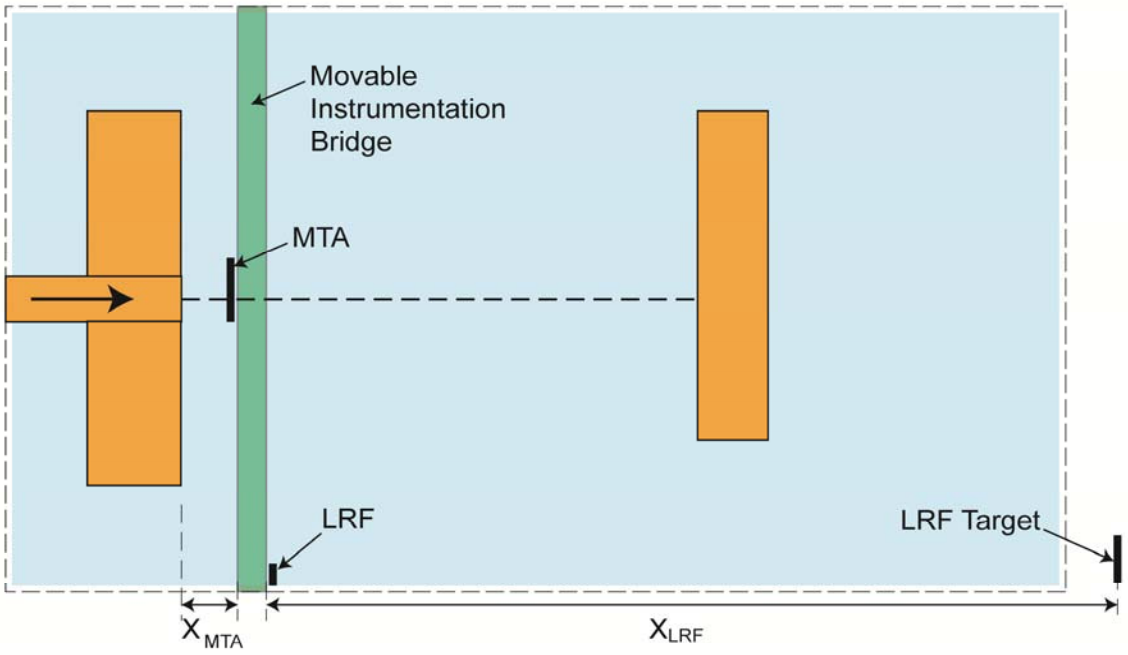

Figure 28: Multi-transducer acoustic (MTA) array setup in the tsunami wave basin.

During each experimental trial the MTA is above the water to avoid disturbing the water surface and wave profile measurements. After each experimental trial the MTA is lowered in the water. The MTA and LRF begin to acquire data on a dedicated computer. The bridge is moved over the slide deposit for the MTA to profile the deposit and basin floor. The bottom profiles describe the deposit shape, volume and runout length.

3.6.5 Data Acquisition System

Various instruments acquire data for different time spans during an experimental trial. Hence five separate acquisition systems are used to record the measured data. The camera array is recorded to a central network server where the images are stamped with the local time. The local time stamps are later converted to the experimental time. The PIV camera, high-speed camera and the MTA are each recorded to a dedicated computer. The trigger, wave gauge data and cable extension transducers are stored through a 64 channel 16 bit analog acquisition system. The trigger provides a reference time for the wave gauge and cable extension transducer data. The synchronization of each acquisition system is detailed in Section 3.8.1 Experimental Procedure.

3.7 Uncertainty in Measurements

3.7.1 Error Analysis

Uncertainty in experimental measurements is due to systematic and random errors. Systematic errors may be caused by faulty instrument calibration, temporal drifts in the instrument calibration over extended periods of time or changes in the experimental

environment. These errors are often unknown and cannot be determined my averaging experimental trials. Systematic errors are assumed to be negligible in the present study. Random errors are unpredictable and induce scatter in measurements. Random errors could be due to error in the interpretation of the instrument reading, fluctuations in the instrument measurements or interference of the environment with the measuring process. The actual value measured x_{actual} is obtained as

$$x_{actual} = x_{measured} \pm \Delta x \tag{57}$$

where x is any measured variable and Δx is the total error in the measurement. Potential random errors in the present study are included in the following measurements:

- Shoreline extraction from recorded image sequences
- Landslide measurements from recorded image analysis
- Wave profiles measurements from wave gauge recordings

The errors from the camera measurements can be described as

$$\epsilon_{tot} = \epsilon_v + \epsilon_{optics} \tag{58}$$

where $\boldsymbol{\epsilon_{tot}}$ is the total error, $\boldsymbol{\epsilon_v}$ is the random error and $\boldsymbol{\epsilon_{optics}}$ is the optical imaging error. Random errors are induced by processing the images with an algorithm or manual point extraction from recorded images. The optical error is created by image recording or the image rectification and calibration. The error in spatial errors can be determined during the image rectification. The above water side camera and runup measurement cameras record at an irregular frame rate. The images are captured and stored on a server which assigns a time stamp for each image with a resolution of 1/100th of a second. The spatial and temporal errors for each camera based on image calibration are shown in **Table 4**.

Table 4: Summary of absolute value of errors in image measurements per camera

Error	AW Side Cam	Runup Cam (Planar)	Runup Cam (Conical)	PIV Camera
ϵ_x, ϵ_y	1.0 mm	3.6 mm	6 mm	1.8 mm
ϵ_t	5 ms	5 ms	5 ms	-

3.7.2 Uncertainty in Landslide Measurements

Uncertainty in the landslide measurements can be estimated by the absolute value of error in the camera image measurements. The error estimates are based on the image calibration and scaling. The measured landslide parameters and spatial absolute errors induced by the respective cameras are compared in **Table 5**. The landslide parameters are applied as dimensionless parameters. Therefore, the absolute error in the dimensionless parameters is critical.

Table 5: Camera recording used to measure landslide parameters

Parameter	Camera	Absolute Error
Thickness, s	AW Side Cam	$\epsilon_x = 1.0\ mm$ $\epsilon_y = 1.0\ mm$
Width, b	PIV Cam	$\epsilon_x = 1.8\ mm$ $\epsilon_y = 1.8\ mm$
Front Displacement, x_s	PIV Cam	$\epsilon_x = 1.8\ mm$ $\epsilon_y = 1.8\ mm$
Δt	PIV Cam	$\epsilon_t = 0$

The maximum relative error in the dimensionless landslide parameters cannot exceed the sum of the relative error from the dimensional components (Demidovich and Maron, 1987).

Therefore the maximum error in the landslide front velocity, landslide Froude number, dimensionless landslide thickness and dimensionless landslide width can be given respectively as

$$\left|\frac{\Delta v_s}{v_s}\right| \leq \left|\frac{\Delta x_s}{x_s}\right| + \left|\frac{\Delta t}{t}\right| \tag{59}$$

$$\left|\frac{\Delta F}{F}\right| \leq \left|\frac{\Delta v_s}{v_s}\right| + \frac{1}{2}\left|\frac{\Delta h}{h}\right| \tag{60}$$

$$\left|\frac{\Delta S}{S}\right| \leq \left|\frac{\Delta s}{s}\right| + \left|\frac{\Delta h}{h}\right| \tag{61}$$

$$\left|\frac{\Delta B}{B}\right| \leq \left|\frac{\Delta b}{b}\right| + \left|\frac{\Delta h}{h}\right| \tag{62}$$

where x_s is the distance along the hill slope, t is time, h is the water depth, s is the landslide thickness and b is the landslide width. The maximum uncertainty for the dimensional landslide parameters is estimated from each of the measurements and a maximum is determined. The maximum uncertainties for the landslide front velocity, thickness and width are estimated as 3%, 2.7% and 3%, respectively. The uncertainty in the measurement of the water depth is estimated as 1.7%. The landslide parameters are measured as functions of the landslide propagation down the hill slope, which could induce additional error in the measurement of the landslide front position from the recorded image sequences. The maximum uncertainty in the incremental landslide front position is estimated as 1.6%. The maximum uncertainty for the nondimensional landslide parameters are shown in **Table 6**.

Table 6: Maximum uncertainty in the experimental measurements of the nondimensional landslide parameters

Nondimensional Landslide Parameter	**Maximum Uncertainty (%)**
Landslide Froude Number, F	3.8
Relative Slide Thickness, S	4.4
Relative Slide Width, B	4.7
Relative Slide Volume, V	5.0

3.7.3 Experiment Repeatability

Certain experimental trial conditions were repeated to estimate the accuracy of the experimental repetition. The landslide initial position remained unchanged at all water depths and on the planar and convex conical hill slopes, which changes the landslide parameters at impact. Due to the identical slide box motion and landslide dynamics prior to impact, the error estimation of the landslide velocity, thickness, width and volume measurements from recorded image sequences are independent of the water depth. The measured parameters for experimental trials on a planar hill slope and convex conical hill slope are compared in **Table 7**.

Table 7: Experiment repeatability. Measurements from two experimental conditions with initial pneumatic launch pressure of P = 10 bar on the planar and convex conical hill slopes.

		Planar Hill Slope			Convex Conical Hill Slope		
Parameter	Dimension	Run 1	Run 2	Δ	Run 1	Run 2	Δ
h	(m)	0.601	0.601	0	0.302	0.303	0.001
v_s	(m/s)	5.53	5.49	0.04	6.60	6.63	0.03
s	(m)	0.174	0.170	0.004	0.139	0.144	0.005
b	(m)	1.78	1.83	0.05	3.02	2.98	0.04
V_s	(m^3)	0.756	0.756	0	0.378	0.378	0

3.8 Experiment Methodology

3.8.1 Experimental Procedure

- The water level was set to the correct depth and any residual waves in the basin are allowed to dissipate. Wave gauges are calibrated during the basin filling and draining.
- The pneumatic parameters are adjusted on the landslide tsunami generator (LTG) and the gravel sled is set in a retracted position.
- An aggregate hopper is maneuvered with an overhead crane to fill the slide box with the gravel.
- The video recordings are initiated.
- The LTG is set to launch and an electric voltage trigger is sent to initiate the wave gauge, cable extension transducers and particle image velocimetry (PIV) camera recordings.
- The slide box is launched by the four pneumatic pistons towards the water. The gravel exits the slide box as the sled decelerates. The gravel landslide continues to accelerate down the slope and impacts the water.
- The PIV camera stops after recording 341 single exposure images at a frame rate of 28.59 fps. Wave gauges and data acquisition (DAQ) system record for 100 seconds after the trigger initiates recording. The video cameras are manually stopped at the same approximate time that the wave gauges stop recording.
- The multi-transducer acoustic array (MTA) is lowered from the instrumentation bridge until the transducers are covered in water. The MTA and laser range finder (LRF) are activated and begin recording. The instrumentation bridge is manually moved over the gravel deposit until it reaches the landslide slope. The deposit is rescanned as the bridge is pushed away from the landslide slope to allow for the slide recovery and the recording is stopped. The MTA is raised out of the water and secured.

- The gravel slide is recovered from the basin floor and is placed in an aggregate hopper to refill the LTG gravel sled.
- The instrumentation bridge is returned to the recording position.
- The LTG pneumatic parameters are adjusted and the process repeats.

The 2010 phase of experiments was performed from August 2 – October 1, 2010 which consisted of 80 trials in the fjord scenario, 37 trials in the curved headland scenario and 27 experimental trials in the basin-wide propagation and runup scenario. The 2011 phase of experiments was conducted from July 27 – September 8, 2011and consisted of 132 experimental trials in the conical island scenario of which 90 used the gravel landslide material and 42 used the cobble landslide material. A total of 276 experimental trials were performed in the two phases.

The gravel was recovered to the aggregate hopper two ways. At the 1.2 m water depth, the gravel was recovered into the aggregate hopper with an airlift. The airlift consists of a 0.1 meter diameter flexible hose which is approximately 4.5 meters long. An air hose with a 0.05 m diameter and a gate valve to control the airflow is attached to the suction end of the larger flexible hose. The other end of the air hose is connected to an air compressor. The air induces enough suction in the larger flexible hose to suck the gravel through it. The airlift did not work at shallower depths.

At shallower depths the gravel was recovered with a three hinged plate which rested on the basin bottom. The plate would partially collapse when rigged to a crane to contain the gravel. A lever activated gate could open on the lower end of the gate to release the gravel into the aggregate hopper. The two methods are shown in the figure below.

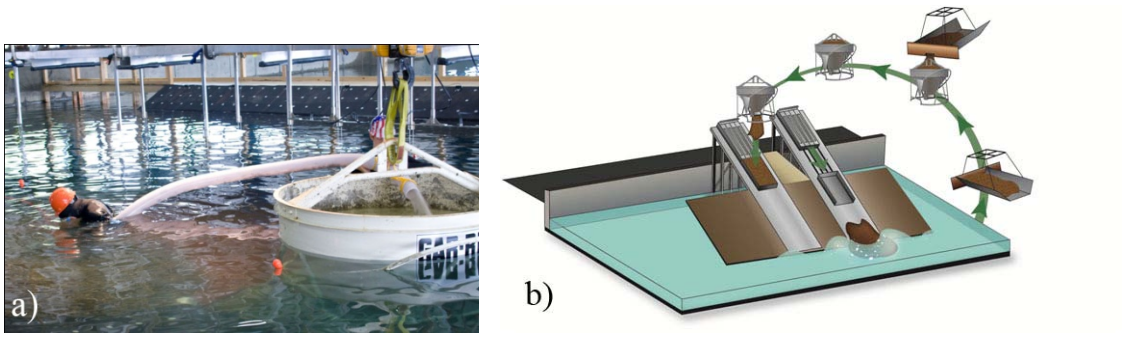

Figure 29: Gravel slide recovery with (a) the airlift method and with (b) the three hinged plate (Mohammed, 2010).

3.8.2 Range of Nondimensional Parameters

A total of 144 experimental trials were conducted with the LTG on the planar hill slope and 132 experimental trials were conducted on the convex conical hill slope in the conical island scenario. The following parameters were varied over the experimental trials:

- Water depth
- Landslide volume
- Initial pneumatic pressure in the LTG to control the slide box velocity

The range of experimental parameters tested is shown in **Table 8**.

Table 8: Experimental parameters varied during the experimental operation

Varied Parameter	Parameter Values			
Water depth, h (m)	1.2	0.9	0.6	0.3
Maximum slide box velocity, v_{box} (m/s)	4.0	3.23	2.76	2.33
Slide Volume, V_s (m^3)	0.756	0.378	-	-

The dimensional analysis determined the nondimensional parameters which govern tsunami generation by granular landslides. The hill slope angle and landslide density remained constant and are not included in the analysis. Although two landslide materials were used, both materials had the same grain and landslide bulk densities. The nondimensional propagation distance, directional angle and angle around the conical island describe the wave propagation characteristics.

The investigated nondimensional parameters that govern tsunami generation by granular landslides are the landslide Froude number F, relative slide thickness S, relative slide width B, relative landslide volume V, and relative shoreline radius R_c. The landslide Froude number is defined as $F = v_s/\sqrt{gh}$ where v_s is the landslide impact velocity. The landslide Froude number is the ratio of the landslide impact velocity and the linear shallow water celerity approximation $\sqrt{gh}$. Since the landslide Froude number F is proportional to $h^{-0.5}$, the slide Froude number is more sensitive to the landslide impact velocity than the water depth. The landslide Froude number was tested in the range $1.05 < F < 3.85$. Typical real world subaerial landslide generated tsunamis are the in range of $1 < F < 3$ and submarine landslide generated tsunamis are typically in the range $F < 1$. The subaerial landslide generated tsunami in Lituya Bay, Alaska in 1958 produced the largest recorded wave height and runup with a landslide Froude number of $F = 3.2$,

which was determined with a water depth of h = 122 m and landslide impact velocity of v_s = 110 m/s (Fritz et al., 2001).

The relative slide thickness and width are respectively defined as $S = s/h$ and $B = b/h$. The relative slide thickness S is dependent on the water depth, landslide motion and distance the landslide travels on the hill slope. The relative thickness is in the range of $0.08 < S < 0.46$. The relative landslide width is dependent on the water depth, landslide motion, distance the landslide travels on the hill slope, and the lateral hill slope curvature. The convex conical hill slope of the conical island scenario produced larger landslide widths at impact than the planar hill slope. The relative landslide width at impact on the planar hill slope was in the range $1 < B < 7$. A minor difference was observed in the slide width between the gravel and cobble landslides on the convex conical hill slope. The relative slide width on the convex conical hill slope was in the range $1.4 < B < 11.7$ for the gravel landslide and $1.4 < B < 11.2$ for the cobble landslide.

The relative landslide volume is defined as $V = V_s/h^3$. The relative landslide volume is dependent on the dimensional landslide volume and the water depth. The relative landslide volume was tested in the range $0.2 < V < 28$. The relative shoreline radius is only applicable to the conical island scenario and is defined as $R_c = r_c/h$. The relative shoreline radius is an important parameter for describing the curvature of the shoreline and was tested in the range $2.2 < R_c < 14.7$.

CHAPTER IV

GRANULAR LANDSLIDES

4.1 Introduction

The study of granular landslides in a mass flow generated tsunami process is a daunting task due to the changing dynamics and granular deformation of the landslide from the initial static position on a hill slope down to the submarine deposit. Field observations from landslide generated tsunami events are mostly limited to landslide scarps and submarine deposits where mapped. Physical experiments provide an insight to the complex behavior of the landslide kinematics. This chapter describes the characteristics of unconfined granular landslides using a pneumatic landslide tsunami generator (LTG) in the three-dimensional tsunami wave basin. The landslides are modeled with naturally rounded gravel and cobble landslide materials on planar and convex conical hill slopes as seen in **Figure 30**. Additional details about the landslide material are in Section 3.5 Granular Landslide Material. The landslides were tested with volumes of 0.756 and 0.378 m^3 corresponding to landslide masses of 1,350 and 675 kg. The physical modeling of the tsunamigenic landslide characteristics consist of the following experimental phases:

1. The landslide material moves as a solid block in the slide box.
2. The landslide material collapses out of the slide box and accelerates by gravity down slope.
3. The subaerial landslide impacts the water surface.
4. The subaqueous landslide runs out and deposits underwater.

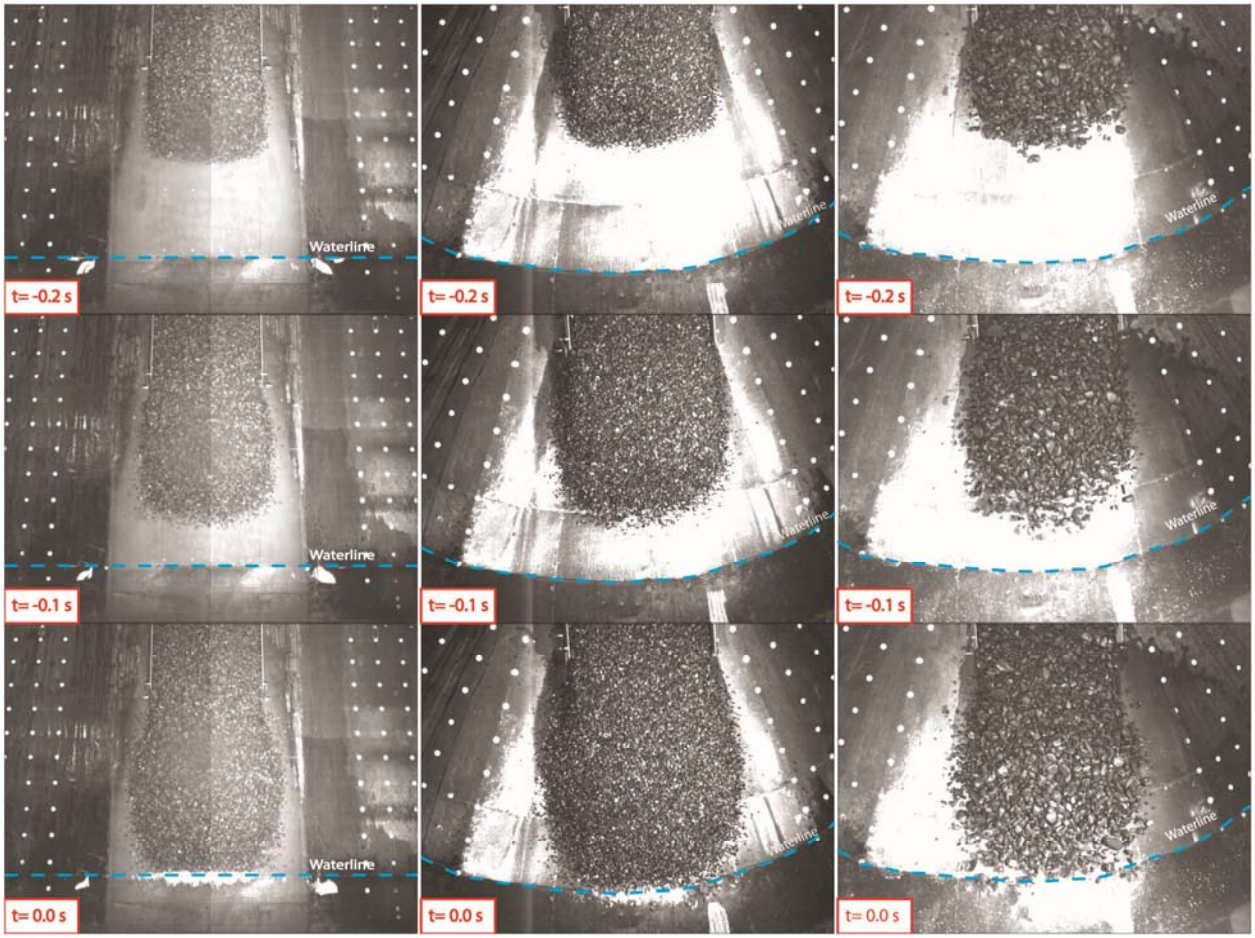

Figure 30: Landslide motion of gravel slide material on the planar hill slope (column 1) and convex conical hill slope (column 2), and cobble material on the convex conical hill slope (column 3). The time datum is set to the landslide impact with the water surface.

In each experiment the landslide kinematics are measured during the four phases to constrain the wave generation source parameters. The landslide characteristics during each phase are measured using the following techniques:

- The position of the gravel filled slide box is measured with cable extension transducers. The displacement time series are denoised with a wavelet filter and the slide box's velocity and acceleration are determined by the first and second derivative of the box position data, respectively.

- The slide exits the box at the peak velocity. The slide thickness, width and front velocity are measured from camera recordings above and below the waterline.
- The instantaneous slide shape is measured by extracting images from the camera video, rectifying them using an in-situ calibration board and delineating the landslide shape using a graphical user interface.
- The landslide front velocity is measured with calibrated images from the overhead high speed camera in combination with side cameras.
- The front velocity is validated with the landslide surface velocity distribution measured using particle image velocimetry (PIV) above the water surface.
- The stereo PIV setup deployed during selected runs in the conical island scenario will allow the measurement of the surface velocities and surface reconstruction of the deforming slide.
- The slide deposit is scanned with a multi-transducer acoustic (MTA) array mounted on a moveable instrumentation bridge. The transducers measure the vertical distance to the surface of the slide, while the horizontal distance is measured with a laser range finder (LRF) mounted on the instrumentation bridge.

Details of the instrument setup can be found in Chapter III - Experimental Setup. The landslide shape, deformation, kinematics and deposit are compared between the planar and convex hill slope for the gravel material. Effects of landslide granulometry are tested in the conical island scenario with gravel and cobble slide materials.

4.2 Landslide Shape

The landslide shape is measured using a rectified image sequence from a side camera. The image sequence is rectified using a pinhole calibration model, which allows extrapolation of

the calibration for the entire view based on the partial coverage provided by the calibration plate. The model is based on the theorem of intersecting lines. During the calibration the translation lengths from the camera to the calibration board, rotation, barrel distortion and scaling ratio from camera pixel to basin coordinates are accounted for and corrected. **Figure 24** shows the side camera attached to the planar slope focusing on a calibration board for in-situ image rectification.

The landslide shape is primarily described by the slide thickness *s* and width *b* as function of time and space. The thickness measurements were taken at uniform cross-sectional spacing on the hill slope above the water surface to describe the slide shape. The number of cross-sectional measurement locations varies dependent on the water level. Along the centerline down slope x_s axis, $x_s = 0$ is established at the front of the initially static slide box position and serves as position datum for the subaerial landslide motion. This static slide box hill slope coordinate system describes the slide box movement independent of the water depth. The time datum is set as $t = 0$ at the time the landslide impacts the water surface. The locally averaged bulk slide thickness is determined for cobble slides to avoid bias due to individual protruding cobbles and facilitate direct comparisons between gravel and cobble slide profiles.

Landslide thickness measurements were recorded for each combination of experimental parameters such as slide mass m_s, slide box velocity v_b, landslide material and water depth h. The spatial and temporal slide thickness profiles for multiple runs with identical launch parameters are combined in the static slide box hill slope coordinate system. The landslide thickness measurements are described as a function of time and space above the water surface. The slide shape of the gravel slide material on the planar slope is discussed in Mohammed (2010). The initial slide thickness corresponds to the box thickness of 0.3 m. The slide thickness evolution is shown in **Figure 31** along the x_s axis from the landslide collapse out the slide box to the $h = 0.3$ m water depth shoreline, $x_s = 4.062$ m. **Figure 31** and **Figure 32**

show the landslide thickness evolution for gravel landslide material on the convex conical island hill slope with landslide masses of 1,350 kg and 675 kg, respectively.

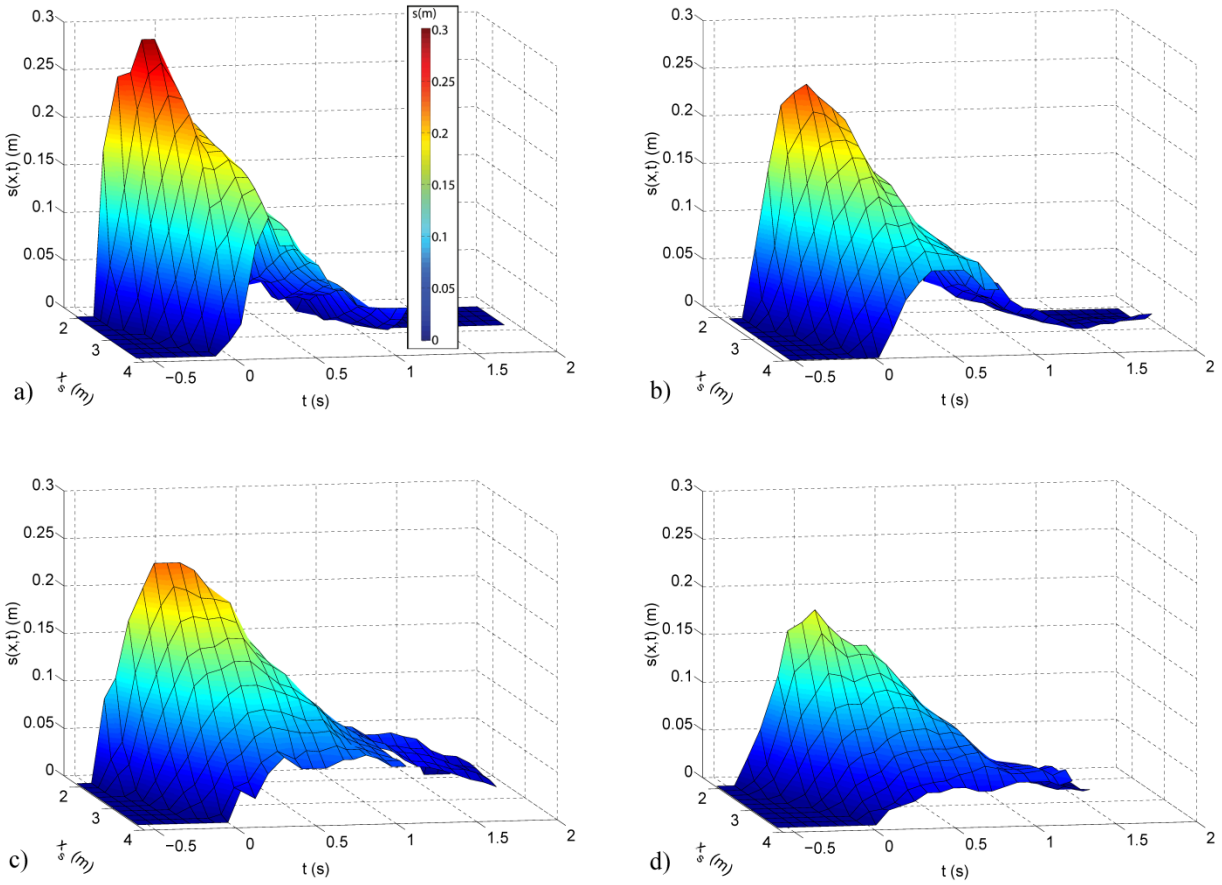

Figure 31: Gravel landslide thickness, s, evolution on a convex conical hill slope for a landslide mass m_s = 1,350 kg and volume V_s = 0.756 m^3 shown for the peak slide box velocities, v_b, of (a) 3.7 m/s, (b) 3.2 m/s, (c) 2.8 m/s and (d) 2.3 m/s.

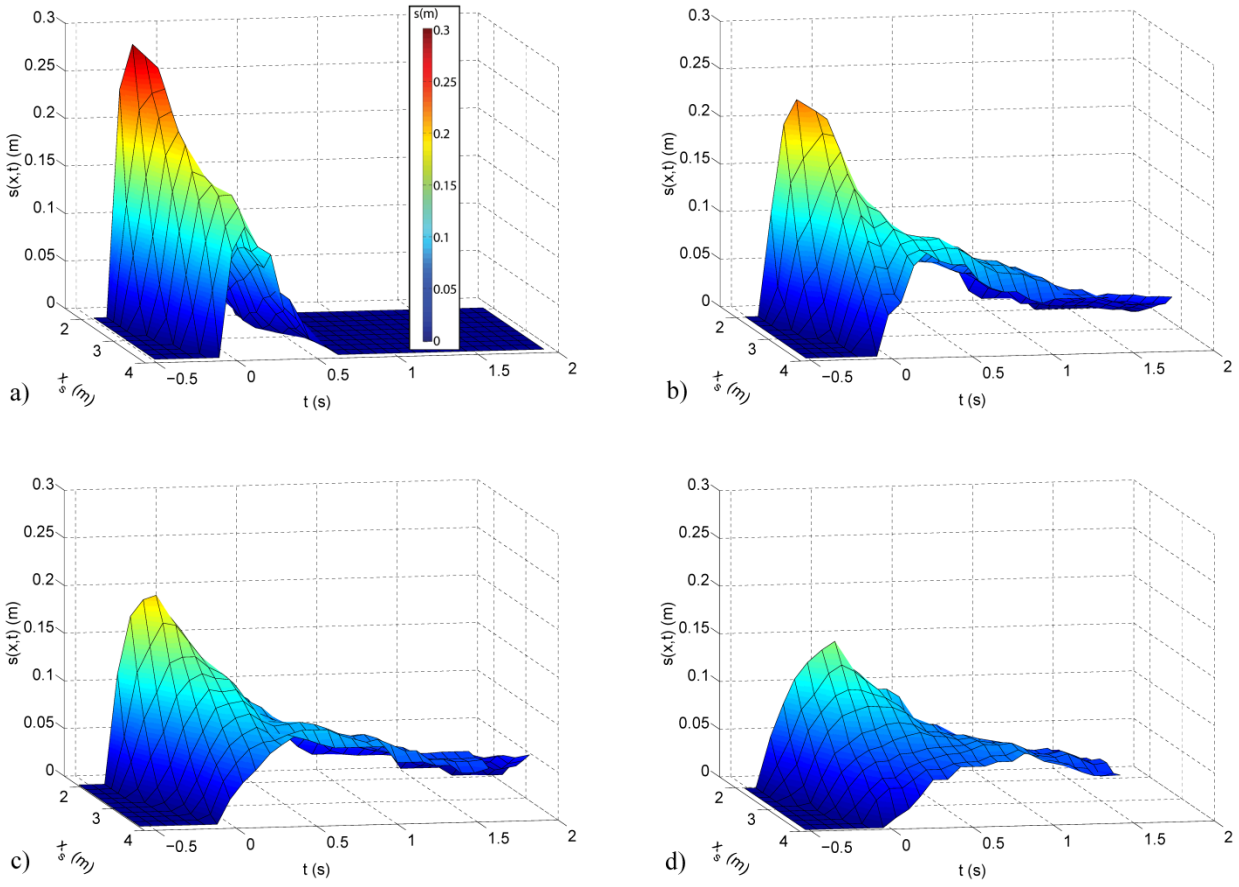

Figure 32: Gravel landslide thickness, s, evolution on a convex conical hill slope for a landslide mass m_s = 675 kg and volume V_s = 0.378 m^3 shown for the peak slide box velocities, v_b, of (a) 4.0 m/s, (b) 3.2 m/s, (c) 2.7 m/s and (d) 2.2 m/s.

Figure 33 and **Figure 34** show the landslide thickness evolution for cobble landslide material on the convex conical island hill slope with a landslide mass of 1,350 kg and 675 kg, respectively. Both the thickness evolution plots for the cobble and gravel slide materials exhibit similar features like the steep face up to the slide peak and a gradual decrease in thickness towards the tail of the slide. The peak thickness also decays as the slide moves down the hill slope due to unconfined spreading. A reduced box velocity results in a decrease in the mass and momentum flux of the landslide and lowering of the profile peak. The effects of the landslide mass and volume can be observed in the landslide peak decay rate down the hill slope as the reduction of landslide volume results in more compact landslide profiles. To better observe the

differences between the two landslide materials, the maximum slide thickness as a function of distance down the hill slope is analyzed.

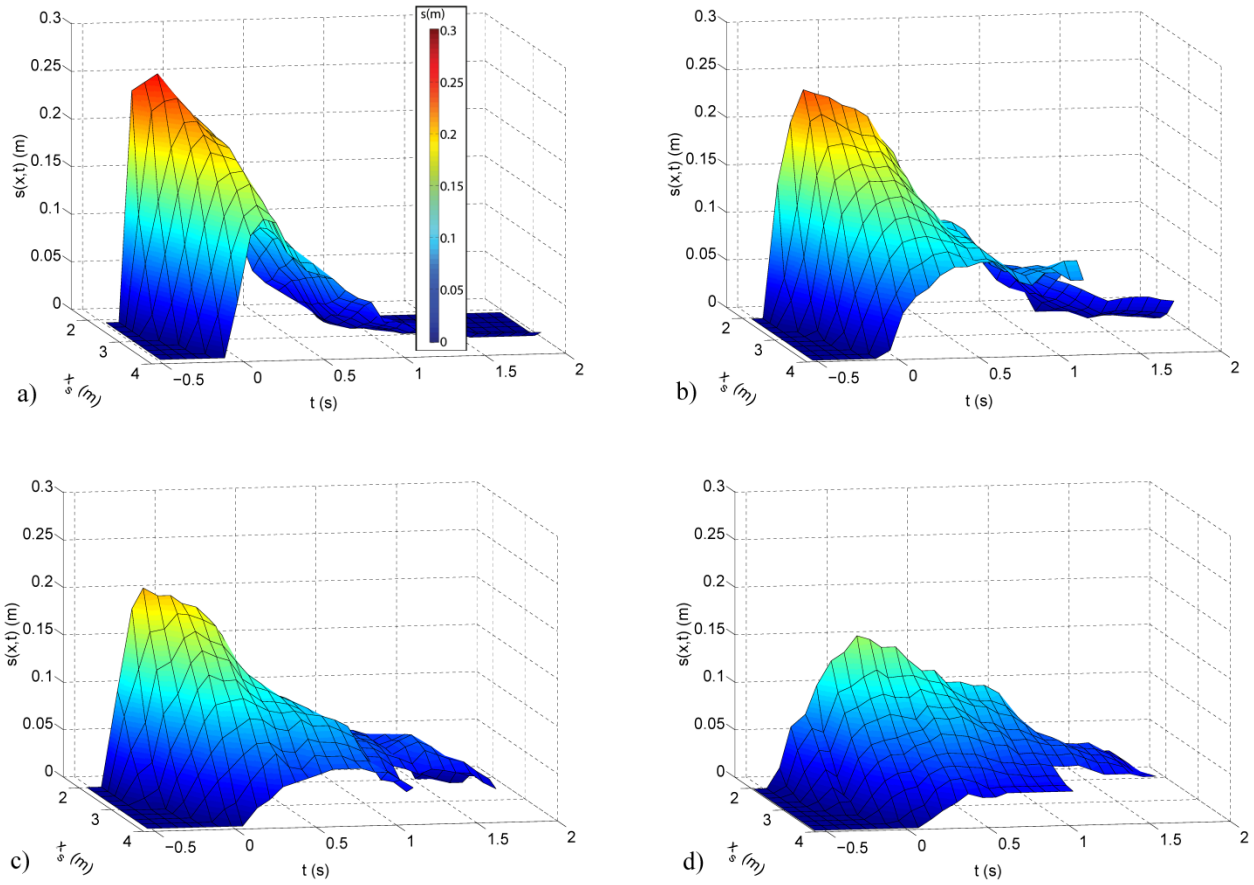

Figure 33: Cobble landslide thickness, s, evolution on a convex conical hill slope for a landslide mass m_s = 1,350 kg and volume V_s = 0.756 m^3 shown for the peak slide box velocities, v_b, of (a) 3.7 m/s, (b) 3.2 m/s, (c) 2.8 m/s and (d) 2.3 m/s.

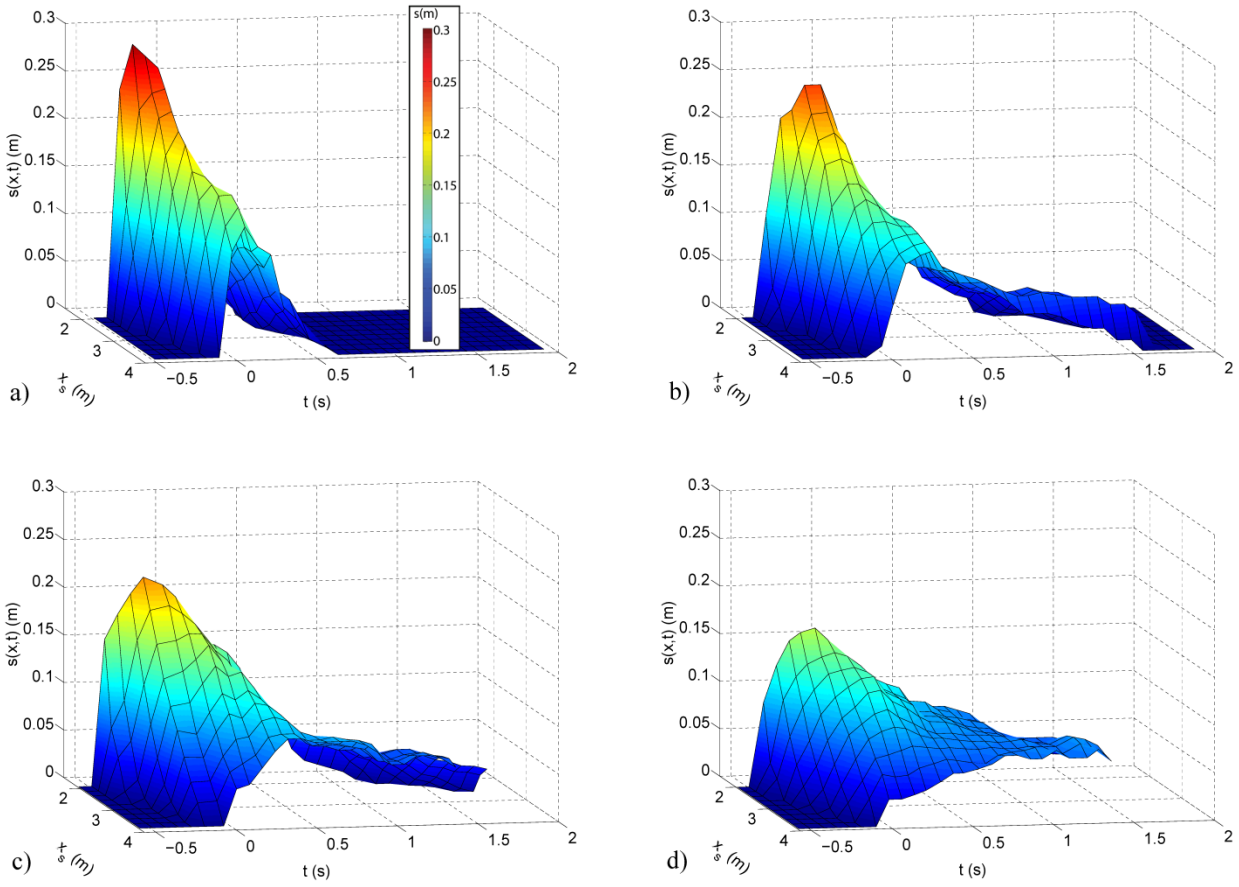

Figure 34: Cobble landslide thickness, s, evolution on a convex conical hill slope for a landslide mass m_s = 675 kg and volume V_s = 0.378 m^3 shown for the peak slide box velocities, v_b, of (a) 4.0 m/s, (b) 3.2 m/s, (c) 2.7 m/s and (d) 2.2 m/s.

To study the effects of the lateral hill slope curvature and the slide granulometry on the landslide thickness, the maximum slide thickness, s_m, as a function of the distance down the hill slope. **Figure 35** and **Figure 36** compares the maximum slide thickness after exiting the slide box for the gravel landslide material on the planar and convex conical hill slopes, and the cobble landslide material on the convex hill slope. The maximum slide thickness for the slide mass of m_s = 1,350 kg shows no dependence on the hill slope curvature or slide granulometry. The maximum slide thickness of both the gravel and cobble landslide materials on the convex conical hill slope with a slide mass of m_s = 1,350 kg decay similarly with distance traveled down the hill slope. The maximum slide thickness occurs in the center of the slide mass. Although lateral

spreading on the edges rapidly increased the slide width on the conical island, the maximum thickness in the center of the mass remains consistent between the planar and convex conical hill slopes for the gravel landslide material.

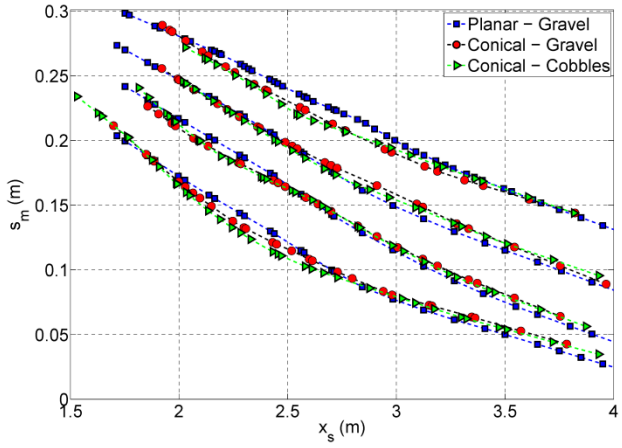

Figure 35: Maximum landslide thickness, s_m, as a function of the hill slope distance, x_s, for the gravel and cobble landslide materials on planar and convex conical hill slopes for a landslide mass of m_s = 1,350 kg and box velocities, v_b, of 3.7, 3.2, 2.8 and 2.3 m/s for the top set of lines to the bottom set of lines, respectively.

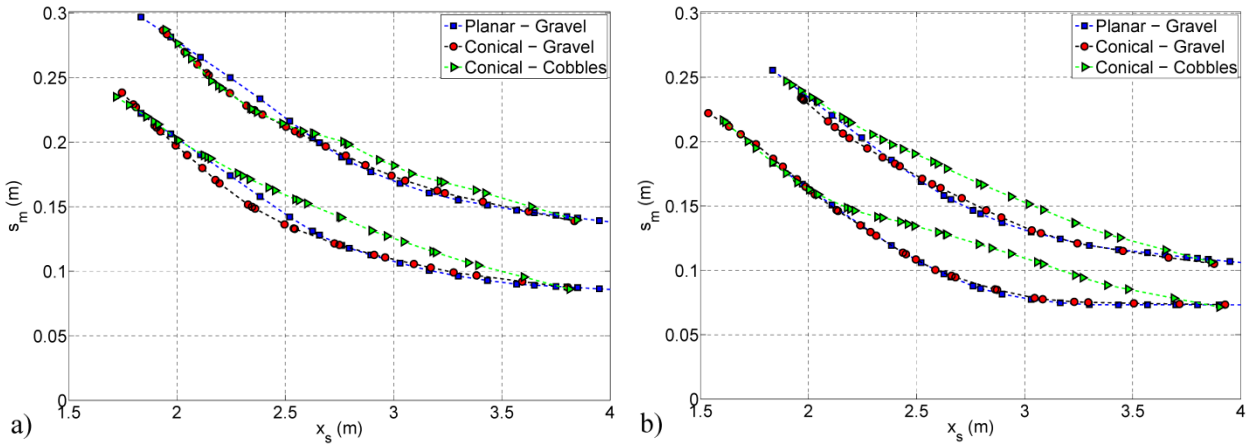

Figure 36: Maximum landslide thickness, s_m, as a function of the hill slope distance, x_s, for the gravel and cobble landslide materials on planar and convex conical hill slopes for a landslide mass of m_s = 675 kg and box velocities, v_b, of (a) 4.0 and 2.7, and (b) 3.2 and 2.2 m/s for the top and bottom sets of lines, respectively.

The maximum slide thickness for the slide mass of m_s = 675 kg shows no dependence on the lateral hill slope curvature, but the cobble slide maximum thickness does not decay as quickly as the gravel slide and the difference becomes more pronounced as the slide velocity decreases. This is most likely caused by the irregular granulometry of the cobble landslide and differential acceleration of granulates within the landslide material. The faster moving large cobbles push the smaller gravel in front of the cobbles inducing a larger slide thickness in front of cobbles and leaving small voids in the slide thickness behind the cobbles. One possible reason this slide thickness irregularity is observed in the smaller slide mass and not in the larger slide mass may be due to the larger mass having more slide material to embed cobbles. The larger cobbles inducing the thickness irregularities can produce hummock features in the deposit. **Figure 37** shows the slide thickness irregularities and the cobbles inducing the slide irregularities.

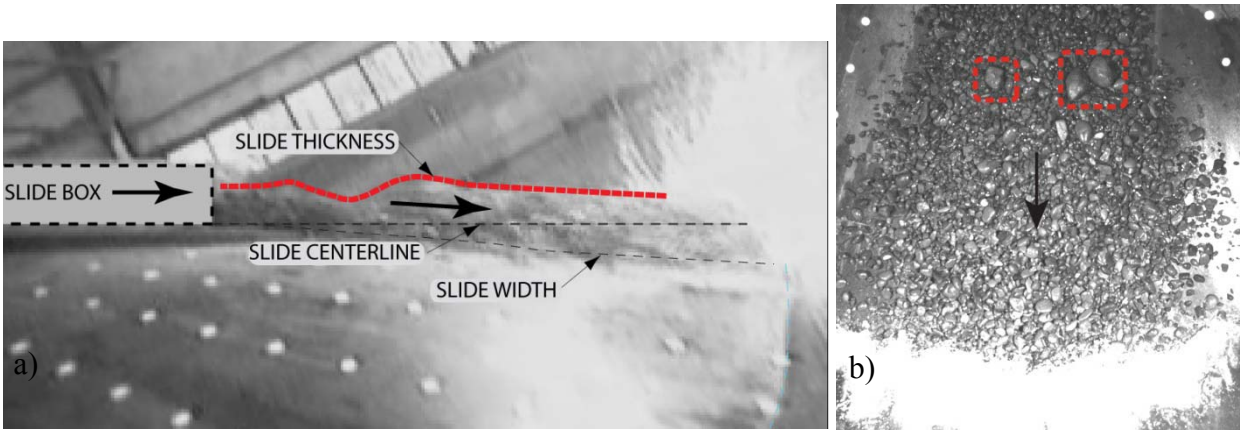

Figure 37: Irregularities in the cobble and gravel slide thickness are created when large cobbles are accelerated by inertial and gravitational forces faster than the gravel. (a) The instantaneous slide thickness is measured with a side mounted camera and (b) the cobbles causing the thickness irregularities viewed by an overhead camera.

The incorporation of cobbles in otherwise deformable granular landslides represent an attempt at mimicking the rheology of actual large landslides characterized by the presence of the

hummocks and rigid "Toreva Blocks". These are typically transported by volcanic debris avalanches and other large landslides and create a blocky surface on the landslide. In the real world many of these hummocks represent the upthrust blocks of horst and graben systems generated within moving landslides, and demonstrate that parts of the moving slide retain their rigidity and coherence (Voight et al., 1981; 1983). Other hummocks are formed by coherent blocks or pieces of the original mountain that are transported downslope with the slide mass, while some form in situ as material in landslides decelerates due to differential basal or lateral shear (Glicken, 1996).

4.3 Landslide Width

When the landslide collapses out of the slide box, the landslide spreads laterally unconfined on planar and conical hill slopes under the influence of inertial and gravitational forces. The slide width at impact with the water surface affects the water displacement, the wave amplitude and decay functions. The slide width was measured using an image sequence from the overhead PIV camera and the slide width was traced with a graphical user interface. The image sequences on the planar slope were rectified using the same pin hole model discussed in Section4.2 Landslide Shape. The raw image sequences of the conical island were analyzed and the pixel locations converted to the basin coordinates using a polynomial spatial transformation based on control points measured with the LiDAR scan of the conical surface.

The landslide width, *b,* is measured as the shortest distance between two points along the hill slope surface normal to the axis of the landslide motion, which corresponds to a straight line at constant elevation along the planar hill slope and a direct rope length across the conical island. A diagram describing the landslide width measurement is shown in **Figure 38**. If the cone is described in polar coordinates (r_c, Φ, z) and z is a function of r_c and Φ such that $z = r_c \tan(\alpha)$,

then the equation describing the slide width measurement between the two points (r_{c1}, Φ_1, z_1) and (r_{c2}, Φ_2, z_2) is given as $r_{c2}\ \cos(\Phi \sin(\pi - \alpha)) = r_{c1}$ where $\Phi = \Phi_2 - \Phi_1$.

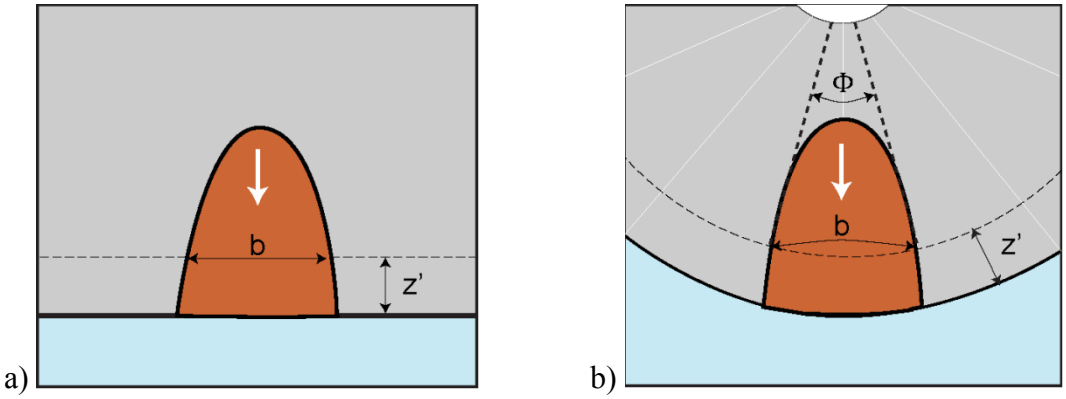

Figure 38: The slide width is measured normal to the landslide axis on the surface of the hill slope: (a) straight line at elevation on a planar slope, (b) direct rope length across the conical island surface.

The planar slide width measurements are extended downhill by a larger camera field of view in this study compared to Mohammed (2010). The maximum slide width measurements overlap and match the previous study's measurements for x_s = 2.5 – 3.6 m. Minor differences were observed in the maximum landslide width as the landslide collapses out of the slide box with some loose gravel rocks saltating laterally only to be absorbed again downhill by a widening bulk mass. **Figure 39** shows the maximum lateral spreading of the gravel landslide material on the planar and convex hill slopes and the cobble landslide material on the convex hill slope.

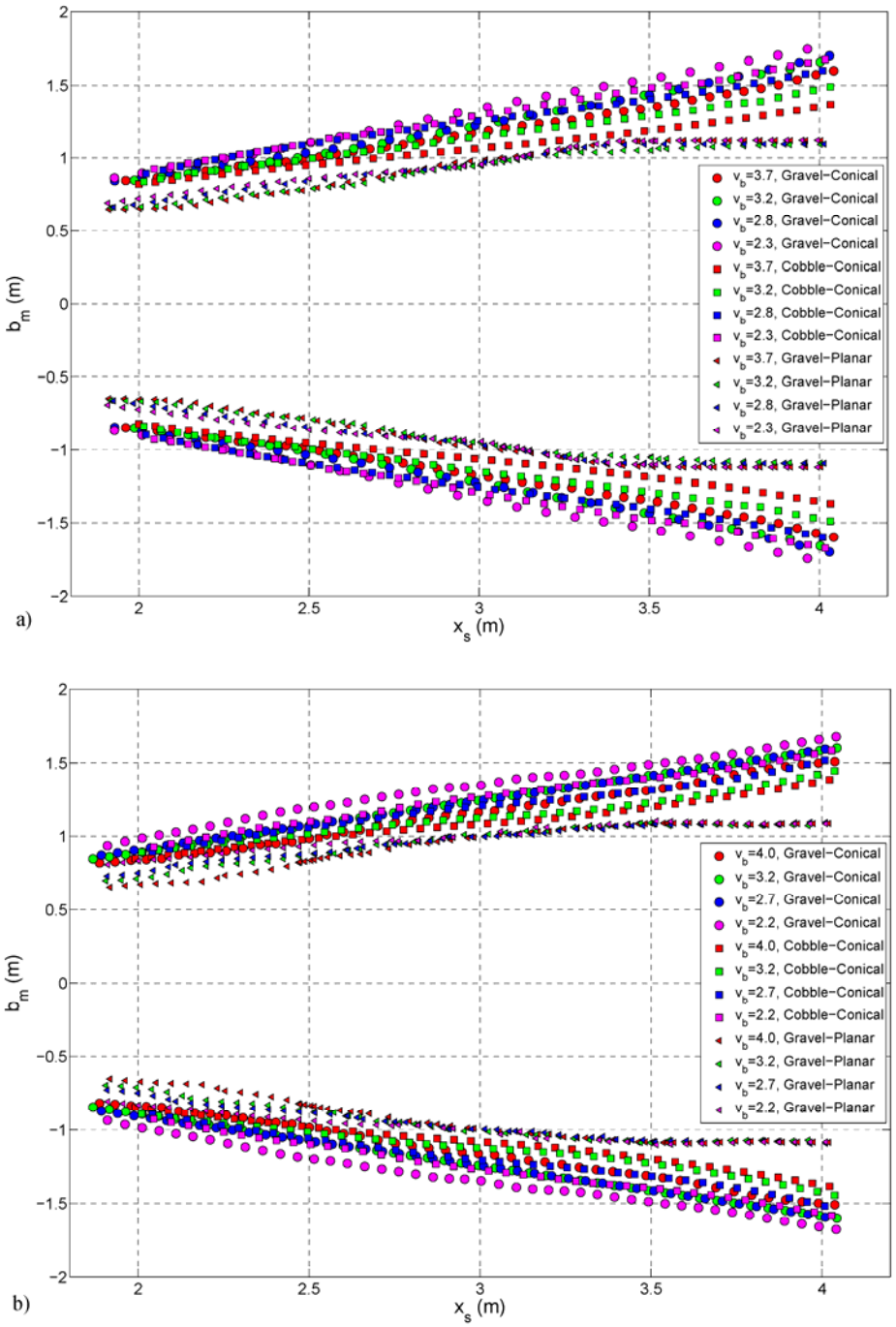

Figure 39: The maximum extent of lateral landslide spreading for landslides with (a) mass, m_s = 1350 kg and (b) mass, m_s = 675 kg. The filled circles are from experimental trials with gravel landslide material on a conical slope, filled squares are from the cobble landslide material on a conical slope and the filled triangles are from the gravel landslide material on a planar slope.

The maximum landslide width on the planar hill slope asymptotically approaches a maximum landslide width of approximately two times the slide box width. The asymptotic maximum landslide width could be estimated using the basal friction angle on steel (23°) which would counter the landslide spreading force in a dynamic moving landslide. If it is assumed that the basal friction is the only force opposing the spreading force induced by the box height, the maximum slide width would be 2.1 slide box widths, which is close the observed asymptotic value of two box widths.

The maximum landslide width b_m on the convex conical surface appears to follow a linear trend. The linear trend is described with the following nondimensional landslide parameters to increase the applicability of equations derived:

$$B_m = \frac{b_m}{b_o} \tag{63}$$

$$X_s = \frac{x_s}{s_o}$$

$$F_s = \frac{v_s}{\sqrt{g\, s_o}}$$

$$S_m = \frac{s_m}{s_o}$$

$$V_{ls} = \frac{V_s}{{s_o}^2\, b_o}$$

where B_m is the dimensionless maximum landslide width, X_s is the dimensionless propagation down the hill slope, F_s is the dimensionless landslide Froude number using only landslide parameters, S_m is the dimensionless maximum landslide thickness and V_{ls} is the dimensionless landslide volume. It should be noted that these dimensionless parameters are nondimensionalized exclusively with initial landslide characteristics, which differs from the dimensionless parameters used in tsunami generation, so derived equations can be used in landslide analysis.

The linear equation describing the maximum landslide width on the convex conical hill slope follows the form:

$$B_m = (1 + m_b\, X_s + c_b) \tag{64}$$

where m_b is landslide lateral spreading function, X_s is the distance traveled down the slope and c_b is a nonlinear function of the landslide discharge from the slide box. The specific m_b and c_b values for the two different landslide materials are given in Equations 65 and 66, respectively with an r^2 correlation coefficient of 0.99 for both sets of equations when applied to Equation 64. **Figure 40** compares the measured versus predicted values of the dimensionless maximum landslide width.

The spreading and discharge coefficients for the gravel landslide material are given as

$$m_b = 0.1\, {F_s}^{-0.08} {S_m}^{-0.05} {V_{ls}}^{0.2} \tag{65}$$

and $$c_b = -0.055\, {F_s}^{0.7} {S_m}^{0.1} {V_{ls}}^{0.6}$$

The spreading and discharge coefficients for the cobble landslide material are given as

$$m_b = 0.2\, {F_s}^{-0.7} {S_m}^{-0.2} {V_s}^{0.1} \tag{66}$$

and $$c_b = -0.2\, {F_s}^{-0.7} {S_m}^{-0.2} {V_s}^{0.5}$$

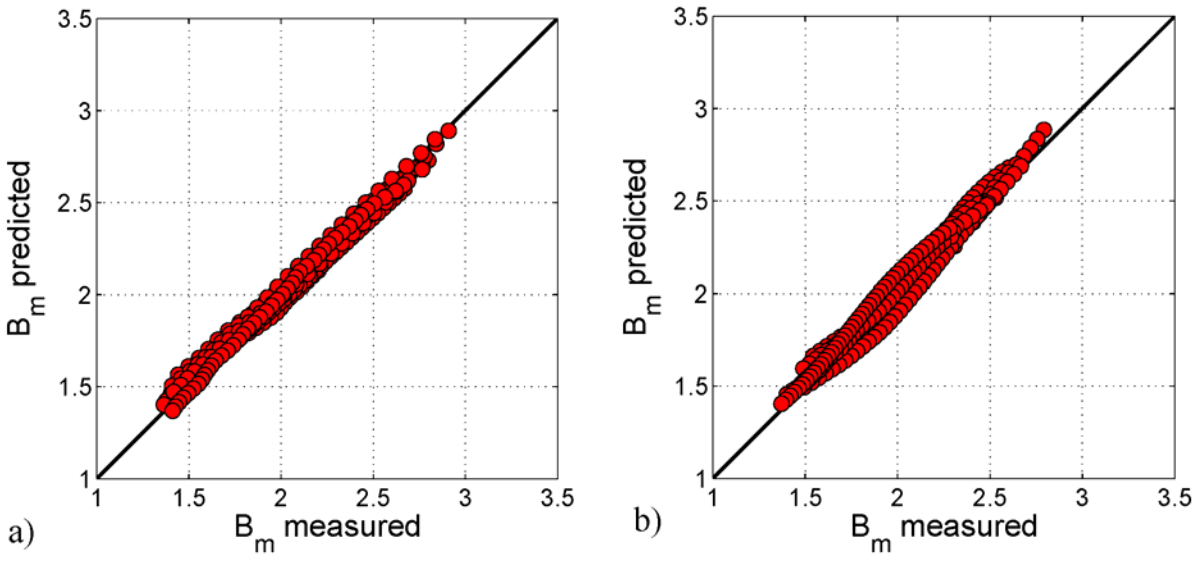

Figure 40: Comparison of the measured versus the predicted maximum slide width, B_m, for the (a) gravel landslide material and (b) cobble landslide material. The predicted values match the measured values with a correlation coefficient of r^2=0.99, for both landslide materials.

4.4 Landslide Motion

After the landslide collapses out of the slide box, it continues to gain speed by gravitational acceleration until impact with the water. Ideally the landslide centroid velocity would be measured and applied to the mass, momentum and landslide energy equations, but the unconfined, continually deforming landslide shape make measuring the centroid velocity impractical. Therefore, the landslide front velocity is measured and applied to the nondimensional parameters described in 3.2 Dimensional Analysis.

The landslide front velocity is measured with image sequences from the PIV and high speed cameras. The velocity measurements from different experiment trials with the same slide mass and slide box velocity are combined to study the complete landslide evolution from initial static box position until impact with the water surface. The slide box's front velocity from its initial static position to maximum box speed is taken as the landslide front velocity, and is

measured with the cable extension transducers. The landslide collapses out of the slide box at the maximum box speed and continues to accelerate downhill, while the landslide front velocity is recorded by the image sequences from the overhead PIV and high speed cameras. The measured landslide front velocities from rest until impact with the water surface are shown in **Figure 41**. The dimensionless landslide front velocity is shown as functions of the landslide Froude number, F_s, and the dimensionless distance down the hill slope, X_s, in **Figure 42**.

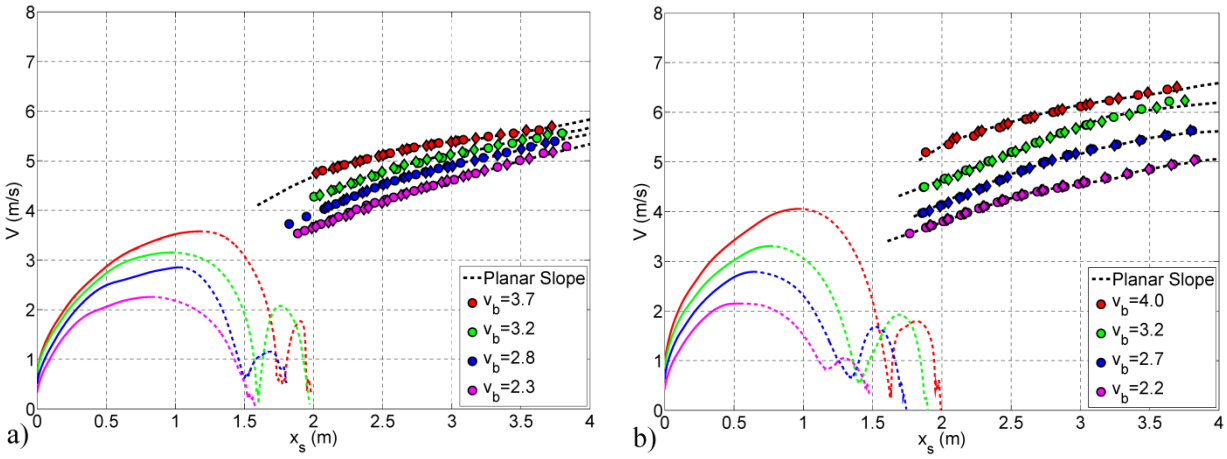

Figure 41: Landslide front velocity of both gravel (circles) and cobble (diamonds) landslides as a function of propagation distance x_s on the hill slope for landslide mass (a) m_s = 1350 kg and (b) m_s = 675 kg.

The two different lateral hill slope curvatures do not impact the landslide front velocity. This is because the front velocity is greatest at the center of the landslide. The slide front velocity is insensitive to the lateral curvature as the planar and convex conical hill slopes have the same incline angle along the center of the landslide. Similarly the landslide front velocity remains insensitive to the gravel and cobble landslide materials launched down the conical island. Both slide materials have the same bulk slide density and the landslide front velocity behaved similarly when subjected to the same inertial and gravitational forces.

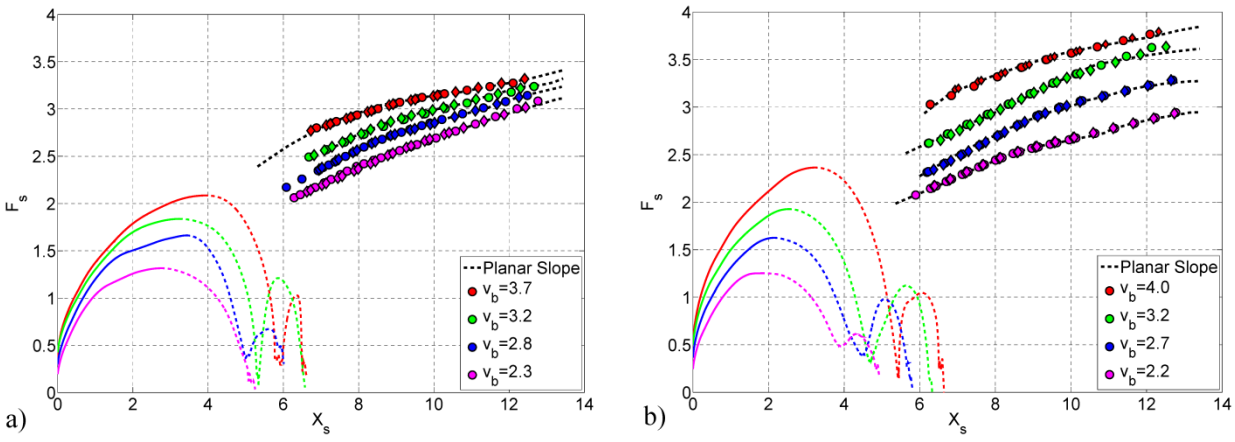

Figure 42: Dimensionless landslide front velocity of both gravel (circles) and cobble (diamonds) landslides as a function of the dimensionless propagation distance X_s on the hill slope for landslide mass (a) m_s = 1350 kg and (b) m_s = 675 kg.

4.5 Landslide Deposit

The landslide deposit is measured after each experimental trial to improve the understanding of subaqueous landslide dynamics by analyzing the deposit shape, runout distance, water depth and landslide material. The landslide deposits are measured with a multiple-transducer acoustic (MTA) array which was mounted on the moveable instrumentation bridge. The MTA was raised above the water during the experimental trial to avoid disturbing the water surface measurements and wave profiles. After each experimental trial the MTA was lowered into the water and the instrumentation bridge was slowly moved over the landslide deposit for the MTA to measure the deposit shape. The landslide deposits from gravel landslides on planar hill slopes are analyzed in Mohammed (2010). This section focuses on the landslide deposits of gravel and cobble landslides from a convex conical hill slope.

The coordinate system used in the landslide deposit analysis is shown in **Figure 43**. Each axis in this coordinate system is marked with the subscript "d" for clarification. The datum of

the z_d-axis is established as the basin floor. The x_d-axis is the centerline of the longitudinal axis of the wave basin and is positive away from the hill slope. The x_d-axis datum, $x_d = 0$ is at the base of the hill slope with island angle of $\Phi = 0°$. The origin of the y_d-axis is centered on the x_d-axis.

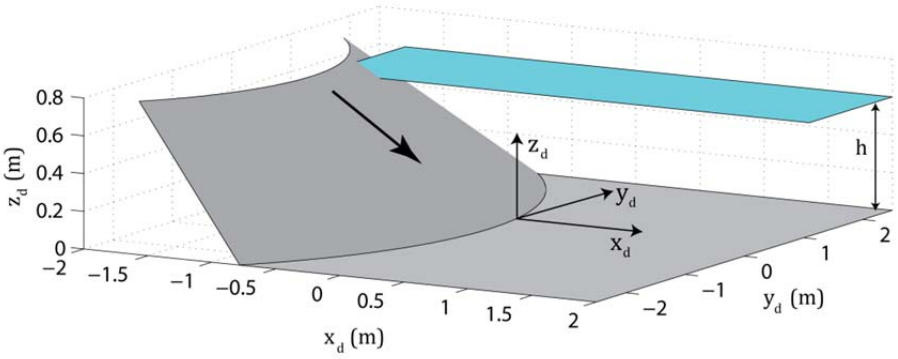

Figure 43: Coordinate system applied to the deposit measurements.

The acoustic array has an overall width of 2.56 m and is shifted 0.92 m off center of the x_d-axis to be able to scan from the edge of the deposit to 0.36 m beyond the deposit centerline. The slide deposit is assumed to be symmetric about the x_d-axis, which was shown in Mohammed (2010) and verified in the present study with axially symmetric sensors. Cantilever wave gauges mounted on the instrumentation bridge and protruding into the water prevent access of the bridge from getting closer to the hill slope shoreline, thereby allowing the acoustic array to only measure a portion of the landslide tail on the hill slope.

The landslide emplacement is similar between the gravel and cobble landslides. The pneumatic landslide tsunami generator accelerates the landslide over a short distance on the hill slope. The landslide exits the slide box at the box's peak velocity and continues to gain speed by gravitational acceleration while spreading laterally and longitudinally. The landslide impacts the water surface and deforms. The subaqueous landslide decelerates quickly due to energy

conversion into tsunami waves, drag forces, basal friction and reduction of gravitational acceleration after the landslide reaches the horizontal runout on the basin floor. The characteristic deposit shape is observed in the deposit with a narrower tail and wider front due to lateral spreading.

The measured underwater landslide deposits are shown in **Figure 44** for gravel and cobble landslides with a landslide mass of m_s = 1,350 kg, volume V_s = 0.756 m^3 and peak box velocity of v_b = 3.7 m/s in water depth of h = 0.3 m. Both landslide materials produce a bulging deposit thickness at the transition from the hill slope to the basin bottom. The gravel landslide deposit thickness decreases from the hill slope transition to the maximum runout length. The gravel landslide produces a much smoother deposit compared the cobble landslide. The cobble landslide deposit becomes less smooth with increased distance from the hill slope, producing hummock type features near the maximum runout length. Hummocks and rigid "Toreva Blocks" are characteristically transported by volcanic debris avalanches and other large landslides and typically create a blocky surface on the landslide deposit (Voight et al., 1981; 1983; Moore et al., 1989; Glicken, 1996).

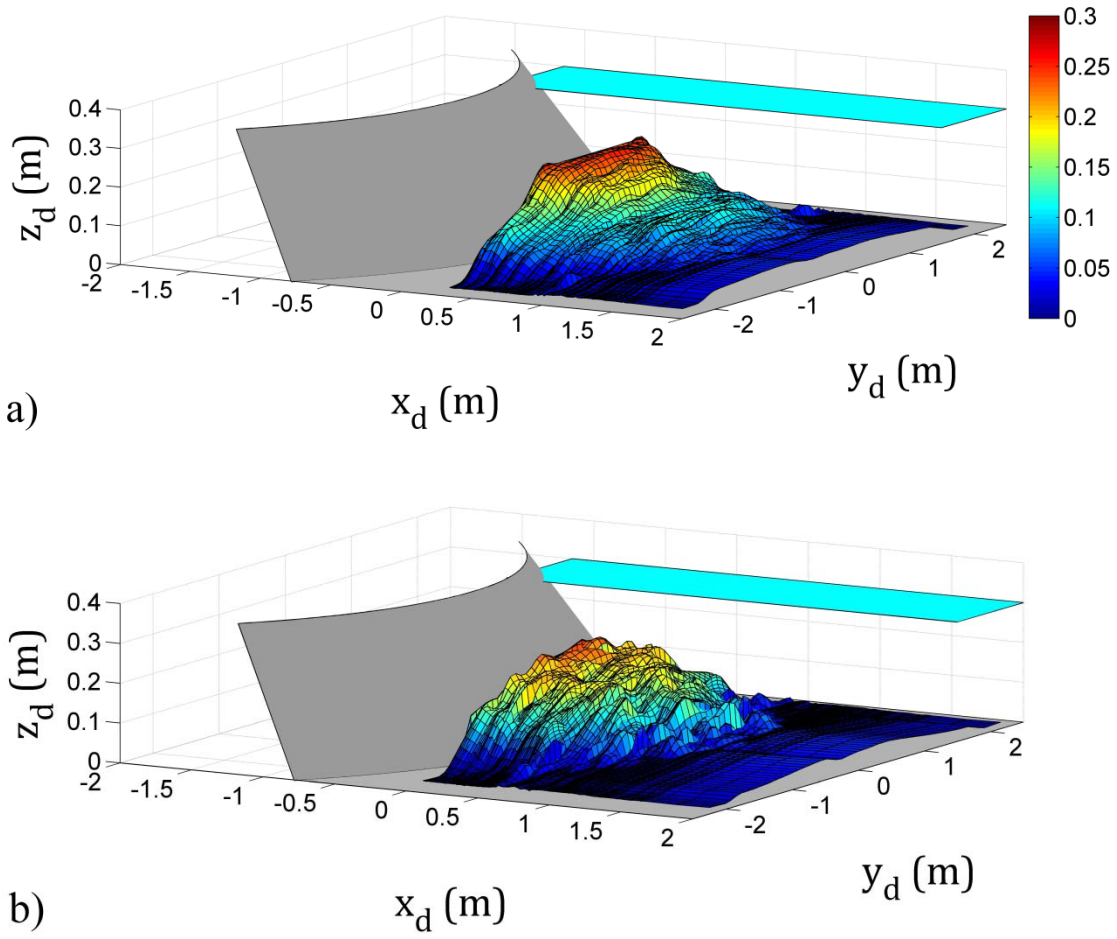

Figure 44: Measured landslide deposit at water depth h = 0.3 m on a convex conical hill slope with landslide mass m_s = 1,350 kg, volume V_s = 0.756 m^3 and peak slide box velocity v_b = 3.7 m/s for (a) gravel and (b) cobble landslides.

The measured underwater gravel and cobble landslide deposits with a landslide mass of m_s = 675 kg, volume V_s = 0.378 and peak box velocity of v_b = 4.0 m/s in water depth of h = 0.3 m are shown in **Figure 45**. Similar to the larger landslide volume shown in **Figure 44**, the gravel landslide deposit is much smoother than the cobble landslide deposit and the cobble deposit produces hummock type features near the maximum runout length.

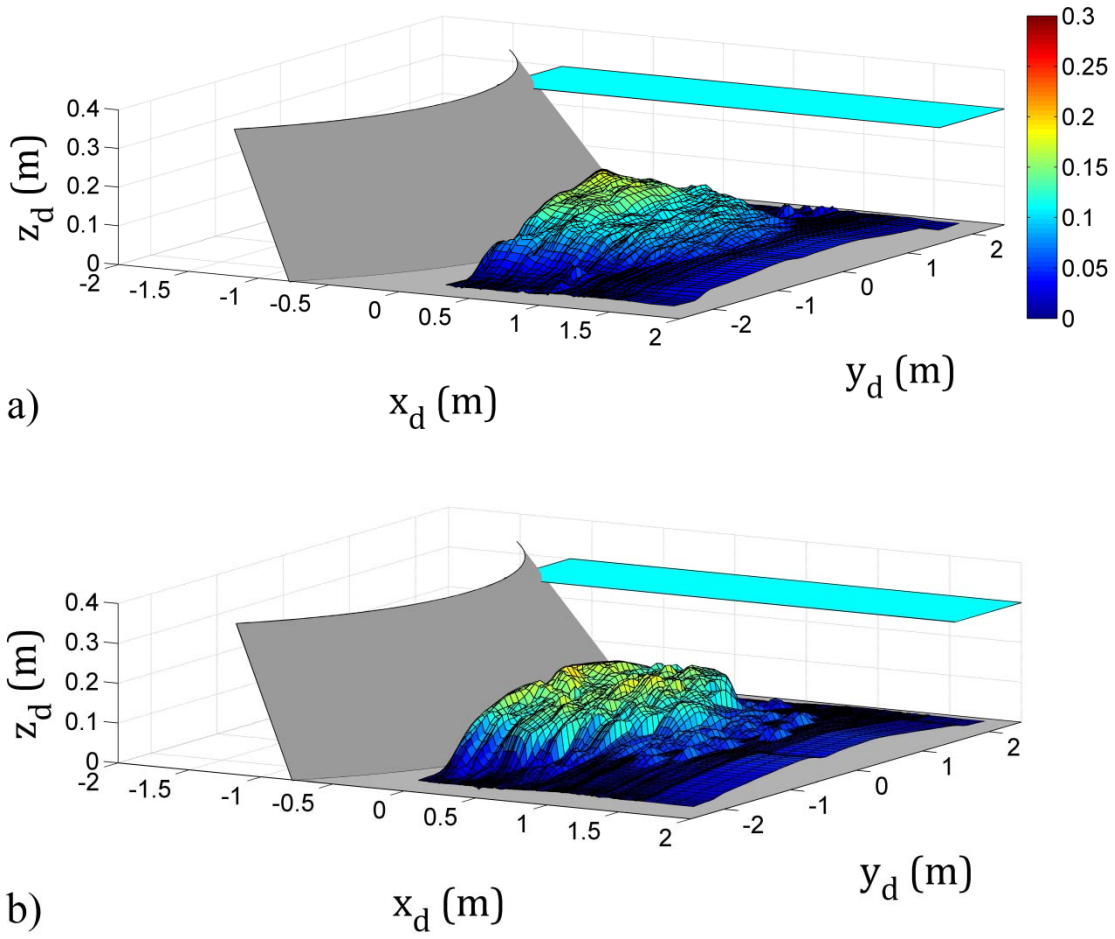

Figure 45: Measured landslide deposit at water depth h = 0.3 m on a convex conical hill slope with landslide mass m_s = 1,350 kg, volume V_s = 0.378 m^3 and peak slide box velocity v_b = 4.0 m/s for (a) gravel and (b) cobble landslides.

Larger cobbles with increased runout distance could be visually observed for qualitative analysis as shown in **Figure 46**. The decreased deposit smoothness with increased runout distance appears to correlate to an increased grain diameter with increased runout distance as observed in **Figure 46a**. The increased runout distance of the larger cobbles mimics the hummock features observed in submarine deposits (Moore et al., 1989).

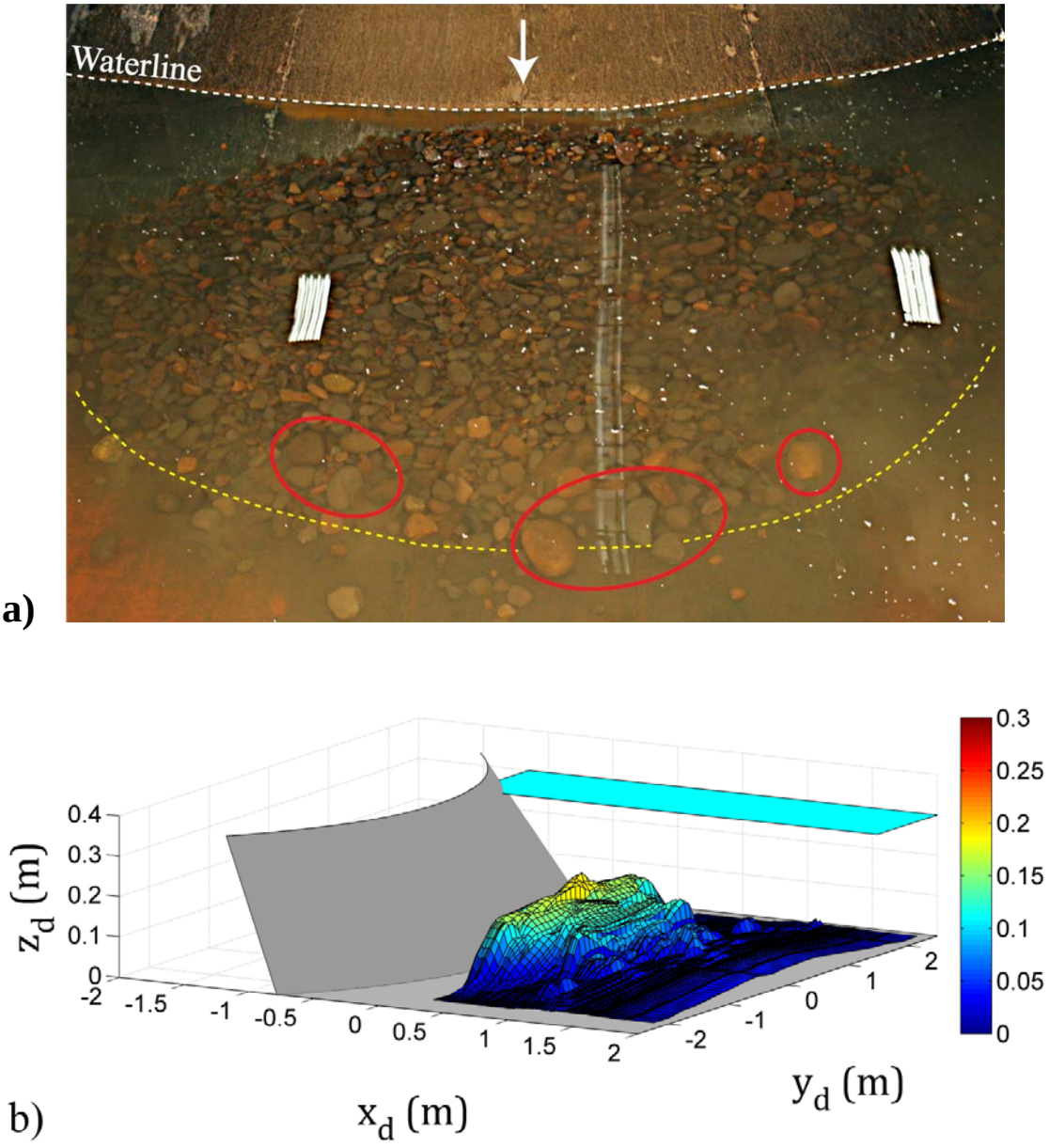

Figure 46: Cobble landslide deposit at water depth h = 0.3 m on a convex conical hill slope with landslide mass m_s = 1,350 kg, volume V_s = 0.378 m^3 and peak slide box velocity v_b = 3.2 m/s: (a) overhead view of the landslide deposit (Note the increased grain diameter with increased runout distance) and (b) measured landslide deposit.

The gravel and cobble landslide deposits produce similar runout distances, but the key difference between the deposits of the two landslide materials is observed in the smoothness of the deposit thickness. Both landslide materials produce a large deposit thickness at the transition

from the hill slope to the basin floor and the thickness decreases with increased runout distance. The surfaces of the gravel landslide deposits are much smoother than those of the cobble landslide deposits with large cobbles producing irregularities in the deposit surface. The hummock type features in the cobble landslide deposits formed by the increased runout distance of the larger cobbles qualitatively mimic seafloor deposits of giant landslides. A separation in the grain size can be observed in some of the cobble landslide deposits with larger grains running out farther than the smaller grains. This is most likely caused by differential acceleration of granulates within the landslide material due to the irregular granulometry of the cobble landslide, and the larger cobbles are less susceptible to frictional forces.

CHAPTER V

OFFSHORE WAVE PROPAGATION

5.1 Introduction

The landslide tsunami generation process is a transient multi-phase flow involving unsteady interaction between the landslide material, air and water. The landslide kinematics and deformation both prior to water surface impact and during the tsunami generation are described in Chapter 4. This chapter focuses on the wave generation and propagation in the offshore direction. The studied tsunami waves were generated by gravel landslides on a planar and convex conical hill slope, and with cobble landslides on a convex conical hill slope. An image sequence of wave generation from a granular landslide on a convex conical hill slope is shown in **Figure 47**.

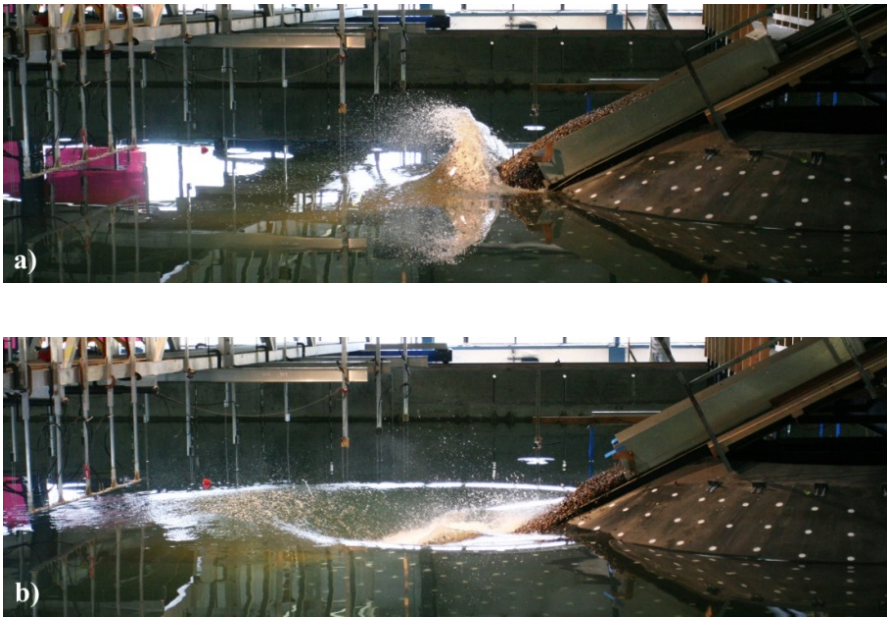

Figure 47: Wave generation at water depth h = 1.2 m: (a) gravel landslide impacting the water body with initial water displacement (b) crater formation and leading wave crest radially propagating.

The offshore waves were investigated in the basin-wide propagation and the conical island scenarios. In the basin-wide propagation and runup scenario 18 offshore wave gauges are analyzed between the two planar hill slopes. The two wave gauges in proximity to the opposing hill slope were omitted from this offshore wave propagation analysis due to interfering wave reflections. The analyzed offshore gauges are spaced in a radial and angular array within the ranges of $3 < r/h < 50$ and $0° < \theta < 75°$. Similarly, in the conical island scenario 21 offshore wave gauges were analyzed in a radial and angular array within the ranges of $3 < r/h < 50$ and $0° < \theta < 90°$. The gauge locations in the basin-side propagation and the conical island scenarios are shown in **Figure 15b** and **Figure 16**, respectively.

The relative position of the wave gauges, *r/h* and θ, are dependent on the water depth. In both scenarios 10 wave gauges were cantilevered from the instrumentation bridge, while the remaining wave gauges were mounted in the basin. The instrumentation bridge was placed close enough to the wave generation source to measure the water surface elevation in the near field region while avoiding landslide runout. The gauge locations were strategically placed to directly compare the waves between the two scenarios and investigate the influence of the lateral hill slope on the offshore propagating wave.

The offshore propagating wave characteristics are dependent on the landslide impact characteristics (Fritz et al., 2003, Mohammed and Fritz, 2012). The landslide tsunami generation process for a gravel landslide on a divergent convex conical hill slope is shown in **Figure 48** and **Figure 49**. The initial moment of the landslide impacting the water is shown in **Figure 48a**. The landslide transfers kinetic energy to the water body and displaces the water in the impact region primarily in the landslide motion direction, but also laterally around the landslide front as shown in **Figure 48b**. The arrows show the water displacement direction. This displacement

produces a radial wave crest which propagates away from the impact site as seen in **Figure 48c** and **Figure 48d**.

The landslide creates an impact crater by drawing down the water surface in the impact region as shown in the **Figure 48c**. This crater becomes the leading wave trough as shown in **Figure 48d**. Crater collapse and gravitational restoring forces drive the fluid uprush and onshore runup evolving into the second wave crest as shown in **Figure 49a** and **Figure 49b**. As the trailing wave crest propagates away from the impact site, the conservation of mass requires a drawdown which becomes the trailing wave trough as shown in **Figure 49d**. After the first two primary waves are generated, several oscillating water surface elevations and depressions occur with corresponding wave runup and rundown on the hill slope producing the subsequent trailing waves. The size of the impact crater generated on both planar and convex conical lateral hill slopes varies with the landslide impact velocity, slide thickness and slide width. This is due to the mass and momentum flux being dependent on these impact parameters.

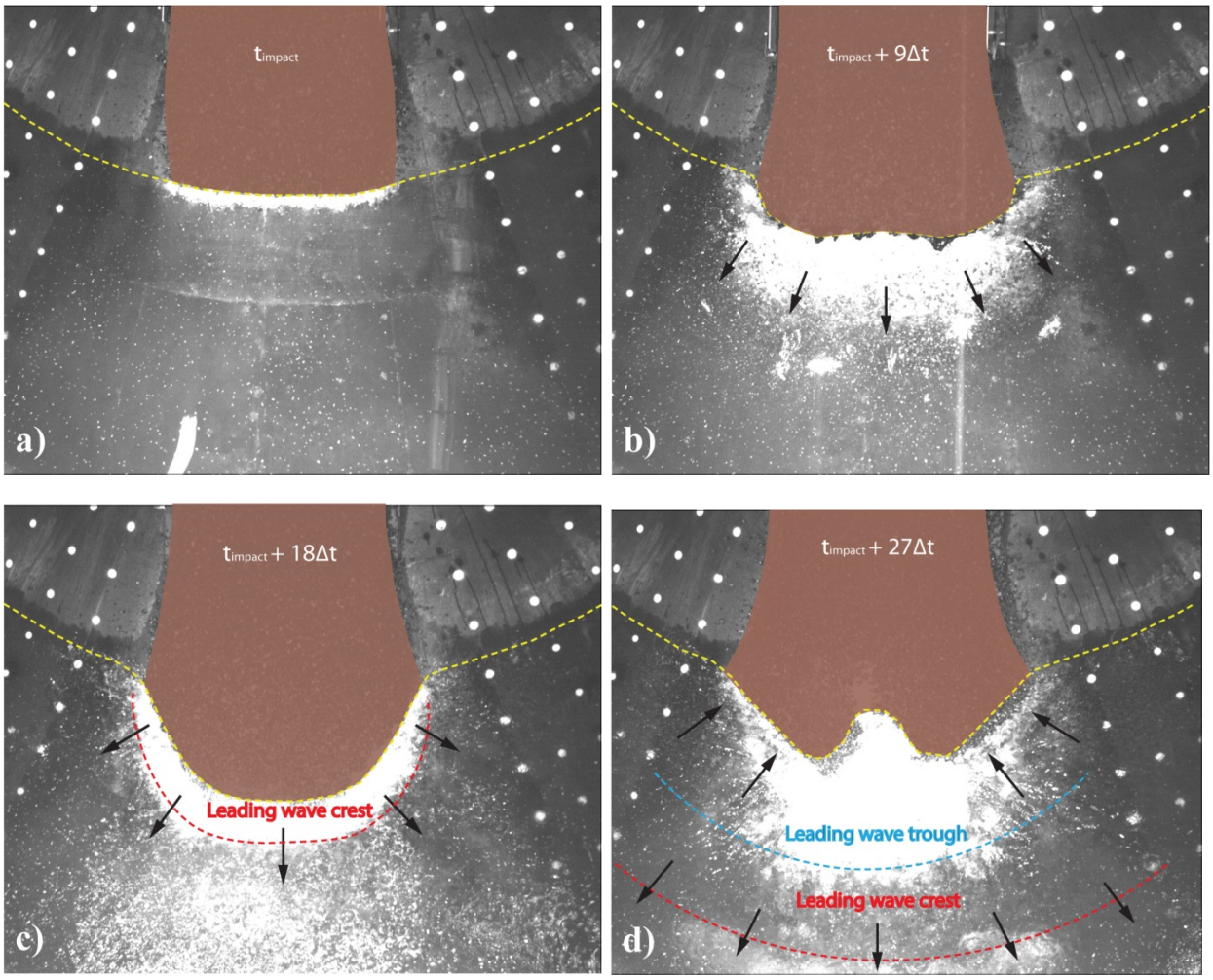

Figure 48: Tsunami generation by a gravel landslide on a divergent convex conical hill slope with landslide Froude number F = 1.8, relative thickness S = 0.23, relative volume V = 1.04 at water depth h=0.9 m at (a) time of landslide front impact with the water, (b) initial water displacement from the landslide, (c) impact crater formation, and (d) initiation of crater collapse. The image recording rate is Δt = 1/30 s.

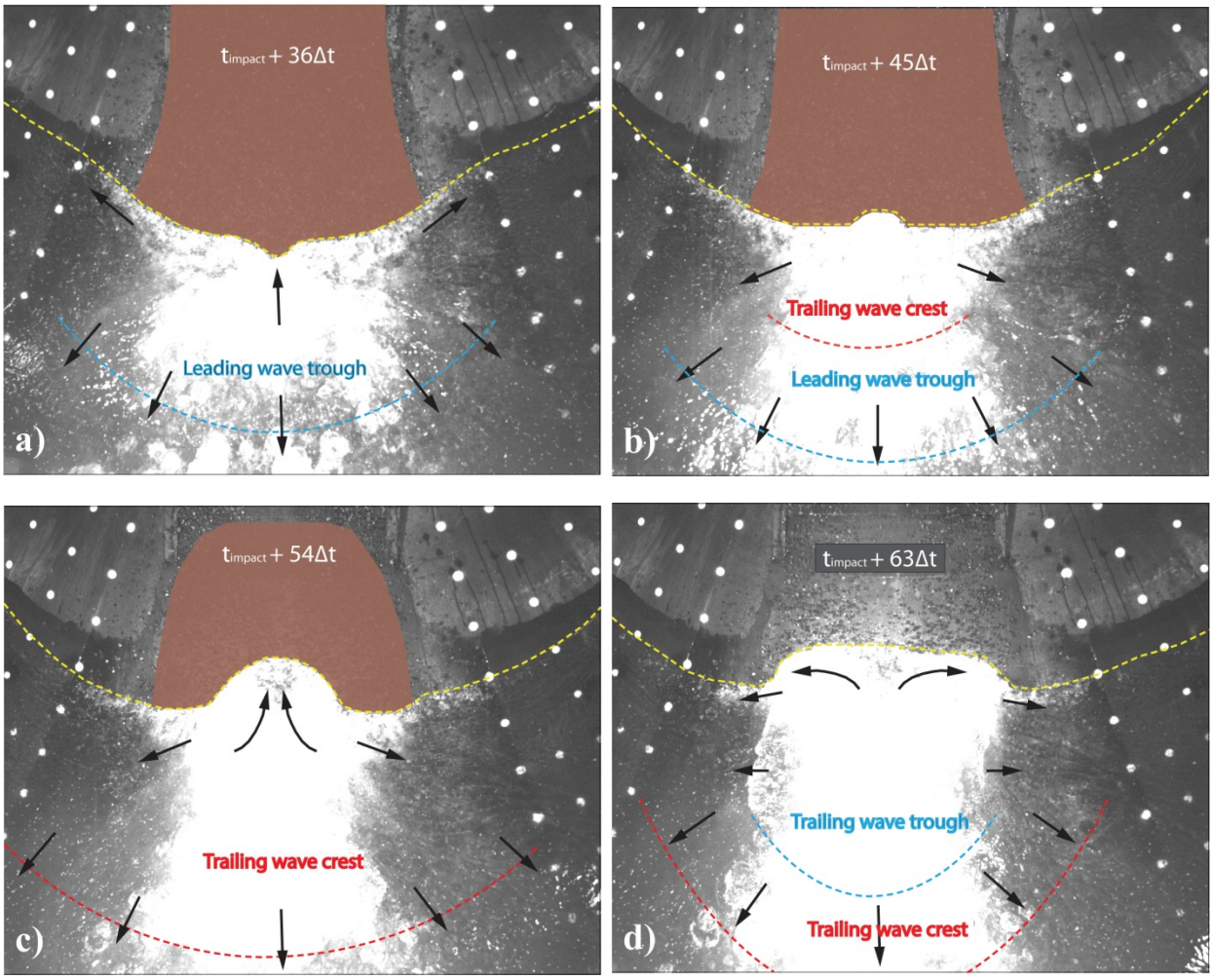

Figure 49: Tsunami generation by a gravel landslide on a divergent convex conical hill slope with landslide Froude number F = 1.8, relative thickness S = 0.23, relative volume V = 1.04 at water depth h=0.9 m at (a) crater collapse and leading wave trough propagation, (b) trailing wave crest formation and leading wave trough propagation, (c) backward runup on the hill slope after crater collapse, and (d) end of the crater collapse. The image recording rate is Δt = 1/30 s.

5.2 Wave Amplitude Attenuation

Tsunami wave crest and trough amplitudes are critical hazard assessment wave characteristics with each posing its own danger. Waves amplitudes in the linear wave regime are equipartitioned, meaning the wave crest amplitude is equal to the wave trough amplitude (Dean and Dalrymple, 1991). In the near field region impulsively generated waves are generally in the

nonlinear regime, characterized by pronounced crests and elongated troughs. Individual wave crest and trough amplitudes are analyzed individually because of the varying amplitudes and celerities of each component.

The definitions of the leading wave amplitudes are shown in **Figure 50a**. The subscripts of *c* and *t* denote the crest and trough amplitudes forming the total wave height $H = a_c + a_t$. The radially propagating waves are measured in a cylindrical coordinate system as shown in **Figure 50b**.

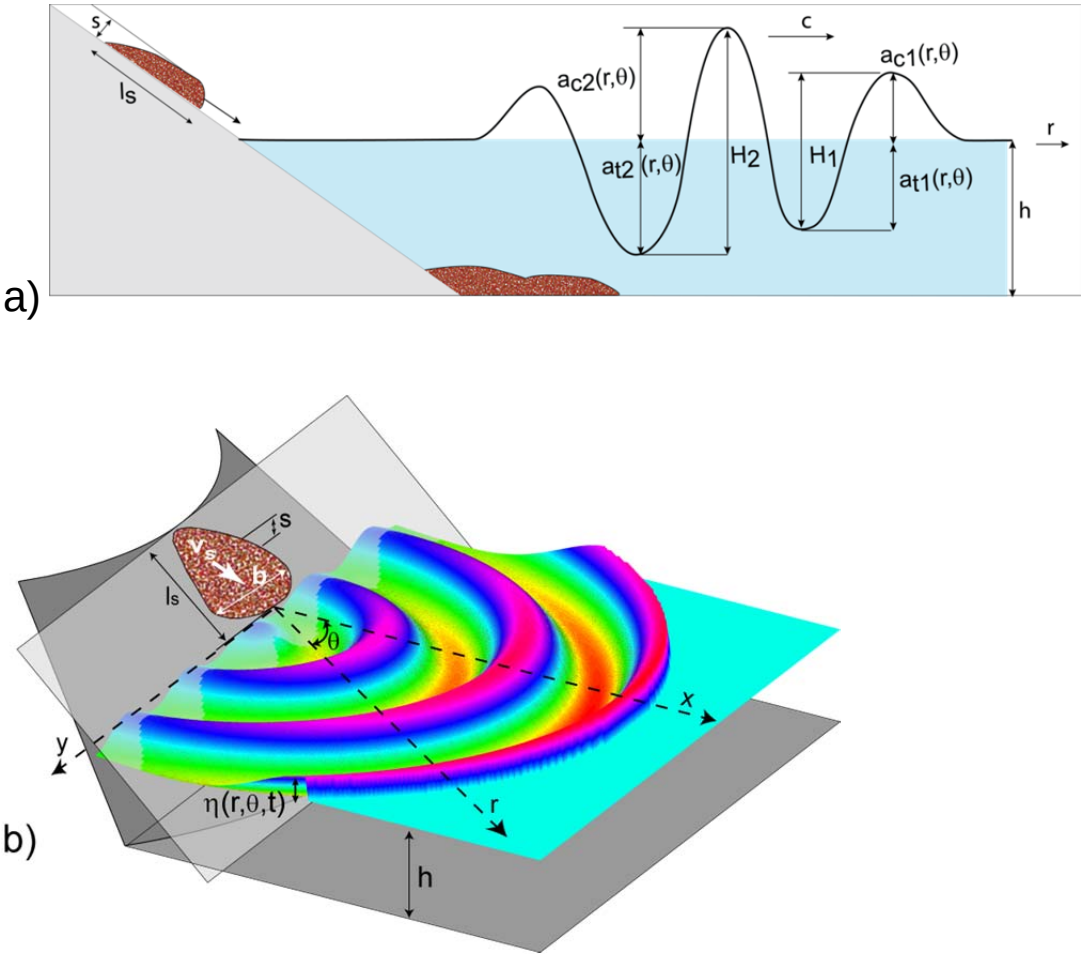

Figure 50: Tsunami amplitude definition sketches: (a) Section view of the wave amplitudes through $\theta = 0°$ and (b) Isometric view of the radial landslide generated waves from planar and conical hill slopes in a cylindrical coordinate system.

5.2.1 Wave Amplitude Attenuation - Planar Hill Slope

Mohammed and Fritz (2012) produced the predictive equations for the leading wave crest and trough amplitudes using the form $a/h = k(r/h)^n \cos\theta$, where k is the wave generation function and n is the amplitude decay function with propagation distance from the source. The leading wave crest amplitude generated on a planar hill slope is given as

$$\frac{a_{c1}}{h} = 0.31\, F^{2.1} S^{0.6} \left({}^{r}/_{h}\right)^{-1.2F^{0.25}S^{-0.02}B^{-0.33}} \cos\theta \tag{67}$$

with the landslide Froude number $F = v_s/\sqrt{gh}$, the relative slide thickness $S = s/h$, the relative distance r/h from the source and the relative slide width $B = b/h$. Equation 60 applied to the leading wave crest amplitude in the present study results in an r^2 correlation coefficient of 0.94. The measured versus predicted leading wave crest amplitude generated by a gravel landslide on a planar hill slope using Equation 67 is shown in **Figure 51**. The associated 50% and 30% error lines are shown, which respectively correspond to 88% and 65% confidence intervals.

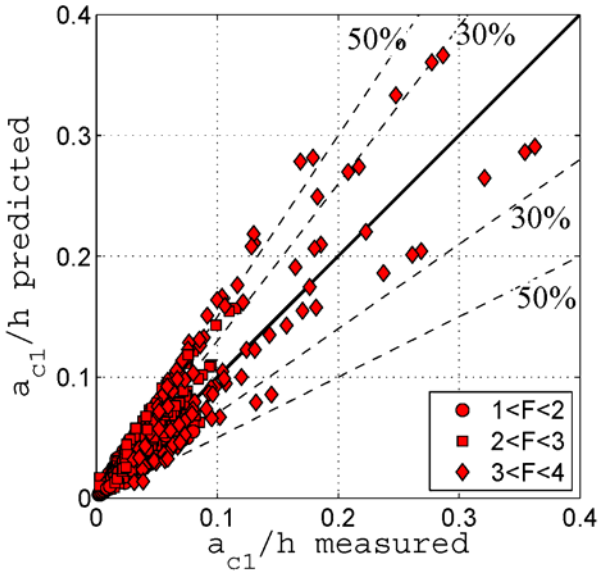

Figure 51: Measured versus predicted first wave crest amplitude a_{c1}/h, generated by a gravel landslide on planar hill slope using Equation 67. The dashed lines denote the 30% and 50% error thresholds.

Measurements of the second crest's amplitude at the water depth h = 0.3 m in the present study can extend the range of parameters incorporated in the second wave crest amplitude predictive equation compared to Mohammed and Fritz (2012). The amplitude data from the first wave trough and second wave crest from the physical model described in Mohammed and Fritz (2012) were combined with amplitude data from the planar hill slope in the present study. The resulting predictive equation for the leading wave trough generated on a planar hill slope has been modified to

$$\frac{a_{t1}}{h} = 0.7\, F^{0.6} S^{0.55} L^{-0.2} \left(r/h\right)^{-1.3\, F^{-0.3} B^{-0.02} L^{-0.2}} \cos\theta \tag{68}$$

where F is the landslide Froude number, S is the relative slide thickness and L is the relative slide length $L = V_s/(sbh)$, resulting in an r^2 correlation coefficient of 0.94 for the combined data set. The predictive equation for the second wave crest can be given as

$$\frac{a_{c2}}{h} = 0.9\, F^{0.7} S^{0.6} B^{-1} L^{-0.5} \left(r/h\right)^{-1.7\, F^{-1} B^{-0.2} L^{-0.4}} \cos^2\theta \tag{69}$$

with an r^2 correlation coefficient of 0.87. The measured versus predicted leading wave trough and second wave crest amplitudes generated on a planar hill slope from the combined data set of Mohammed and Fritz (2012) and the present study are shown in **Figure 52**. The 89% and 84% confidence intervals correspond to the 50% error threshold for the leading wave trough and second wave crest, respectively.

The leading wave crest amplitude is a function of the landslide Froude number and slide thickness and is inversely proportional to the slide width. The strong dependency of the wave amplitude on the landslide Froude number and the slide thickness were shown in 2D granular experiments by Fritz et al. (2004). Increasing the landslide Froude number produces a larger initial displacement of water, resulting in a larger leading wave crest. Decreasing the slide width leads to a generation mechanism closer to a point source with increasing radial decay. The leading wave trough is a function of the landslide Froude number, slide thickness and slide

length. The leading wave trough is generated by the drawdown produced when the landslide impacts the water surface and is dependent on the landslide velocity and length scales, as noted in the equation. The second wave crest is generated by the collapse of the impact crater and is a function of the landslide Froude number, thickness, width and length. The 50% error lines shown in **Figure 52** correspond to confidence intervals of 93% and 84% for the leading wave trough and second wave crest, respectively. The majority of predicted values with more than 50% error from the measured amplitude value occur with very small amplitudes, causing minor deviations to become large error percentages. Error in predictive equations from physical models commonly exceed 50% for small values as observed in Heller and Spinneken (2013).

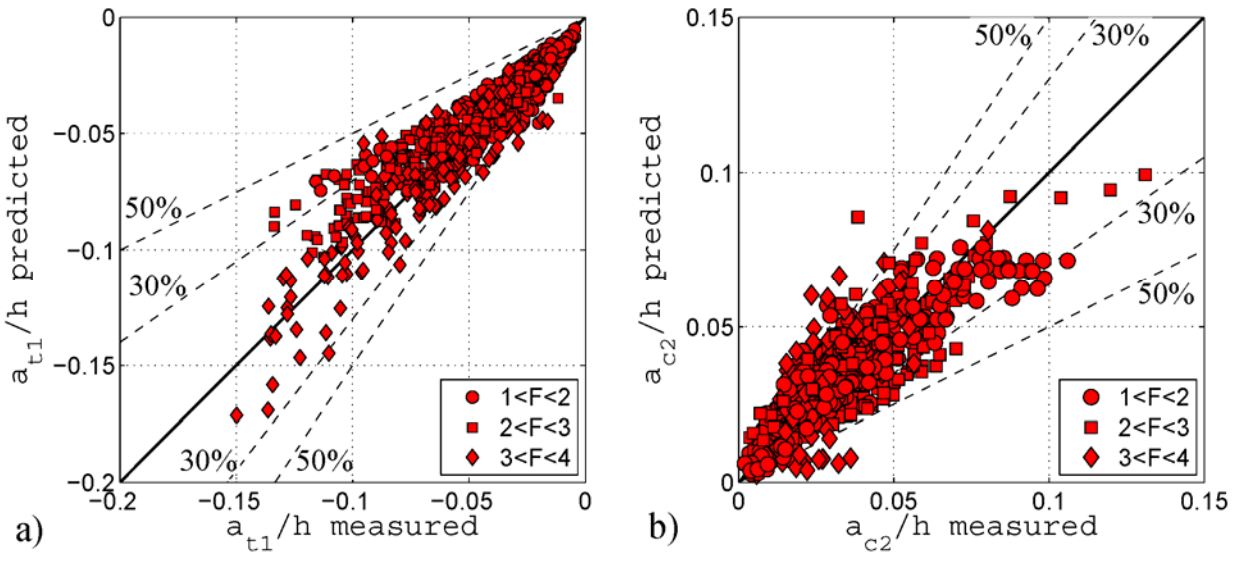

Figure 52: Measured versus predicted wave amplitude generated by a gravel landslide on planar hill slope for (a) the first wave trough a_{t1}/h, using Equation 68 and (b) second wave crest a_{c2}/h, using Equation 69. The 30% and 50% error thresholds are shown with dashed lines.

5.2.2 Comparison With Previous Studies

Panizzo et al. (2005) physically modeled landslide generated tsunamis in a three-dimensional basin with a sliding block down a rectangular trolley ramp. Shock absorbers at the toe of the ramp abruptly stopped the block cropping the runout along the basin floor. Similar to Watts (2000), the relative time of underwater motion was determined to be an important factor which is given as

$$t_s^* = 0.43\left(\frac{b_s}{h^2}\right)^{-0.27} F^{-0.66}(\sin\alpha)^{-1.32} \tag{70}$$

The predicted first wave height by Panizzo et al. (2005) is given by

$$\frac{H_1}{h} = 0.07\, {t_s^*}^{-0.3} {A_w^*}^{0.88}(\sin\alpha)^{-0.8}\exp(1.37\cos\theta)\left(\frac{r}{h}\right)^{-0.81} \tag{71}$$

where A_w^* is the dimensionless front cross-section such that $A_w^* = (bs)/h^2$. The mechanical absorbers at the toe of the ramp cropped the underwater slide runout and significantly reduced the duration of slide motion compared to the granular landslide runout of the present study. This results in an under prediction by a factor of two when applying Equation 71 to the present study as shown in **Figure 53a**. Doubling the predicted values produces an r^2 correlation coefficient of 0.94 with the leading wave height generated with a gravel landslide on a planar hill slope, matching the results discussed in Mohammed and Fritz (2012).

Huber (1980) conducted 3-D physical experiments on landslide generated tsunamis with granular material released by a rotating flap on a ramp that was laterally confined by sidewalls forming a chute for the subaerial portion of the ramp. The lack of sidewalls and lateral hill slope extensions in the basin produced complex hydrodynamics around the edges of the ramp in the landslide impact site. Huber and Hager (1997) used wave amplitude data from Huber (1980) to

produce a radial wave height distribution and decay figure without showing the underlying experimental data and derived the predictive equation for the maximum wave height as

$$\frac{H_m}{h} = 2 \times 0.88 \sin\alpha \cos^2\left(\frac{2\theta}{3}\right)\left(\frac{\rho_s}{\rho_w}\right)^{0.25}\left(\frac{V_s}{b_s h^2}\right)^{0.5}\left(\frac{r}{h}\right)^{-0.81} \quad (72)$$

where α is the ramp slope angle, ρ_s is the landslide density and ρ_w is water density. Equation 72 over predicts the majority of the leading wave height measurements in the present study with an r^2 correlation coefficient of 0.73. Equation 72 does not include the landslide Froude number F or any other dynamic parameter, relative slide thickness or relative slide width at impact. This leads to an over prediction and scatter in the comparison shown in **Figure 53b**.

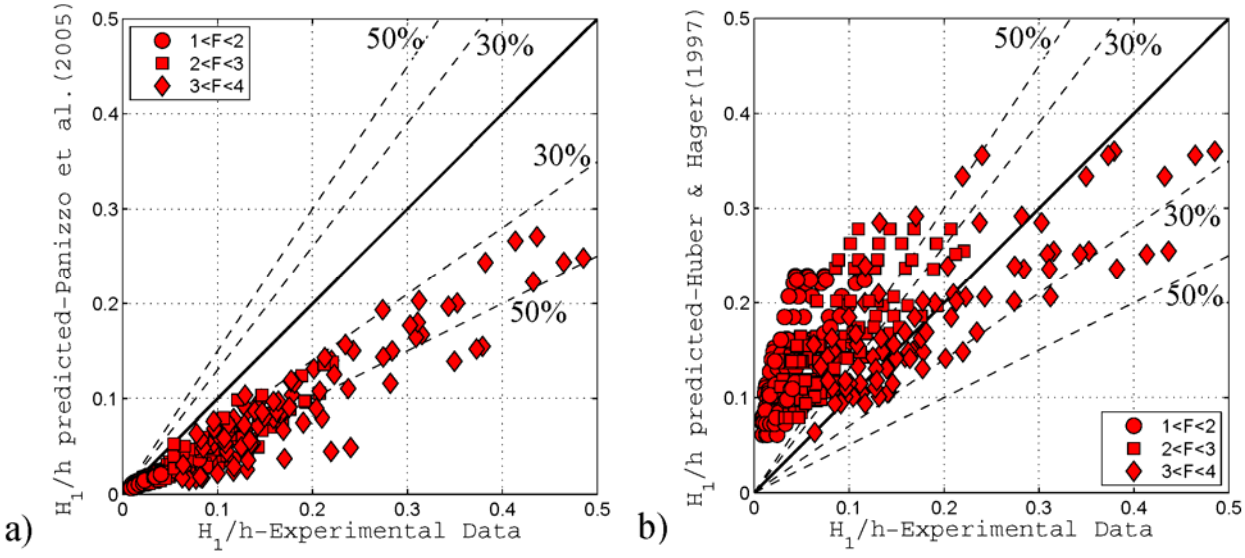

Figure 53: Measured leading wave height H_1/h, generated by a granular landslide on a planar hill slope compared to the predicted leading wave height from (a) Panizzo et al. (2005) and (b) Huber and Hager (1997).

5.2.3 Wave Amplitude Attenuation – Convex Conical Hill Slope

The applicability of Equation 67, which was derived by Mohammed and Fritz (2012), has been extended for application to a convex conical hill slope with the addition of a coefficient to the wave generation function, *k*, of the equation and to the amplitude decay function, *n*, of the function. The leading wave crest amplitude generated on a convex conical hill slope can be given as

$$\frac{a_{c1}}{h} = 0.31\, F^{2.1} S^{0.6} C_{kc1} \left(\frac{r}{h}\right)^{-1.2\, F^{0.25} S^{-0.02} B^{-0.33} C_{nc1}} \cos\theta \tag{73}$$

where C_{kc1} is the wave generation conical coefficient given by

$$C_{kc1} = \frac{tanh\left(F\, S^{3.05} B^2 {R_c}^{0.4}\right)}{tanh\left(F^{0.4} S^{2.8} B^{1.1} {R_c}^{0.94}\right)} \tag{74}$$

and C_{nc1} is the amplitude decay conical coefficient given by

$$C_{nc1} = \frac{tanh\left(F^{-1} S^{0.63} {R_c}^{1.6}\right)}{tanh\left(F^{-0.68} S^{0.06} {R_c}^{0.34}\right)} \tag{75}$$

where R_c is the relative shoreline radius $R_c = r_c/h$, with an r^2 correlation coefficient of 0.93. The generation conical coefficient C_{kc1} is a function of the landslide Froude number, thickness, width and shoreline radius, and the decay conical coefficient C_{nc1} is a function of the Froude number, thickness and shoreline radius. The conical coefficients for the leading wave crest were in the ranges of $0.6 < C_{kc1} < 2.1$ and $0.8 < C_{nc1} < 1.4$. The impact parameters *F*, *S* and *B* are mass and momentum flux variables and R_c describes the shoreline curvature of the lateral hill slope. As R_c gets larger, the conical coefficient becomes asymptotic to 1 and the equation transitions back to the planar hill slope equation. Likewise the following equations for the subsequent troughs and crests smoothly transition from conical island to planar hill slopes.

Similar to the leading wave crest, the applicability of Equation 68 was extended to predict the leading wave trough a_{t1}/h generated on a convex conical hill slope by adding two coefficients. The leading wave trough amplitude generated on convex conical hill slope is given by

$$\frac{a_{t1}}{h} = 0.7\, F^{0.6} S^{0.55} L^{-0.2} C_{kt1} \left(r/h\right)^{-1.3\, F^{-0.3} B^{-0.02} L^{-0.2} C_{nt1}} \cos\theta \tag{76}$$

where C_{kt1} is the generation convex conical coefficient given by

$$C_{kt1} = \frac{tanh\left(S^{-1} B^{2.5} {R_c}^{0.9}\right)}{tanh\left(S^{0.3} B^{0.1} {R_c}^{0.1}\right)} \tag{77}$$

and C_{nt1} is the decay convex conical coefficient given by

$$C_{nt1} = \frac{tanh\left(S^{-2.4} L^{0.75} {R_c}^{0.05}\right)}{tanh\left(S^{0.25} L^{-0.06} {R_c}^{0.6}\right)} \tag{78}$$

resulting in an r^2 correlation coefficient of 0.95. The conical coefficients for the leading wave trough were in the ranges of $1 < C_{kt1} < 2$ and $1 < C_{nt1} < 1.5$. The measured versus predicted leading wave tough amplitude generated on a convex conical hill slope using Equation 76 is shown in **Figure 54**.

The amplitude of the second wave crest a_{c2}/h generated on a convex conical hill slope is given as

$$\frac{a_{c2}}{h} = 0.9\, F^{0.7} S^{0.6} B^{-1} L^{-0.5} C_{kc2} \left(r/h\right)^{-1.7\, F^{-1} B^{-0.2} L^{-0.4} C_{nc2}} \cos^2\theta \tag{79}$$

where C_{kc2} is the generation conical coefficient given by

$$C_{kc2} = \frac{tanh\left(S^{-2.9} L^{0.3} {R_c}^{2.5}\right)}{tanh\left(S^{-0.03} L^{-0.3} {R_c}^{0.2}\right)} \tag{80}$$

and C_{nc2} is the decay conical coefficient given by

$$C_{nc2} = \frac{tanh\left(B^{-5}V^{0.25}{R_c}^4\right)}{tanh\left(B^{0.55}V^{-0.12}{R_c}^2\right)} \quad (81)$$

with an r^2 correlation coefficient of 0.88. The wave generation of the second wave amplitude on the convex conical hill slope was determined to be dependent on the landslide Froude number, thickness, width, length and shoreline radius. The decay function was determined to be dependent on the landslide Froude number, width, length, volume and shoreline radius. The conical coefficients for the second wave crest were in the ranges of $1.1 < C_{kc2} < 1.8$ and $0.4 < C_{nc2} < 1$. The predicted second wave crest amplitude generated on a convex conical hill slope using Equation 79 is compared to the measured values in **Figure 54a**.

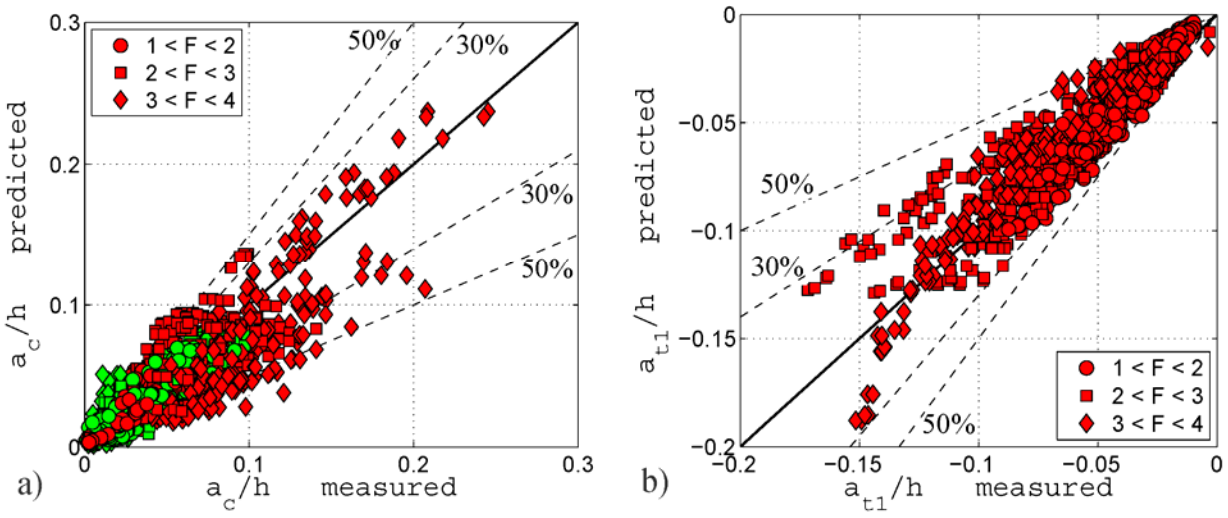

Figure 54: Measured versus predicted wave amplitude generated on a convex conical hill slope for (a) first wave crest a_{c1}/h (red) and second wave crest a_{c2}/h (green), and (b) first wave trough a_{t1}/h. The 30% and 50% error thresholds are shown with dashed lines.

5.2.4 Lateral Hill Slope Effects

The lateral hill slope effects on the wave amplitude are compared between the planar and convex conical hill slopes. The ratio of wave amplitudes generated by a gravel landslide on planar (a_{plan}) and convex conical (a_{con}) hill slopes for the first wave crest, first wave trough and second wave crest are in the ranges $1.01 < a_{c1plan}/a_{c1con} < 1.09$, $0.76 < a_{t1plan}/a_{t1con} <$

0.9 and $0.77 < a_{c2plan}/a_{c2con} < 0.85$. The mean values for the lateral hill slope ratios for the first wave crest, first wave trough and second wave crest are 1.03, 0.85 and 0.80, respectively. The measured wave amplitudes generated by a gravel landslide on planar and convex conical hill slopes are shown in **Figure 55**. The leading wave crest amplitude was on average larger when generated on the planar hill slope than the convex conical hill slope. The leading wave trough and second wave crest were on average smaller when generated on the planar hill slope than the convex conical hill slope. The lateral hill slope plays a more significant role in the impact crater formation and crater collapse which become the leading wave trough and second wave crest. The increased amplitude of the leading wave trough and second wave crest on the convex conical hill slope may be due to the curvature of the island shoreline being closer to normal with the wave rays of the offshore propagating radial waves than the planar hill slope.

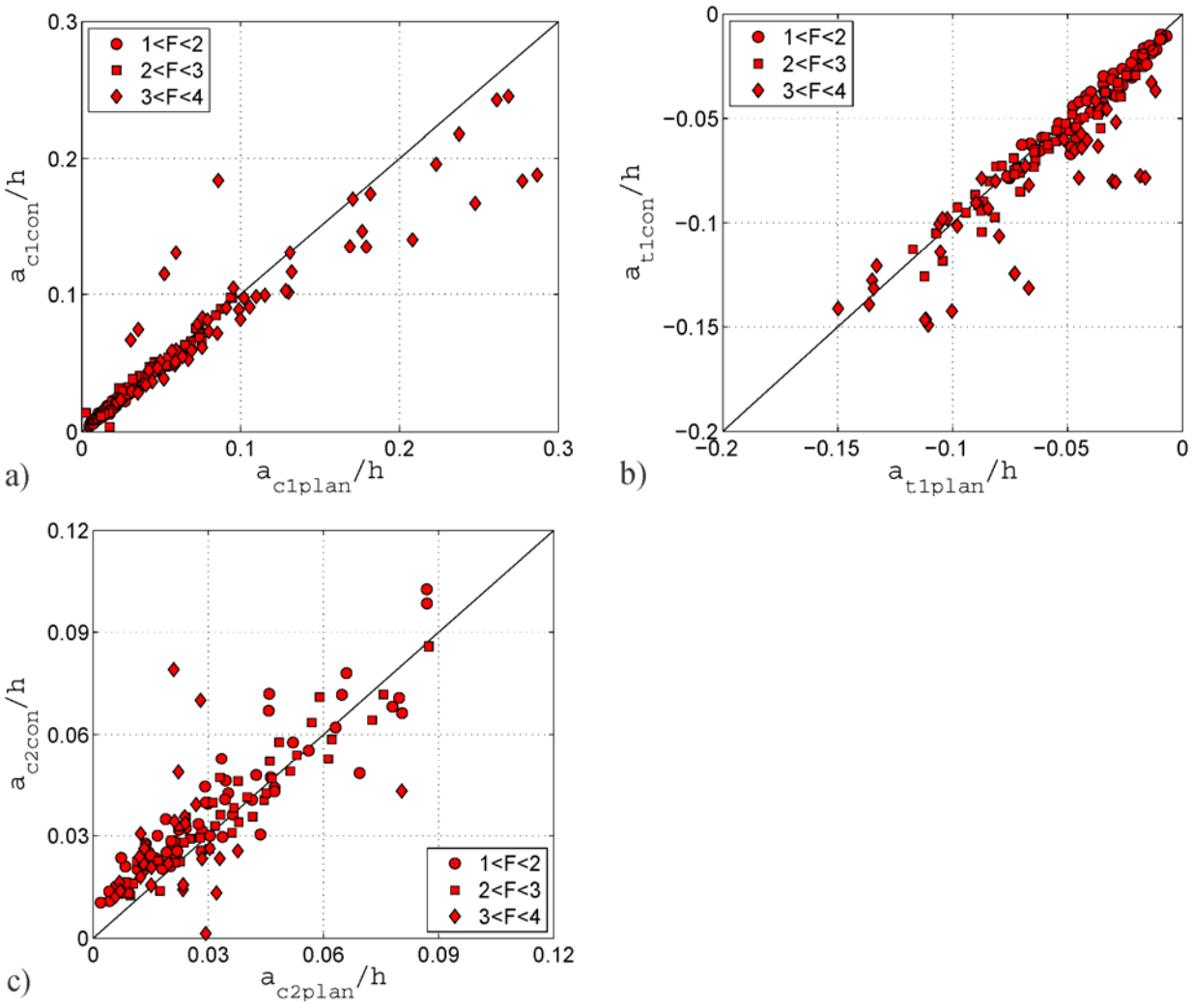

Figure 55: Wave amplitudes generated on a planar versus conical lateral hill slope comparison for (a) first wave crest $a_{c1plan}/\ a_{c1con}$, (b) first wave trough $a_{t1plan}/\ a_{t1con}$, and (c) second wave crest $a_{c2plan}/\ a_{c2cob}$.

5.2.5 Landslide Granulometry Effects

The effects of the landslide granulometry on the wave amplitudes are compared with gravel and cobble landslides on the convex conical hill slope. The ratios of the wave amplitudes generated by cobble (a_{cob}) and gravel (a_{grav}) landslides for the first wave crest, first wave trough

and second wave crest are in the ranges $1.08 < a_{c1cob}/a_{c1grav} < 1.51$, $1.08 < a_{t1cob}/a_{t1grav} < 1.46$ and $0.82 < a_{c2cob}/a_{c2grav} < 1.28$. The mean values for the granulometry ratios are 1.25, 1.20 and 1.11 for the first wave crest, first wave trough and second wave crest, respectively. On average the cobble landslide produced mostly larger wave amplitudes than the corresponding gravel landslide with the differences being most pronounced for the first wave crest and trough. The wave amplitudes generated by cobble and gravel landslides on the convex conical hill slope are shown in **Figure 56**.

The larger wave amplitude created by the cobble landslide than the gravel landslide could be due to a more efficient energy transfer from the landslide to the wave. It was observed that the cobble landslide width was narrower than the gravel landslide on the convex conical hill slope and although the maximum thickness in the center of the landslide was equivalent between the landslide materials, the cobble landslide thickness would decay less rapidly across the width of the landslide front compared to the gravel. The larger cobbles would also have more inertia to displace water than smaller gravel granulates. This becomes clear in the deposits with larger cobbles producing larger runout than smaller material.

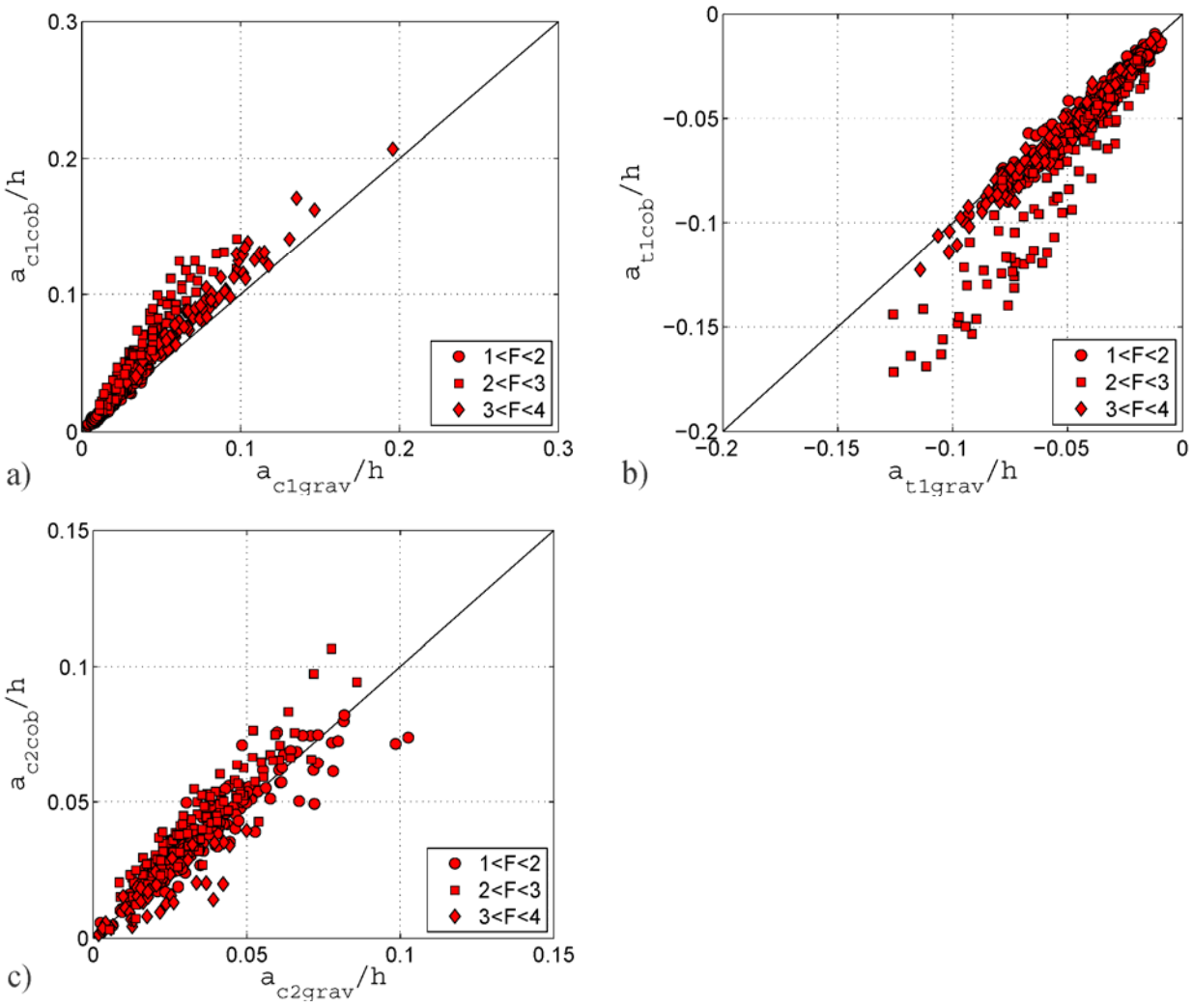

Figure 56: Wave amplitude comparison generated by gravel and cobble landslides on a convex conical hill slope for (a) first wave crest $a_{c1cob}/\ a_{c1grav}$, (b) first wave trough $a_{t1cob}/\ a_{t1grav}$, and (c) second wave crest $a_{c2cob}/\ a_{c2grav}$.

5.3 Wave Period

The tsunami wave periods are measured from the water surface elevation time series recordings at each wave gauge in the array. The individual waves in the wave train are measured with a zero up-crossing point technique adequate for the characterization of positive leading N-

waves. The wave gauges record the wave profiles in the time domain and the zero up-crossing points provide the time coordinates of the waves. The time difference between the up-crossing points is the wave period. The first up-crossing point is defined as 5% of the first wave crest amplitude, $\eta = 0.05\, a_{c1}$. The wave gauges are spaced in a radial array (r, θ) to describe the wave period evolution in the spatial domain. The wave period measurement definition using the up-crossing method is shown in **Figure 57**.

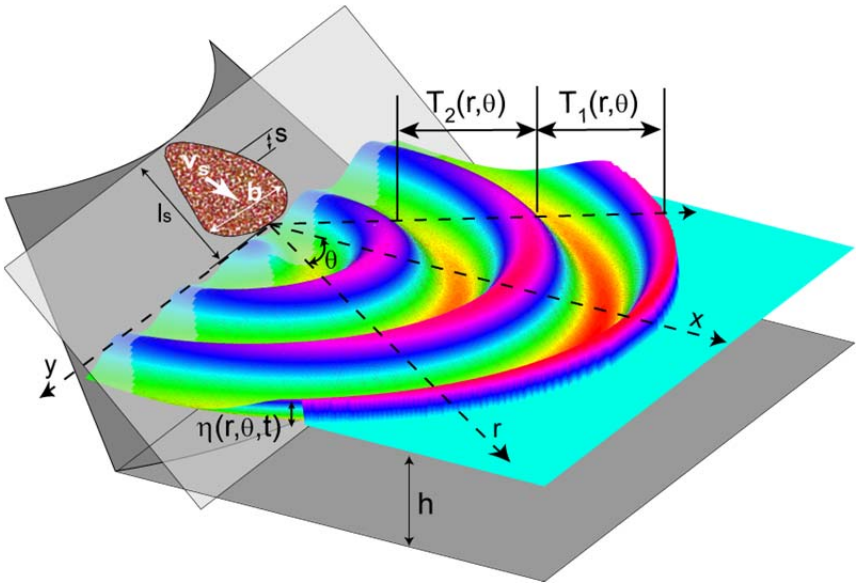

Figure 57: Wave period definition using the up-crossing method for radial positive leading N-waves generated by deformable granular slides on planar and convex conical hill slopes.

The first two wave periods are analyzed and predictive equations are derived for them. The usable portion of the wave profiles was truncated by wave reflections, prohibiting the analysis of additional wave periods for some wave gauges. The offshore propagating wave periods were measured in the spatial ranges of $3 < r/h < 50$ and $0° < \theta < 75°$ with the planar hill slope and $3 < r/h < 50$ and $0° < \theta < 90°$ with the convex conical hill slope. The offshore propagating tsunami wave periods generated by a granular landslide on a planar hill slope are

invariable in the angular direction, producing a nearly constant radial wave front (Mohammed, 2010).

The first two offshore propagating wave periods were in the ranges of $5 < T_1\sqrt{g/h} < 22$ and $2 < T_2\sqrt{g/h} < 10$ for waves generated on both the planar and convex conical hill slopes. Mohammed and Fritz (2012) produced predictive wave period equations for impulsively generated waves by granular landslides on a planar hill slope. The first offshore propagating wave period is described as

$$T_1\sqrt{\frac{g}{h}} = 4.8\, F^{0.21} S^{0.05} L^{0.04} \left(\frac{r}{h}\right)^{0.3} \tag{82}$$

with the landslide Froude number $F = v_s/\sqrt{gh}$, the relative slide thickness $S = s/h$, the relative slide length $L = V/(bsh)$, and *r/h* is the relative distance from the slide impact. Equation 82 matches the measured first wave period of the present study with an r^2 correlation coefficient of 0.94. The second wave period is described as

$$T_2\sqrt{\frac{g}{h}} = 3.0\, F^{0.03} S^{0.03} L^{0.01} \left(\frac{r}{h}\right)^{0.25} \tag{83}$$

with an r^2 correlation coefficient of 0.89. The measured versus predicted wave periods for waves generated by granular landslides on a planar hill slope are shown in **Figure 58a** and **Figure 58b**. The 50% error lines correspond to a confidence interval of 95% for the first two wave periods on a planar hill slope.

An additional coefficient is added to the existing planar hill slope wave period equations to make them applicable to a convex conical hill slope. The first offshore propagating wave period from a convex conical hill slope is given as

$$T_1\sqrt{\frac{g}{h}} = 4.8\, F^{0.21} S^{0.05} L^{0.04} C_{T1} \left(\frac{r}{h}\right)^{0.3} \tag{84}$$

where C_{TI} is the conical hill slope coefficient for the first wave period and is given as

$$C_{T1} = \coth\left(R_c{}^{0.57}\right) \tag{85}$$

where R_c is the dimensionless shoreline radius $R_c = r_c/h$. Equation 84 corresponds to the measured first wave period generated from a conical hill slope with an r^2 correlation coefficient of 0.96. The conical coefficient for the leading wave period was in the range of $1.0 < C_{T1} < 1.1$. Similarly, a coefficient was added to the planar hill slope second wave period predictive equation to transition to the conical hill slope. The second offshore propagating wave period from a convex conical hill slope is given as

$$T_2\sqrt{\frac{g}{h}} = 3.0\, F^{0.03} S^{0.03} L^{0.01} C_{T2} \left(\frac{r}{h}\right)^{0.25} \tag{86}$$

where the conical hill slope coefficient C_{T2} is

$$C_{T2} = \coth\left(R_c{}^{1.4}\right) \tag{87}$$

producing an r^2 correlation coefficient with the measured second wave period of 0.92. The conical coefficient for the leading wave period was in the range of $1.0 < C_{T2} < 1.05$. The conical hill slope coefficients are asymptotic to 1 as relative shoreline radius goes to infinity, transforming the conical hill slope equation into planar hill slope equation for large shoreline radiuses. The measured versus predicted wave periods for waves generated on a convex conical hill slope are shown in **Figure 58c** and **Figure 58d**.

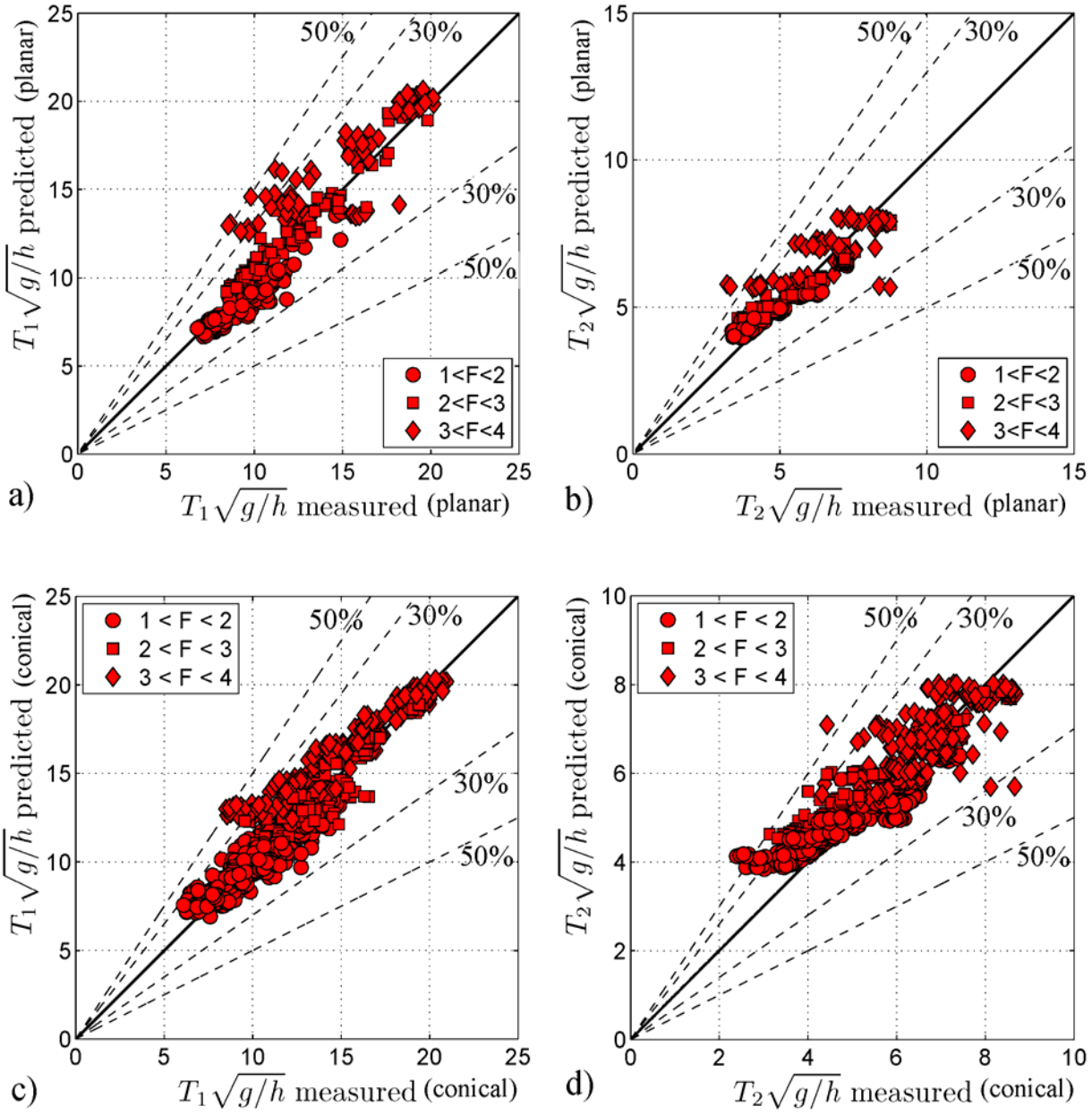

Figure 58: Measured versus predicted wave period (a) first wave period $T_1\sqrt{g/h}$ from a planar hill slope using Equation 82, (b) second wave period $T_2\sqrt{g/h}$ from a planar hill slope, (c) first wave period from a convex conical hill slope using Equation 84 and (d) second wave period from convex conical hill slope. The 30% and 50% error thresholds are shown with dashed lines.

The influence of the lateral hill slope on the wave period is analyzed by comparing the ratio of the wave periods generated on planar and convex conical hill slopes. The ratio of the

wave periods generated with gravel landslide material on a planar hill slope T_{plan} and a convex conical hill slope T_{con} are in the ranges $0.75 < T_{1plan}/T_{1con} < 1.37$ and $0.66 < T_{2plan}/T_{2con} < 1.35$ with practically equal mean values of 1.01 and 0.99 for the first and second wave periods, respectively. **Figure 59** compares the wave periods generated by gravel landslides on planar and convex conical hill slopes. The lateral hill slope appears to play a minor role in the offshore propagating wave period.

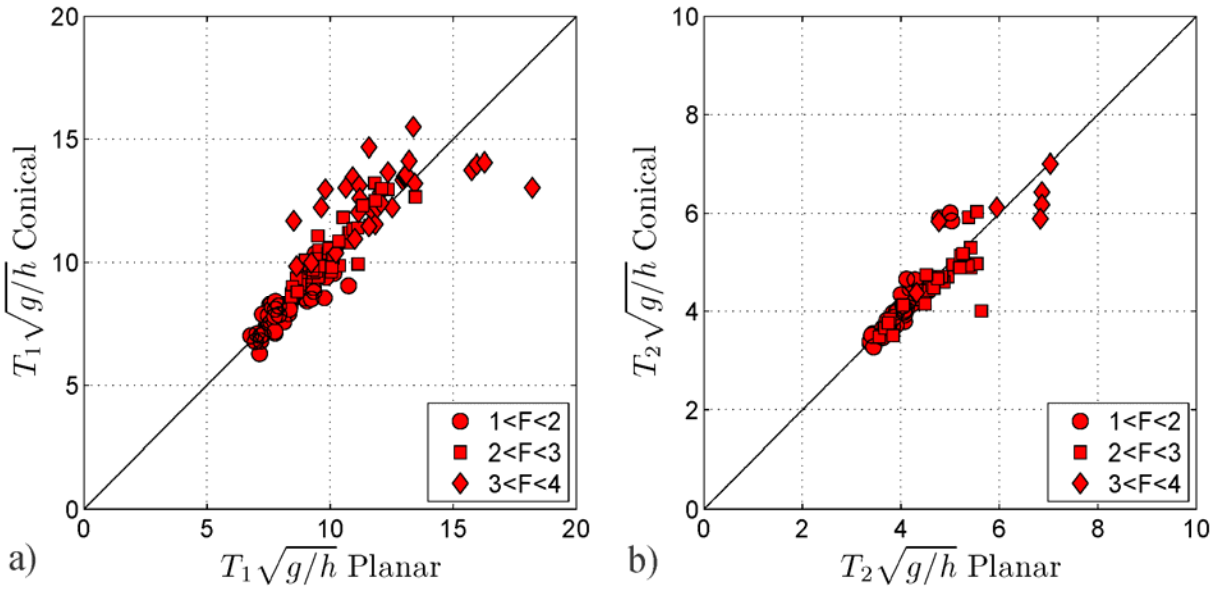

Figure 59: Comparison of the wave periods generated by a gravel landslide on planar T_{plan} and convex conical T_{con} hill slopes for (a) first wave period $T_1\sqrt{g/h}$ and (b) second wave period $T_2\sqrt{g/h}$.

The effects of the landslide granulometry on the offshore propagating wave period generated on the convex conical hill slope are analyzed. The ratios of the cobble landslide generated wave periods T_{1cob} to the gravel landslide generated wave periods T_{1grav} are in the

ranges of $0.73 < T_{1cob}/T_{1grav} < 1.40$ and $0.81 < T_{2cob}/T_{2grav} < 1.41$. **Figure 60** compares the wave periods generated by cobble and gravel landslides on a convex conical hill slope. The landslide granulometry appears to have a minor effect on the wave period.

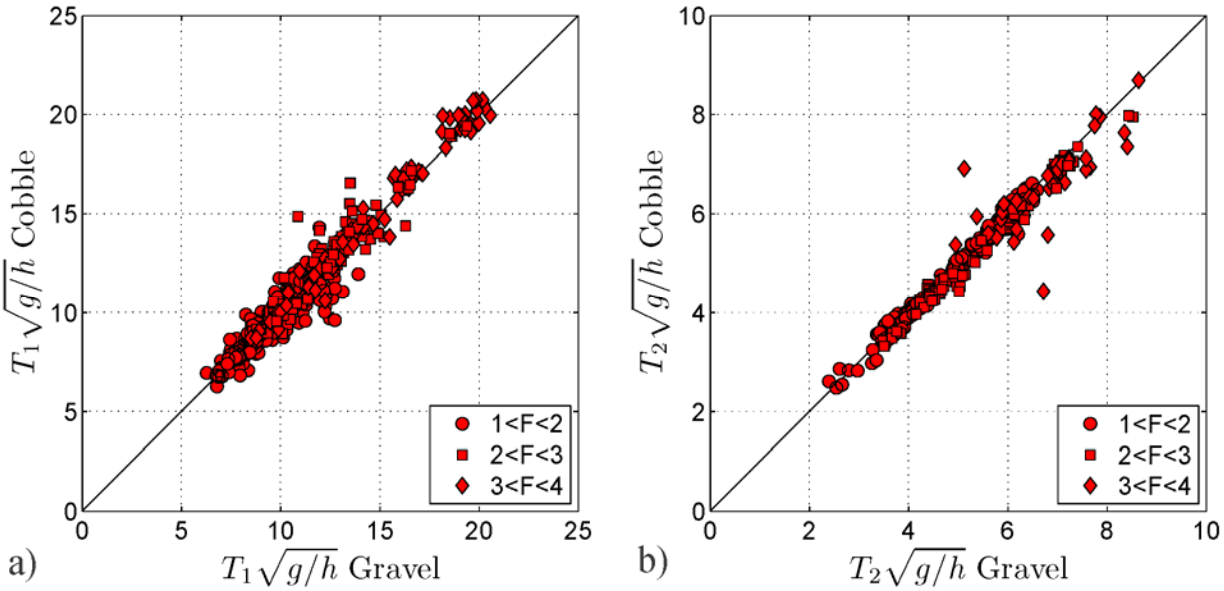

Figure 60: Comparison of the wave periods generated on a convex conical hill slope by gravel T_{1grav} and cobble T_{1cob} landslides for (a) first wave period $T_1\sqrt{g/h}$ and (b) second wave period $T_2\sqrt{g/h}$.

5.4 Wave Celerity

The tsunami wave celerity is important to calculate tsunami arrival times for issuing and canceling tsunami warnings. The wave celerity of a linear wave can be determined if the wave period or length and the water depth are known using the linear dispersion relationship. Linear wave mechanics are only appropriate when *a/h* < 0.03 (Dean and Dalrymple, 1991). The range

of *a/h* in the present study is in the range $0.001 < a/h < 0.35$. The measured wave amplitudes are typically nonlinear in the near field region, but may become linear with increased distance from the impact location.

The nonlinear solitary wave theory celerity has been used to predict the wave celerity of impulsively generated waves (Russell, 1844; Fritz, 2002; Mohammed and Fritz, 2012). The speed of a solitary wave is given as

$$\frac{c_{c1}}{\sqrt{gh}} = 1 + \frac{a_{c1}}{2h} \tag{88}$$

where $a_{c1} = H$ for a solitary wave (Boussinesq, 1872; Laitone, 1960). The breaking limit for a solitary wave was given by McCowan (1894) as $H_b/h = 0.78$, hence the non-breaking solitary wave celerity can exceed the linear shallow water celerity of $c = \sqrt{gh}$ by 39%. This increased celerity can lead to early tsunami arrival times when compared to the linear shallow water celerity.

The wave celerity is measured for the individual wave crests and troughs as each component propagates from gauge to gauge along an angular wave ray. The celerity is obtained by dividing the distance between wave gauges by the travel time of the wave crests and troughs to pass the successive wave gauges in an angular array. The offshore propagating wave ranged in the angular dimension from 0° to 75° in the basin-wide propagation and runup scenario and 0° to 90° in conical island scenario. The measured wave celerity as a function of the wave amplitude for waves generated on planar and convex conical hill slopes are shown in **Figure 61** and **Figure 62**, respectively. A combined data set from Mohammed and Fritz (2012) and the present study is shown in **Figure 61** to show the complete data set that was used in the derivation of the new amplitude attenuation equations for the leading wave trough and second crest. The measured wave celerity is nondimensionalized with the linear shallow water celerity and the solitary wave celerity is shown with a dashed line.

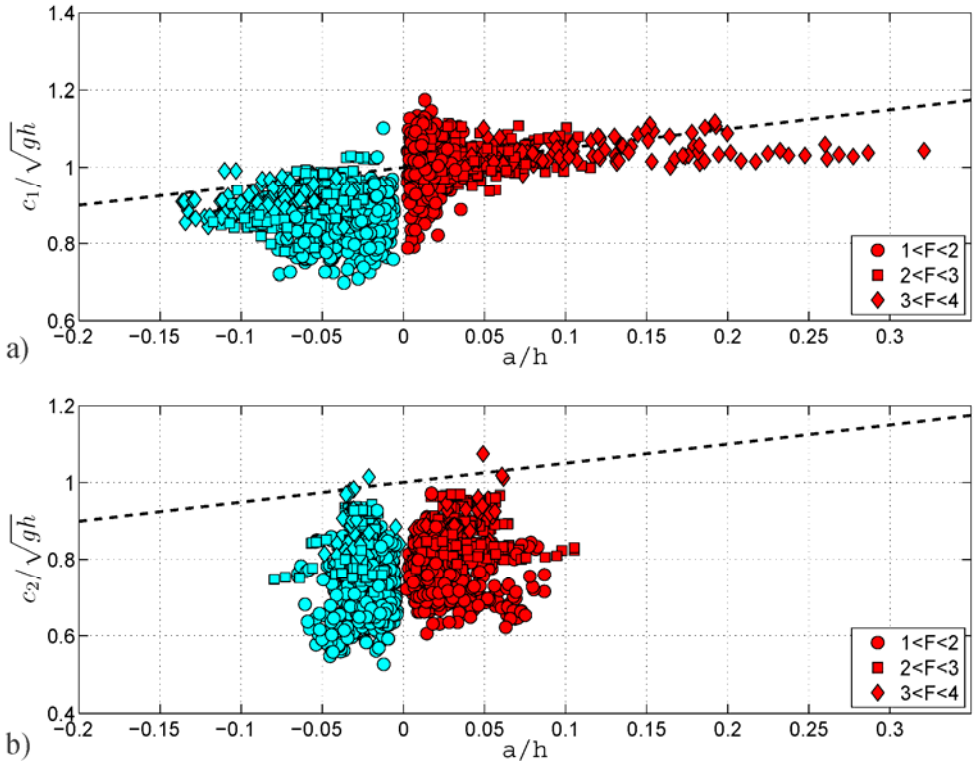

Figure 61: Wave propagation celerity for wave crests (red) and troughs (cyan) generated on a planar hill slope for (a) first wave and (b) second wave. Solitary wave celerity (Equation 88) is shown as the dashed line.

The offshore propagating wave celerity is measured in the range of $4 < r/h < 50$. The measured wave celerity for the first wave crest and trough generated with a gravel landslide on planar and convex conical hill slopes and a cobble landslide on the convex conical hill slope were in the range of $0.75 < c_{c1}/\sqrt{gh} < 1.3$ and $0.70 < c_{t1}/\sqrt{gh} < 1.05$. The mean celerity of the first wave's crest and trough were 0.99 and 0.87 on the planar hill slope and 1.03 and 0.88 on the convex conical hill slope. Essentially the leading wave celerities were equal with small differences likely due to nonlinearities. The celerity ranges for the second wave's crest and trough were $0.60 < c_{c2}/\sqrt{gh} < 1.0$ and $0.50 < c_{t2}/\sqrt{gh} < 0.97$. The mean celerity of the second wave's crest and trough were 0.78 and 0.73 on the planar hill slope and 0.80 and 0.75 on

the convex conical hill slope. The leading wave trough celerity was on average 14% lower than the leading wave crest celerity. The second wave crest and trough were on average 23% and 28% respectively lower than the first wave crest celerity. The reduction of wave celerity between the first and second wave is due to frequency dispersion in the intermediate water depth wave regime given the shorter wave lengths of the trailing waves.

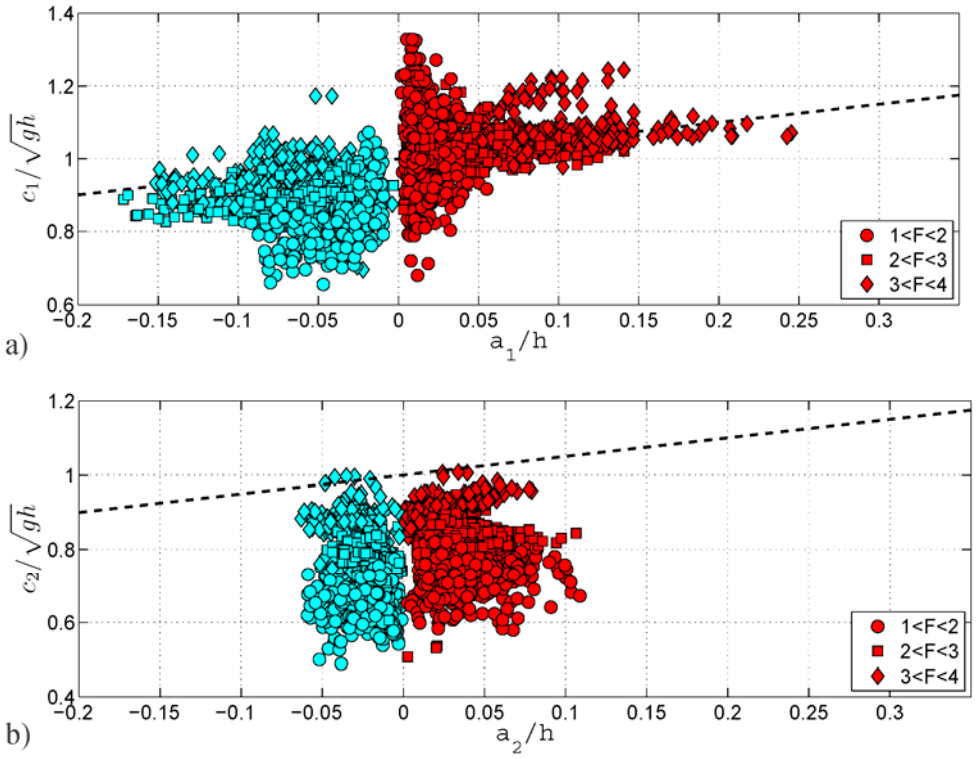

Figure 62: Wave propagation celerity for wave crests (red) and troughs (cyan) generated on a convex conical hill slope for (a) first wave and (b) second wave. Solitary wave celerity approximation (Equation 88) shown in the dashed line.

The importance of amplitude dispersion in the wave celerity is observed in the dependence of the first wave's crest and trough celerity on the wave's amplitude. The first wave propagates at velocities up to the approximate solitary wave celerity. The celerity of the second wave is less than solitary wave celerity and linear shallow water celerity. The second wave tends to be in the intermediate water depth and nonlinear wave regimes. Therefore, neither solitary

wave theory nor linear wave theory are applicable to the second wave. Solitary wave celerity could be viewed as an upper bound for the celerity of the second wave, and linear wave theory may be appropriate when $a/h < 0.03$ (Dean and Dalrymple, 1991).

5.5 Wave Length

The tsunami wave length is an important wave characteristic. The wave length is defined as the horizontal distance between zero up-crossings in the wave profile. The wave lengths were measured by multiplying the wave period by the wave celerity. This measurement technique is only applicable to transient waves and assumes the wave celerity is steady in reference frame moving at the speed of the wave. For impulsively generated waves, the wave celerity for the different waves in the wave train varies, inducing a bias in the wave length measurement from the wave period and celerity. The celerity applied in the present study is the mean of crest and trough celerity between wave gauges in an angular array. The wave period is measured using a zero up-crossing method. The wave length measurement is given as

$$\frac{L_i}{h} = T_i\sqrt{\frac{g}{h}}\frac{c_i}{\sqrt{gh}} \tag{89}$$

where *i* denotes the number of the wave in the wave train. The definition of the measured wave lengths are shown in **Figure 63**.

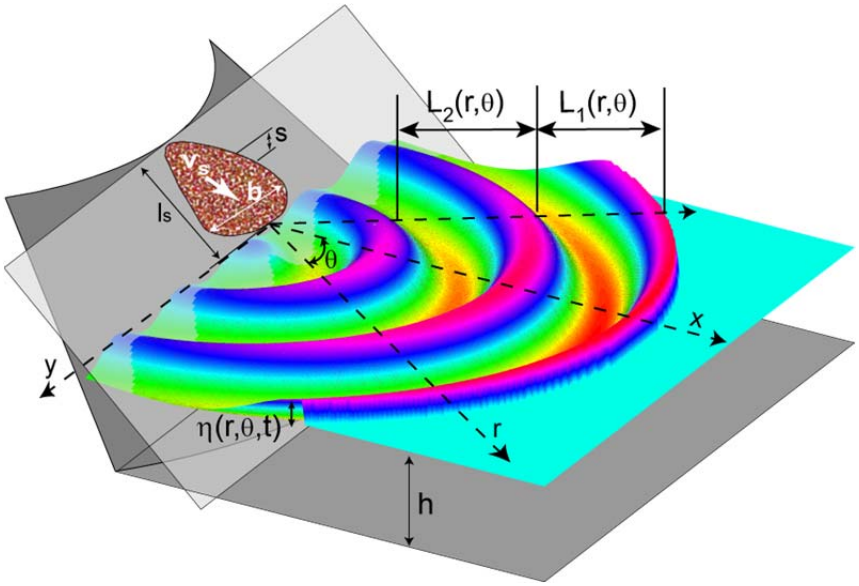

Figure 63: Wave length definition using the up-crossing method for radial waves generated by deformable granular slides on planar and convex conical hill slopes.

The first two wave lengths were analyzed on the planar and divergent convex conical hill slopes using gravel and cobble landslides. The predictive equation for the first wave length generated by a gravel landslide on a planar hill slope is given by Mohammed and Fritz (2012) as

$$\frac{L_1}{h} = 4.3\, F^{0.22} S^{0.06} L^{0.03} \left(\frac{r}{h}\right)^{0.3} \tag{90}$$

where F is the landslide Froude number, S is the relative slide thickness, L is the relative slide length and r/h is the relative distance from the landslide impact. Equation 90 matches the measured first wave length generated by a gravel landslide on a planar hill slope in the present study with an r^2 correlation coefficient of 0.94. The second wave length is given as

$$\frac{L_2}{h} = 2.0\, F^{0.22} S^{0.04} L^{0.07} \left(\frac{r}{h}\right)^{0.25} \tag{91}$$

with an r^2 correlation coefficient of 0.84 compared to the measured second wave length generated by a granular landslide on a planar slope. The measured versus predicted wave lengths generated by gravel landslides on a planar hill slope are shown in **Figure 64a** and **Figure 64b**.

The 30% error lines correspond to confidence intervals of 99% and 92% for the first two wave lengths on a planar hill slope.

An additional coefficient was added to extend the planar hill slope equations to be applicable to a convex conical hill slope. The first wave length generated by gravel or cobble landslides on a convex conical hill slope is given as

$$\frac{L_1}{h} = 4.3\, F^{0.22} S^{0.06} L^{0.03} C_{L1} \left(\frac{r}{h}\right)^{0.38} \tag{92}$$

where the convex conical hill slope coefficient C_{L1} is given as

$$C_{L1} = \tanh\left(R_c{}^{0.1}\right) \tag{93}$$

and R_c is the dimensionless shoreline radius to produce an r^2 correlation coefficient of 0.97. The conical coefficient for the leading wave length was in the range of $0.6 < C_{L1} < 0.9$. The form of C_{L1} was chosen to allow the convex conical hill slope coefficient to be less than 1. The second wave length generated by gravel or cobble landslides on a convex conical hill slope is given by

$$\frac{L_2}{h} = 2.0\, F^{0.22} S^{0.04} L^{0.07} C_{L2} \left(\frac{r}{h}\right)^{0.25} \tag{94}$$

where the convex conical hill slope coefficient is given as

$$C_{L2} = \coth(R_c) \tag{95}$$

to produce an r^2 correlation coefficient of 0.89 compared to the measured data. The conical coefficient for the second wave length was in the range of $1.0 < C_{L2} < 1.05$. The measured versus predicted wave lengths generated by gravel and cobble landslides on a convex conical hill slope are shown in **Figure 64c** and **Figure 64d** for the first and second wave length, respectively.

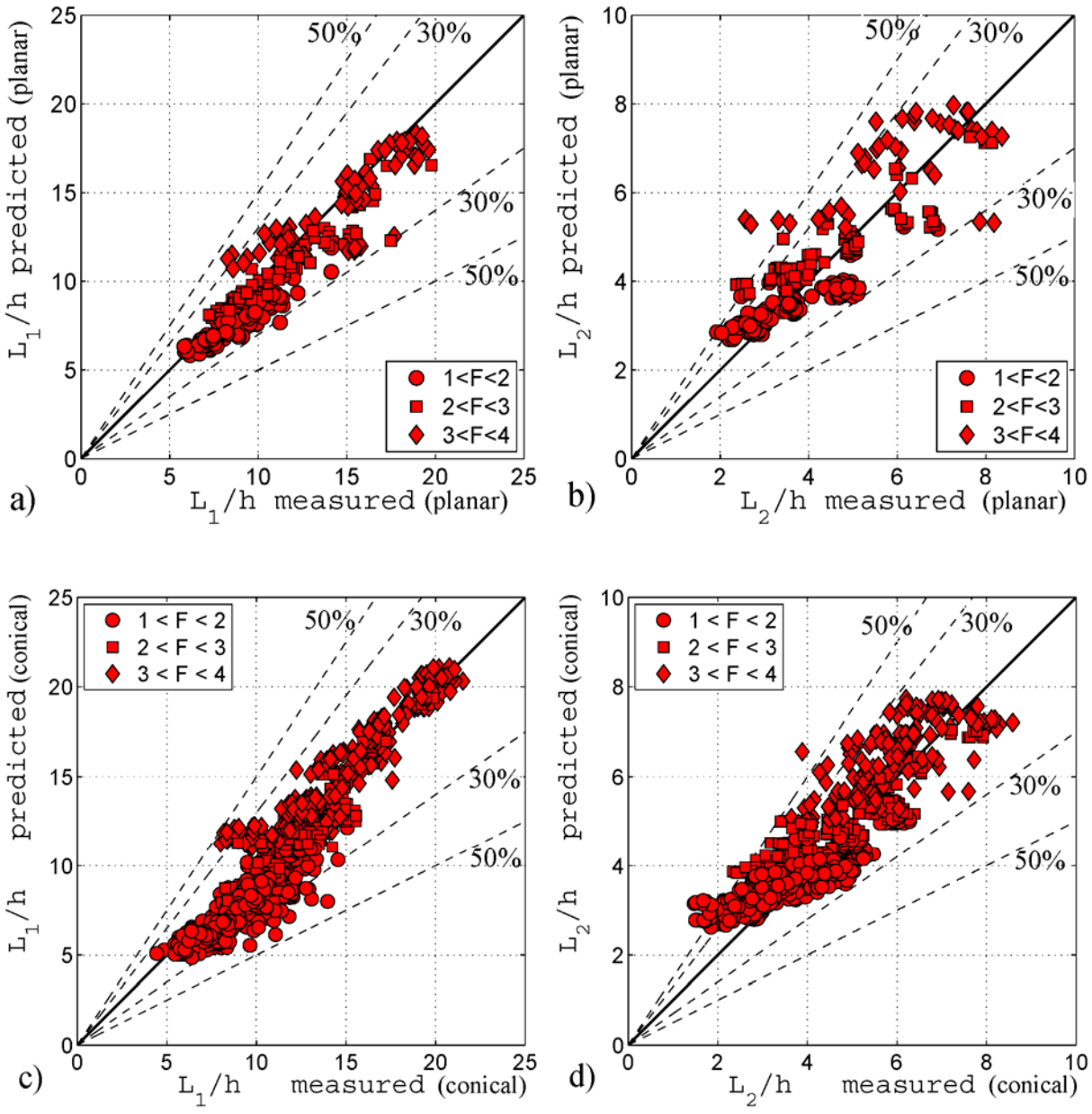

Figure 64: Measured versus predicted wave length (a) first wave length L_1/h from a planar hill slope using Equation 90, (b) second wave length L_2/h from a planar hill slope using Equation 91, (c) first wave length from a convex conical hill slope using Equation 92 and (d) second wave length using Equation 94 from convex conical hill slope. The dashed lines denote the 30% and 50% error thresholds.

The effects of the lateral hill slope are studied by analyzing the ratio of the wave lengths generated by a gravel landslide on a planar hill slope L_{1plan} and a convex conical hill slope

L_{1con}. The ratio of the first wave length was in the range of $0.71 < L_{1plan}/L_{1con} < 1.39$ with a mean value of 0.98 or practically equal. The ratio of the second wave length was in the range of $0.81 < L_{2plan}/L_{2con} < 1.39$ with a mean value of 0.99 or practically equal. The planar versus conical wave lengths are shown in **Figure 65** for the first two wave lengths.

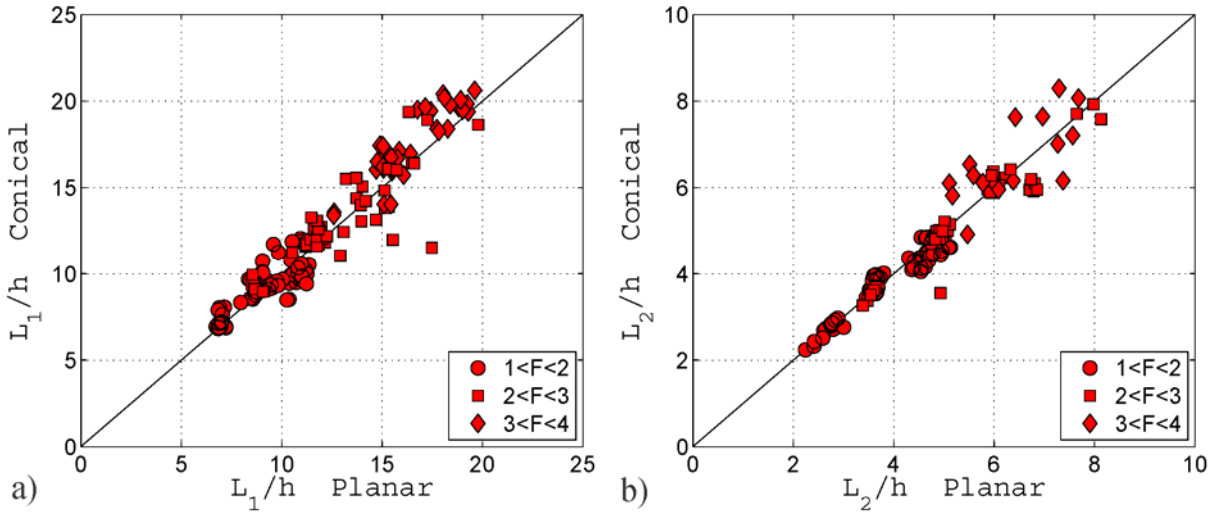

Figure 65: Comparison of the wave lengths generated by a gravel landslide on planar L_{1plan} and convex conical L_{1con} hill slopes for (a) first wave length L_1/h and (b) second wave length L_2/h.

The effects of the landslide granulometry are analyzed on the convex conical hill slope by comparing the ratio of the wave length generated by a cobble landslide L_{1cob} to the wave length generated by a gravel landslide L_{1grav}. The ratio for the first wave length is within the range $0.75 < L_{1cob}/L_{1grav} < 1.37$ with an equal mean of 1.00. The ratio for the second wave length is within the range $0.63 < L_{2cob}/L_{2grav} < 1.47$ with an essentially equal mean of 0.99. The gravel versus cobble landslide generated wave length is shown in **Figure 66**.

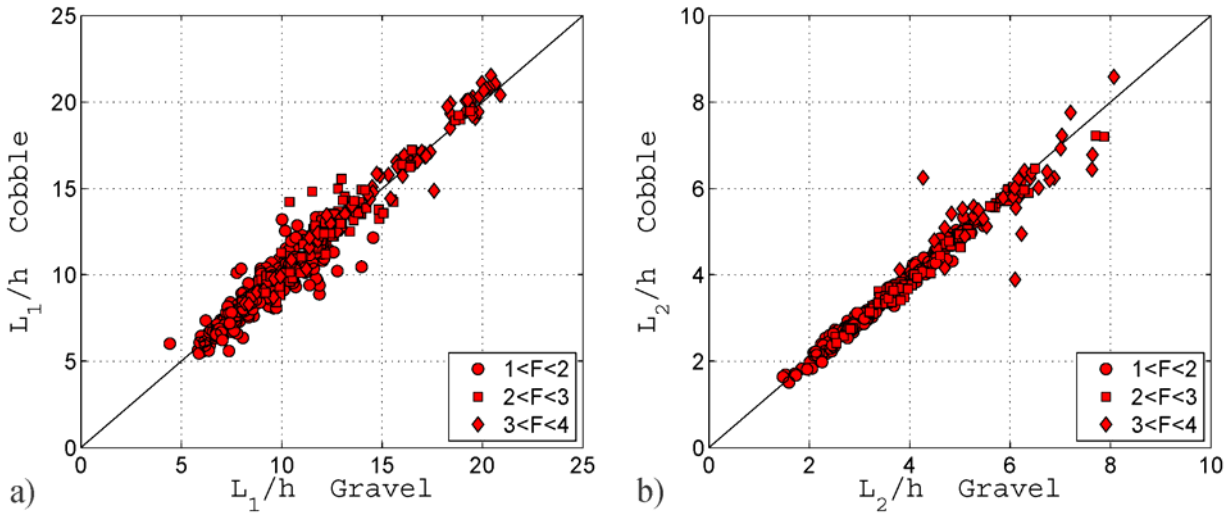

Figure 66: Comparison of the wave lengths generated on a convex conical hill slope by gravel L_{1grav} and cobble L_{1cob} landslides for (a) first wave length L_1/h and (b) second wave length L_2/h.

5.6 Wave Nonlinearity

The wave nonlinearity can be surmised with the following three wave parameters whose importance varies depending on the water depth regime:

- Wave steepness: H/L
- Relative wave height: H/h or a/h
- Ursell number: $U = (a_c L^2)/h^3$

In the deep water regime $L/h > 20$, the most relevant parameter to quantify wave nonlinearity is the wave steepness. In the shallow water regime $L/h < 2$, the relative wave height is the most relevant parameter to quantify the wave nonlinearity. The majority of the waves generated in the

present study are in the intermediate water depth regime $2 < L/h < 20$. In the intermediate water depth regime, the most relevant parameter is the Ursell number, while the other two parameters should be considered. The measured wave crest amplitudes were in the range $0.001 < a_c/h < 0.35$. The effects of amplitude dispersion were observed in the offshore propagation celerity in **Figure 61** and **Figure 62**, therefore the higher order nonlinear dispersion effects may be important in the description of the wave unlike linear wave dispersion which only takes frequency dispersion into account.

The wave steepness evolution of the first wave is shown in **Figure 67**. The wave steepness of the offshore propagating waves were measured in the ranges of $3 < r/h < 50$ and $0° < \theta < 75°$ from the planar hill slope and $3 < r/h < 50$ and $0° < \theta < 90°$ from the convex conical hill slope. The wave steepness decays with propagation distance from the impact site. The wave steepness for the leading wave generated by a gravel landslide on a planar hill slope is in the range $0.001 < H_1/L_1 < 0.04$. The wave steepness for the leading wave generated on a convex conical hill slope with gravel and cobble landslides are in the range $0.001 < H_1/L_1 < 0.04$. The wave steepness condition for linear wave theory applicability is $H/L = 0.006$, which is eventually attained in the far field.

The Ursell number is analyzed to study the wave nonlinearity due to the importance of the parameter in the intermediate water depth regime. The evolution of the Ursell number for the first wave generated is shown in **Figure 68**. The Ursell number of the leading wave generated by a gravel landslide on a planar hill slope is in the range $0.25 < U_1 < 88$. The leading wave generated on a convex conical hill slope by gravel or cobble landslides have an Ursell number in the range $0.25 < U_1 < 55$. The Ursell number increased with propagation distance from the impact site. The condition for linear wave applicability using the Ursell number is $U < 1$ (Lighthill, 2001) and the condition for the applicability of cnoidal wave theory is $U > 26$. The

majority of the measured leading wave Ursell numbers were nonlinear and not applicable to cnoidal wave theory.

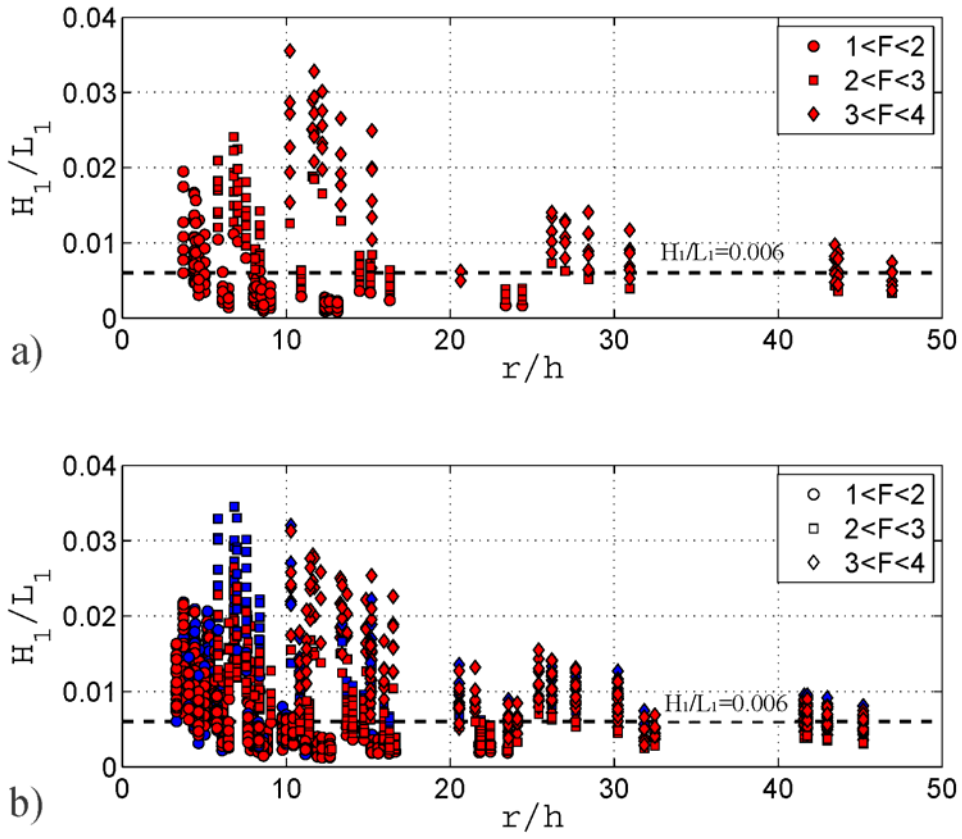

Figure 67: Wave steepness evolution of the leading wave generated by (a) gravel landslide on a planar hill slope and (b) gravel (red) and cobble (blue) landslides on a convex conical hill slope.

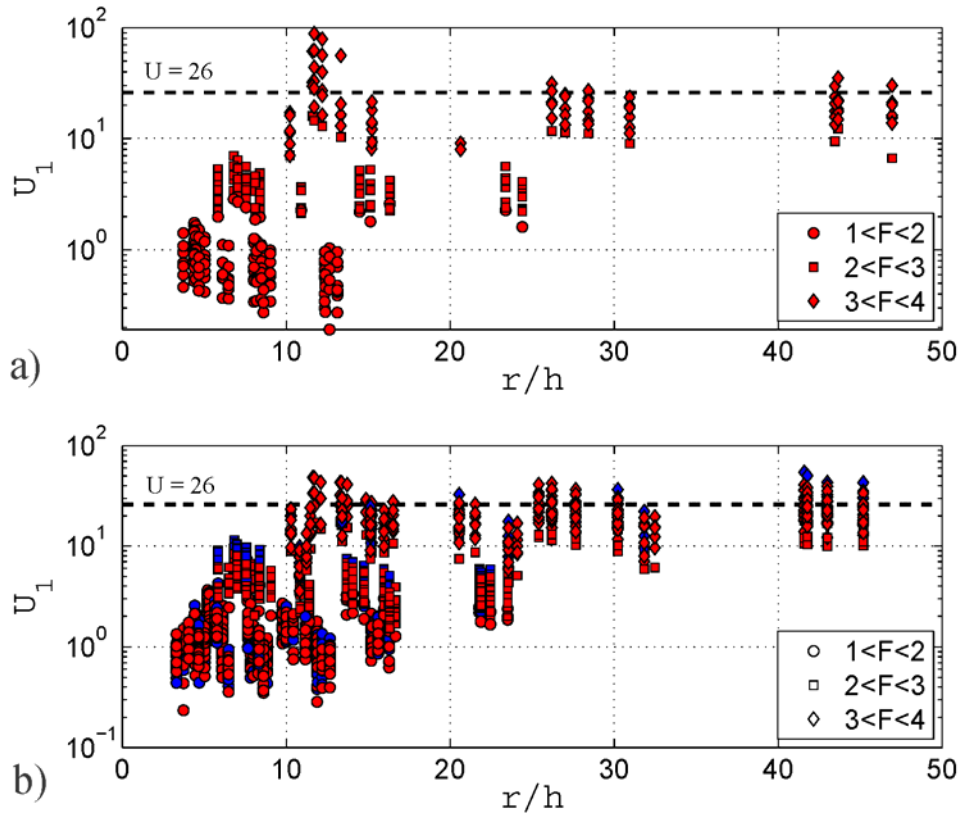

Figure 68: Ursell number evolution for the leading wave generated by (a) gravel landslide on a planar hill slope and (b) gravel (red) and cobble (blue) landslides on a conical hill slope.

The wave steepness and Ursell number evolutions of the second wave are shown in **Figure 69** and **Figure 70**, respectively. The wave steepness decays more quickly with propagation distance from the impact site in the second wave than the leading wave. The majority of wave steepness measurements do not adhere to the linear wave theory steepness condition of $H/L = 0.006$, similar to the leading wave. The second wave has larger wave steepness near the slide impact than the leading wave due to the shorter wave length of the second wave. The wave steepness for the second wave of all experimental conditions is in the range $0.002 < H_2/L_2 < 0.07$ and the Ursell number of the second wave for all experimental conditions is in the range $0.01 < U_2 < 4$. The Ursell number of the second wave is generally smaller in comparison to the leading wave's Ursell number. While the wave steepness of some

second waves are classified as linear waves, the Ursell number provides that the waves are linear if $U_2 < 1$ in intermediate water depths. According to the Ursell parameter, the majority of the second waves would be applicable to linear wave theory. However the Ursell number increases with propagation distance, while the wave steepness decreases.

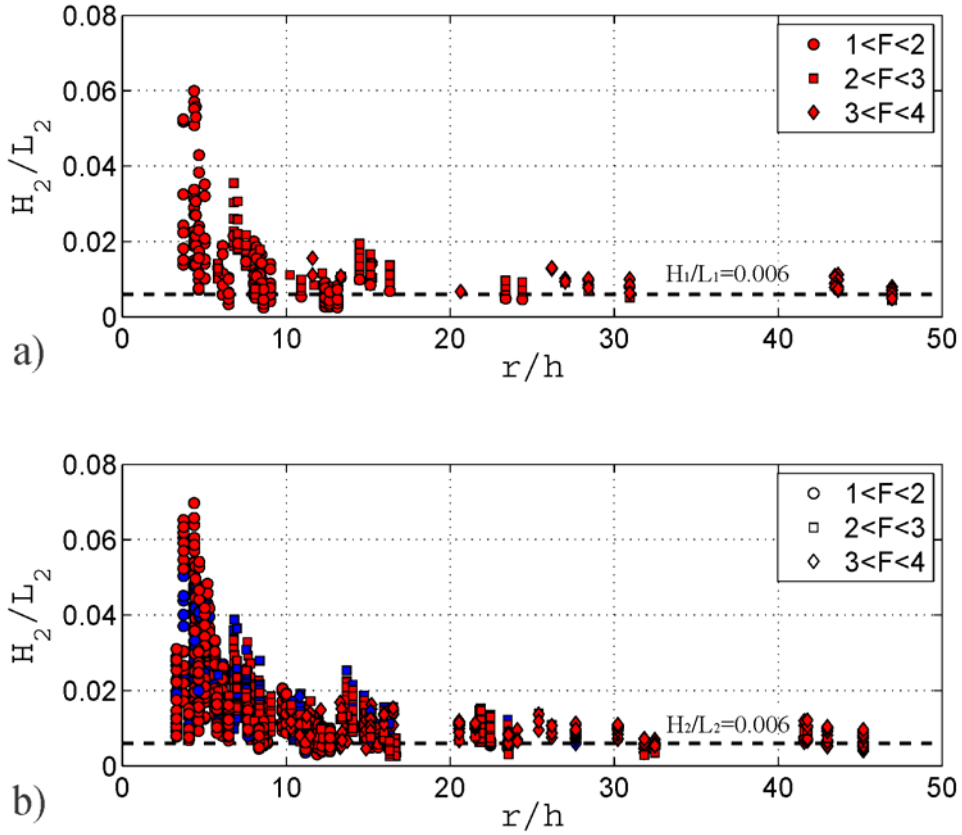

Figure 69: Wave steepness evolution of the second wave generated by (a) gravel landslide on a planar hill slope and (b) gravel (red) and cobble (blue) landslides on a convex conical hill slope.

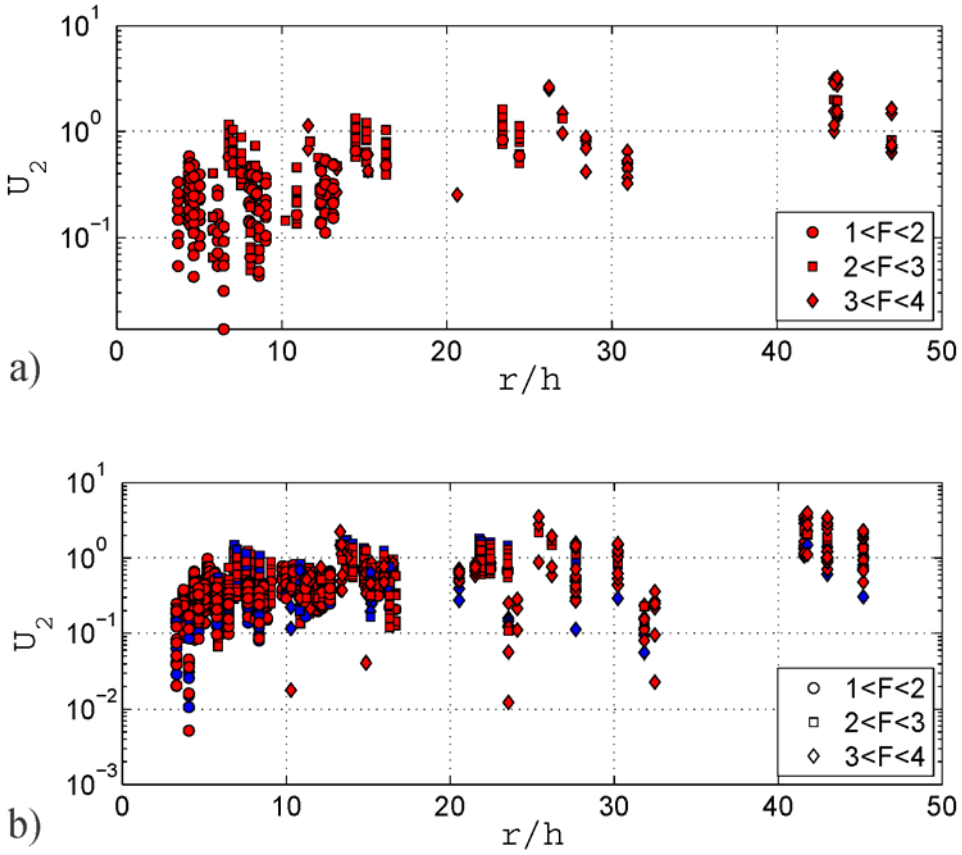

Figure 70: Ursell number evolution for the second wave generated by (a) gravel landslide on a planar hill slope and (b) gravel (red) and cobble (blue) landslides on a conical hill slope.

5.7 Wave Energy Conversion

The tsunami wave energy conversion describes the transfer of kinetic energy from the landslide impacting the water to the tsunami wave. The nondimensional form of the landslide kinetic energy is given as

$$E_s = \frac{1}{2} D V F^2 \qquad (96)$$

where D is the ratio of landslide density to the water density $D = \rho_s/\rho_w$, V is the dimensionless volume $V = V_s/h^3$, and F is the landslide Froude number at impact $F = v_s/\sqrt{gh}$.

The wave energy is composed of two parts: kinetic and potential energy. The kinetic energy is due to the water particle motion in the water body and the potential energy is due to the displacement of the water surface from the mean position. The dimensionless wave potential energy for a radial wave in cylindrical coordinates in the angular range $-\pi/2 < \theta < \pi/2$ is given as

$$E_{pot} = \int_{-\frac{\pi}{2}}^{\frac{\pi}{2}} \left(\frac{1}{2} \frac{c}{\sqrt{gh}} \int_0^{T\sqrt{g/h}} \left(\frac{\eta}{h}\right)^2 dt\sqrt{g/h} \right) \frac{r}{h} d\theta \tag{97}$$

at propagation distance *r/h* from the landslide impact site. To account for the varying wave crest and trough celerities, the potential energy was measured for each individual crest and trough in the wave train. The spatial variation of the potential energy for the first wave crest follows the form

$$dE_{pot}(r/h, \theta) = k_{E_{c1}} \left(\frac{r}{h}\right)^n \cos^2 \theta \tag{98}$$

within the ranges of $0 < r/h \leq (r/h)_{max}$ and $-\pi/2 < \theta < \pi/2$ where *n* is analogous to the wave amplitude decay rate in Section 5.2 Wave Amplitude Attenuation.

The kinetic energy of the measured waves is difficult to estimate without measurements of the water particle kinematics in the water column. The total wave energy may be estimated as $E_{tot} \approx 2\, E_{pot}$ by assuming equipartition of potential and kinetic energy as in linear waves (Lamb, 1932). Williams (1985) found that the total wave energy ($E_{tot} = E_{pot} + E_{kin}$) computed numerically may exceed the equipartition assumption by 11% for the extreme case of a solitary wave approaching the breaking height, but is typically only a few percent for the present studies wave characteristics. Using the equipartition assumption, the dimensionless total wave energy for the first wave crest is given as

$$E_{cr1} = \int_{-\frac{\pi}{2}}^{\frac{\pi}{2}} \left(\frac{c}{\sqrt{gh}} \int_{0}^{T_{cr1}\sqrt{g/h}} \left(\frac{\eta}{h}\right)^2 dt\sqrt{g/h} \right) \frac{r}{h} d\theta \tag{99}$$

where T_{cr1} is the period of the leading wave crest from the initial rise to the first down-crossing.

The decay of the leading wave crest energy as a function of relative distance from the source is shown in **Figure 71**. The energy conversions from landslides to the first wave crest are compared in **Table 9**.

Table 9: Landslide energy conversion to the first wave crest

Study	Lateral Hill Slope	Slide Material	E_{cr1}/E_s Range
Mohammed and Fritz (2012)	Planar	Gravel	$0.5\% < E_{cr1}/E_s < 3\%$
Present Study	Planar	Gravel	$0.5\% < E_{cr1}/E_s < 3\%$
Present Study	Convex Conical	Gravel	$0.5\% < E_{cr1}/E_s < 5\%$
Present Study	Convex Conical	Cobble	$1\% < E_{cr1}/E_s < 11\%$

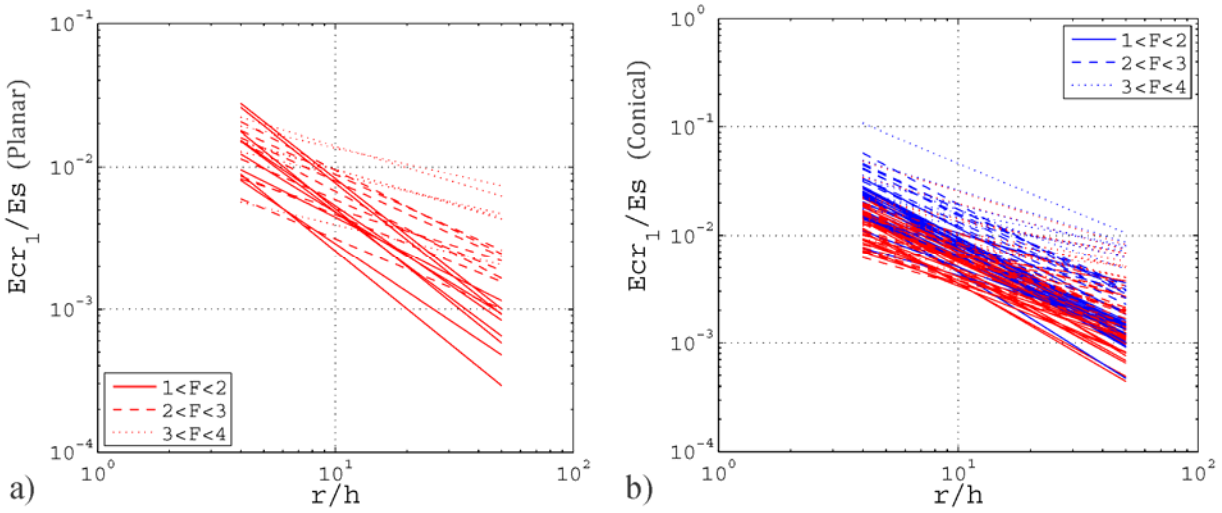

Figure 71: First wave crest energy, E_{cr1}, conversion from landslide, E_s: (a) on planar hill slope with gravel landslide and (b) on convex conical hill slope with gravel (red) and cobble (blue) landslides.

The energy measurement for the wave train is analogous to the method used for the first wave crest. Due to the varying wave celerity of the waves in the wave train, the energy of the individual wave crests and troughs are determined and summed for the wave energy of the total wave train. The wave train measurement is the energy packet contained in the first three waves. The dimensionless wave train energy is given as

$$E_{wt} = \sum_{i=1}^{6} \frac{c_i}{\sqrt{gh}} \int_{T_i}^{T_{i+1}} \left(\frac{\eta}{h}\right)^2 dt \sqrt{\frac{g}{h}} \tag{100}$$

where the water surface between T_i and T_{i+1} represent a wave crest or trough depending on the index i. The decay of the wave train as a function of relative distance from the source is shown in **Figure 72**. The energy conversions from landslides to the wave train are compared in

Table 10.

Table 10: Landslide energy conversion to the wave train

Study	Lateral Hill Slope	Slide Material	$\boldsymbol{E_{wt}/E_s}$ Range
Mohammed and Fritz (2012)	Planar	Gravel	$1\% < E_{wt}/E_s < 15\%$
Present Study	Planar	Gravel	$1\% < E_{wt}/E_s < 20\%$
Present Study	Convex Conical	Gravel	$1\% < E_{wt}/E_s < 21\%$
Present Study	Convex Conical	Cobble	$1\% < E_{wt}/E_s < 24\%$

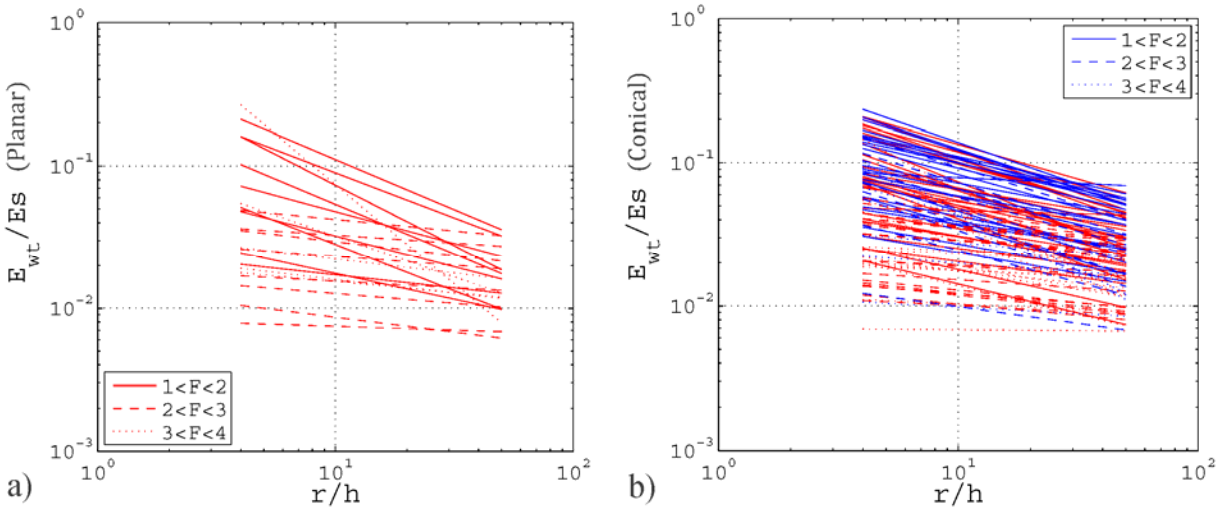

Figure 72: Wave train energy, $E_{cr1,}$ conversion from landslide, E_s: (a) on planar hill slope with gravel landslide and (b) on convex conical hill slope with gravel (red) and cobble (blue) landslides.

The landslide energy conversion for 2D experiments is shown in **Table 11**. The energy conversion from the landslide to the wave energy is much larger in the 2D experiments than the 3D experiments of Mohammed and Fritz (2012) and the present study. Tsunami generation in 2D experiments is efficient because it confines both the landslide and water body to the channel limiting the landslide and water deformations to the vertical plane. In contrast, in the 3D experiments the water can flow laterally around the slide. Landslide energy is dissipated by friction during the subaerial and subaqueous motion. Landslide energy is also dissipated by the impact on the basin floor at the hill slope-basin floor transition requiring the landslide material to abruptly deform resulting in energy dissipation due to landslide internal friction. Other sources of landslide energy dissipation include form and skin friction drag as well as the turbulence and multiphase mixing in the impact region.

Table 11: Landslide to wave energy conversion for various 2D experiments

Study	Landslide	Landslide to Wave Energy Conversion
Kamphuis and Bowering (1970)	Block	10-50%
Huber (1980)	Granular	1-40%
Fritz (2002)	Granular	2-30% at *x/h=8* (leading wave crest) 4-50% at *x/h=8* (wave train)
Watts (2000)	Block (Submarine)	2-13%
Ataie-Ashtiani and Nik-Khah (2008)	Block	5-50%
Heller (2008)	Granular	11.3-85.7%

The effects of the lateral hill slope curvature on the wave energy conversion from a gravel landslide on planar and convex conical hill slopes are compared in **Figure 73**. It was noted in Section 5.2 Wave Amplitude Attenuation the first wave crest amplitude was generally larger when generated on the planar hill slope than the conical hill slope, but the first wave trough and second wave crest amplitudes were typically smaller when generated on the planar hill slope. Similarly, the first wave crest energy is on average 2% larger on the planar hill slope than on the conical hill slope and 9% smaller for the wave train.

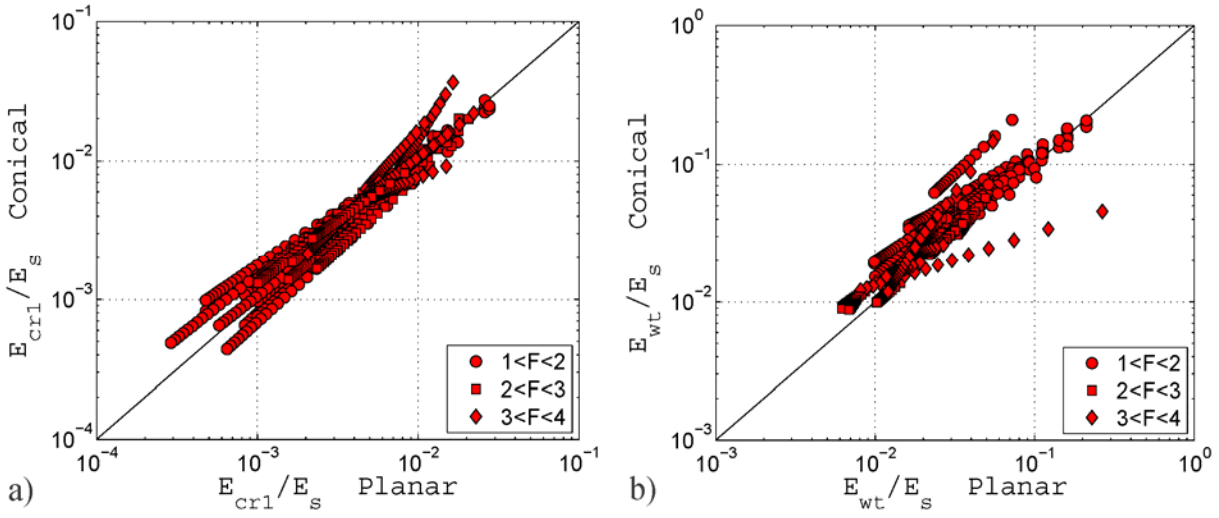

Figure 73: Energy conversion comparison between gravel landslides on planar and convex conical hill slopes: (a) first wave crest and (b) wave train.

The effects of the landslide granulometry on the wave energy conversion from a convex conical hill slope with gravel and cobble landslides are shown in **Figure 74**. The leading wave crest energy generated by a cobble landslide was on average 31% larger than by a gravel landslide and the wave train energy was on average 43% larger.

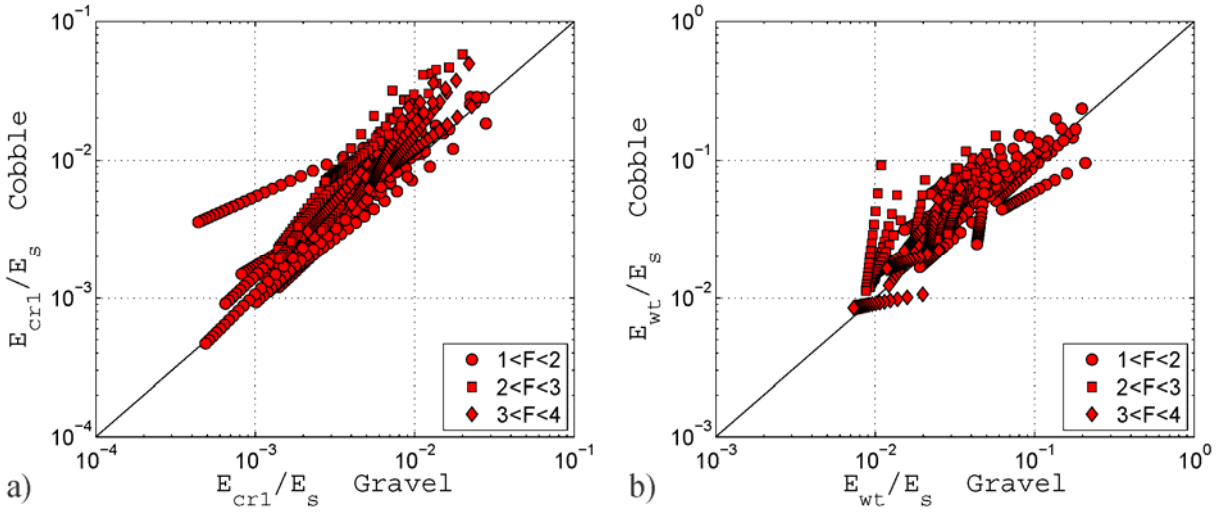

Figure 74: Energy conversion comparison on a convex conical hill slope between gravel and cobble landslides: (a) first wave crest and (b) wave train.

CHAPTER VI

WAVE RUNUP AND RUNDOWN

6.1 Introduction

The tsunami wave runup and rundown are very important for tsunami hazard assessments and can be significantly influenced by bathymetric and topographical features at various scales. This chapter analyzes the runup and rundown measured during the physical modeling of landslide generated tsunamis. The wave runup and rundown investigated can be broken into two categories:

1. Lateral wave runup and rundown

2. Opposing hill slope runup and rundown

The lateral wave runup and rundown occur on the same hill slope as the tsunami generating landslide and the opposing hill slope runup and rundown is produced by an incident tsunami wave generated off another hill slope. Hill slopes directly opposing the landslide source are particularly at risk for extreme runup heights in confined water bodies such as reservoirs, lakes, bays and fjords. The lateral wave runup and rundown are discussed in Section 6.2 Lateral Wave Runup and the opposing hill slope runup and rundown are discussed in Section 6.3 Opposing Hill Slope Runup. The definition sketches of the pertinent runup and rundown parameters are shown in **Figure 75**.

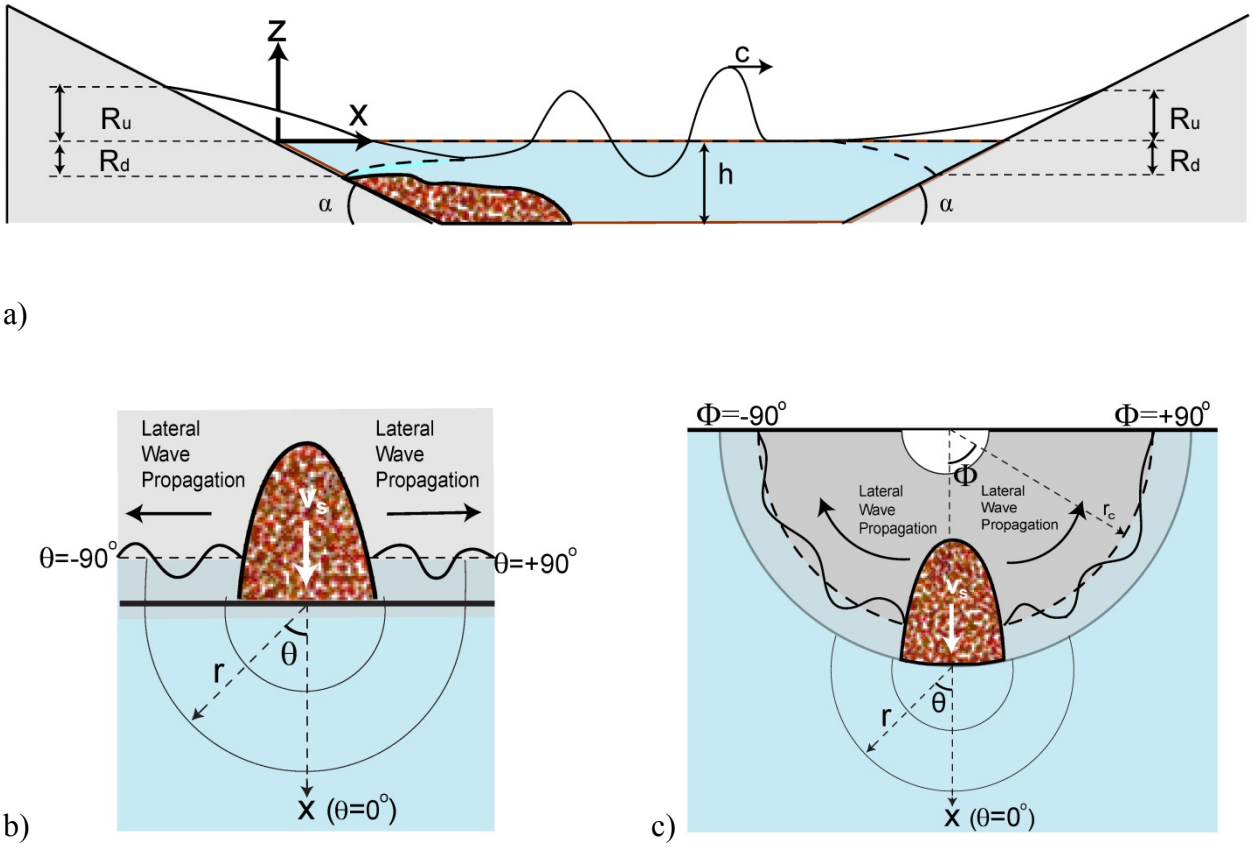

Figure 75: Tsunami runup and rundown definition sketches: (a) Landslide generated tsunami runup and rundown definitions on a (b) planar hill slope and (c) convex conical hill slope.

6.2 Lateral Wave Runup

6.2.1 Lateral Wave Runup Introduction

A critical feature of subaerial landslide generated tsunamis is the lateral wave propagation. The lateral wave can be described as the portion of the wave that propagates perpendicular to the landslide motion on a hill slope. Landslide generated tsunamis can produce very large amplitude lateral waves in the near field region (Lynett and Liu, 2005). Lateral waves are generally slower than the offshore propagating wave because of the shallower water depths, but the waves can arrive

early depending on the proximity to the generation source. The tsunami waves arrived within less than one minute of the co-seismically generated coastal landslide at Petit Paradis, Haiti in 2010 (Fritz et al., 2013).

The unique landslide tsunami generator (LTG) was redeployed on a laterally significantly extended planar hill slope in the 2010 series of experiments and on a conical island in 2011. The lateral waves are measured with a hybrid system of runup wave gauges and overlapping camera recordings. The runup and rundown in the landslide impact region are measured with image sequences recorded by the PIV system's high-resolution CCD cameras. The viewing areas from two additional cameras on the planar hill slope and four additional cameras on the convex conical hill slope cover the remaining sections of the lateral hill slope instrumented with runup gauges.

The image sequence recorded by cameras focused on the planar hill slope are calibrated with the pinhole model using a calibration board in the impact region and a pattern of dots spaced 0.3 m apart on the hill slope. After the calibration was performed on the image sequence from the planar hill slope, the water surface was delineated using a graphical user interface every 50 pixels across the width of the image. In contrast to the planar hill slope, the waterline is delineated on the raw recorded image sequences of the lateral wave on the conical island. The conical hill slope water surface elevation data is then converted from pixel locations to basin coordinates using a polynomial spatial transformation based on control points measured with the LiDAR scan of the conical surface. The waterline is traced every $\Delta\Phi = 7.5°$ around the island. **Figure 76** shows the waterline delineation on the planar and convex conical hill slopes. Wave characteristics are extracted from the runup gauges and the image analysis using an up crossing method.

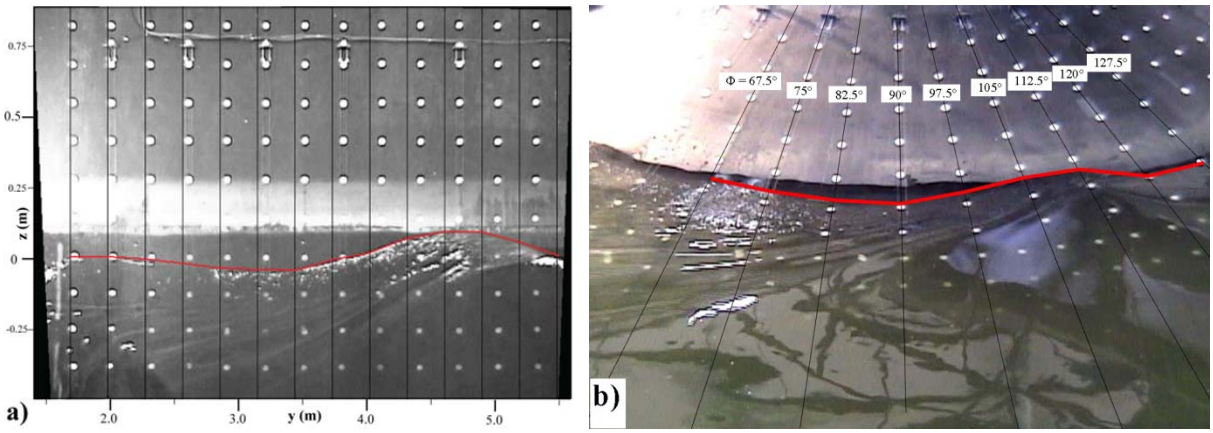

Figure 76: Lateral wave video processing for (a) a lateral wave on a planar hill slope with the water surface delineated every 50 pixels across the width of the rectified image and (b) a lateral wave on the convex conical hill slope with the water surface delineated every 7.5° of the conical island, while the runup gauges are positioned in overlapping 15° increments.

Lateral tsunami wave generation by subaerial landslide impact occurs simultaneously to the generation of the offshore propagating wave described in the Section 3.7 Uncertainty in Measurements. The initial water displaced by the landslide penetration and subsequent depression in the water surface produce the first lateral wave crest and trough. The lateral wave is fully formed at a certain propagation distance from the slide impact location which is dependent on the landslide impact characteristics. The maximum runup can occur in the slide impact region or on the hill slope adjacent to the landslide where the lateral wave is fully formed. The slide impact region contains the area within the maximum landslide width at the water surface interface. The absolute maximum rundown occurs in the impact region, while a second smaller rundown maximum is observed outside of the impact region as the lateral wave is fully formed. Farther afield local runup and rundown amplifications are observed on the lee side of the conical island scenario at $\Phi = 180°$, where the encircling edge waves collide.

Section 6.2 Lateral Wave Runup is organized after this introduction as follows: First, the maximum runup and rundown are investigated both within and outside the landslide impact region

on the planar and convex conical hill slopes. Predictive empirical equations are derived for the maximum runup and rundown inside and outside the landslide impact region and the location of the maximum runup and rundown outside slide impact region. Second, the runup and rundown attenuations are described from the maxima outside the impact region. Third, the runup and rundown amplifications on the lee side of the conical island scenario are investigated and predictive equations are derived. Fourth, the lateral wave periods, celerities and lengths of the first two waves are studied and predictive equations are produced. Fifth, the measured lateral wave characteristics are analyzed with edge wave dispersion relationships from literature.

6.2.2 Maximum Runup and Rundown

The maximum runup and rundown of the lateral tsunami waves are key points of interest in studying the lateral tsunami wave for hazard assessment. The first two lateral waves were considered on the planar hill slope. The first five lateral waves are considered on the conical hill slope due to the continuous lateral slope and the dispersive nature of the waves. From a practical standpoint knowing the maximum runup and rundown heights is more important than knowing which wave produces them. **Figure 77** and **Figure 78** show the maximum runup and rundown for the gravel landslide on the planar and convex conical hill slope and the cobble landslide on the convex conical hill slope at a water depth, $h = 0.6$ m. The maximum runup and rundown in the slide impact region and adjacent area are measured with image analysis from the PIV camera. The maximum runup and rundown outside of the slide impact region are measured with runup gauges and image analysis from overlapping camera viewing areas.

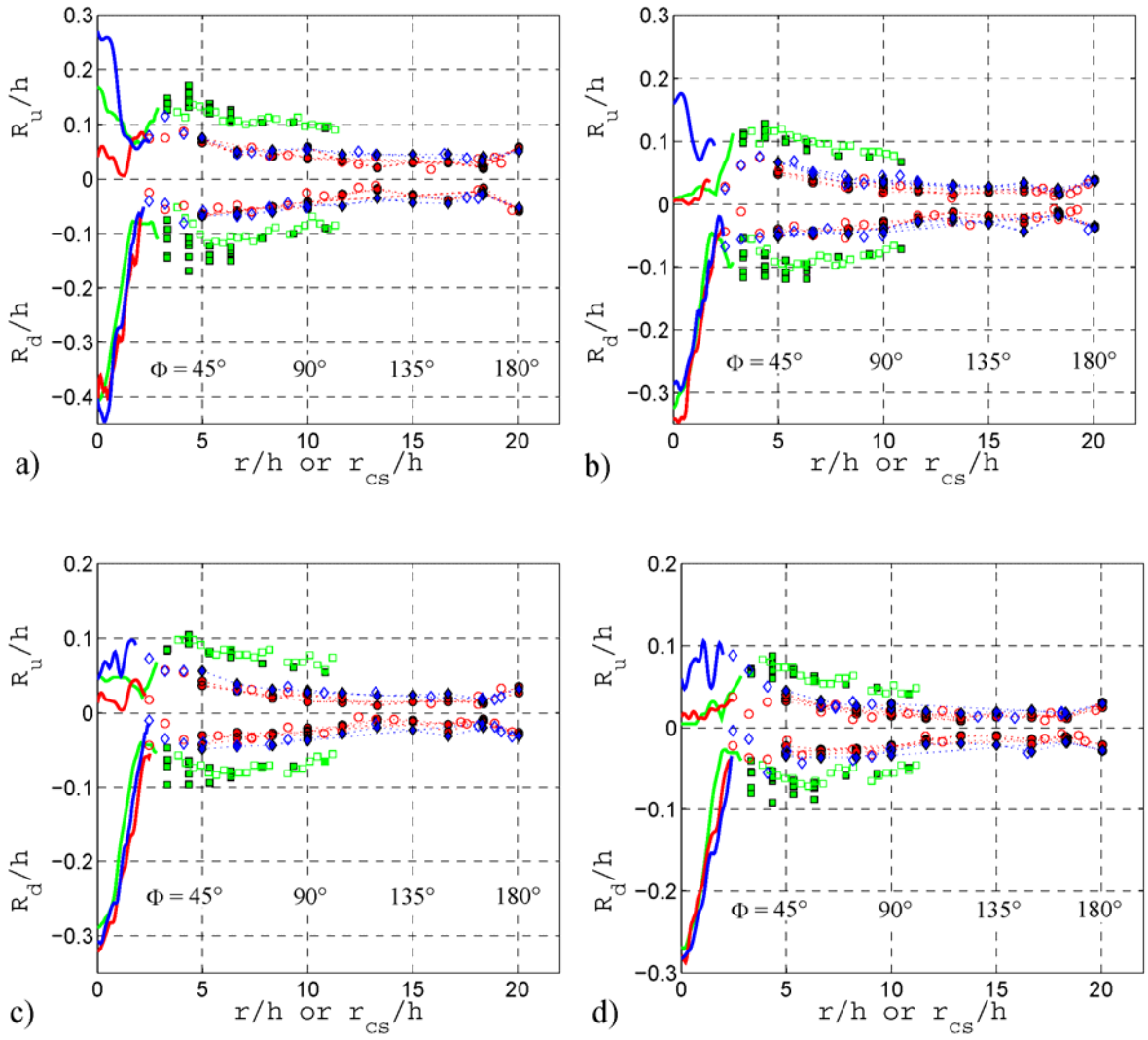

Figure 77: Maximum runup and rundown generated by a landslide volume V = 3.5 and landslide Froude number F of (a) 2.3, (b) 2.2, (c) 2.1 and (d) 2.0 at a water depth h = 0.6 m. Symbols: Runup generated by gravel landslides on the planar (green) and convex conical hill slope (red), and the cobble landslide on the convex conical hill (blue); solid lines: image analysis of the PIV camera, filled symbols: runup wave gauges, and hollow symbols: image analysis of overlapping cameras

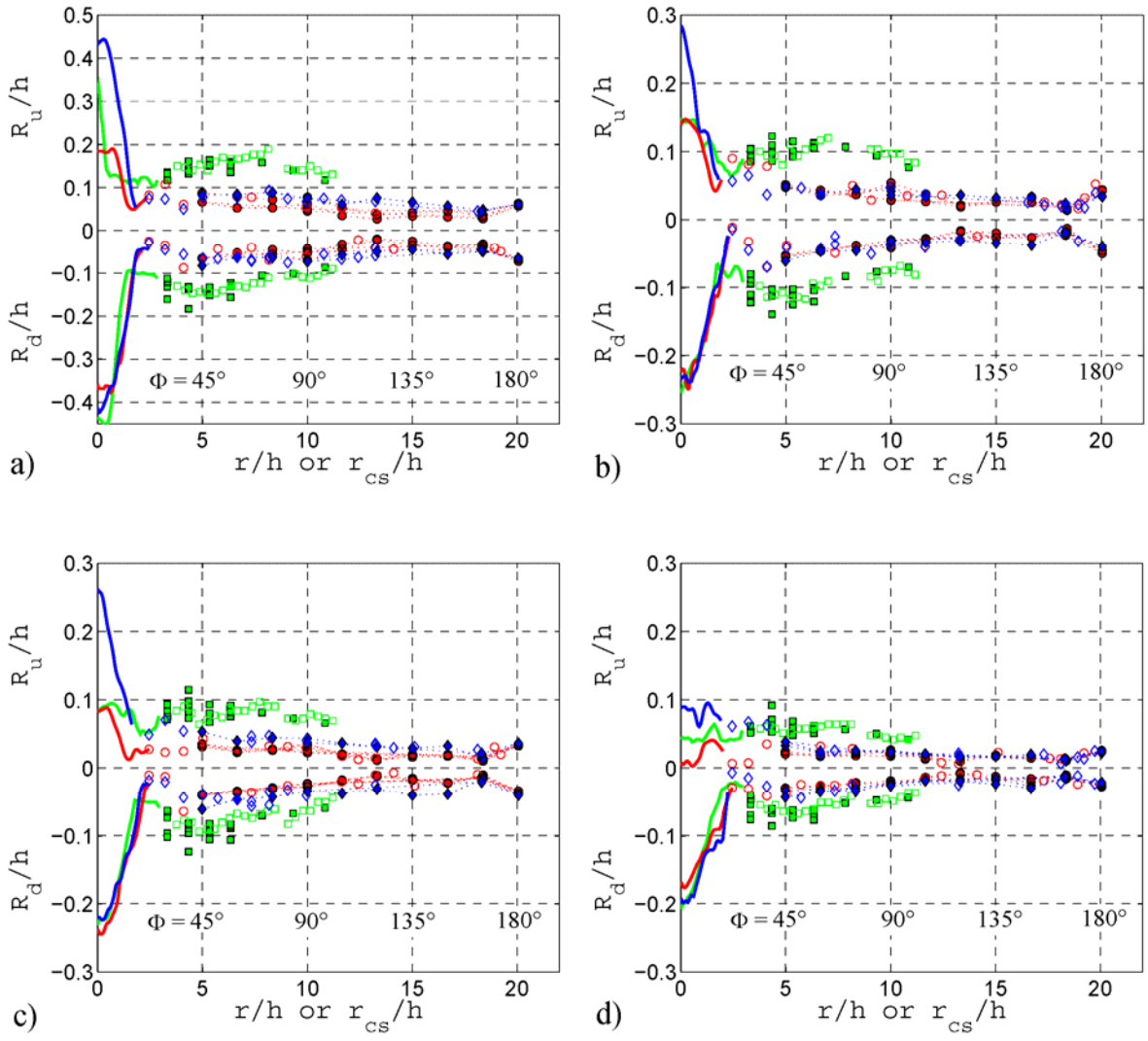

Figure 78: Maximum runup and rundown generated by a landslide volume $V = 1.75$ and landslide Froude number F of (a) 2.4, (b) 2.2, (c) 2.0 and (d) 1.9 at a water depth $h = 0.6$ m. Symbols: Runup generated by gravel landslides on the planar (green) and convex conical hill slope (red), and the cobble landslide on the convex conical hill (blue); solid lines: image analysis of the PIV camera, filled symbols: runup wave gauges, and hollow symbols: image analysis of overlapping cameras.

Several common key features are observed in the maximum runup and rundown examples shown in **Figure 77** and **Figure 78**. There is a maximum runup and rundown in the slide impact region and another outside the impact region. The impact region is defined as the area within the maximum landslide width at the water surface interface. The maximum heights decay as the radial distance from the source increases and a localized amplification occurs on the lee side of the conical

island scenario. Generally the maximum rundown in the impact region is larger than the runup. This is caused by the landslide creating a large drawdown during impact. The runup in the impact region is generally larger for thick landslides with short lengths compared to long, thin landslides. This can be due to the longer tail of the long, thin landslides impeding the runup after the crater collapse, while the shorter slide length penetrates the water more quickly clearing the hill slope in the impact area to allow for unobstructed runup.

The maximum runup and rundown outside of the impact region is larger on the planar hill slope than on the convex conical hill slope. This is expected because the convex conical hill slope cannot completely trap the lateral wave energy (Longuet-Higgins, 1967). Minor differences are observed between the gravel and cobble landslide materials outside of the impact region.

Figure 79 and **Figure 80** show the maximum runup and rundown generated by sample gravel landslides on the convex conical island for the water depth, $h = 0.6$ m. The dashed blue line in the figure is the still water level, the bold red lines are the maximum runup and rundown, and the solid black circles provide a vertical scale of R_u/h and $R_d/h = 0.1$. This figure layout allows for a more intuitive relationship between the island angle, Φ, and the maximum runup and rundown.

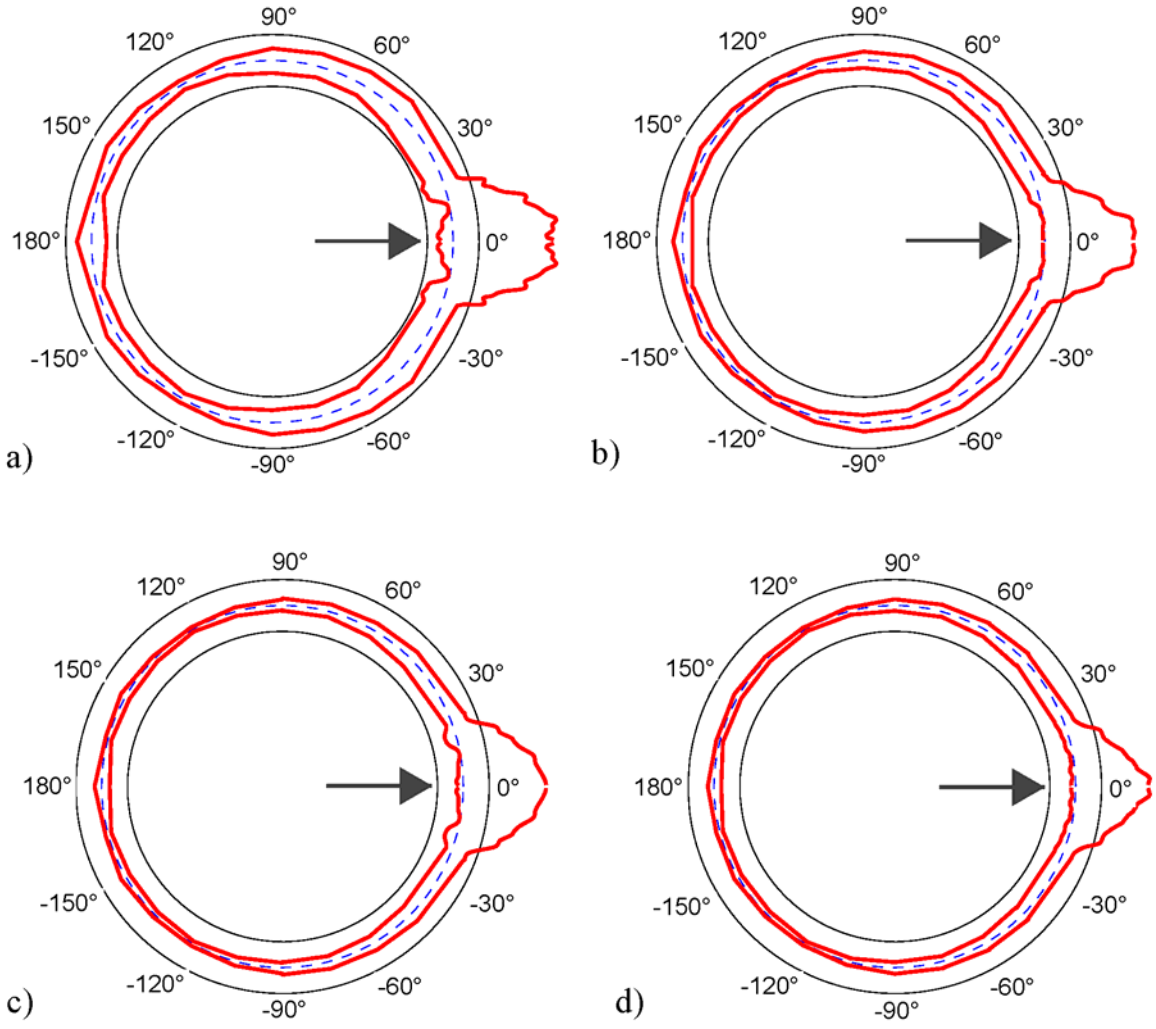

Figure 79: The maximum runup and rundown on the convex conical hill slope for a gravel landslide with a slide volume V = 3.5 and impact Froude number F = (a) 2.3, (b) 2.2, (c) 2.1 and (d) 2.0. Symbols: Maximum runup and rundown (red), still water (dashed blue line) and R_u/h and R_d/h = 0.1 (black).

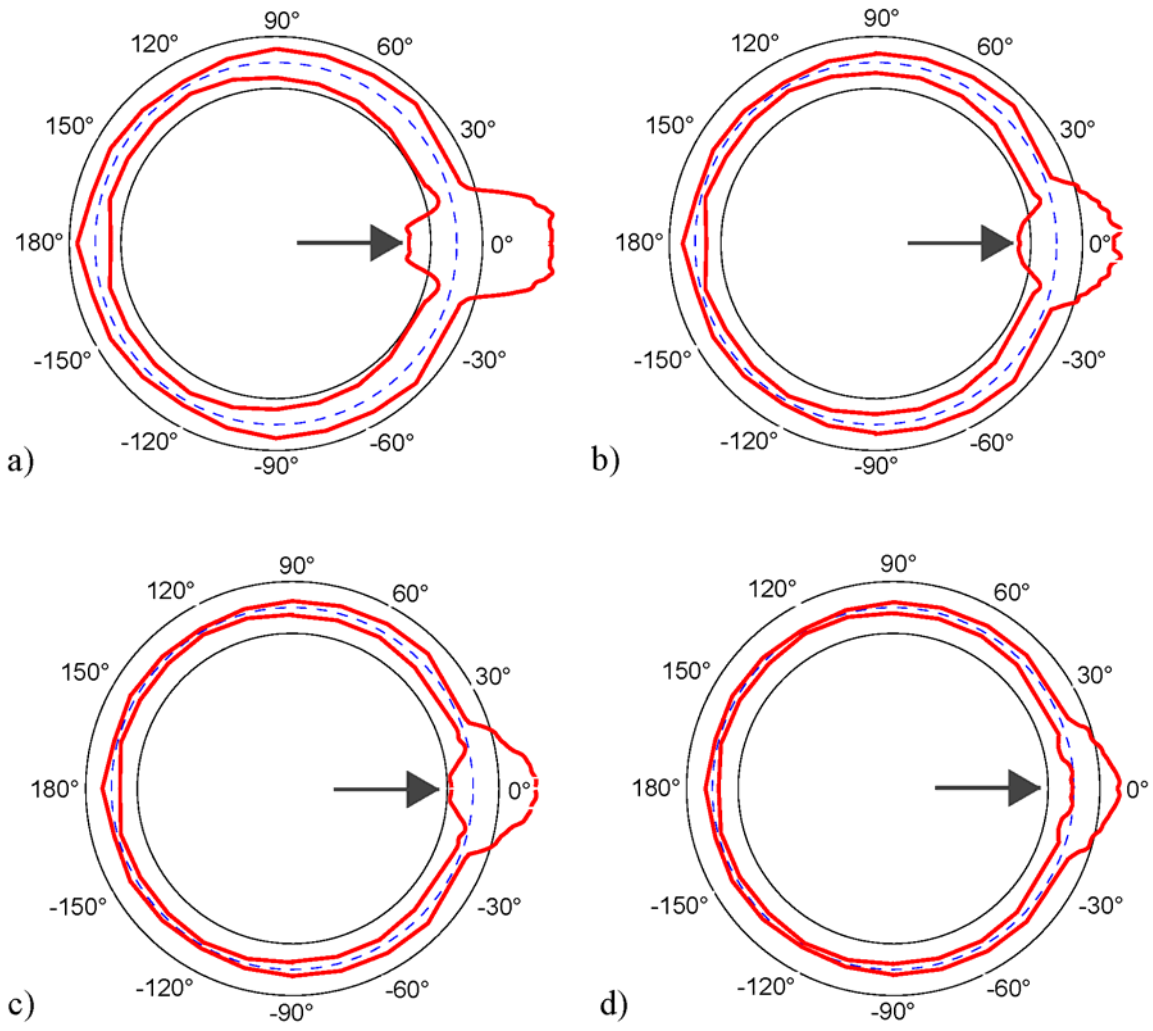

Figure 80: The maximum runup and rundown on the convex conical hill slope for a gravel landslide with a slide volume $V = 1.75$ and impact Froude number F = (a) 2.4, (b) 2.2, (c) 2.0 and (d) 1.9. Symbols: Maximum runup and rundown (red), still water (dashed blue line) and R_u/h and $R_d/h = 0.1$ (black).

6.2.3 Maximum Runup at Slide Impact Prediction

The maximum runup and rundown heights in the impact region on a planar hill slope are given by Mohammed (2010) as

$$\frac{R_{uI}}{h} = \frac{1}{4} F^{1.4} S^{0.7} B^{-0.5} V^{-0.1} \quad (101)$$

$$\frac{R_{dI}}{h} = \frac{2}{5} F^{1.8} S^{0.3} B^{-1.22} V^{0.18} \quad (102)$$

where F is the landslide Froude number given as $F = v_s/\sqrt{gh}$, S is the dimensionless slide thickness given by $S = s/h$, B is the dimensionless slide width given by $B = b/h$, and V is the dimensionless slide volume given as $V = V_s/h^3$. These equations matched maximum runup and rundown in the impact region from the 2010 planar hill slope with r^2 correlation coefficients of 0.75 and 0.81, respectively. The 87% and 90% confidence intervals correspond to the 30% error threshold for the runup and rundown, respectively. The maximum runup and rundown in the impact region are strongly related the water displacement and drawdown from the landslide motion. As a result, the landslide Froude number F, slide thickness S, slide width B, and slide volume V, govern the maximum runup and rundown in the impact region. **Figure 81** compares the measured versus predicted values for the maximum runup and rundown in the impact region of the planar hill slope.

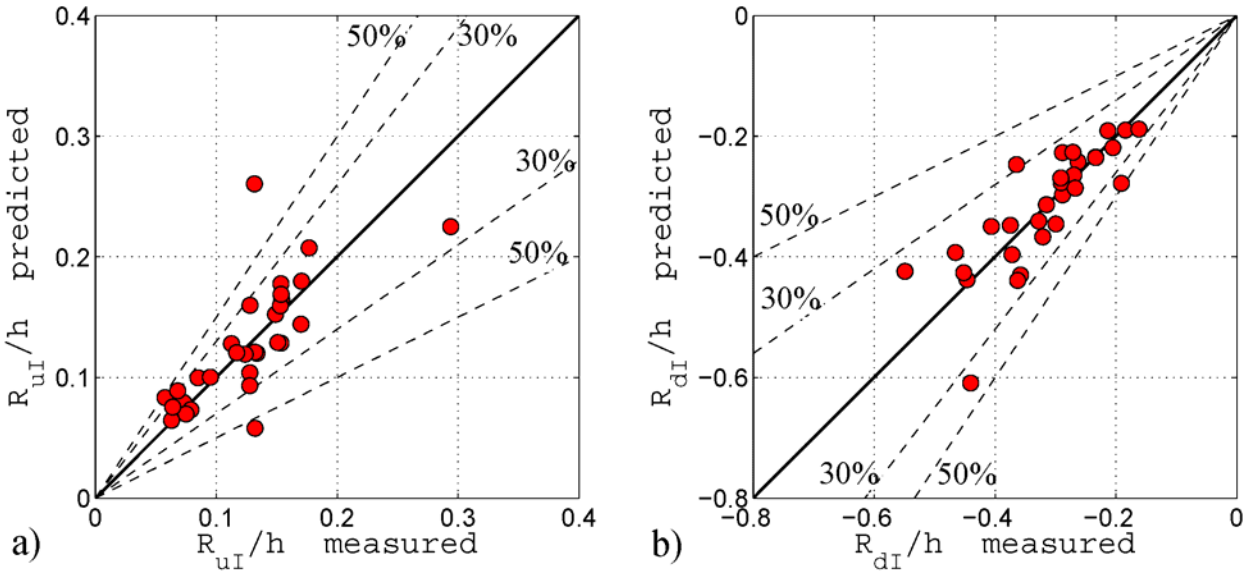

Figure 81: Measured versus predicted maximum (a) runup R_{ul}/h using Equation 101 and (b) rundown R_{dl}/h using Equation 102 in the impact region on a planar slope. The 30% and 50% error thresholds are shown with dashed lines.

Equations 101 and 102 have been extended to describe the maximum runup and rundown on a convex conical hill slope by including an additional coefficient to describe the influence of the dimensionless hill slope radius. The maximum runup in the slide impact region on a diverging convex conical hill slope is given as

$$\frac{R_{uI}}{h} = \frac{1}{4} F^{1.4} S^{0.7} B^{-0.5} V^{-0.1} C_{RuI} \tag{103}$$

where F, S, B and V are the dimensionless landslide Froude number, thickness, width and volume, respectively. The additional conical hill slope coefficient C_{RuI} is given as

$$C_{RuI} = \frac{tanh\left(S^5 B^{2.4} {R_c}^{1.8}\right)}{tanh\left(S^{4.6} B^{3.7} {R_c}^{0.1}\right)} \tag{104}$$

where R_c is the dimensionless radius of the cone at the still waterline given by $R_c = r_c/h$. The maximum runup R_{ul}/h in the impact region on a convex conical hill slope is predicted with an r^2 correlation coefficient of 0.77.

The maximum rundown R_{dI}/h in the impact region on a convex conical hill slope is given as

$$\frac{R_{dI}}{h} = \frac{2}{5} F^{1.8} S^{0.3} B^{-1.22} V^{0.18} C_{RdI} \tag{105}$$

where F, S, B and V are the nondimensionalized landslide Froude number, thickness, width and volume, and the conical hill slope coefficient C_{RdI} is given by

$$C_{RdI} = \frac{tanh\left(S^{1.5} B^{3.3} {R_c}^{5.4}\right)}{tanh\left(S^{0.35} B^{-0.7} {R_c}^{0.6}\right)} \tag{106}$$

The maximum rundown R_{dI}/h in the impact region on a convex conical hill slope is predicted with an r^2 correlation coefficient of 0.91.

As the dimensionless hill slope radius approaches infinity, the C_{RuI} and C_{RdI} terms become asymptotic to 1 and the equations transition into the planar hill slope equations. The two convex

conical hill slope coefficients, C_{RuI} andC_{RdI}, are functions of the slide thickness *S*, slide width *B* and hill slope radius R_c. The slide width and hill slope radius are the two parameters that change the most dramatically from the planar to the divergent convex conical hill slope, and the slide thickness is affected by the landslide granulometry in some experimental conditions. For the experimental data set C_{RuI} is in the range $0.8 < C_{RuI} < 2.0$ and C_{RdI} is in the range $1.2 < C_{RuI} < 2.7$. **Figure 82** shows the measured versus predicted runup R_{uI}/h and rundown R_{dI}/h in the impact region on the convex conical hill slope.

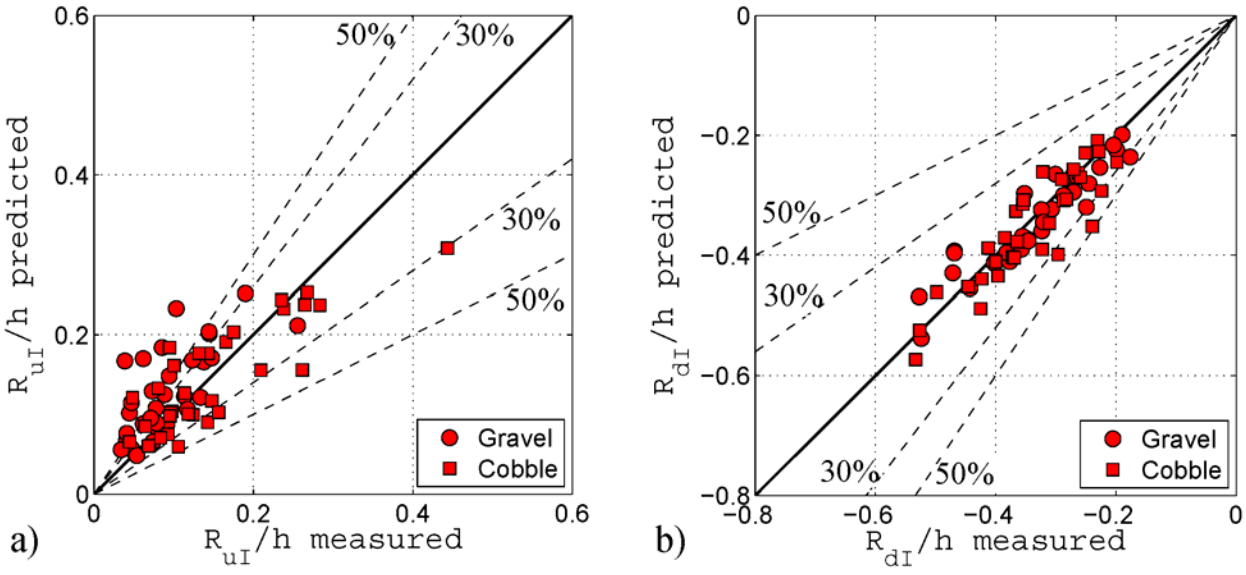

Figure 82: Measured versus predicted maximum (a) runup R_{uI}/h using Equation 103 and (b) rundown R_{dI}/h using Equation 105 in the impact region on a convex conical hill slope with both gravel and cobble slide materials. The dashed lines denote the 30% and 50% error thresholds.

6.2.4 Maximum Runup Adjacent to Slide Impact Prediction

Any infrastructure within the landslide impact region would be overrun by the landslide prior to tsunami runup therefore the maximum runup and rundown outside the landslide impact region may be more relevant in hazard analysis. The maximum runup, R_{um}/h, and rundown, R_{dm}/h, outside the impact region is defined as the maximum runup or rundown beyond the maximum slide width. The maximum runup and rundown decay laterally with propagation distance away from the location of the maximum. The maximum runup R_{um}/h and rundown R_{dm}/h outside the impact region on a planar hill slope are given by

$$\frac{R_{um}}{h} = \frac{1}{4} F^{1.2} S^{0.4} B^{-1.1} V^{0.3} \tag{107}$$

$$\frac{R_{dm}}{h} = \frac{1}{25} F^{2.65} S^{-0.005} B^{-1.1} V^{-0.1} \tag{108}$$

with an r^2 correlation coefficients of 0.90 and 0.80, respectively. Similar to the maximum runup and rundown in the impact region, R_{um}/h and R_{dm}/h are functions of the landslide Froude number *F*, slide thickness *S*, slide width *B*, and slide volume *V*. The maximum R_{um}/h outside the impact region on the planar hill slope is in the range $0.05 < R_{um}/h < 0.28$ and R_{dm}/h is in the range $-0.15 < R_{dm}/h < -0.05$. **Figure 83** shows the measured versus predicted maximum runup and rundown outside of the impact region on a planar hill slope.

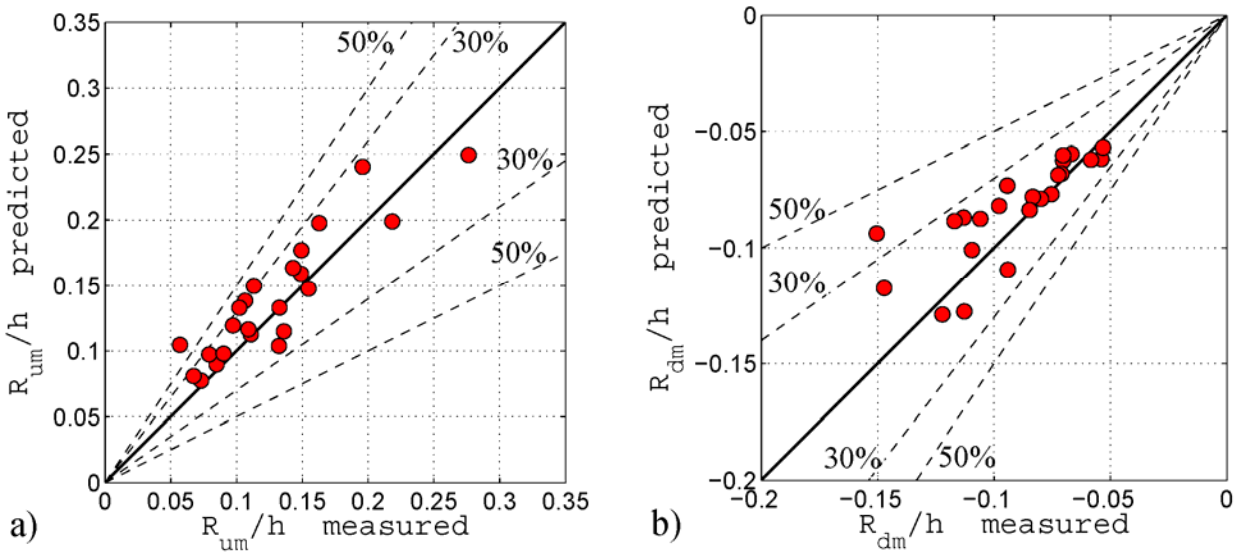

Figure 83: Measured versus predicted maximum (a) runup R_{um}/h using Equation 107 and (b) rundown R_{dm}/h using Equation 108 outside the impact region on a planar slope with noted 30% and 50% error thresholds.

In some experimental conditions with long, thin landslides, the maximum runup and rundown may occur at the defined landslide impact region boundary (maximum slide width intersection with the water surface). When this occurs, the maximum runup and rundown measurements are included in both the impact region and outside of impact region runup and rundown equations.

The maximum runup outside the impact region on the convex conical island is described by

$$\frac{R_{um}}{h} = \frac{1}{4} F^{1.2} S^{0.4} B^{-1.1} V^{0.3} C_{Ru} \tag{109}$$

where the convex conical hill slope coefficient C_{Ru} is given as

$$C_{Ru} = \frac{tanh\left(S^{1.6} B^{2.5} {R_c}^{0.1}\right)}{tanh\left(S^{1.8} B^{0.05} {R_c}^{2.2}\right)} \tag{110}$$

with the predicted R_{um}/h from Equation 109 corresponds to measured values with an r^2 correlation coefficients of 0.69. The maximum rundown outside the impact region on the convex conical hill slope is given by

$$\frac{R_{dm}}{h} = \frac{1}{25} F^{2.65} S^{-0.005} B^{-1.1} V^{-0.1} C_{Rd} \tag{111}$$

where the convex conical hill slope coefficient is given by

$$C_{Rd} = \frac{tanh\left(S^{0.65} B^{0.4} {R_c}^{0.4}\right)}{tanh\left(S^{0.55} B^{-1.1} {R_c}^{1.4}\right)} \tag{112}$$

with the R_{dm}/h matching the measured values with an r^2 correlation coefficients of 0.80. As the dimensionless convex island radius goes to infinity the maximum runup and rundown equations are asymptotic to the planar hill slope equations. The C_{Ru} term is in the range $0.6 < C_{Ru} < 1.4$ and the C_{Rd} term is in the range $0.7 < C_{Rd} < 1.5$. The maximum R_{um}/h outside the impact region on the convex hill slope is in the range $0.02 < R_{um}/h < 0.15$ and the maximum R_{dm}/h outside the impact region is in the range $-0.10 < R_{dm}/h < -0.03$. **Figure 84** shows the measured versus predicted runup outside the landslide impact region on the convex conical hill slope. This maximum runup and rundown do not describe the runup and rundown amplification on the lee side of the conical island. The amplified runup and rundown on the lee side of the island are described with another set of equations (Equations 127 and 128).

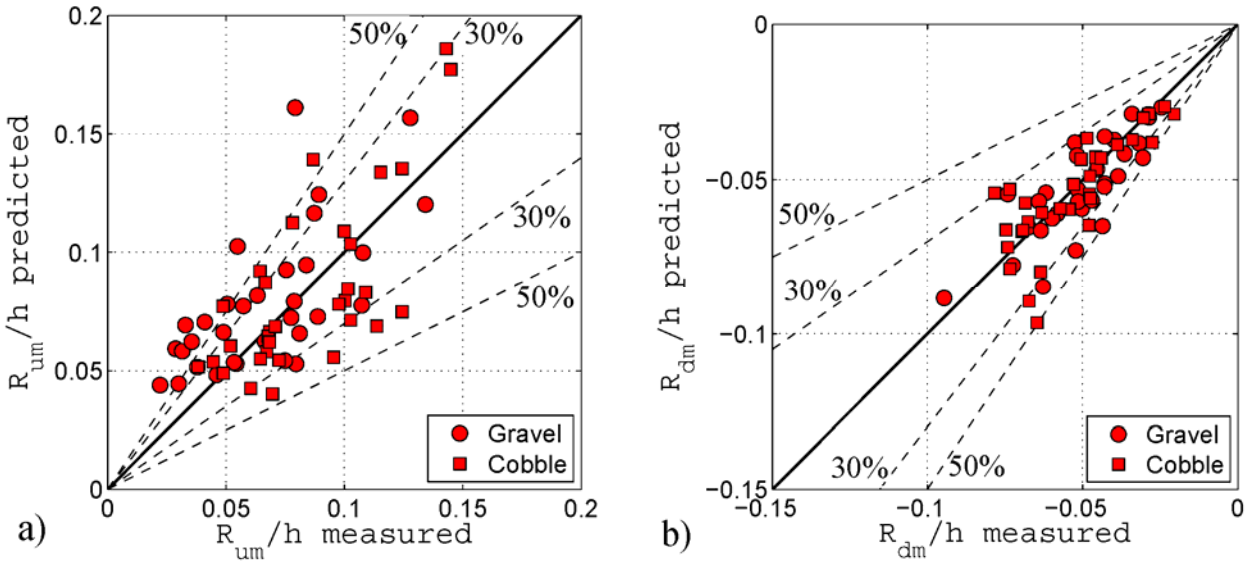

Figure 84: Measured versus predicted maximum (a) runup R_{um}/h using Equation 109 and (b) rundown R_{dm}/h using Equation 111 outside the impact region on a convex conical hill slope with gravel and cobble slide materials.

In the majority of cases, the maximum runup outside the impact region tends to be larger than the maximum rundown, independent of the landslide granulometry or divergence of the lateral hill slope. **Figure 85** shows a comparison of the maximum runup and rundown outside of the impact region for gravel landslides on planar and convex hill slopes and cobble landslides on a convex conical hill slope.

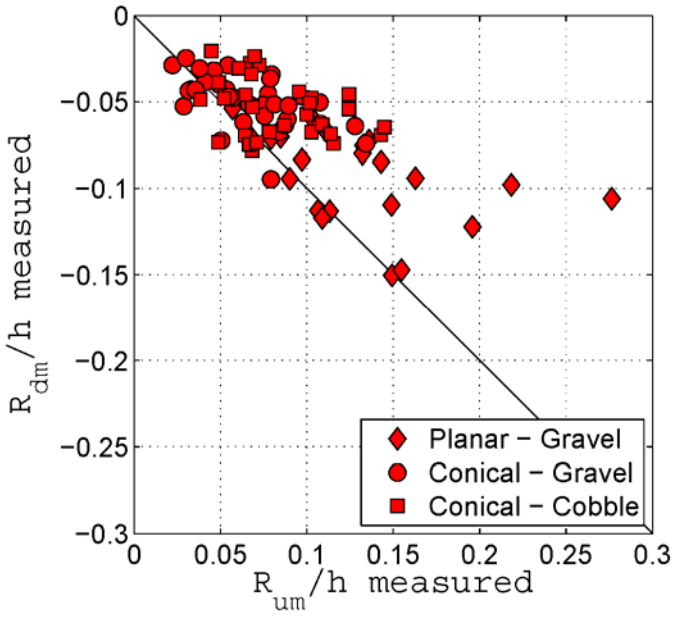

Figure 85: Comparison of the maximum runup R_{um}/h and rundown R_{dm}/h outside of the landslide impact region generated with a gravel landslide on a planar hill slope (diamonds) and convex conical hill slope (circles), and with a cobble landslide on a divergent conical hill slope (squares).

6.2.5 Location of Maximum Runup Adjacent to Slide Impact Prediction

The location of the maximum runup and rundown outside the impact region on the planar hill slope is important and can be predicted with

$$\frac{r_{Rum}}{h} = \frac{4}{5} S^{-0.1} B^{1.25} \tag{113}$$

$$\frac{r_{Rdm}}{h} = \frac{8}{3} S^{0.05} B^{0.7} \tag{114}$$

with r^2 correlation coefficients of 0.96 and 0.94, respectively. The location of the maximum runup and rundown outside the impact region is predominately influenced by the landslide width B and

secondarily influenced by the slide thickness S. On the planar hill slope ${}^{r_{Rum}}/_{h}$ is in the range $0.6 < {}^{r_{Rum}}/_{h} < 9.7$ and ${}^{r_{Rdm}}/_{h}$ is in the range $2.0 < {}^{r_{Rdm}}/_{h} < 13.5$.

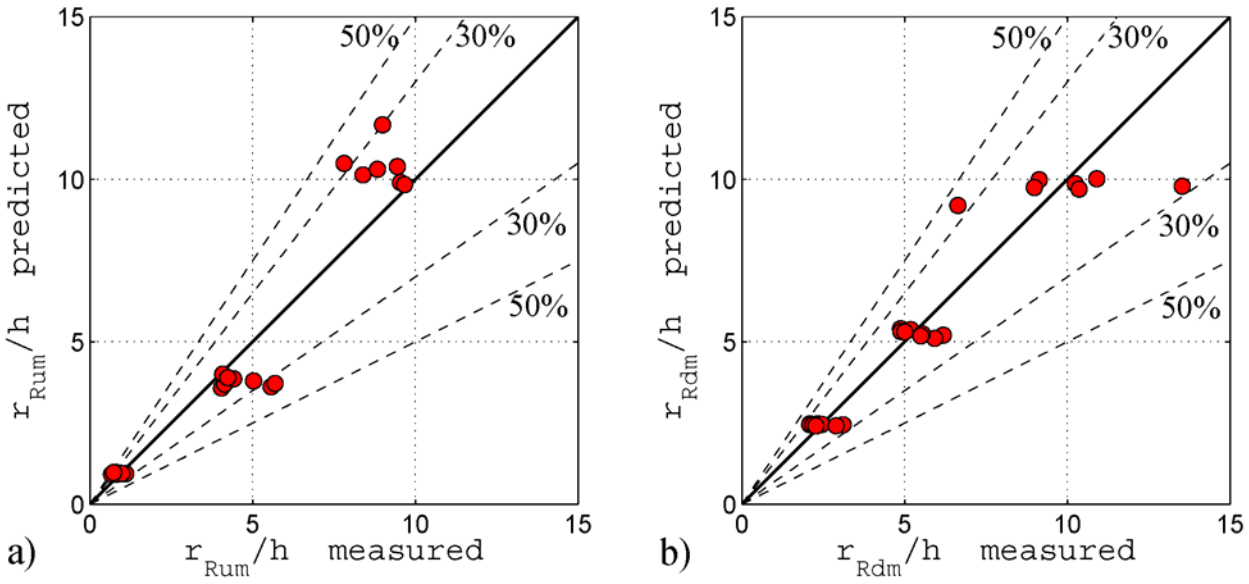

Figure 86: Measured versus predicted maximum (a) runup location ${}^{r_{Rum}}/_{h}$ using Equation 113 and (b) rundown location ${}^{r_{Rdm}}/_{h}$ using Equation 114 outside the impact region on a planar slope. The 30% and 50% error thresholds are shown with dashed lines. The data points cluster into three groups corresponding to the three water depths tested on the planar slope.

The location of the maximum runup ${}^{r_{Rumcs}}/_{h}$ outside the impact region on the conical hill slope is predicted with

$$\frac{r_{Rumcs}}{h} = \frac{4}{5} S^{-0.1} B^{1.25} C_{Rur} \tag{115}$$

with the convex conical hill slope coefficient C_{Rur} given by

$$C_{Rur} = \frac{tanh\left(S^{0.55} B^{-2.7} L^{0.34} {R_c}^{2.1}\right)}{tanh\left(S^{0.5} B^{-7.9} L^{3.1} {R_c}^{5.55}\right)} \tag{116}$$

and the maximum rundown outside the impact region is given with

$$\frac{r_{Rdmcs}}{h} = \frac{8}{3} S^{0.05} B^{0.7} C_{Rdr} \tag{117}$$

with the convex conical hill slope coefficient C_{Rdr} given by

$$C_{Rdr} = \frac{tanh\left(S^{0.5} B^{-0.4} L^{0.4} {R_c}^{0.6}\right)}{tanh\left(S^{3.5} B^{8.3} L^{0.9} {R_c}^{4}\right)} \tag{118}$$

The maximum runup ${r_{Rumcs}}/{h}$ and rundown ${r_{Rdmcs}}/{h}$ locations from Equations 115 and 117 have r^2 correlation coefficients of 0.95 and 0.94, respectively.

The location is given in terms of the circular segment of the shoreline circumference rather than angular degrees of the Φ dimension shown in the definition sketch in this chapter's introduction. This coordinate system was chosen for a smooth transition from the planar hill slope and the convex conical hill slope. The circular segment distance r_{cs}/h can be converted to conical angle Φ by $\Phi = r_{cs}/h * 1/R_c * 180/\pi$. On the convex hill slope r_{Rumcs}/h is in the range $0.5 < {r_{Rumcs}}/{h} < 11.5$ and r_{Rdmcs}/h is in the range $1.4 < {r_{Rdmcs}}/{h} < 17$. **Figure 87** shows the measured versus predicted location of the maximum runup and rundown outside of the landslide impact region on a convex conical hill slope.

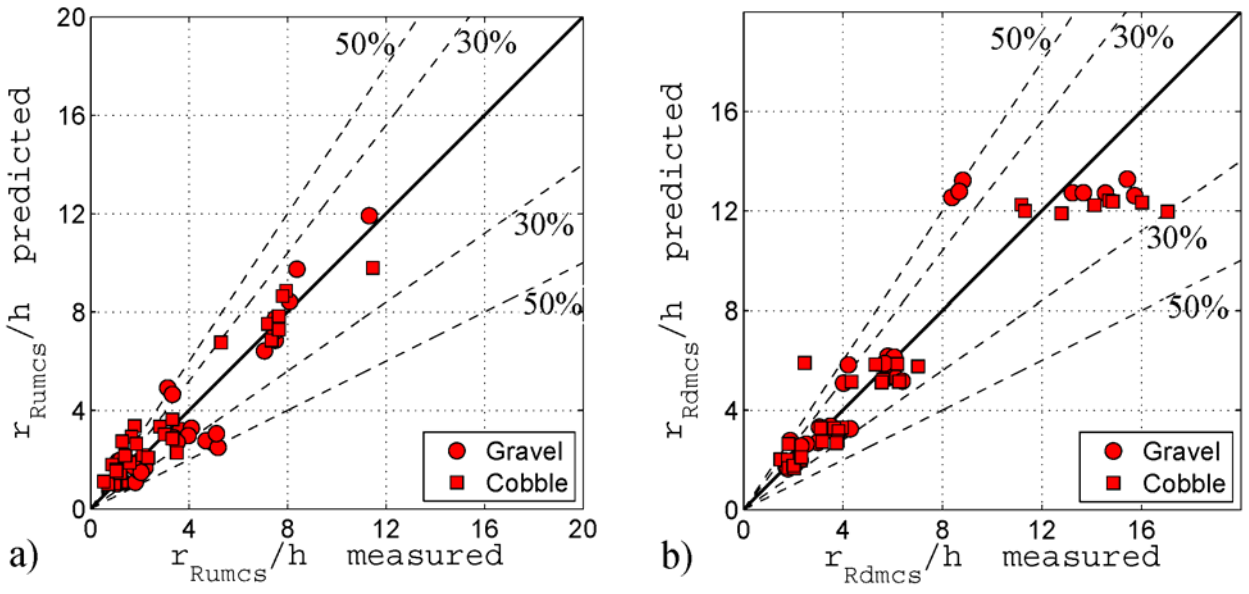

Figure 87: Measured versus predicted (a) maximum runup location r_{Rumcs}/h using Equation 115 and (b) maximum rundown location r_{Rdmcs}/h using Equation 117 outside the impact region on a convex conical hill slope with gravel and cobble slide materials.

Maximum runup and rundown outside of the subaerial slide impact have been observed using block slides on a plane slope by Lynett and Liu (2005) and Di Risio et al. (2009a) at an approximate distance of 2 slide widths from the block slide center. The maximum runup outside the slide impact region, nondimensionalized with the impact slide width rather than the water depth, on the plane slope in our experiments occurs in the range $0.6 < r_{Rum}/b < 1.9$ with a mean distance of 1.23 slide widths. The maximum rundown occurs in the range $0.9 < r_{Rdm}/b < 3.1$ from the slide centerline with a mean value of 1.9 slide widths. The unconfined lateral spreading of the landslide in this experiment produces much larger slide widths, thereby reducing the lateral distance relative to the slide widths from the slide centerline to the runup maximum outside the impact region compared to block slides.

6.2.6 Lateral Wave Amplitude Attenuation Prediction

The decay curve of the maximum lateral tsunami runup beyond the maximum is important to predict the extent of the runup hazard. The runup decay beyond the maximum runup height follows the equation form $^{R}/_{h} = k\,(^{r}/_{h})^{n}$. The empirics of this format separate into the generation function, k, and the propagation function, f (r/h). A multivariable regression analysis defined the decaying runup and rundown heights beyond the maximum on a planar hill slope as

$$\frac{R_u}{h} = 0.2\,F^{1.15}S^{0.5}V^{0.12}\left(\frac{r}{h}\right)^{-0.2\,F^{0.35}B^{0.08}V^{-0.3}} \tag{119}$$

$$\frac{R_d}{h} = 0.1\,F^{1.7}S^{0.25}L^{-0.03}\left(\frac{r}{h}\right)^{-0.3\,F^{-0.17}B^{0.7}V^{-0.09}} \tag{120}$$

with correlation coefficients for the runup R_u/h and rundown R_d/h decay as $r^2 = 0.86$ and 0.91, respectively. **Figure 88** shows the best fit line of the decaying portion of the data on the planar hill slope using Equations 119 and 120. The 30% error lines correspond to the 82% and 96% confidence intervals for the runup and rundown, respectively.

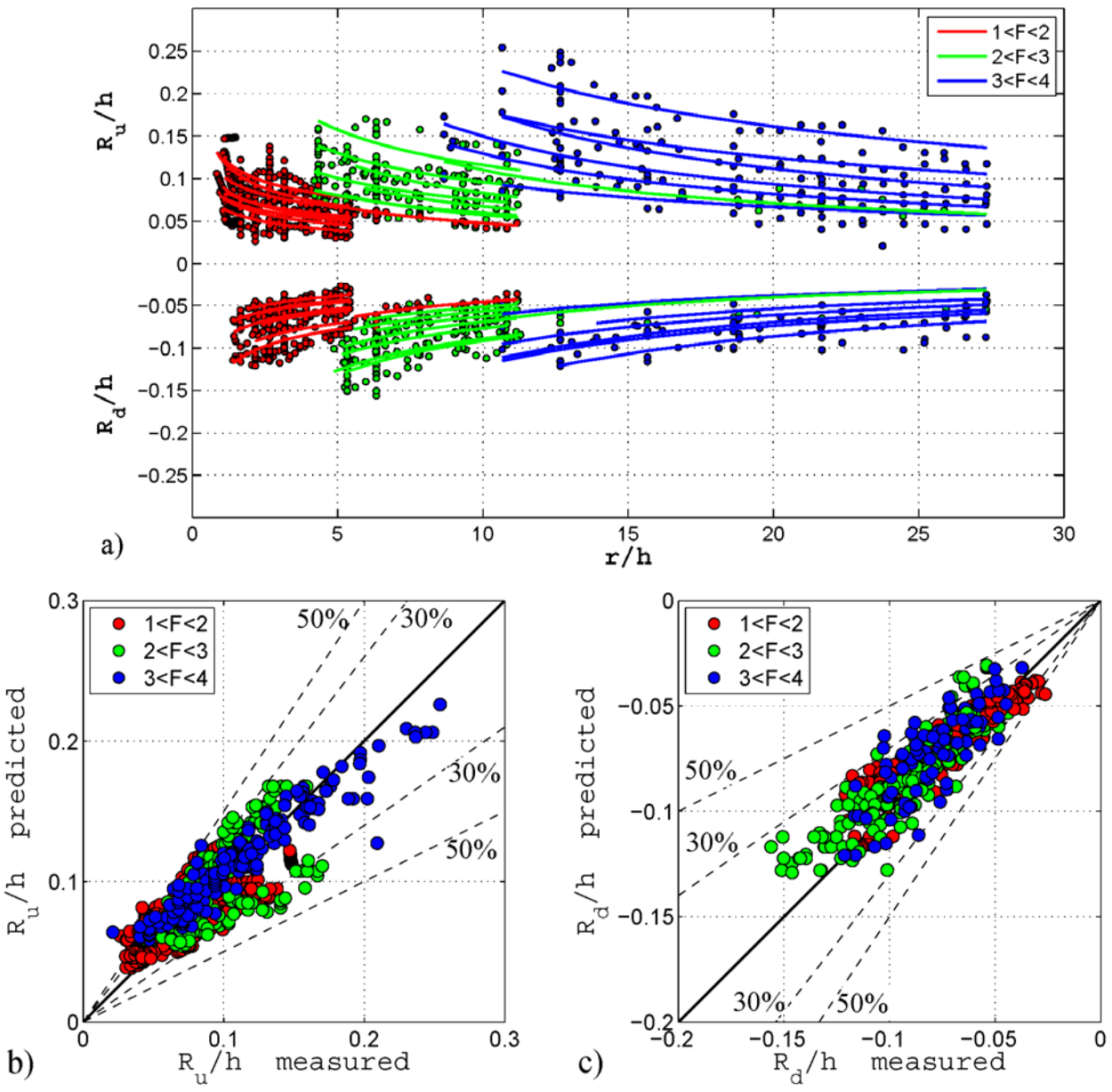

Figure 88: (a) Lateral tsunami wave runup R_u/h decay using Equation 119 and rundown R_d/h decay using Equation 120 beyond the maxima on a planar hill slope, and comparison between the predicted and measured (b) runup and (c) rundown in the decay portion beyond the maxima with noted 30% and 50% error thresholds.

The decay portion on the convex conical hill slope spans from the location of the maxima outside of the impact region to Φ = 165°. Two additional terms were added to the planar hill slope equations to transition it to the conical hill slope. One term was added to the generation function, *k*, and one term was added to the propagation function, *n*. Each of the new terms are asymptotic to 1 as the dimensionless radius goes to infinity, transitioning the convex conical hill slope equations (Equations 121 and 124) back to the planar hill slope equations (Equations 119 and 120). The runup decay from the maximum on the conical hill slope can be described as

$$\frac{R_u}{h} = 0.2\, F^{1.15} S^{0.5} V^{0.12} C_{Ru1} \left(\frac{r_{cs}}{h}\right)^{-0.2\, F^{0.35} B^{0.08} V^{-0.3} C_{Ru2}} \tag{121}$$

with the first runup convex conical hill slope coefficient C_{Ru1} given as

$$C_{Ru1} = \frac{tanh\left(S^{0.6} L^{0.03} {R_c}^{0.2}\right)}{tanh\left(S^{-0.08}\, L^{-1.5} {R_c}^{1.4}\right)} \tag{122}$$

the second runup convex conical hill slope coefficient C_{Ru2} is given as

$$C_{Ru2} = \frac{tanh\left(S^{1.3} B^{0.4} L^{1.7} {R_c}^{0.1}\right)}{tanh\left(S\, B^{-1.5} L^{6.5} {R_c}^{2.5}\right)} \tag{123}$$

to produce an r^2 correlation coefficient of 0.78. The rundown from the maximum can be described as

$$\frac{R_d}{h} = 0.1\, F^{1.7} S^{0.25} L^{-0.03} C_{Rd1} \left(\frac{r_{cs}}{h}\right)^{-0.3\, F^{-0.17} B^{0.7} V^{-0.09} C_{Rd2}} \tag{124}$$

with the first rundown convex conical hill slope coefficient C_{Rd1} given as

$$C_{Rd1} = \frac{tanh\left(S^{7}\, L^{3.4}\, {R_c}^{2}\right)}{tanh\left(S^{6.7}\, L^{3.5}\, {R_c}^{2.1}\right)} \tag{125}$$

the second rundown convex conical hill slope coefficient C_{Rd2} is given as

$$C_{Rd2} = \frac{tanh\left(S^{0.4}L^{-0.07}\ {R_c}^{0.4}\right)}{tanh\left(S^{2.2}L^{0.75}{R_c}^{3.6}\right)} \tag{126}$$

to produce an r^2 correlation coefficient of 0.76.

Figure 89 shows the best fit line of the runup amplitude attenuation decay beyond the maxima outside the landslide impact region for gravel and cobble landslides on the convex conical hill slope. **Figure 90** shows the measured versus predicted runup and rundown values beyond the maxima outside the landslide impact region using Equations 121 and 124.

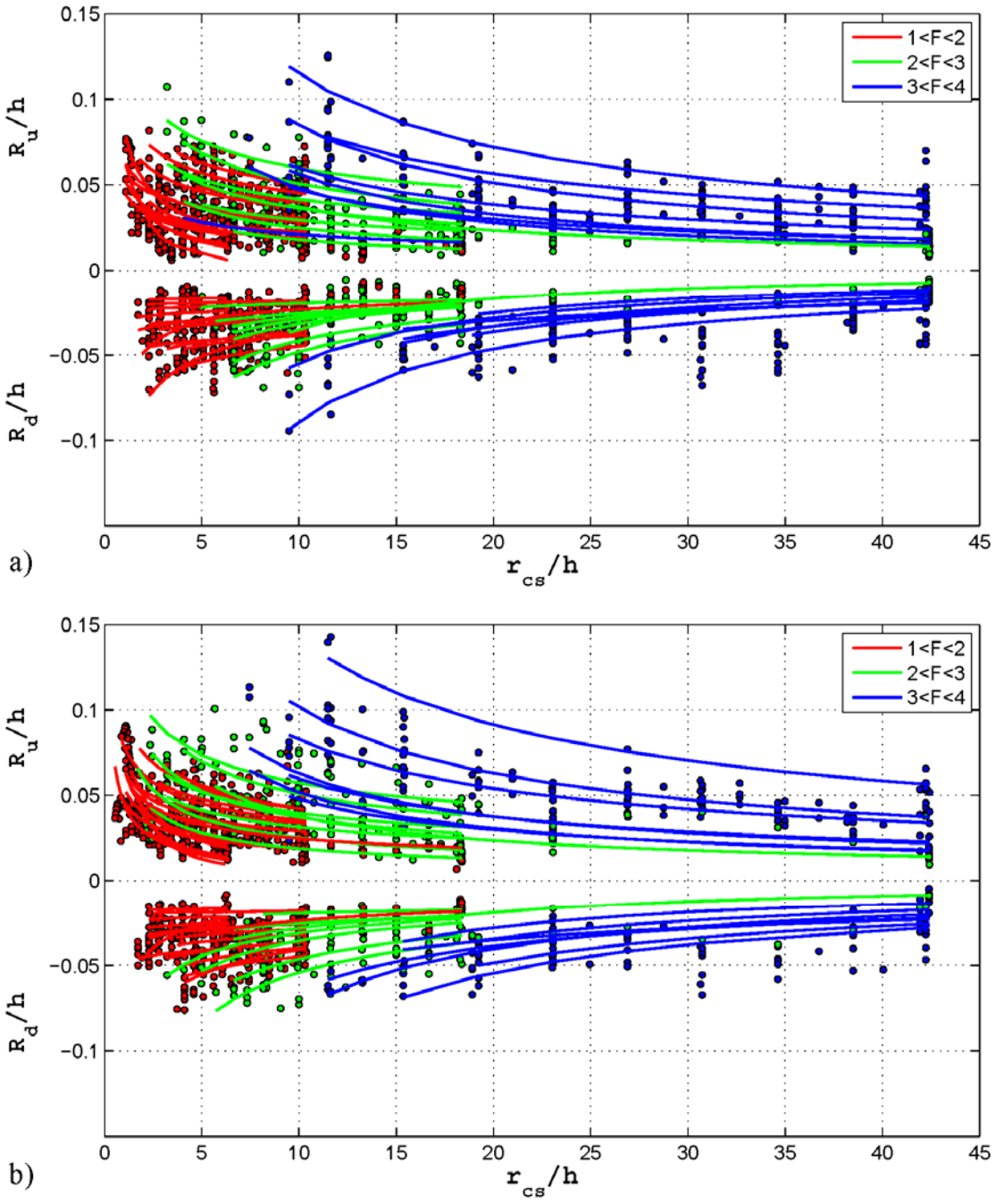

Figure 89: Lateral tsunami wave runup R_u/h decay using Equation 121 and rundown R_d/h decay using Equation 124 beyond the maxima on the convex conical hill slope with (a) gravel slide material and (b) cobble slide material.

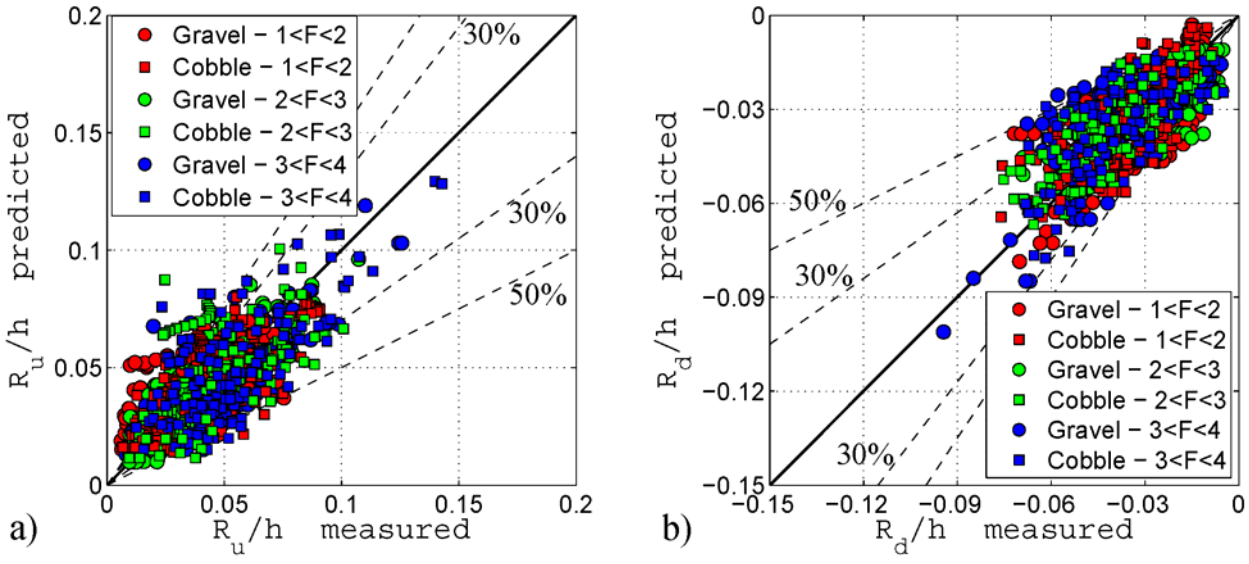

Figure 90: Lateral tsunami wave measured versus predicted (a) runup R_u/h decay using Equation 121 and (b) rundown R_u/h decay using Equation 124 beyond the maximum on the convex conical hill slope with gravel and cobble slide material with noted 30% and 50% error thresholds.

6.2.7 Island Lee Side Runup and Rundown Amplification

One of the unique features of the runup and rundown on the convex conical hill slope is the lee side runup and rundown amplification caused by the trapped lateral edge waves propagating around both sides of the island and colliding on the lee side. Island lee side runup amplification is often considered when tsunamis are generated offshore and attack the conical island. The tsunami generated by the 11 December 1992 Flores earthquake in Indonesia approached the island from the north and refraction caused the tsunami to wrap around the island resulting in an unexpectedly large runup of 7.2 m on the southern side destroying two fishing villages (Yeh et al., 1994). The Babi Island effect was physically modelled with a conical island setup and offshore tsunami attack by Briggs et al. (1995). In contrast, in this study the tsunami is generated by a landslide along the coast of the island simulating a landslide off an island or a volcanic flank collapse. The physical

models of Di Risio (2009b) and Romano (2013) used a block slide emplaced on the coast of a conical island to study the lateral wave propagation and lee side runup and rundown amplification. A similar runup amplification on the lee side of the island was observed in this study. **Figure 91** shows a time series of the runup and rundown amplification on the lee side of the island.

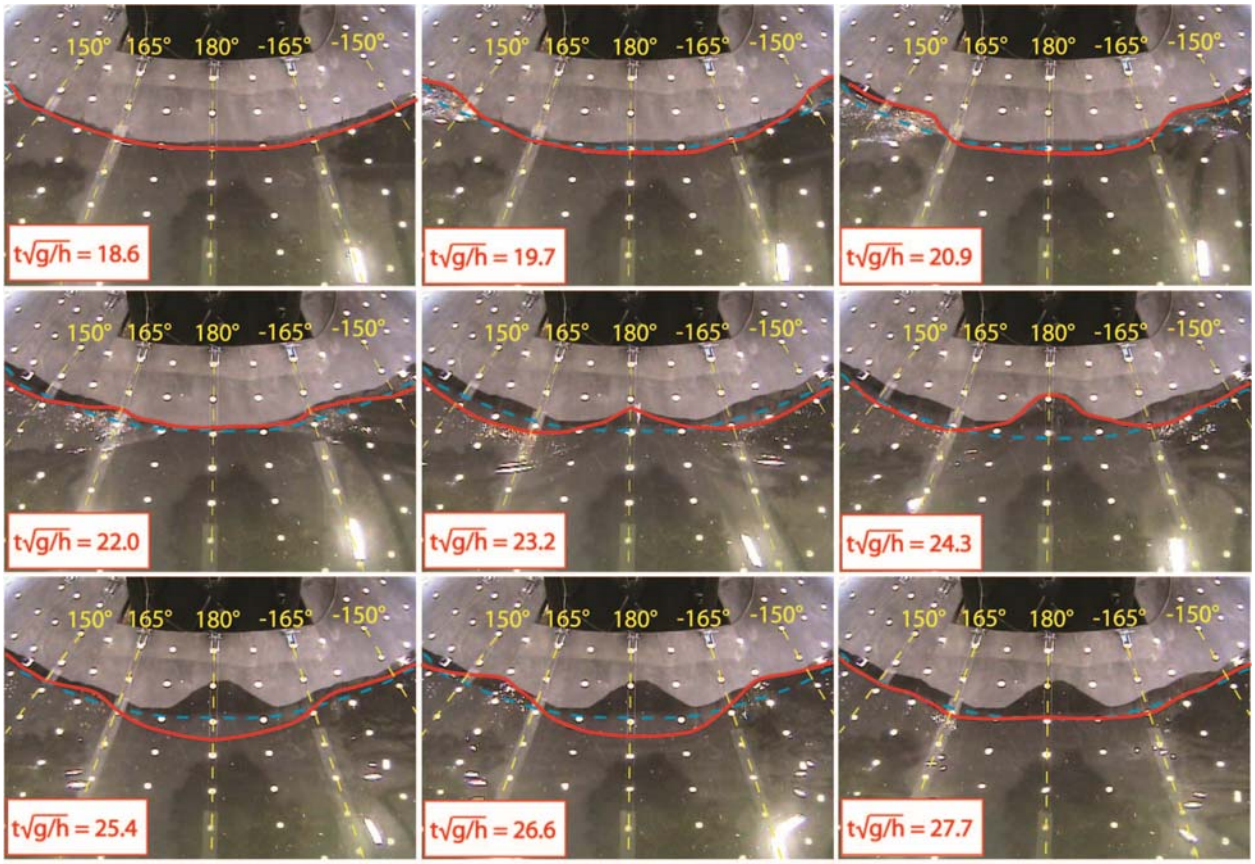

Figure 91: Video image sequence of the lee side island runup and rundown amplification showing the instantaneous waterline (——) and still waterline (– – –) at a water depth of h = 1.2 m with a landslide Froude number F = 1.4. $t\sqrt{g/h}$ = 0 corresponds to the landslide impacting the water surface.

In **Figure 77** and **Figure 78** it can be observed that the decay from the runup and rundown maxima ends at the island angle of Φ = 165°. Between Φ = 165° and 180° the superposition and

collision effects of the two trapped edge waves amplify both the runup and rundown. If both trapped edge waves were true linear waves without further dispersion and energy dissipation between Φ = 165° and 180°, then a direct superposition of the wave runup and rundown at Φ = 180° would correspond to twice the values at 165° (Dean and Dalrymple, 1991). The wave nonlinearities observed in subaerial landslide generated waves prohibit the use of a direct superposition method. **Figure 92** compares the measured maximum runup and rundown at Φ = 165° and Φ = 180°. The leeside tsunami runup amplification ratio R_{u180}/R_{u165} for all the test landslide impact characteristics include gravel and cobble landslide materials was in the range $1.28 < R_{u180}/R_{u165} < 4.64$ with a mean value of 2.19. The R_{d180}/R_{d165} ratio was in the range $1.00 < R_{d180}/R_{d165} < 3.77$ with a mean value of 1.98.

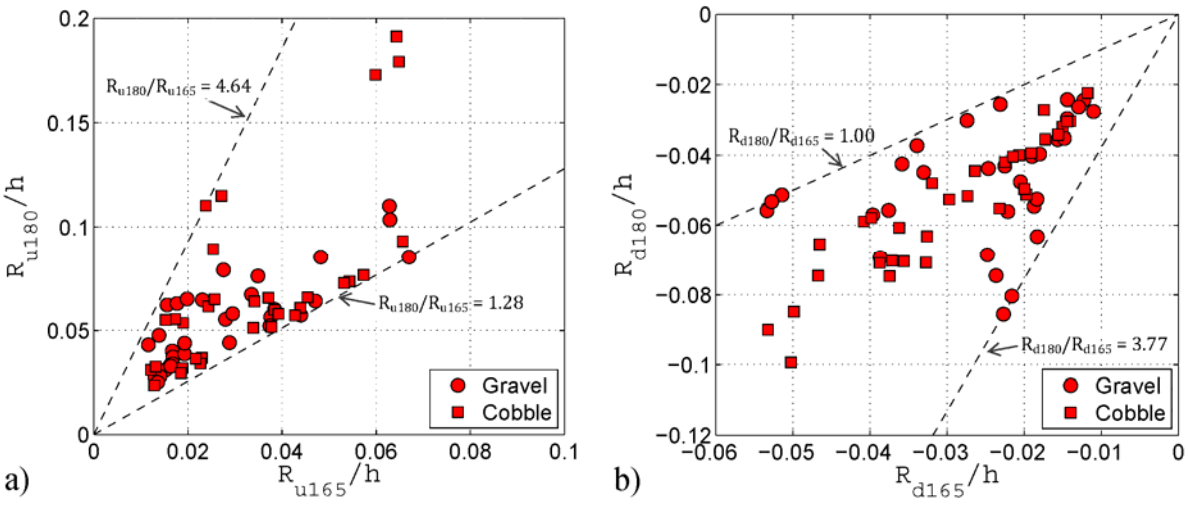

Figure 92: Tsunami amplification on the lee side of the conical island characterized by the ratio of the maximum dimensionless (a) runup and (b) rundown at Φ = 165° and Φ = 180°.

The incident runup R_{u165}/h prior to the lee side collision can be predicted if the landslide impact parameters and shoreline radius are determined using Equation 121. The relationship between the maximum runup at Φ = 180° to Φ = 165° can be described as

$$\frac{R_{u180}}{R_{u165}} = 2.6\, F^{-1.2} B^{-0.2} {R_c}^{0.5} \tag{127}$$

with a correlation coefficient of $r^2 = 0.70$. **Figure 93** shows the measured versus predicted ratio of R_{u180}/R_{u165}. The maximum rundown at Φ = 180° can be directly related to the landslide parameters and the convex conical island radius at the still waterline as

$$R_{d180} = 0.08\, F^{1} S^{0.25} B^{-1.25} {R_c}^{0.6} \tag{128}$$

with an r^2 correlation coefficient of 0.74. The rundown at Φ = 180° can be directly derived from landslide impact parameters and island radius R_c because the slide thickness S and width B describe the impacting landslide front cross-sectional area, the slide Froude number F describes the slide velocity impacting the water and island radius R_c describes the propagation distance to the lee side of the island. **Figure 93** shows the measured versus predicted values for the rundown at Φ = 180°.

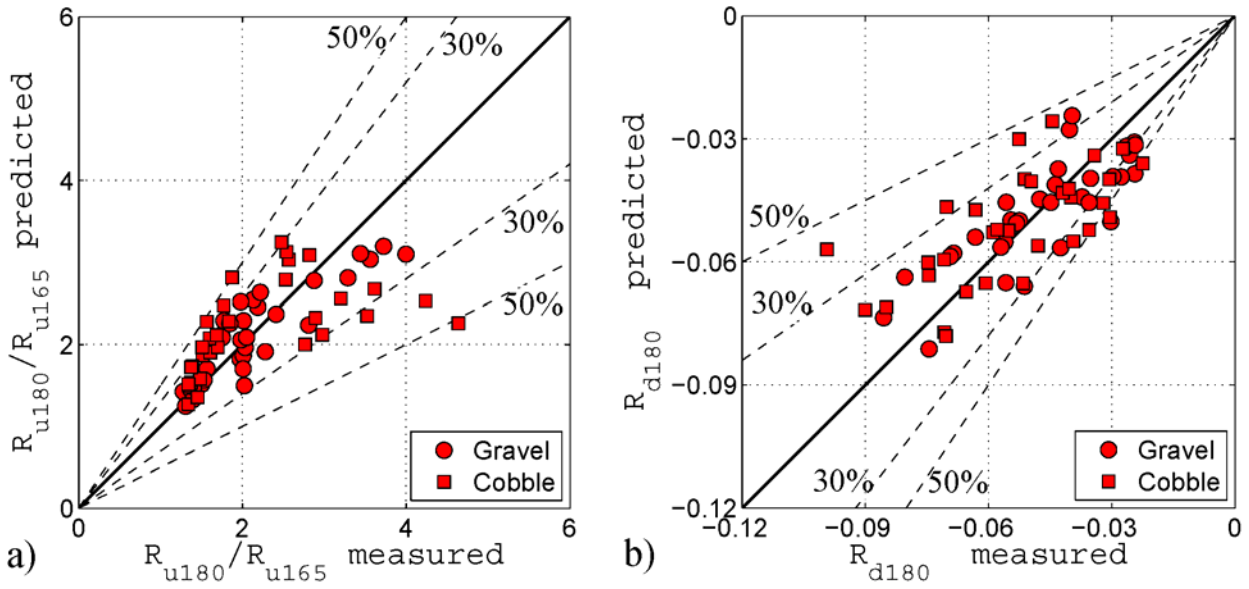

Figure 93: Maximum runup and rundown at $\Phi = 180°$: (a) Measured versus predicted runup amplification between $\Phi = 180°$ and $\Phi = 165°$ using Equation 127 and the (b) measured versus predicted rundown at $\Phi = 180°$ using Equation 128. The dashed lines denote the 30% and 50% error thresholds.

6.2.8 Lateral Wave Period Prediction

The wave period of the first and second lateral waves was determined using the up crossing point technique. The first up crossing point was established as 5% of the first wave crest amplitude, $\eta = 0.05\, a_{c1}$. The wave period of the leading lateral tsunami wave on the planar hill slope is measured in the propagation distance range of $0 < r/h < 25$ and the wave periods are in the range of $5 < T\sqrt{g/h} < 25$. The evolution of the lateral first tsunami wave period on a planar hill slope is given by

$$T_1\sqrt{g/h} = k_{T1}\left(\frac{r}{h}\right)^{0.35} \tag{129}$$

where k_{T1} is given in Chapter 5 as

$$k_{T1} = 4.8\ \mathrm{F}^{0.21} S^{0.05} L^{0.04} \tag{130}$$

with a correlation coefficient of $r^2 = 0.98$. Data from the second lateral tsunami wave was truncated by the reflective wave returning from the edge of the ramp. The second lateral wave was measured in the propagation distance of $0 < r/h < 20$ and the wave periods are in the range of $5 < T_2\sqrt{g/h} < 12$. The evolution of the second lateral tsunami wave is given by

$$T_2\sqrt{g/h} = k_{T2}\left(\frac{r}{h}\right)^{0.45} \tag{131}$$

where k_{T2} is given in Chapter 5 as

$$k_{T2} = 3.0\ \mathrm{F}^{0.03} S^{0.03} L^{0.01} \tag{132}$$

with a correlation coefficient of $r^2 = 0.36$. The poor correlation coefficient is the result of the small range of values for the second wave period on the planar hill slope. The evolution of the normalized leading wave periods with propagation distance and the comparison of the measured to the predicted values of the normalized lateral wave periods for the first two waves are shown in **Figure 94**.

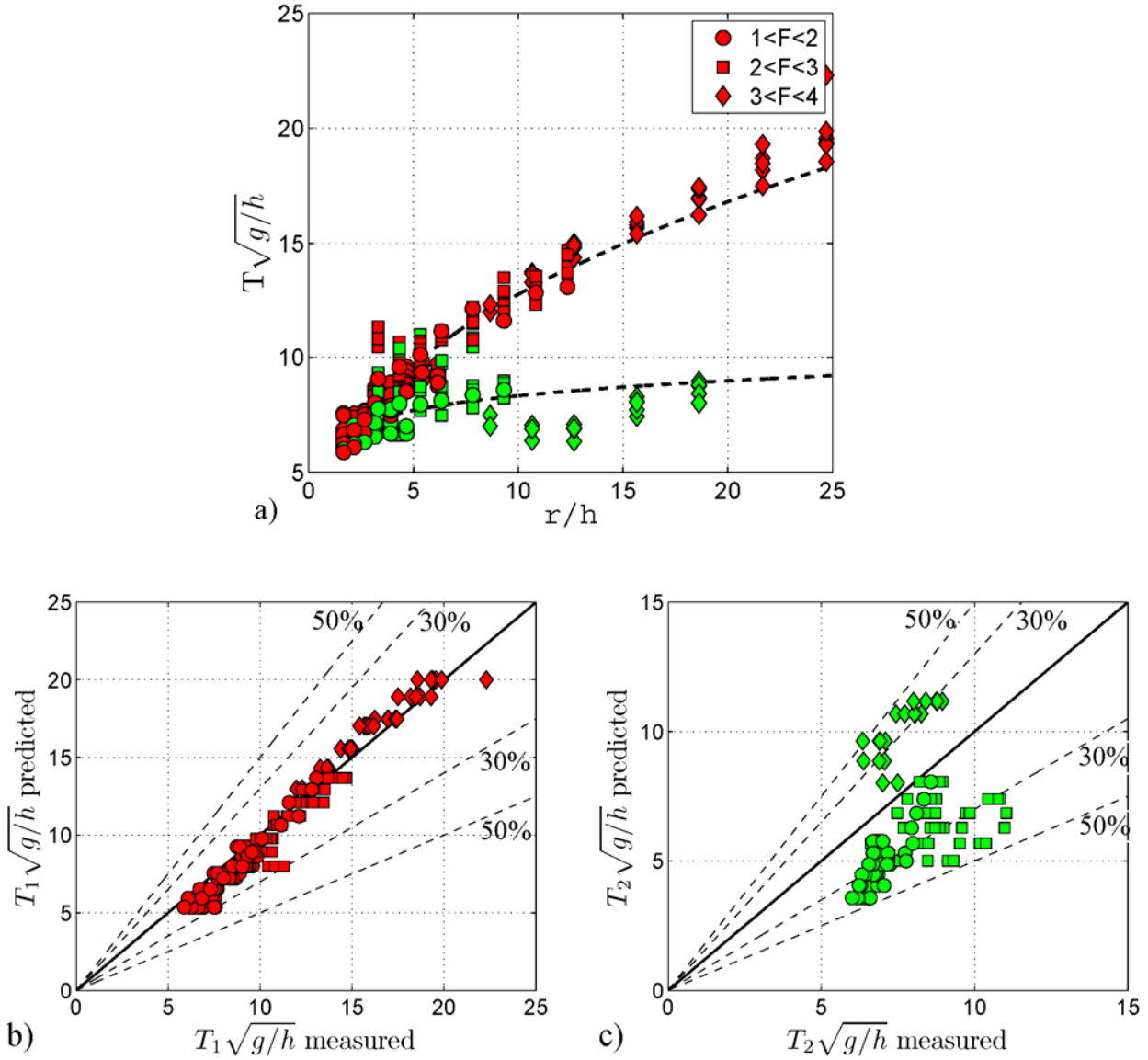

Figure 94: Lateral wave periods on planar hill slope: (a) $T\sqrt{g/h}$ along propagation distance *r/h* for the leading wave period T_1 (red) and the second wave period T_2 (green), (b) comparison of the measured versus the predicted values of the leading lateral wave period from Equation 129 and (c) comparison of the measured versus the predicted values of the second lateral wave period from Equation 131 with noted 30% and 50% error thresholds.

Similar results to the lateral wave periods on the planar hill slope are observed on the convex conical hill slope. The wave period of the first two lateral waves are measured in the range

of $0 < r_{cs}/h < 50$ and the wave periods are in the range of $5 < T_{cs}\sqrt{g/h} < 23$. The evolution of the first wave period on the conical hill slope is given as

$$T_{cs1}\sqrt{g/h} = k_{T_{cs\,1}}\left(\frac{r_{cs}}{h}\right)^{0.3} \tag{133}$$

where $k_{T_{cs}1}$ is given in Chapter 5 as

$$k_{T_{cs}1} = 4.8\ \mathrm{F}^{0.21}S^{0.05}L^{0.04}\coth(R_c^{0.57}) \tag{134}$$

with an r^2 correlation coefficient of 0.95. The evolution of the second lateral wave on the conical hill slope is given as

$$T_{cs2}\sqrt{g/h} = k_{T_{cs\,2}}\left(\frac{r_{cs}}{h}\right)^{0.35} \tag{135}$$

where $k_{T_{cs}2}$ is given in Chapter 5 as

$$k_{T_{cs}2} = 3.0\ \mathrm{F}^{0.03}S^{0.03}\mathrm{L}^{0.01}\coth(R_c^{1.4}) \tag{136}$$

with an r^2 correlation coefficient of 0.83. The evolution of the normalized lateral tsunami wave period on the convex conical hill slope and the comparison of the measured data to the predicted equations are shown in **Figure 95**.

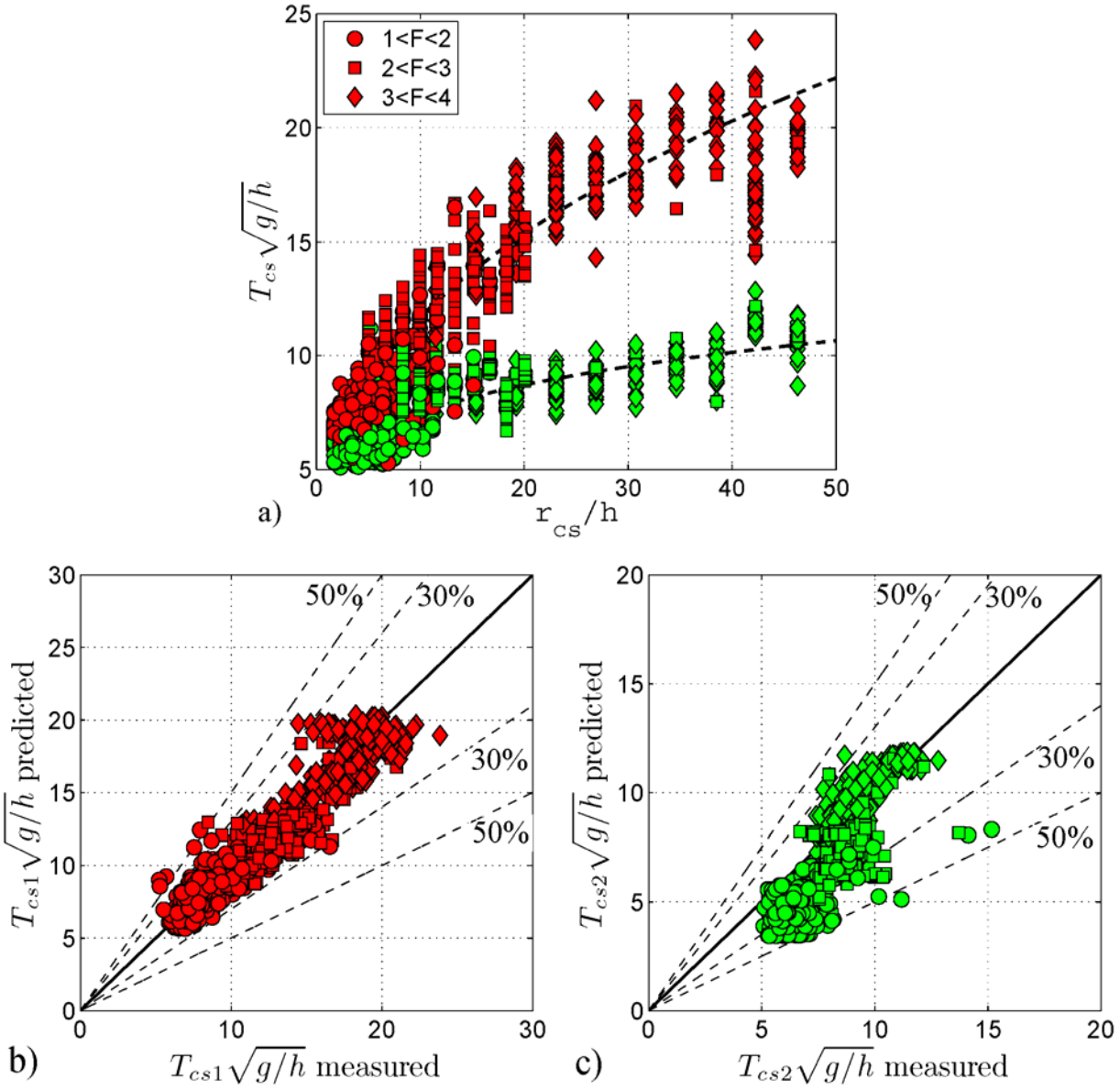

Figure 95: Lateral wave period on convex conical hill slope: (a) $T_{cs}\sqrt{g/h}$ along propagation distance r_{cs}/h with the leading wave period T_{cs1} shown in red and the second wave period T_{cs2} shown in green, (b) comparison of the measured versus the predicted values of the leading lateral wave period from Equation 133 and (c) comparison of the measured versus the predicted values of the second lateral wave period from Equation 135 with noted 30% and 50% error thresholds.

6.2.9 Lateral Wave Celerity

The celerity of the lateral tsunami wave is measured between the runup gauges on the hill slope as the wave propagates. The wave crest and trough velocities are independently measured to better understand the speed difference between the wave crest and the wave trough. The lateral wave speed of the first wave on the planar hill slope is measured in the propagation distance range of $0 < r/h < 25$ and the range of the second wave is truncated by reflections to be measured in the range of $0 < r/h < 20$. The leading wave crest celerity on the planar hill slope is in the range $0.40 < c_{cr1}/\sqrt{gh} < 1.05$ and the leading trough is in the range $0.4 < c_{tr1}/\sqrt{gh} < 0.95$. The celerity of the second wave on the planar hill slope is in the range of $0.35 < c_{cr2}/\sqrt{gh} < 0.75$ for the crest and $0.30 < c_{tr2}/\sqrt{gh} < 0.75$. The speed of the second wave is on average 25% less than the first wave, which is slightly more than the 15% decrease observed by Mohammed (2010) but both celerity lags are in the range observed in dispersive trailing waves. The lateral wave celerities of the first two waves on the planar hill slope are shown in **Figure 96** and compared to the solitary wave celerity based on the basin water depth h shown with the dashed line.

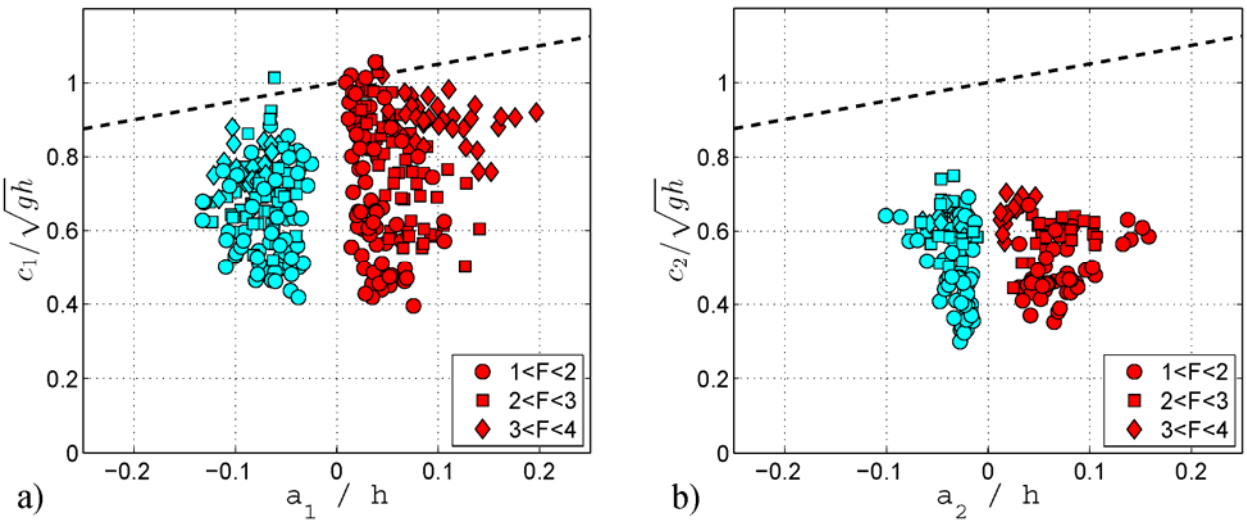

Figure 96: Lateral wave celerity on the planar hill slope of the runup crest (red) and trough (cyan) for the (a) first wave and (b) second wave. Solitary wave celerity is shown with the dashed line.

The evolution of the lateral wave celerity on the planar hill slope as a function of the propagation distance is shown in **Figure 97**. The wave velocity initially increases with the propagation distance and then levels off. The leading wave crest is generally faster than the leading wave trough and second wave crest which leads to the wave length increasing with the propagation distance.

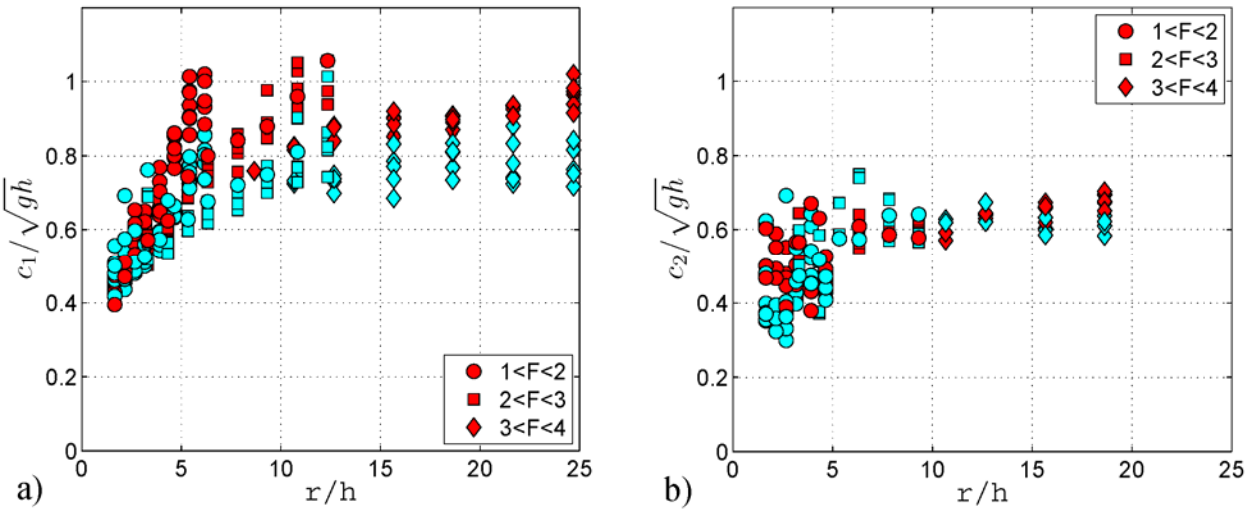

Figure 97: Lateral wave celerity evolution on the planar hill slope of the (a) first wave c_1 and (b) second wave c_2 with the measured crest celerity (red) and measured trough celerity (cyan). Solitary wave celerity is shown with the dashed line.

On the convex conical hill slope the lateral wave celerity exhibits similar trends as on the planar hill slope. The wave speed of the lateral waves on the convex conical hill slope are measured in the propagation distance range of $0 < r_{cs}/h < 50$. The leading wave crest celerity on the convex conical hill slope is in the range $0.2 < c_{cs-cr1}/\sqrt{gh} < 1.05$ and the leading trough is in the range $0.2 < c_{cs-tr1}/\sqrt{gh} < 1.0$. The celerity of the second wave on the conical hill slope is in the range of $0.2 < c_{cs2}/\sqrt{gh} < 0.9$ for the crest and trough. The speed of the second wave is on average 11% less than the first wave, corresponding to a reduced celerity lag of the second wave

compared to the planar hill slope. **Figure 98** shows the lateral wave celerity of the crest and trough for the first two waves on the convex conical hill slope.

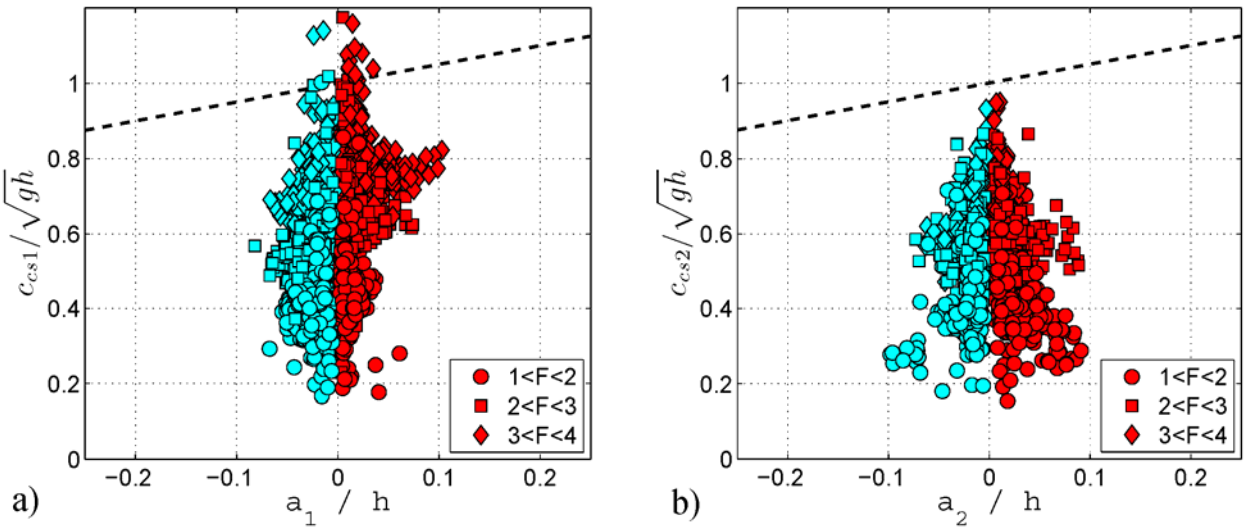

Figure 98: Lateral wave celerity on the convex conical hill slope of the runup crest (red) and trough (cyan) for (a) first wave c_{cs1} and (b) second wave c_{cs2} generated with gravel and cobble landslides. Solitary wave celerity is shown with the dashed line.

The lateral wave celerity evolutions of the first and second wave on the convex conical hill slope are shown in **Figure 99**. The lateral crest celerity is generally larger than the trough celerity on the conical hill slope, but the delineation between the wave crest and trough velocities on the conical hill slope is weaker compared to the planar hill slope shown in **Figure 97**.

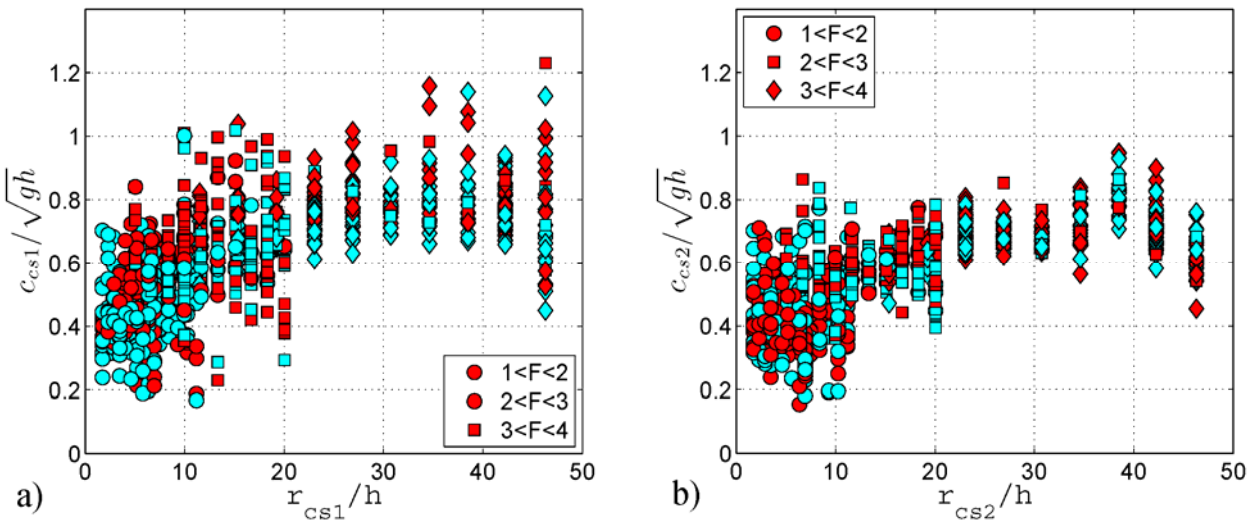

Figure 99: Lateral wave celerity evolution on convex conical hill slope of the (a) first wave c_{cs1} and (b) second wave c_{cs2} with the measured crest celerity (red) and trough celerity (cyan). Solitary wave celerity is shown with the dashed line.

6.2.10 Lateral Wave Length Prediction

The lateral wave length, L, is determined by multiplying the wave period by the wave celerity at a wave gauge which is given as

$$\frac{L}{h} = \frac{c}{\sqrt{gh}} T \sqrt{\frac{g}{h}} \tag{137}$$

The wave length of the leading lateral tsunami wave is measured on the planar hill slope in the propagation distance range of $0 < r/h < 25$ and measured wave length is in the range of $2 < L_1/h < 20$. The evolution of the first lateral tsunami wave length follows:

$$\frac{L_1}{h} = k_{L1}\left(\frac{r}{h}\right)^{0.3} \tag{138}$$

where k_{L1} is given in Chapter 5 as

$$k_{L1} = 4.3\ \mathrm{F}^{0.22} S^{0.06} L^{0.03} \tag{139}$$

with a correlation coefficient of $r^2 = 0.95$. The measurable propagation distance of the second lateral wave length was truncated by the reflected wave, but was measured in the range of $0 < r/h < 20$ with a wave length of $2 < L_2/h < 8$. The evolution of the second lateral wave length with an r^2 correlation coefficient of 0.61 is given by:

$$\frac{L_2}{h} = k_{L2}\left(\frac{r}{h}\right)^{0.3} \tag{140}$$

where k_{L2} is given in Chapter 5 as

$$k_{L2} = 2.0\ \mathrm{F}^{0.22} S^{0.04} L^{0.07} \tag{141}$$

The poor correlation coefficient for the second lateral wave length on the planar hill slope is due to the small range of values.

The evolution of the normalized wave length with propagation distance on the planar hill slope and the comparison of the measured to the predicted values of the normalized lateral wave length are shown in **Figure 100**.

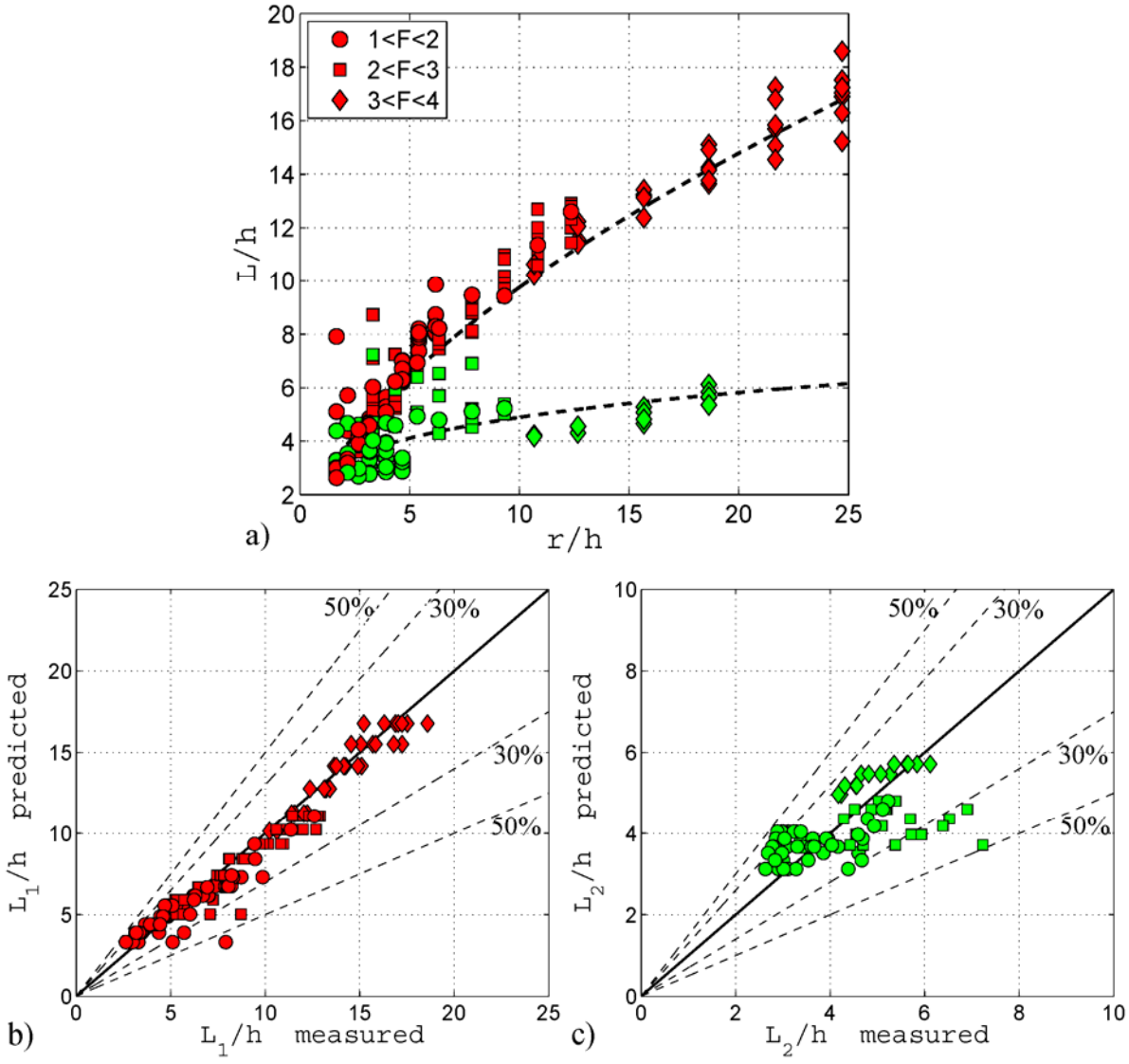

Figure 100: Lateral tsunami wave length on the planar hill slope: (a) L/h for the first wave (red) and the second wave (green) along propagation distance r/h, comparison of the measured versus the predicted values for (b) the first wave length L_1/h using Equation 138 and (c) the second wave length L_2/h using Equation 140 with noted 30% and 50% error thresholds.

Similar lateral wave length results are observed on the conical hill slope as the planar hill slope. The wave length of the first two lateral tsunami waves are measured on the convex conical hill slope in the propagation distance range of $0 < r_{cs}/h < 50$. The measured first wave length is in

the range of $2 < L_{cs1}/h < 22$ and the second wave length is in the range of $2 < L_{cs2}/h < 10$. The evolution of the first lateral tsunami wave length follows:

$$\frac{L_{cs1}}{h} = k_{L_{cs}1}\left(\frac{r_{cs}}{h}\right)^{0.3} \tag{142}$$

where $k_{L_{cs}2}$ is given in Chapter 5 as

$$k_{L_{cs}1} = 4.3\ \mathrm{F}^{0.22} S^{0.06} L^{0.03} \tanh(R_c^{0.1}) \tag{143}$$

with a correlation coefficient of $r^2 = 0.94$. The form of $k_{L_{cs}1}$ allows for a reduction in the planar generation function. The evolution of the second lateral wave length with an r^2 correlation coefficient of 0.89 is given by:

$$\frac{L_{cs2}}{h} = k_{L_{cs}2}\left(\frac{r_{cs}}{h}\right)^{0.25} \tag{144}$$

where $k_{L_{cs}2}$ is given in Chapter 5 as

$$k_{L_{cs}2} = 2.0\ \mathrm{F}^{0.22} S^{0.04} L^{0.07} \coth(R_c) \tag{145}$$

The evolution of the normalized wave length with propagation distance on the convex conical hill slope and the comparison of the measured to the predicted values of the normalized lateral wave length are shown in **Figure 101**.

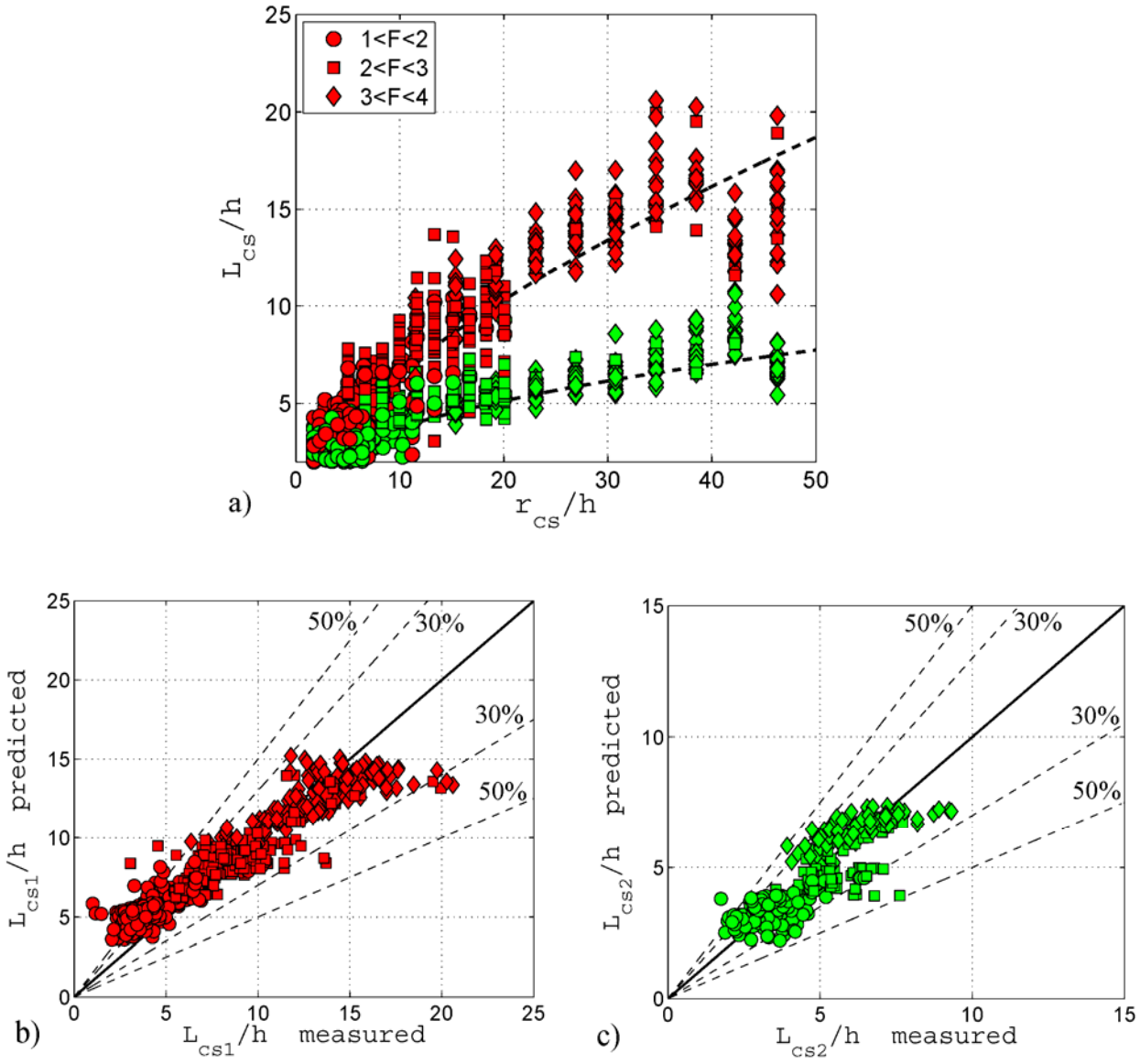

Figure 101: Lateral tsunami wave length on the convex conical hill slope: (a) L_{cs}/h for the first wave (red) and the second wave (green) along propagation distance r/h, comparison of the measured versus the predicted values for (b) the first wave length L_{cs1}/h using Equation 142 and (c) the second wave length L_{cs2}/h using Equation 144 with noted 30% and 50% error thresholds.

6.2.7 Edge Wave Dispersion Relationship

The wave length and the celerity of the first and second wave on the planar hill slope corresponds to the zeroth mode of the edge wave dispersion relationship on a sloping plane beach given by Ursell (1952) as

$$\omega^2 = g k_y \sin(2n+1)\,\alpha \tag{146}$$

with n=0 for the zeroth mode, wave frequency ω, lateral wave number k_y and hill slope angle α. A comparison of the measured first and second waves' frequencies and wave numbers with the zeroth mode edge wave dispersion relationship is shown in **Figure 102a**. The lateral waves on the planar hill slope match the first mode of the edge wave dispersion relationship with an r^2 correlation coefficient of 0.97 for the first and 0.91 for the second wave. A comparison of the measured nondimensionalized celerity and frequency with the nondimensionalized zeroth mode edge wave dispersion relationship is shown in **Figure 102b**. The lateral wave measurements where $\omega/\sqrt{g/h} < 0.4$ corresponds to measured wave lengths in the range $12 \leq L/h \leq 19$, which approaches the linear shallow water wave criteria of $L/h \geq 20$. These small frequency measurements are observed in **Figure 102b** deviating from the edge wave dispersion relationship and asymptotically approaching the non-dispersive linear shallow water wave celerity, $c/\sqrt{gh} = 1$. The maximum celerity of a solitary wave without breaking is $c/\sqrt{gh} \leq 1.39$. Hence celerity values greater than the breaking limit are not observed for gravity driven waves.

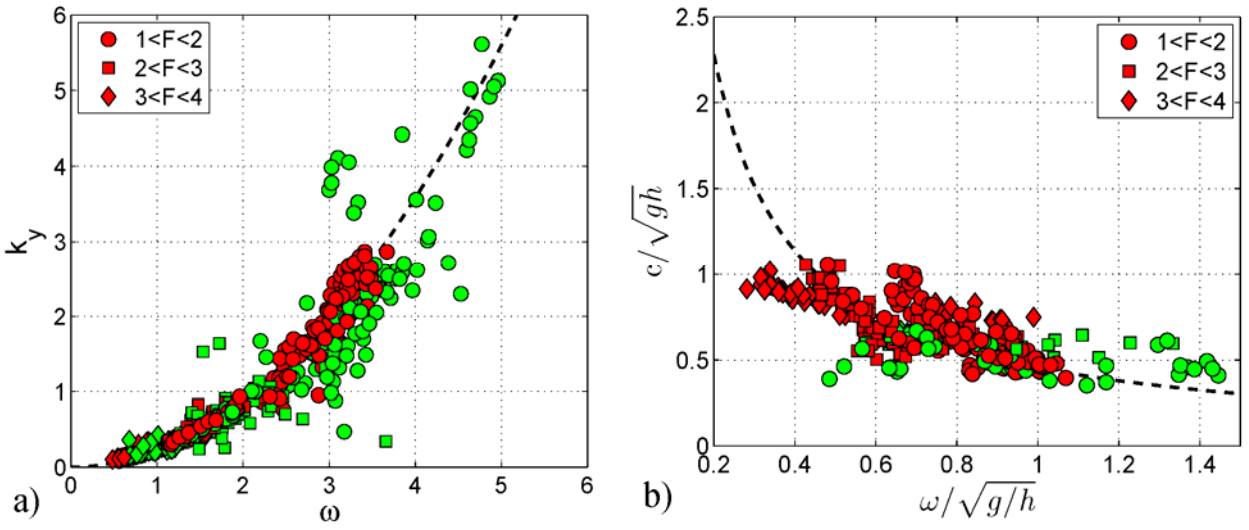

Figure 102: Planar edge wave dispersion relationship: (a) Tsunami wave frequency ω on a plane hill slope for the first wave (red) and the second wave (green) versus wave number k_y compared with the zeroth mode of the Ursell (1952) dispersion relation, (b) Normalized tsunami wave frequency $\omega/\sqrt{g/h}$ of the first wave (red) and the second wave (green) versus normalized celerity $c/\sqrt{gh}$ compared with the zeroth mode of the Ursell (1952) dispersion relation.

Smith and Sprinks (1975) obtained the asymptotic zeroth mode edge wave dispersion relationship on a curvilinear shoreline using long wave theory as

$$\omega^2 = \frac{g k_y}{4\,\pi^2} \tan\,\alpha \left(1 - \frac{1}{4}\left(k_y r_c\right)^{-1}\right)^2 \tag{147}$$

where k_y is the lateral wave number, r_c is the shoreline radius and α is the beach slope. The edge wave dispersion relationships for the planar and conical island slopes produce similar results with differences only appearing in the very low frequencies.

The leading lateral wave number, frequency and celerity on the convex conical hill slope are compared to the planar lateral edge wave dispersion relationship (Ursell, 1952) and the convex conical hill slope long wave edge wave dispersion relationship (Smith and Sprinks, 1975) in **Figure 103**.

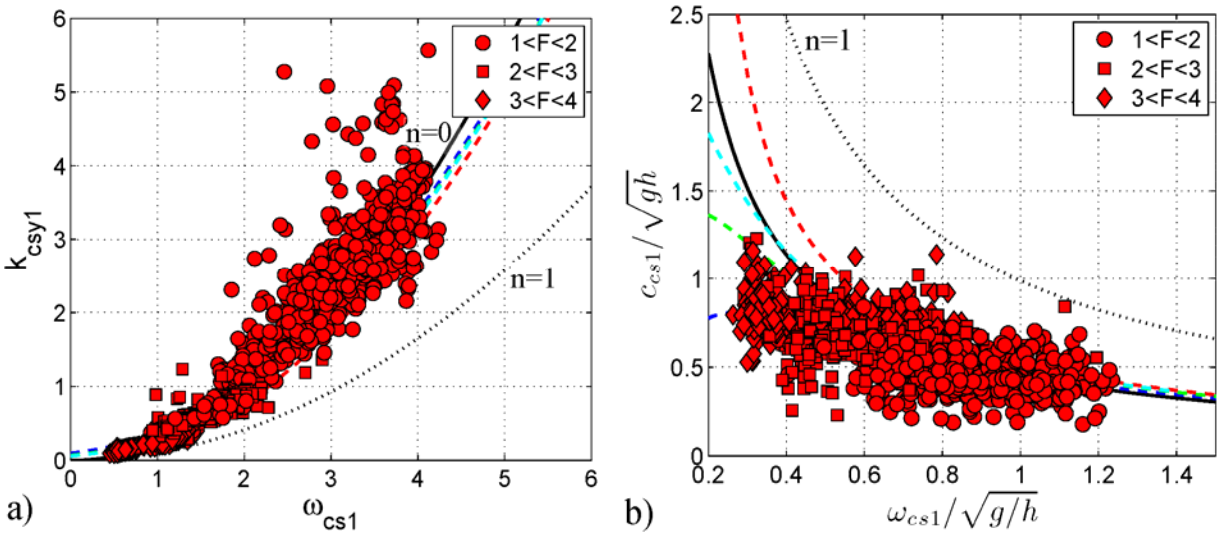

Figure 103: Convex conical edge wave dispersion relationship: (a) Leading wave frequency ω on a convex conical hill slope versus wave number k_y (b) Normalized leading tsunami wave frequency $\omega/\sqrt{g/h}$ versus normalized celerity $c/\sqrt{gh}$. Planar edge wave dispersion relationship (Ursell, 1952) is the black lines (zeroth mode-solid and first mode-dotted). The convex conical edge wave dispersion relationship (Smith and Sprinks, 1975) is shown with blue, red, green and cyan dashed lines for the basin water depths h = 1.2, 0.9, 0.6 and 0.3 m, respectively.

Although the Ursell (1952) lateral edge wave dispersion relationship was derived for a plane hill slope, it is applied to the convex conical hill slope to investigate the rigidity of the equation. The first wave corresponded to the zeroth mode of the dispersion relationship with an r^2 correlation coefficient 0.94. Unlike the planar hill slope, the second wave on the convex conical hill slope poorly matched all modes of the edge wave dispersion relationship and produced an r^2 correlation coefficient of 0.44 with the zeroth mode. The convex conical hill slope edge wave dispersion relationship from long wave theory (Smith and Sprinks, 1975) matched the lateral wave data with an r^2 correlation of 0.94 for the leading wave and 0.44 for the second wave, which are the same correlation coefficients determined using the analytical solution from Ursell (1952). As observed on the planar hill slope, the waves with small frequencies $\left(\omega/\sqrt{g/h} \leq 0.4\right)$ correspond to wave lengths in the range $12 \leq L/h \leq 21$, and become asymptotic to the linear shallow water wave celerity, $c/\sqrt{gh} = 1$.

The dimensionless lateral wave celerity and frequency shown in **Figure 103b** displays the sensitivity of the convex conical hill slope edge wave dispersion relationship to the island radius. The planar lateral edge wave dispersion relationship appears to be robust and applicable to the convex conical hill slope. Romano et al. (2013) similarly observed a good correlation between the zeroth mode edge wave relationship to their lateral wave characteristics on a conical island and concluded that the Ursell (1952) planar lateral edge wave dispersion relationship (Equation 146) was a reliable tool to estimate the first tsunami wave celerity a planar or convex conical coast.

6.3 Opposing Hill Slope Runup

6.3.1 Maximum Runup and Wave Refraction

The maximum wave runup on an opposing hill slope was studied in the fjord scenario with the instrumentation bridge positioned adjacent to the runup slope as shown in **Figure 104**. The two-dimensional solitary wave predictive runup equations of Equation 41 from Hall and Watts (1953) and Equation 42 from Synolakis (1987) were applied using the measured leading wave crest to calculate the maximum runup height. Adjusting the original equations to the current study's variables with $H = a_c$ for solitary waves, the Hall and Watts (1953) and Synolakis (1987) runup equations respectively become

$$\frac{R_u}{h} = 3.05 \tan(\alpha)^{-0.13} \left(\frac{a_c}{h}\right)^{1.15 \tan(\alpha)^{0.02}} \tag{148}$$

$$\frac{R_u}{h} = 2.831\ (\cot\alpha)^{1/2}\ \left(\frac{a_c}{h}\right)^{5/4} \tag{149}$$

where α is the runup hill slope angle and a_c is the wave crest amplitude measured before the runup on the opposing hill slope. The derivation of Equation 149 requires $(a_c/h)^{1/2} \gg 0.288 \tan\alpha$ and the wave to be non-breaking. Synolakis (1987) determined the wave non-breaking criteria as $a_c/h < 0.479\ (\cot\alpha)^{-10/9}$. Applying the runup hill slope angle from this experiment, the applicable dimensionless wave crest amplitude range for Equation 149 becomes: $0.022 \ll a_c/h < 0.227$. Approximately 1/3 of the wave crest amplitude measurements are less than the minimum crest amplitude requirement, but these measurements were still applied to the equation. The three largest wave heights exceeded the maximum crest amplitude due to the runup breaking limit.

The wave height was measured with a resistance wave gauge positioned 0.09 m in front of the opposing hill slope. The runup height was measured with a hybrid system using runup resistance gauges and overlapping cameras recording the runup slopes. A diagram of the camera, wave and runup gauges is shown in **Figure 104**.

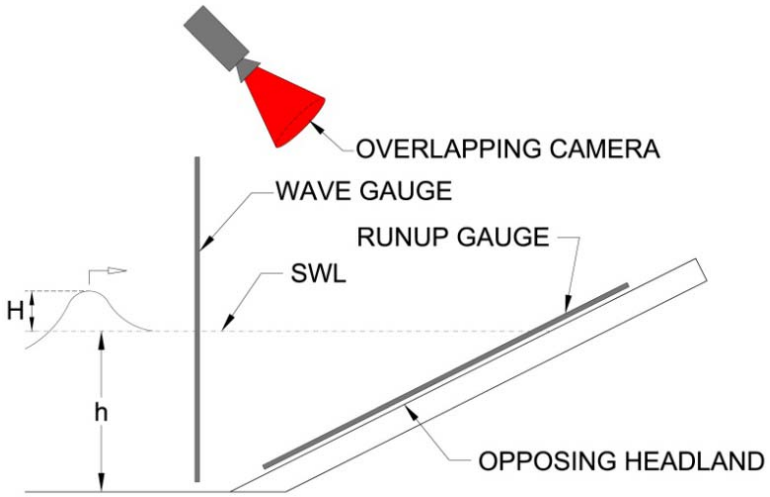

Figure 104: Instrumentation used to measure the incident wave and runup heights

The first wave crest of a landslide generated tsunami is created by the initial water displaced by the landslide impact resulting in a positive leading N-wave with the rise of the first crest being similar to a solitary wave. The celerity from the first wave crest in 2D and 3D physical models is mostly comparable to solitary wave theory (Mohammed, 2010). Since Equations 148 and 149 are derived for solitary waves, only the leading wave crest amplitude was applied to the equations and the subsequent wave trough was not considered. **Figure 105** shows the measured versus predicted runup using the Hall and Watts (1953) and Synolakis (1987) equations and both have a correlation coefficient $r^2 = 0.992$. The different colored nodes indicate the data collected at different incident wave ray angles as seen in **Figure 106**.

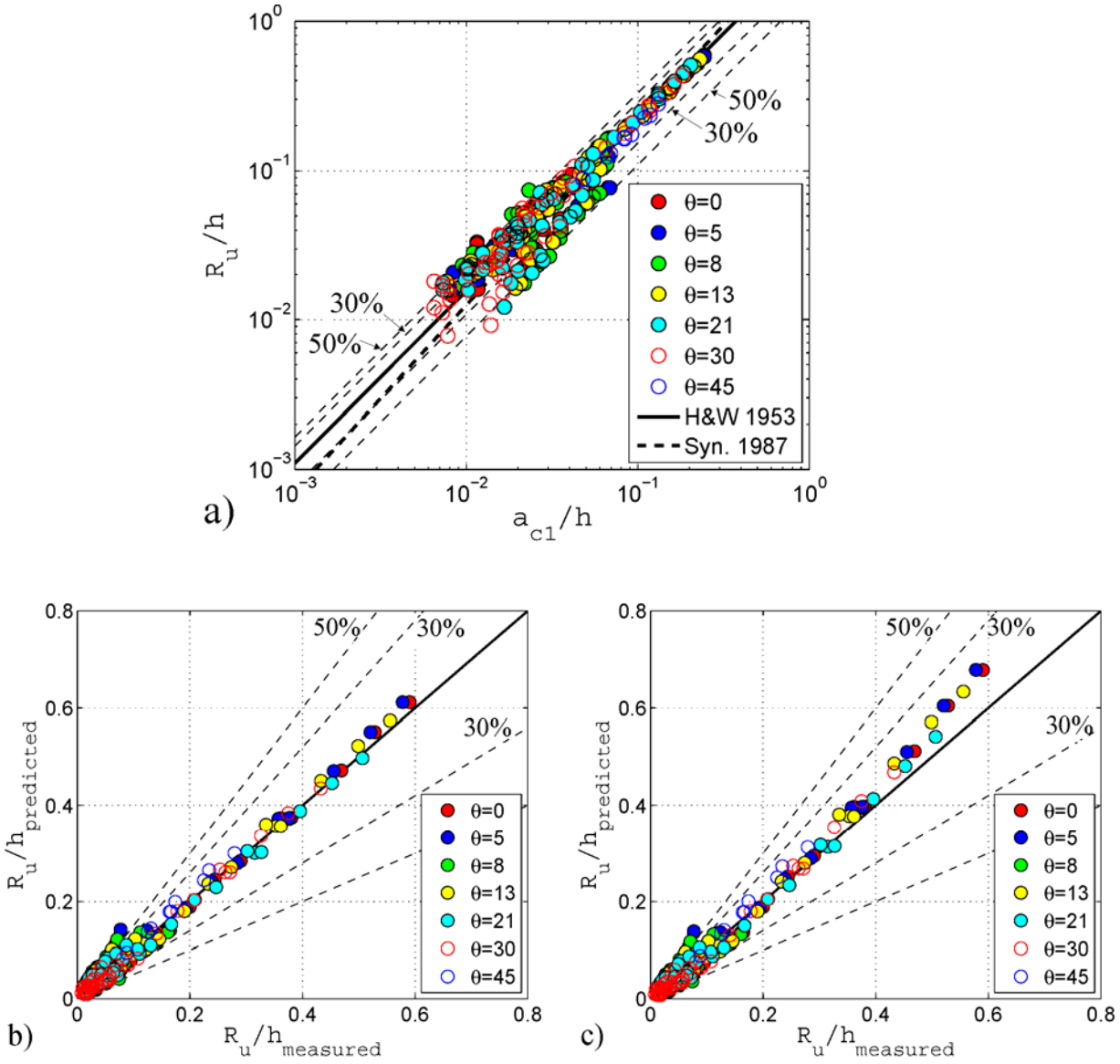

Figure 105: Wave runup for the first wave crest: (a) Runup versus wave height and comparing Hall and Watts (1953) and Synolakis (1987), (b) measured versus Hall and Watts (1953) predicted runup with Equation 148 and (c) measured versus Synolakis (1987) predicted runup with Equation 149.

The predicted runup in **Figure 105c** shows an over prediction of the runup for the larger wave heights. The largest 3 wave height and runup measurements exceeded the non-breaking runup criteria for Equation 149. Sælevik et al. (2013) observed an over prediction of the wave runup height using Equation 149 compared to his physical model and noted that the

dimensionless wave height in his model exceeded the breaking runup criteria. The runup height over prediction may be observed in the experimental data comparison of Synolakis (1987) when the wave height approaches the breaking runup criteria .

Angular dependence is not apparent for the first wave crest with incident angles less than 45˚. The lack of angular dependency may be attributed to wave refraction. The celerity was estimated for each centimeter change in water depth on the opposing hill slope using the linear shallow water wave celerity equation, $c = \sqrt{gh}$, and the Boussinesq nonlinear shallow water wave celerity equation, $c = \sqrt{gh}[1 + a/(2h)]$, where *c* is the celerity, *g* is the gravitational constant, *h* is the water depth and *a* is the wave crest amplitude. The wave crest amplitude, *a,* applied to the nonlinear celerity equation was measured at the toe of the slope and treated as a constant. These celerity estimates were applied to Snell's Law to estimate the wave refraction. Snell's Law is given as:

$$\frac{\sin(\theta_1)}{C_1} = \frac{\sin(\theta_2)}{C_2} \tag{150}$$

where the θ is the wave ray angle and C is the wave celerity.

The refraction was calculated for each of the water depths. The calculated angle at the still water level for the minimum and maximum water depths *h* = 0.3 and 1.2 m are shown in **Table 12**. The most obliquely estimated wave ray angle at the still water level was 19.9˚ using the nonlinear shallow water wave celerity refracting from 45˚ in the 0.30 m water depth. The wave refraction was qualitatively verified with the video recordings. **Figure 106** shows a diagram of the refraction of the wave rays as they approach the opposing hill slope based on the linear shallow water wave celerity.

Table 12: The wave ray angle at the still water level of the opposing hill slope caused by refraction

	Linear Celerity		Nonlinear Celerity	
Initial Angle	**Refracted angle at SWL (h=0.30 m)**	**Refracted angle at SWL (h=1.20 m)**	**Refracted angle at SWL (h=0.30 m)**	**Refracted angle at SWL (h=1.20 m)**
0˚	0˚	0˚	0˚	0˚
5˚	0.9˚	0.5˚	3.1˚	1.2˚
13˚	2.6˚	1.2˚	7.9˚	2.9˚
21˚	3.8˚	1.9˚	12.0˚	4.4˚
30˚	5.2˚	2.6˚	16.0˚	5.3˚
45˚	7.4˚	-	19.9˚	-

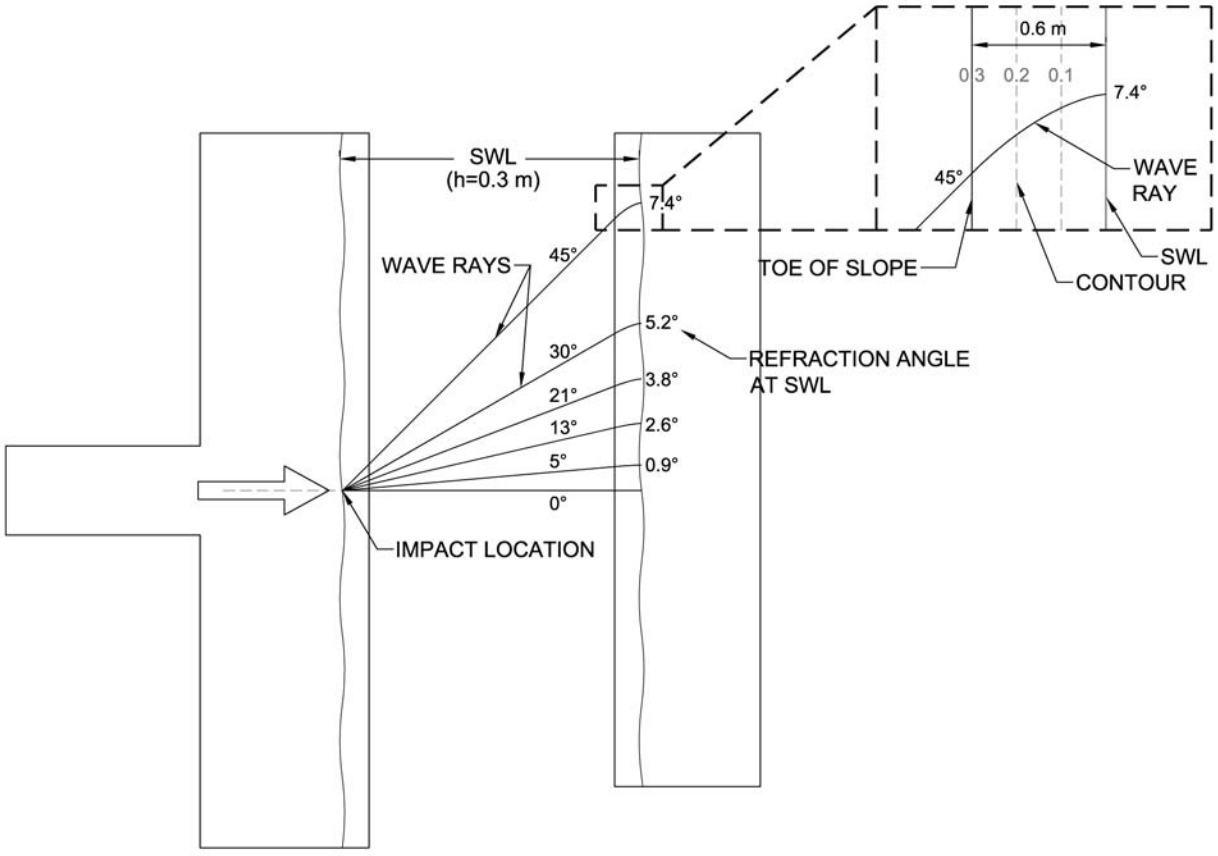

Figure 106: The calculated refracted wave rays from the impact source using the linear shallow water celerity approximation and Snell's Law.

The runup can be visually observed for qualitative analysis in **Figure 107**. The curved features of the center ceiling light reflections on the water surface appear to show wave refraction during the leading wave propagation and runup.

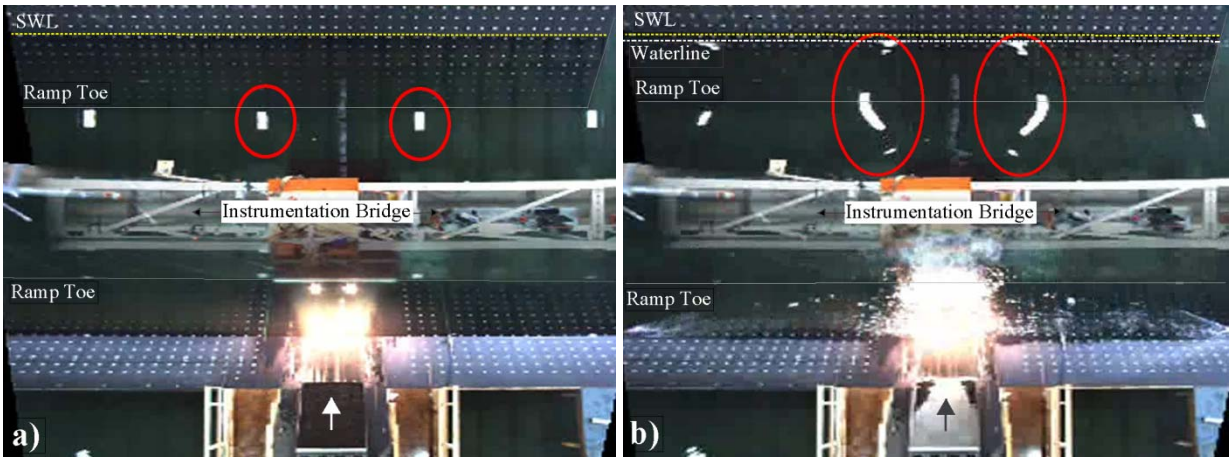

Figure 107: Wave refraction visual observation in the center light reflections: Images merged from two overhead ARGUS cameras focused on the fjord scenario were taken (a) prior to the landslide launch and (b) after the leading wave propagates and runs up the opposing hill slope ($t\sqrt{g/h}$ = 38.6).

6.3.2 Maximum Runup Prediction

The maximum runup is mostly independent on the wave ray angle running up the opposing hill slope, as observed in **Figure 105**, and the runup of the second wave was poorly described by Equations 148 and 149. In order to apply these equations to determine the maximum wave runup, the first wave needs to be larger than the second wave at the point of runup. Mohammed and Fritz (2012; 2013) empirically derived the equations for the first and second wave amplitudes as

$$\frac{a_{c1}}{h} = 0.31\, F^{2.1} S^{0.6} \left(\frac{r}{h}\right)^{-1.2\, F^{0.25} S^{-0.02} B^{-0.33}} \cos\theta \qquad (151)$$

where F is the landslide Froude number $F = v_s/\sqrt{gh}$, S is the relative slide thickness $S = s/h$, B is the relative slide width $B = b/h$, r/h is the relative distance from the landslide impact and θ is the angle from the landslide impact. In Section 5.2 Wave Amplitude Attenuation the second wave crest amplitude is given as

$$\frac{a_{c2}}{h} = 0.9 F^{0.7} S^{0.6} B^{-1} L^{-0.5} \left(r/h\right)^{-1.7 F^{-1} B^{-0.2} L^{-0.4}} \cos^2\theta \qquad (152)$$

where L is the relative landslide length $L = V_s/(bsh)$ and the remaining parameters are previously noted.

Equation 151 predicted the first wave crest amplitude before running up the opposing hill slope with an r^2 correlation coefficient of 0.93. The measured versus predicted leading wave crest amplitude is shown in **Figure 108**.

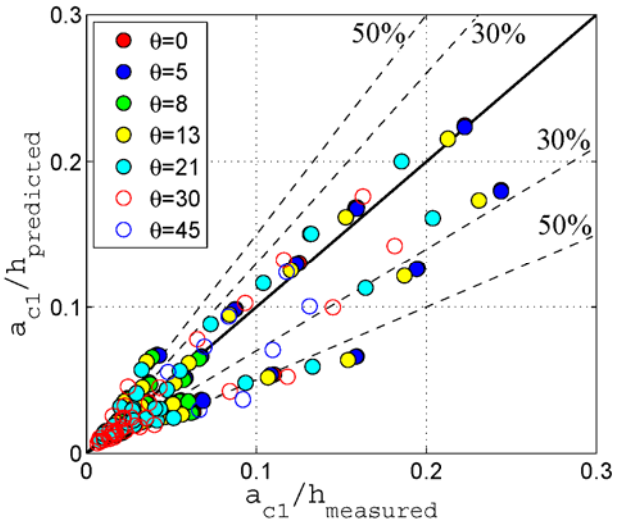

Figure 108: Measured versus predicted leading wave crest amplitude using Equation 151 at different angles from the landslide impact prior to running up the opposing hill slope.

When the predicted leading wave crest amplitude from Equation 151 is applied to Equations 148 and 149, the predicted runup corresponds to the measured runup with an r^2 correlation coefficient of 0.93 for both equations. **Figure 109** shows the measured versus predicted runup heights using the predicted wave amplitude from Equation 151 in the runup prediction equations of Equations 148 and 149.

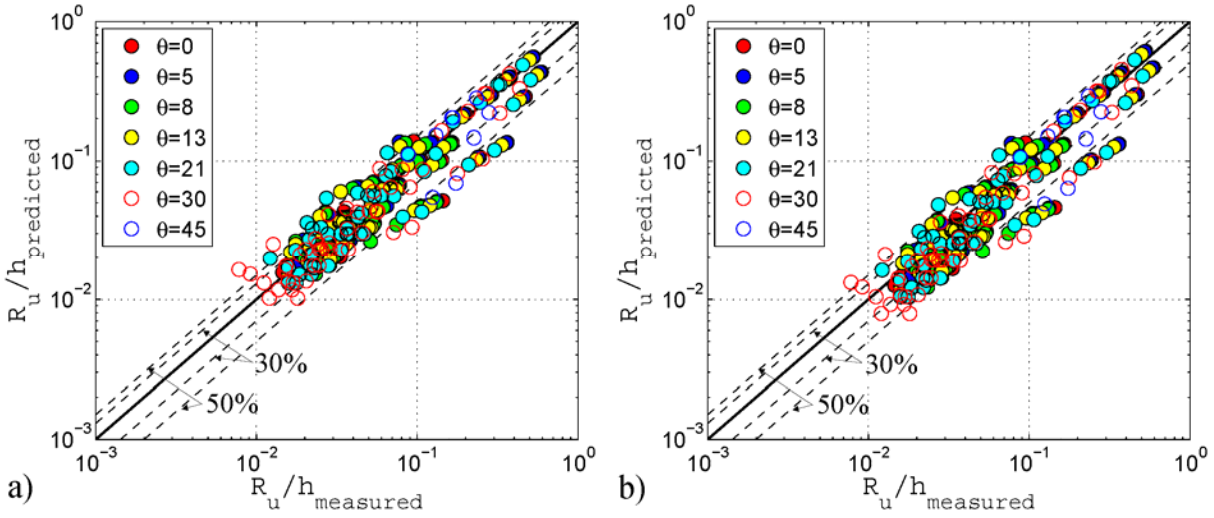

Figure 109: Runup prediction using the leading wave crest amplitude predictive equation by Mohammed and Fritz (2012) and the runup predictive equation of (a) Hall and Watts (1953) and (b) Synolakis (1987).

The first wave crest matches the solitary wave runup equations quite well because the first wave crest has many characteristics similar to a solitary wave. The runup of the second wave poorly corresponds to the solitary wave runup equations because the second wave runs up the opposing hill slope after the leading wave trough creates a shoreline rundown and a lateral wave is propagating in the long shore direction of the opposing hill slope further interfering with the wave runup of the second wave crest. When the first wave is larger than the second wave crest, the prescribed technique of combining the predictive equation of the first wave crest amplitude from Mohammed and Fritz (2012) with the predictive runup equations by Hall and Watts (1953) and Synolakis (1987), can be used to predict the maximum wave runup of an

attacking wave. Equations 151 and 152 can be combined to predict if the first wave will be larger than the second wave crest by knowing that $a_{c1}/a_{c2} > 1$. Dividing Equation 151 by Equation 152 produces:

$$\frac{a_{c1}}{a_{c2}} = 0.34\, F^{1.4}\mathrm{B}\,\mathrm{L}^{0.5}\left(\frac{r}{h}\right)^{\left(1.7F^{-1}B^{-0.2}L^{-0.4}\right)-\left(1.2\,F^{0.25}S^{-0.02}B^{-0.33}\right)}\frac{1}{\cos\theta} > 1 \qquad (153)$$

Once the first wave height is verified to be the largest using Equation 153, the wave height can be estimated using Equation 151 and inserted in to Equations 148 or 149 to estimate the maximum runup height. The first wave was the largest in 41% of the cases tested.

6.3.3 Runup Around a Curved Headland

Topographic and bathymetric features can significantly influence the wave characteristics like the incident wave amplitude and subsequent runup. The opposing hill slope of the fjord scenario was modified to become the more complex topographic scenario of a curved headland as shown in **Figure 110**. The great landslide generated tsunami in Lituya Bay, Alaska in 1958 produced a maximum runup of 524 m on a similar curved headland (Miller, 1960; Fritz et al., 2001; Fritz et al., 2009).

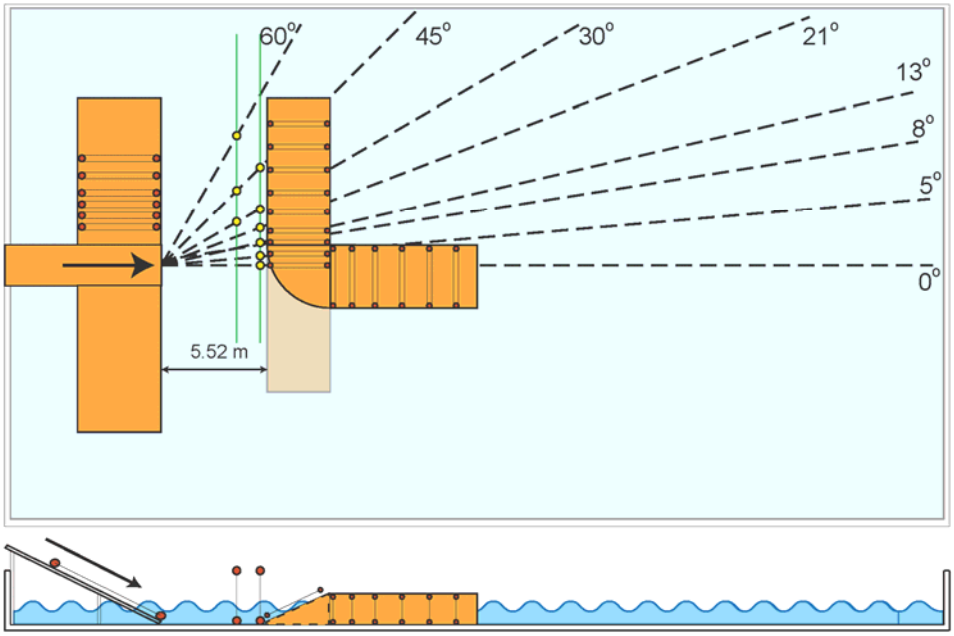

Figure 110: Experimental scenarios of the curved headland scenario with a 90° bend in the opposing hill slope and the superimposed straight opposing hill slope of the fjord scenario.

The wave characteristics in the fjord and curved headland scenarios have been analyzed to compare the wave energy containment between the two scenarios. The maximum runup on the opposing hill slope of the fjord and curved headland scenario are compared in **Figure 111**. The maximum runup was on average 10% larger in the fjord than in the curved headland scenario. The larger wave runup in the fjord scenario is due to the fjord completely trapping the wave energy between the two opposing hill slopes while the curved headland scenario partially leaks the wave energy outward. The fjord contains the wave energy and reflects the waves between the opposing slopes while funneling them through the channel. The curved headland scenario contains part of the wave energy and radiates the rest into the open basin.

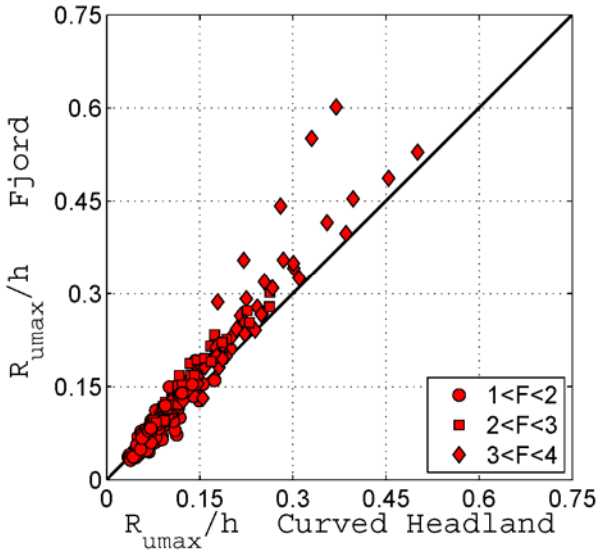

Figure 111: Maximum runup on the opposing hill slope for the fjord and curved headland scenarios.

The differences in the wave energy containment due to the topographic and bathymetric features can be observed in the wave profiles measured by the runup wave gauges on the lateral and opposing headland hill slopes. **Figure 112** shows the runup gauge recordings on the lateral and opposing hill slope of tsunami waves generated by a gravel landslide with landslide Froude number of F=2.3 and dimensionless landslide volume of V=3.5. In the absence of an opposing hill slope or topographic structures, the wave propagates outward and radiates wave energy away from the generation source. The presence of an opposing hill slope contains the wave energy near the generation source and reflects the waves between the opposing hill slopes. The reflected waves from the opposing hill slope can either amplify or reduce the wave amplitude and runup. The superposition of the reflected waves with the initially generated wave train produces complex wave patterns.

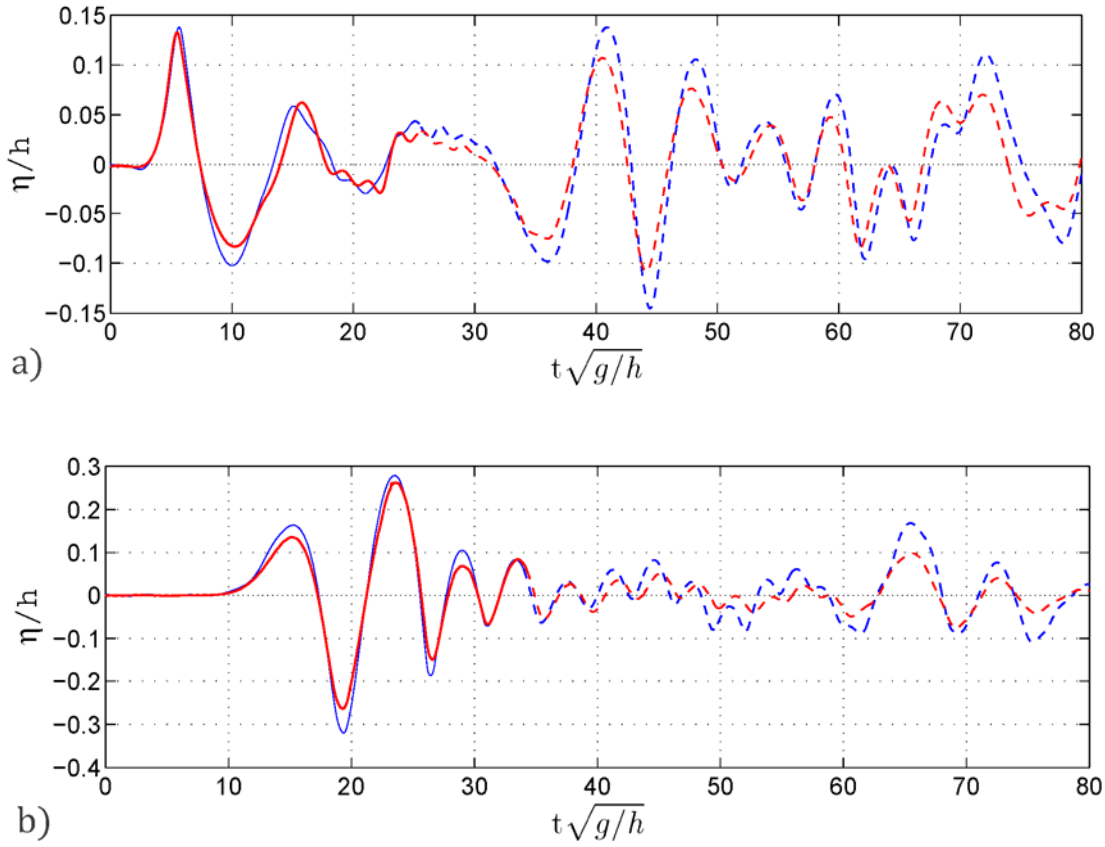

Figure 112: Runup wave profiles measured in the fjord scenario (blue) and the curved headland scenario (red) with waves generated by a gravel landslide with landslide Froude number F=2.3 and dimensionless slide volume V=3.5 for (a) lateral runup gauge at r/h = 3.3 and (b) opposing hill slope runup gauge at r/h = 13.2 and θ = 8°. Solid lines show the valid wave recording and the dashed lines are the wave recording with interference from the hill slope edge reflection.

The wave train amplitude shown in the lateral runup gauge recording in **Figure 112a** initially decays until the third wave when the reflected waves from the opposing hill slope returns and an increased wave amplitude is observed. This increased amplitude coincides with the first seiching mode for the fjord cross section which is $T_{seich}\sqrt{g/h} = 34.3$. The wave crest amplitude of the fjord and curved headland match until the reflected wave interferes with the third wave and more significant differences in the wave amplitudes are observed due to the topographic features trapping the wave energy.

The opposing hill slope runup gauge in **Figure 112b** has maximum trough amplitude in the leading wave trough. The maximum crest amplitude is the second wave crest rather than the first wave crest as observed in the lateral runup gauge due to dispersion effects. The amplitude decays after the maximum in the wave train until the reflected waves return from the landslide hill slope. The runup amplitude increases when the reflected waves return and the amplitude difference between the two scenarios becomes more significant, similar to observations from the lateral runup gauges. The time between the initial waves arriving and the reflected wave returning is slightly more than the first mode of the seiching period, which was observed in the lateral hill slope runup gauge recording. This increased time could be due to the wave seiching calculation technique of Du Boys (1891), which only includes the distance between the still waterlines on the hill slopes while the additional runup distance beyond the still waterline is not included.

The great tsunami wave of Lituya Bay, Alaska in 1958 produced a maximum runup decay marked by the forest trimline on the curved headland similar to the physical model. The runup decay on the lee side of the curved headland in Lituya Bay and the physical model are shown in **Figure 113**. The runup decay on the opposing curved headland in the physical model is more gradual than observed in Lituya Bay. The curved headland in Lituya Bay has a narrower inner angle of land (~70°) compared to the model (90°) resulting in a wave overtopping effect with the noted steep runup decay on the lee side of the curved headland. Beyond the curved headland a gradual decay of the maximum runup is observed in both cases.

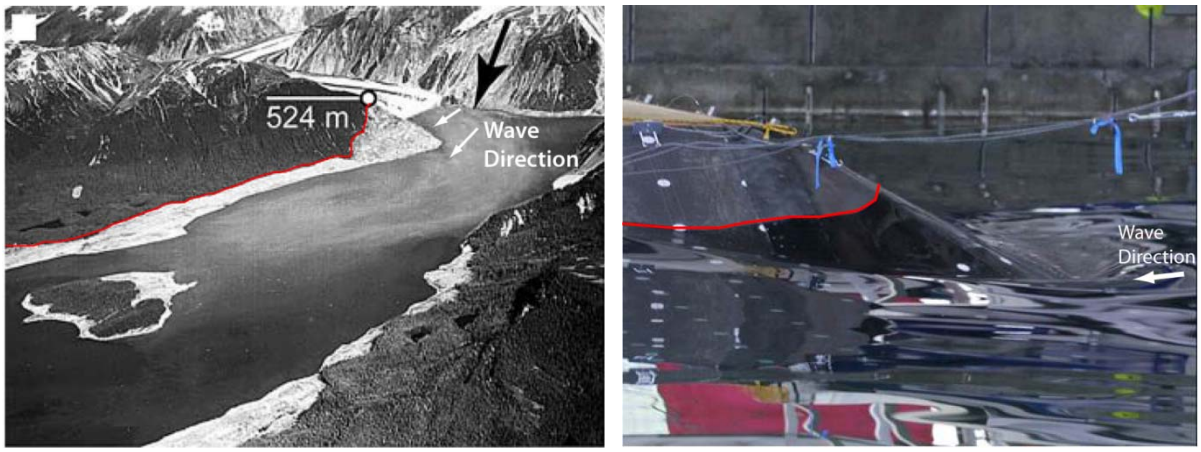

Figure 113: Maximum runup decay (—) around a curved headland on an opposing hill slope for (a) Lituya Bay, Alaska in 1958 (Figure modified from Fritz et al. (2009)) and (b) physical model (image mirrored about vertical axis for comparison.

6.4 Comparison to Field Events

6.4.1 Island Topography and Bathymetry

Froude similarity allows scaling the physical model up to prototype scale for comparison to recorded field cases and testing the models applicability to potential future events. The dimensionless shoreline radius ($R_c=r_c/h$) of the conical island scenario is compared to the approximate dimensionless radius of various islands on earth in **Table 13**. Each island shown in the table has previously produced landslide generated tsunamis or in the case of La Palma western flank is considered a significant landslide generated tsunami hazard for the Atlantic Ocean and the Eastern Seaboard of the United States. The radiuses of irregularly shaped islands were approximated as the average radius. The water depth was established as the depth at maximum landslide runout in historic or predicted events.

Table 13: Dimensionless island shoreline radius for various islands

Island	r_c (km)	h (m)	R_c	Source
Present Study	Varies	Varies	$2.2 < R_c < 14.7$	-
Mount St. Augustine volcano (USA)	5	20	250	Kienle et al., (1987)
O'ahu (USA)	26	4600	5.7	Moore et al. (1989)
Oshima-Oshima Island (Japan)	2	2000	1	Satake (2007)
Ritter Island (Papau New Guinea)	1	1000	1	Ward and Day (2003)
Krakatau volcano (Indonesia)	3.5	20	175	Yokoyama (1981)
Montserrat (British Territory – Caribbean)	6	1000	6	Watt et al. (2012)
Stromboli (Italy)	2	800	2.5	Romano et al., (2013)
La Palma (Canary Islands)	13	4000	3.3	Løvholt et al., (2008)

6.4.2 Chehalis Lake Landslide Tsunami, British Columbia, Canada (2007)

On 4 December 2007, a 3 Mm^3 (3 x 10^6 m^3) landslide impacted the northwest shore of Chehalis Lake in Fraser Valley, British Columbia, Canada. The landslide initiated as a rock mass which slid obliquely into a steep gulley, disintegrated into a debris avalanche and traveled approximately 800 m along slope towards the west shoreline of Chehalis Lake (Roberts et al., 2013). The maximum elevation drop from the head scarp to the lake surface corresponds to 550 m). The resulting tsunami produced runup heights larger than 30 m and caused damage as it propagated the length of the 9 km long lake. Post event surveys included data sets from field measurements, airborne LIDAR, SONAR and terrestrial photogrammetric data (Brideau et al., 2012; Lawrence et al., 2013; Roberts et al., 2013). A diagram of northern Chehalis Lake with measured runup heights and landslide scarp is shown in **Figure 114**.

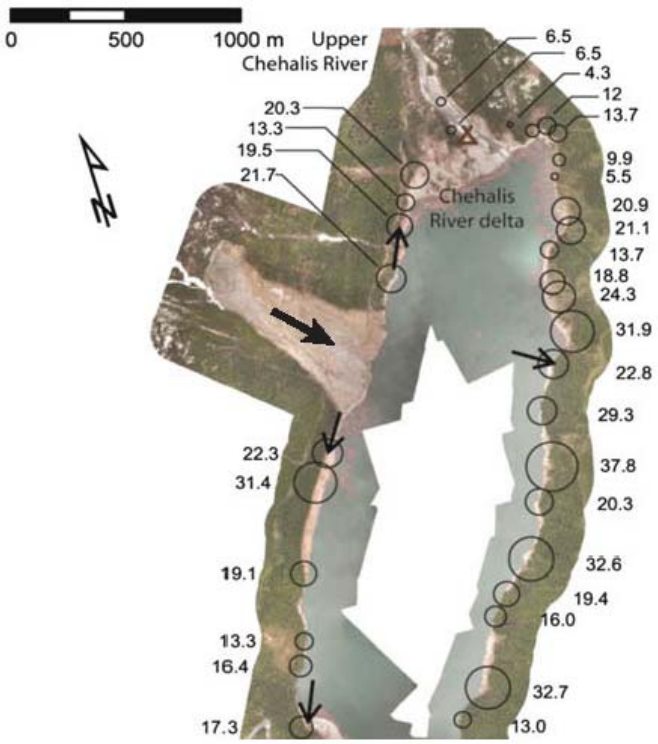

Figure 114: Overall view of the northern Chehalis Lake with field runup measurements superimposed on the orthophotograph mosaic (Figure modified from Roberts, et al.(2013)).

The post-failure topography of the landslide scarp was scanned with terrestrial LIDAR by Brideau (2012). The landslide hill slope angle was determined at impact as $\alpha = 40°$. The vertical drop from the initial static rock mass centroid to the water surface was measured as $\Delta z = 438$ m. The landslide width at impact was estimated by measuring the landslide scarp at the shore as $b = 485$ m. The opposing hill slope angle measurements using topography from the post-failure LIDAR scan were in the range $38° \leq \alpha_{opp} \leq 45$ with a mean value of $\alpha_{opp} = 41°$. The mean opposing hill slope angle was used in runup calculations. Brideau (2012) gave the landslide volume as $V_s = 3$ Mm^3 and the landslide material consisted predominately of quartz diorite with a rock density of $\rho_g = 2.7$ t/m^3, which is similar to the modeled grain density of $\rho_g = 2.6$ t/m^3

The initial static rock mass had a maximum thickness s = 40 m. For conservation of mass and energy, the impact slide thickness was adjusted to compensate for the bulk slide density changing from the solid rock density of ρ_g = 2.7 t/m^3 to the increased porosity disintegrated bulk slide density of ρ_s = 1.76 t/m^3. Additionally, the landslide follows the path of a natural gully into the lake which would induce a larger slide thickness in the center of the impacting landslide, similar to the maximum slide thickness in the centerline of the landslide of the physical model which was applied in the derivation of the predictive equations. The adjusted maximum slide thickness for conservation of mass is calculated as s = 59 m. The water depth is given by Roberts, et al.(2013) as h = 175 m.

The landslide Froude number F is the dominant parameter in the tsunami generation and typically requires estimating the landslide impact velocity v_s, which is controlled by the equivalent coefficient of friction f. In post-failure failure landslide studies, the equivalent coefficient of friction is defined as the maximum drop height divided by the maximum run-out length. Unlike the coefficient of friction, which is a material constant, the value of the equivalent coefficient of friction is a function of the total landslide volume. The equivalent friction was estimated using the friction to landslide volume relationship derived by Fritz (2002) as

$$\log f = 0.15666 \log V_s + 0.62419 \tag{154}$$

where f is the equivalent friction coefficient and V_s is the landslide volume in cubic meters (m^3). The calculated equivalent friction coefficient is f = 0.407, which is very similar the bed friction coefficient of f = 0.424 in the present laboratory study. The impact velocity can be calculated using the Newtonian laws of motion as

$$v_s = \sqrt{2g\,\Delta z(1 - f\cos\alpha)} \tag{155}$$

The calculated impact velocity is v_s = 75 m/s. A list of relevant landslide generated parameters is shown in **Table 14**.

Table 14: Landslide impact parameters

Parameter	Measurement
Landslide volume, V_s	3,000,000 m^3
Landslide centerline thickness, s	59 m
Landslide width, b	485 m
Landslide centroid vertical drop, Δz	438 m
Landslide Impact Velocity, v_s	67 m/s
Landslide hill slope angle, α	40°
Opposing hill slope angle, α_{opp}	41°
Water Depth, h	175 m

The parameters from **Table 14** have been nondimensionalized to be applied to the wave amplitude and runup predictive equations as shown in **Table 15**. The dimensionless landslide impact parameters are within the range of nondimensional parameters tested in the physical model and are similar to the parameters tested at the water depth h = 0.6 m. The approximate model to field scale ratio is 1:300.

Table 15: Dimensionless landslide impact parameters

Parameter	Value
Landslide volume, $V=V_s/h^3$	0.56
Landslide thickness, $S=s/h$	0.34
Landslide width, $B=b/h$	2.77
Landslide length, $L= V_s/(sbh)$	0.60
Landslide Froude number, $F = v_s/\sqrt{gh}$	1.60
Landslide hill slope angle, α	40°
Opposing hill slope angle, α_{opp}	41°

The measured maximum runup heights and locations are taken from Roberts, et al.(2013). The origin of the cylindrical coordinate system used is placed at the shoreline intersection with the impacting landslide centerline. The landslide impacts the water with an angle approximately 10° south of shore-normal and the landslide impact centerline defines θ = 0° in cylindrical coordinates. The maximum lateral wave runup measurements are first investigated using the maximum runup equations for a planar hill slope derived in Section 6.2 Lateral Wave Runup. The maximum runup in the landslide impact region is given as

$$\frac{R_{uI}}{h} = \frac{1}{4} F^{1.4} S^{0.7} B^{-0.5} V^{-0.1} \tag{156}$$

and the maximum runup outside the landslide impact region is given as

$$\frac{R_{um}}{h} = \frac{1}{4} F^{1.2} S^{0.4} B^{-1.1} V^{0.3} \tag{157}$$

where the location of the maximum runup outside the impact region is given as

$$\frac{r_{Rum}}{h} = \frac{4}{5} S^{-0.1} B^{1.25} \tag{158}$$

Using the dimensionless landslide parameters from **Table 15**, the maximum runup in the landslide impact region is R_{ul}/h = 0.144 or R_{ul} = 25 m. The maximum runup outside the landslide impact region is R_{um}/h = 0.078 or R_{um} = 14 m, and the location of the maximum runup outside of the impact region is $r_{Rum}/h = 3.18$ or $r_{Rum} = 557$ m. The predictive equation for the runup decay beyond the maximum was not applied because the lateral hill slope ends at the north shore of the lake shortly after the predicted maximum runup location. One maximum lateral runup measurement was recorded on each side of the landslide scarp within 557 m of the landslide centerline (predicted maximum lateral runup location). Both runup measurements were approximately 22 m, which is within the maximum runup range predicted.

The remaining maximum lateral runup measurements north of the landslide impact exceed the predicted values. The increased measured runup height north of the landslide is most likely due to the close proximity of the north end of the lake which reduces the water depth and confines the wave energy, resulting in increased wave runup. The lateral measured runup heights south of the landslide exceeded the predicted maximum runup values. This is most likely caused by the landslide impacting the water with an angle approximately 10° south of normal to the shoreline. This skewed impact transfers more wave energy south of the impact site. It is also uncertain whether the measured maximum runup heights were generated by the laterally propagating wave or from the reflected waves from the opposing side. The ratio of the distance between shorelines on opposing hill slopes, w, modeled in the fjord scenario to the water depth was in the range $8.5 < w/h < 23$. This ratio for Chehalis Lake where the landslide impacted the water is w/h = 4.75, making it significantly narrower than the fjord scenarios tested and prone to large reflected waves.

The maximum runup heights on the opposing hill slope were analyzed using the method described in Section 6.3.2 Maximum Runup Prediction. The runup procedure is for the runup of the first wave crest. The ratio of the first wave crest to the second wave should be greater than 1

for the maximum wave runup to be calculated with the first wave. The criteria and ratio of the first and second wave crest amplitudes is given as

$$\frac{a_{c1}}{a_{c2}} = 0.34\ F^{1.4}\mathrm{B}\ \mathrm{L}^{0.5}\left(\frac{r}{h}\right)^{\left(1.7F^{-1}B^{-0.2}L^{-0.4}\right)-\left(1.2\ F^{0.25}S^{-0.02}B^{-0.33}\right)}\ \frac{1}{\cos\theta} > 1 \qquad (159)$$

The seven measured maximum runup heights on the opposing hill slope within the range $-35° < \theta < 35°$ were compared to predicted values. The analyzed opposing hill slope measurements were limited to this spatial range given irregularities in the opposing hill slope. All a_{c1}/a_{c2} ratios calculated with Equation 159 were greatere than 1, meaning the runup from the first wave crest is predicted to generate the largest runup height.

To predicted runup on an opposing hill slope, the leading wave crest amplitude prior to running up the opposing hill slope is estimated by Mohammed and Fritz (2012) as

$$\frac{a_{c1}}{h} = 0.31\ F^{2.1}S^{0.6}\left(\frac{r}{h}\right)^{-1.2\ F^{0.25}S^{-0.02}B^{-0.33}}\ \cos\theta \qquad (160)$$

The wave amplitude is then applied the to the runup prediction equation given by Synolakis (1987) as

$$\frac{R_u}{h} = 2.831\left(\cot\alpha_{opp}\right)^{1/2}\ \left(\frac{a_c}{h}\right)^{5/4} \qquad (161)$$

where α_{opp} is the runup hill slope angle. The predicted runup heights match the measured values with an r^2 correlation coefficient of 0.55 and are compared in the **Figure 115**. Anomalies in the topographic and bathymetric features in opposing hill slope combined with the skewed landslide impact angle create variability in the measured runup on the opposing hill slope. Even with variability in the field measured runup heights, the predicted runup for the leading wave crest allows for a first order approximation of the maximum runup height.

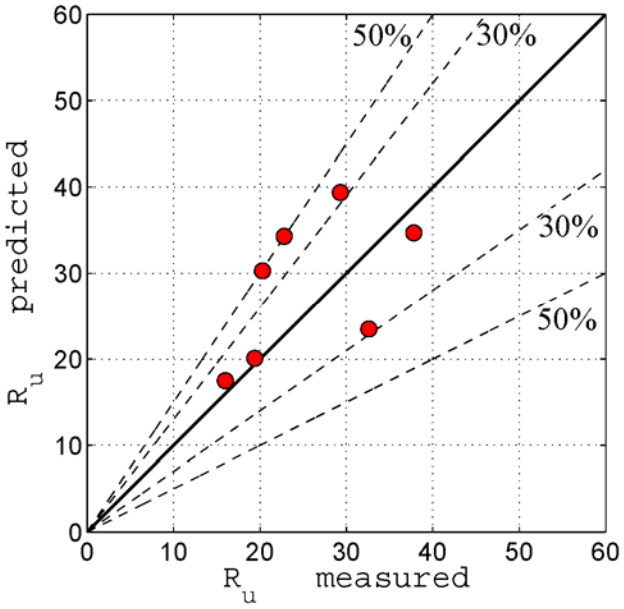

Figure 115: Measured versus predicted runup values on the opposing hill slope

CHAPTER VII

CONCLUSIONS

7.1 Summary

Landslide generated tsunamis were physically modelled with granular materials in various topographic and bathymetric scenarios based on Froude's similarity at the 3D NEES tsunami wave basin at Oregon State University. The scenarios modelled include basin-wide propagation and runup, fjord, curved headland and conical island scenarios. These scenarios fill a research gap by studying the effects of complex topography and bathymetry on the landslide generated waves. The effects of the lateral hill slope on the lateral and offshore propagating waves are analyzed between the planar hill slope used in the basin-wide propagation scenario and the convex conical hill slope of the conical island scenario. The effects of the landslide granulometry on the wave characteristics are studied in the conical island scenario with gravel and cobble landslide materials. Predictive equations for the offshore and lateral wave characteristics allow for a rapid tsunami hazard assessment of a potential landslide.

The wave characteristics are described by landslide impact properties like the landslide velocity v_s, thickness s, width b and landslide volume V_s, as well as the water depth h, and the radial and angular position (r,θ) to the landslide impact. The nondimensional parameters were tested on the planar and convex conical hill slopes in the ranges $1.05 < F < 3.85$, $0.08 < S < 0.46$ and $0.2 < V < 28$. The convex conical hill slope increased the lateral spreading of the landslide compared to the planar hill slope. The nondimensional landslide width on the planar hill slope was in the range of $1 < B < 7$. Minor differences were observed in the nondimensional landslide

width between the gravel with $1.4 < B < 11.7$ and cobble with $1.4 < B < 11.2$ on the convex conical hill slope. The nondimensional shoreline radius of the conical island was in the range $2.2 < R_c < 14.7$, which is comparable to real world events. The landslide Froude number F and relative slide thickness S are critical offshore wave generation parameters and B becomes an important parameter in the lateral wave generation. The dimensionless shoreline radius, R_c, connects the planar predictive equations to the convex conical hill slope of the conical island scenario.

The effects of the lateral hill slope on wave amplitudes are analyzed and the leading wave crest was on average 3% larger when generated on a planar hill slope than the convex conical hill slope, while the leading wave trough and second wave crest were both smaller. The wave amplitudes generated by cobble landslides were 11-25% larger for the first two waves than wave amplitudes generated by gravel landslides. The lateral hill slope and landslide granulometry showed essentially no effect on the offshore propagating wave period and wave length. The leading wave celerity generated by both landslide materials on planar and convex conical lateral hill slopes may be estimated by solitary wave theory. Between 0.5-11% of the landslide kinetic energy is converted to the leading wave crest and 1-24% is converted to the wave train. Landslides with highly supercritical landslide Froude numbers F and bulky relative slide thickness S, converted more energy into the leading wave crest. Minimal differences were observed in the gravel landslide energy conversion between the planar to convex conical hill slopes. The cobble landslides converted on average 31% more energy into the leading wave crest and 43% more energy into the wave train than the gravel landslides.

The lateral waves on the planar and convex conical hill slopes were analyzed. Maximum runup and rundown were observed in the landslide impact region and second maxima were observed outside the impact region after the lateral wave was fully formed. The runup and rundown decayed asymptotically from the second maxima. In the conical island scenario, a

localized runup amplification was observed on the lee side of the island. Outside the landslide impact region, the effects of the landslide granulometry on the lateral wave runup are minimal. The lateral wave runup on the planar hill slope was generally larger than on the convex conical hill slope outside the landslide impact region. This is because the convex conical hill slope traps less lateral wave energy. The zeroth mode of the edge wave dispersion relation matched the first and second lateral waves on the planar hill slope and the first wave on the convex conical hill slope.

Combining the amplitude attenuation prediction equations with solitary runup equations from the literature, surprisingly allows expansion of 2D runup predictions on an opposing hill slope to 3D waves with initial incident angle within $\pm$ 45°. When comparing the maximum runup measurements between the fjord and curved headland scenarios, the fjord was on average 10% larger due to the complete trapping of the wave energy between the opposing hill slopes while the curved headland leaked some wave energy into the open basin. The validity of the predictive equations were tested by scaling the experiment scale to prototype scale and compared to a recent field event at Chehalis Lake, Canada. The intermittent availability of field runup measurements along the shoreline and peculiarities in the field topography and bathymetry make a direct comparison difficult. Practical applicability and scalability was highlighted by the two closest lateral runup measurements to the landslide being within the range of the predicted runup maxima on the landslide hill slope.

7.2 Contribution to Tsunami Research

This present study extends previous 2D and 3D physical modelling of subaerial landslide generated tsunamis to include complex topographic and bathymetric scenarios and different landslide materials. This 3D physical model is the first large scale study to model tsunami

generation by a granular subaerial landslide and the subsequent wave runup on an opposing hill slope. The effects of the lateral hill slope curvature and landslide granulometry on the offshore and lateral wave characteristics have not been analyzed in a 3D physical model prior to this study. Previously produced 3D predictive equations for the wave characteristics generated by granular landslides on a planar hill slope have been extended for application to convex hill slopes. Predictive equations for the lateral wave runup generated by a subaerial granular landslide on planar and convex conical hill slopes have be produced. The predictive equations allow for a rapid initial landslide generated tsunami hazard assessment. The wave amplitude, runup, rundown and celerity are of particular practical importance in predicting the landslide generated tsunami hazard. The experimental data provides high precision benchmark scenarios to advance and validate fully 3D numerical models of complex landslide generated tsunamis.

7.3 Outlook

Landslide generated tsunamis are a complex multiphase process involving the landslide granulate, air and water. Some parameters which remained constant during the present physical model could be modified in future studies, such as the landslide hill slope angle or the landslide density. The landslide material could potentially be changed to lighter density material and heated to simulate the emplacement of pyroclastic flows during volcanic eruptions similar to Mount St. Helens in 1980 or Krakatau in 1883. The present study compared the wave characteristics generated on a planar hill slope and a divergent, convex conical hill slope. The lateral hill slope analysis could be extended by comparing the wave characteristics generated on a convergent, concave hill slope. This could simulate a landslide impacting a narrow end of an enclosed water body. The range of nondimensional parameters could be extended beyond the ranges tested in the present study and future studies could investigate tsunami generation by fully submerged deformable landslides. The application of the present study to field cases beyond the

range of nondimensional parameters tested is cautioned. Field events generally occur in very complex topographic and bathymetric settings, and field measurements from past events are scarce. The combination of additional field measurements, physical models and numerical models will advance the understanding of the landslide generated tsunami phenomenon.

REFERENCES

Abadie, S., Morichon, D., Grilli, S. and Glockner, S., 2010. Numerical simulation of waves generated by landslides using a multiple-fluid Navier-Stokes model. Coastal Engineering, 57(9): 779-794.

Abadie, S., Morichon, D., Grilli, S.T. and Glockner, S., 2008. VOF/Navier-Stokes numerical modeling of surface waves generated by subaerial landslides. La Houille Blanche(1): 21-26.

Abadie, S.M., Harris, J.C., Grilli, S.T. and Fabre, R., 2012. Numerical modeling of tsunami waves generated by the flank collapse of the Cumbre Vieja Volcano (La Palma, Canary Islands): Tsunami source and near field effects. Journal of Geophysical Research: Oceans, 117(C05030).

Amsden, A.A., Ruppel, H.M. and Hirt, C.W., 1980. SALE: a Simplified ALE computer program for fluid flows at all speeds, Los Alamos National Laboratory, Los Alamos, NM, USA.

Antunes do Carmo, J.S. and Carvalho, R.F., 2011. Large dam-reservoir systems: guidelines and tools to estimate loads resulting from natural hazards. Natural hazards, 59(1): 75-106.

Ataie-Ashtiani, B. and Najafi-Jilani, A., 2008. Laboratory investigations on impulsive waves caused by underwater landslide. Coastal Engineering, 55(12): 989-1004.

Ataie-Ashtiani, B. and Nik-Khah, A., 2008. Impulsive waves caused by subaerial landslides. Environmental Fluid Mechanics, 8(3): 263-280.

Ataie-Ashtiani, B. and Yavari-Ramshe, S., 2011. Numerical simulation of wave generated by landslide incidents in dam reservoirs. Landslides, 8(4): 417-432.

Ball, J.W., 1970. Hydraulic model studies, wave action generated by slides into Mica reservoir, Western Canada Hydraulic Laboratories, Vancouver, Canada.

Basu, D., Das, K., Green, S., Janetzke, R. and Stamatakos, J., 2010. Numerical Simulation of Surface Waves Generated by a Subaerial Landslide at Lituya Bay Alaska. Journal of Offshore Mechanics and Arctic Engineering-Transactions of the ASME, 132(4): 041101 (11 pages).

Beget, J.E. and Kowalik, Z., 2006. Confirmation and Calibration of Computer Modeling of Tsunamis Produced by Augustine Volcano, Alaska. Science of Tsunami Hazards, 24(4): 257-266.

Birkhoff, G., 1950. Hydrodynamics: a study in logic, fact and similitude. Dover Press, New York.

Boussinesq, J., 1872. Théorie des ondes et des remous qui se propagent le long d'un canal rectangulaire horizontal, en communiquant au liquide contenu dans ce canal des vitesses sensiblement pareilles de la surface au fond. Journal de Mathématiques Pures et Appliquées, 17: 55-108.

Brideau, M.-A., Sturzenegger, M., Stead, D., Jaboyedoff, M., Lawrence, M., Roberts, N.J., Ward, B.C., Millard, T.H. and Clague, J.J., 2012. Stability analysis of the 2007 Chehalis lake landslide based on long-range terrestrial photogrammetry and airborne LiDAR data. Landslides, 9(1): 75-91.

Briggs, M.J., Synolakis, C.E., Harkins, G.S. and Green, D.R., 1995. Laboratory experiments of tsunami runup on a circular island. Pure and Applied Geophysics, 144(3): 569-593.

Bruggemann, M., 2012. Composite modelling of the influence of geometry on landslide generated impulse waves, Proceedings of 1st Civil and Environmental Engineering Student Conference, Imperial College London, pp. 1-6.

Buckingham, E., 1914. On physically similar systems; illustrations of the use of dimensional equations. Physical Review, 4(4): 345-376.

Bukreev, V. and Gusev, A., 1996. Gravity waves generated by a body falling onto shallow water. Journal of applied mechanics and technical physics, 37(2): 224-231.

Camfield, F.E. and Street, R.L., 1969. Shoaling of solitary waves on small slopes. Journal of the Waterways, Harbors and Coastal Engineering Division, 95(WW): 1-22.

Capone, T., Panizzo, A. and Monaghan, J.J., 2010. SPH modelling of water waves generated by submarine landslides. Journal of Hydraulic Research, 48: 80-84.

Carrier, G. and Greenspan, H., 1958. Water waves of finite amplitude on a sloping beach. Journal of Fluid Mechanics, 4(1): 97-109.

Chan, I.C. and Liu, P.L.-F., 2012. On the runup of long waves on a plane beach. Journal of Geophysical Research, 117(C8): C08006.

Chang, K., 1995. Evolution of landslide-generated edge wave packet. Ph.D. Thesis, University of Washington, Seattle.

Chaudhry, M.H., Mercer, A.G. and Cass, D., 1983. Modeling of slide-generated waves in a reservoir. Journal of Hydraulic Engineering, 109(11): 1505-1520.

Chen, C.-l. and Ling, C.-H., 1996. Granular-flow rheology: role of shear-rate number in transition regime. Journal of Engineering Mechanics, 122(5): 469-480.

Chiang, W.-L., Divrky, D., Parnicky, P. and Weir, W., 1981. Numerical model landslide-generated waves, U.S. Dept. of Commerce, Pasadena, CA, USA.

Cruden, D., 1991. A simple definition of a landslide. Bulletin of Engineering Geology and the Environment, 43(1): 27-29.

Dalrymple, R.A., 1985. Physical modeling in coastal engineering, 9A. Ocean Engineering Science, Balkema, Rotterdam.

Das, M.M. and Wiegel, R.L., 1972. Waves generated by the horizontal motion of a wall. Journal of the Waterways, Harbors and Coastal Engineering Division, 98(WW1): 49-65.

Davidson, D.D. and McCartney, B.L., 1975. Water waves generated by landslides in reservoirs. Journal of the Hydraulics Division, 101(12): 1489-1501.

Davidson, D.D. and Whalin, R.W., 1974. Potential landslide-generated impulse water waves, Libby Dam and Lake Koocanusa, Montana, U.S. Army Corps of Engineers Waterways Experiment Station, Vicksburg, MS.

Dean, R.G. and Dalrymple, R.A., 1991. Water wave mechanics for engineers and scientists. Advanced series on ocean engineering, Vol. 2. World Scientific, Singapore.

Demidovich, B.P. and Maron, I.A., 1987. Computational Mathematics. Mir Publishers, Moscow.

Denlinger, R.P. and Iverson, R.M., 2001. Flow of variably fluidized granular masses across three-dimensional terrain: 2. Numerical predictions and experimental tests. Journal of Geophysical Research, 106(B1): 553-566.

Di Risio, M., Bellotti, G., Panizzo, A. and De Girolamo, P., 2009a. Three-dimensional experiments on landslide generated waves at a sloping coast. Coastal Engineering, 56(5): 659-671.

Di Risio, M., De Girolamo, P., Bellotti, G., Panizzo, A., Aristodemo, F., Molfetta, M. and Petrillo, A., 2009b. Landslide-generated tsunamis runup at the coast of a conical island: New physical model experiments. Journal of Geophysical Research, 114(C1): C01009.

Didenkulova, I., Nikolkina, I., Pelinovsky, E. and Zahibo, N., 2010. Tsunami waves generated by submarine landslides of variable volume: analytical solutions for a basin of variable depth. Natural Hazards and Earth System Science, 10(11): 2407-2419.

Du Boys, P., 1891. Essai théorique sur les seiches. Archives des Sciences Physique et Naturelles Genève (Geneva, Switzerland), xxv(S): 25.

Eckart, C., 1951. Surface waves on water of variable depth, Wave Report (No. 100). University of California, Scripps.

Enet, F. and Grilli, S.T., 2005. Tsunami landslide generation: Modelling and experiments, Proceedings of the 5th International Conference on Ocean Wave Measurement and Analysis (WAVES 2005). paper no. 88, Madrid, Spain.

Enet, F. and Grilli, S.T., 2007. Experimental study of tsunami generation by three-dimensional rigid underwater landslides. Journal of Waterway, Port, Coastal, and Ocean Engineering, 133(6): 442-454.

Erismann, T., 1986. Flowing, rolling, bouncing, sliding: synopsis of basic mechanisms. Acta Mechanica, 64(1): 101-110.

Fedkiw, R.P., Aslam, T., Merriman, B. and Osher, S., 1999. A non-oscillatory Eulerian approach to interfaces in multimaterial flows (the ghost fluid method). Journal of Computational Physics, 152(2): 457-492.

Fritz, H.M., 2002. Initial phase of landslide generated impulse waves. Ph.D. Thesis, Eidgenössische Technischen Hochschule Zürich, Zürich, Switzerland, No. 14871.

Fritz, H.M., Hager, W.H. and Minor, H.-E., 2001. Lituya Bay case rockslide impact and wave run-up. Science of Tsunami Hazards, 19(1): 3-22.

Fritz, H.M., Hager, W.H. and Minor, H.-E., 2003a. Landslide generated impulse waves. 1. instantaneous flow fields. Experiments in fluids, 35(6): 505-519.

Fritz, H.M., Hager, W.H. and Minor, H.-E., 2003b. Landslide generated impulse waves. 2. Hydrodynamic impact craters. Experiments in fluids, 35(6): 520-532.

Fritz, H.M., Hager, W.H. and Minor, H.-E., 2004. Near field characteristics of landslide generated impulse waves. Journal of Waterway, Port, Coastal, and Ocean Engineering, 130(6): 287-302.

Fritz, H.M., Hillaire, J.V., Molière, E., Wei, Y. and Mohammed, F., 2013. Twin tsunamis triggered by the 12 January 2010 Haiti earthquake. Pure and Applied Geophysics, 170(9-10): 1463-1474.

Fritz, H.M., Kongko, W., Moore, A., McAdoo, B., Goff, J., Harbitz, C., Uslu, B., Kalligeris, N., Suteja, D., Kalsum, K., Titov, V., Gusman, A., Latief, H., Santoso, E., Sujoko, S., Djulkarnaen, D., Sunendar, H. and Synolakis, C., 2007. Extreme runup from the 17 July 2006 Java tsunami. Geophysical Research Letters, 34(L12602).

Fritz, H.M., Mohammed, F. and Yoo, J., 2009. Lituya Bay landslide impact generated mega-tsunami 50th anniversary. Pure and Applied Geophysics, 166(1): 153-175.

Fritz, H.M. and Moser, P., 2003. Pneumatic landslide generator. International Journal of Fluid Power, 4(1): 49-57.

Fryer, G.J., Watts, P. and Pratson, L.F., 2004. Source of the great tsunami of 1 April 1946: a landslide in the upper Aleutian forearc. Marine Geology, 203(3): 201-218.

Galvin, C.J., Jr., 1964. Wave-height prediction for wave generators in shallow water, U.S. Army, Coastal Engineering Research Center Tech. Memo. 4, 21 pp, Washington, D.C.

Gharib, M., Rambod, E. and Shariff, K., 1998. A universal time scale for vortex ring formation. Journal of Fluid Mechanics, 360: 121-140.

Glicken, H., 1996. Rockslide-debris avalanche of May, 18, 1980, Mount St.Helens Volcano, Washington, U.S. Geological Survey. Open-File Report 96-677.

Goguel, J., 1978. Scale-dependent rockslide mechanisms, with emphasis on the role of pore fluid vaporization. Rockslides and avalanches, 1: 693-705.

Gonzalez, F., Satake, K., Boss, E. and Mofjeld, H., 1995. Edge wave and non-trapped modes of the 25 April 1992 Cape Mendocino tsunami. Pure and Applied Geophysics, 144(3): 409-426.

Gozali, S. and Hunt, B., 1989. Water waves generated by close landslides. Journal of Hydraulic Research, 27(1): 49-60.

Gray, J., Wieland, M. and Hutter, K., 1999. Gravity-driven free surface flow of granular avalanches over complex basal topography. Proceedings of the Royal Society of London. Series A: Mathematical, Physical and Engineering Sciences, 455(1985): 1841-1874.

Grilli, S.T., Skourup, J. and Svendsen, I.A., 1989. An efficient boundary element method for nonlinear water waves. Engineering Analysis with Boundary Elements, 6(2): 97-107.

Grilli, S.T., Vogelmann, S. and Watts, P., 2002. Development of a 3D numerical wave tank for modeling tsunami generation by underwater landslides. Engineering Analysis with Boundary Elements, 26(4): 301-313.

Grilli, S.T. and Watts, P., 1999. Modeling of waves generated by a moving submerged body. Applications to underwater landslides. Engineering Analysis with Boundary Elements, 23(8): 645-656.

Grilli, S.T. and Watts, P., 2005. Tsunami generation by submarine mass failure. I: Modeling, experimental validation, and sensitivity analyses. Journal of Waterway, Port, Coastal, and Ocean Engineering, 131(6): 283-297.

Guza, R.T. and Thornton, E.B., 1982. Swash oscillations on a natural beach. Journal of Geophysical Research, 87(C1): 483-491.

Habib, P., 1975. Production of gaseous pore pressure during rock slides. Rock Mechanics and Rock Engineering, 7(4): 193-197.

Hall Jr, J.V. and Watts, G.M., 1953. Laboratory investigation of the vertical rise of solitary waves on impermeable slopes, DTIC Document.

Hammack, J.L., 1973. A note on tsunamis: their generation and propagation in an ocean of uniform depth. Journal of Fluid Mechanics, 60((04)): 769-799.

Hampton, M.A., Lee, H.J. and Locat, J., 1996. Submarine landslides. Reviews of geophysics, 34(1): 33-60.

Harbitz, C.B., Pedersen, G. and Gjevik, B., 1993. Numerical simulations of large water waves due to landslides. Journal of Hydraulic Engineering, 119(12): 1325-1342.

Heim, A., 1932. Landslides and human lives (German: Bergsturz und Menschenleben). BiTech Publishers, Vancouver, B.C.

Heinrich, P., 1992. Nonlinear water waves generated by submarine and aerial landslides. Journal of Waterway, Port, Coastal, and Ocean Engineering, 118(3): 249-266.

Heller, V., 2008. Landslide generated impulse waves: Prediction of near field characteristics. Ph.D. Thesis, Eidgenössische Technischen Hochschule Zürich, Zürich, Switzerland, No. 17531.

Heller, V. and Hager, W., 2011. Wave types of landslide generated impulse waves. Ocean Engineering, 38(4): 630-640.

Heller, V. and Hager, W.H., 2010. Impulse product parameter in landslide generated impulse waves. Journal of Waterway, Port, Coastal, and Ocean Engineering, 136(3): 145-155.

Heller, V., Hager, W.H. and Minor, H.-E., 2009. Landslide generated impulse waves in reservoirs-basics and computation. In: R. Boes (Editor), VAW-Mitteilung (211). ETH Zürich, pp. 172.

Heller, V., Moalemi, M., Kinnear, R.D. and Adams, R.A., 2012. Geometrical effects on landslide-generated tsunamis. Journal of Waterway Port Coastal and Ocean Engineering-ASCE, 138(4): 286-298.

Heller, V. and Spinneken, J., 2013. Improved landslide-tsunami prediction: effects of block model parameters and slide model. Journal of Geophysical Research: Oceans, 118(3): 1489-1507.

Holman, R., 1986. Extreme value statistics for wave run-up on a natural beach. Coastal Engineering, 9(6): 527-544.

Hornbach, M.J., Braudy, N., Briggs, R.W., Cormier, M.-H., Davis, M.B., Diebold, J.B., Dieudonne, N., Douilly, R., Frohlich, C. and Gulick, S.P., 2010. High tsunami frequency as a result of combined strike-slip faulting and coastal landslides. Nature Geoscience, 3(11): 783-788.

Horrillo, J.J., 2006. Numerical methods for tsunami calculation using full Navier-Stokes equations and the volume of fluid method. Ph.D. Thesis, University of Alaska, Fairbanks, AK, USA.

Hsü, K.J., 1975. Catastrophic debris streams (sturzstroms) generated by rockfalls. Geological Society of America Bulletin, 86(1): 129-140.

Huang, B.L., Yin, Y.P., Liu, G.N., Wang, S.C., Chen, X.T. and Huo, Z.T., 2012. Analysis of waves generated by Gongjiafang landslide in Wu Gorge, three Gorges reservoir, on November 23, 2008. Landslides, 9(3): 395-405.

Huber, A., 1980. Schwallwellen in Seen als Folge von Bergstürzen. *VAW-Mitteilung* 47, Ed. Vischer, D., Versuchsanstalt für Wasserbau, Hydrologie und Glaziologie, ETH Zürich. (in German)

Huber, A. and Hager, W.H., 1997. Forecasting impulse waves in reservoirs. *Dix-neuvième Congrès des Grands Barrages*, C31: 993-1006.

Hughes, S., 1993. Physical models and laboratory techniques in coastal engineering. Advanced series on ocean engineering, 7. World Scientific, Singapore.

Hunt, B., 1988. Water waves generated by distant landslides. Journal of Hydraulic Research, 26(3): 307-322.

Imamura, F. and Gica, E., 1996. Numerical model for tsunami generation due to subaqueous landslide along a coast. Science of Tsunami Hazards, 14(1): 13-28.

Iverson, R.M., 1997. The physics of debris flows. Reviews of Geophysics, 35: 245-296.

Iverson, R.M., Logan, M. and Denlinger, R.P., 2004. Granular avalanches across irregular three-dimensional terrain: 2. Experimental tests. Journal of Geophysical Research, 109(F1): F01015.

Jiang, L. and LeBlond, P.H., 1992. The coupling of a submarine slide and the surface waves which it generates. Journal of Geophysical Research, 97(C8): 12731-12,744.

Jiang, L. and LeBlond, P.H., 1993. Numerical modeling of an underwater Bingham plastic mudslide and the waves which it generates. Journal of Geophysical Research, 98(C6): 10303-10,317.

Jiang, L. and Leblond, P.H., 1994. Three-dimensional modeling of tsunami generation due to a submarine mudslide. Journal of physical oceanography, 24(3): 559-572.

Johnson, C. and Mader, C.L., 1994. Modeling the 105 Ka Lanai Tsunami. Science of Tsunami Hazards, 12: 33-36.

Johnson, J.W. and Bermel, K.J., 1949. Impulsive waves in shallow water as generated by falling weights. Trans. American Geophysical Union, 30(2): 223-230.

Jorstad, F., 1968. Waves generated by landslides in Norwegian fjords and lakes. Norwegian Geotechnical Institute Publ, 79: 13-32.

Kajiura, K., 1990. Tsunami. John Wiley, New York.

Kamphuis, J. and Bowering, R., 1970. Impulse waves generated by landslides, 12th Coastal Engineering Conference. ASCE, pp. 575-588.

Keller, J.B. and Keller, H.B., 1964. Water wave run-up on a beach, DTIC Document (AD0608864), Office of Naval Research, Washington, D.C.

Kent, P., 1966. The transport mechanism in catastrophic rock falls. The Journal of Geology, 74: 79-83.

Keulegan, G.H., 1948. Gradual damping of solitary waves. J. Res., Nat. Bur. Stand. , 40: 487-498.

Kienle, J., Kowalik, Z. and Murty, T.S., 1987. Tsunamis generated by eruptions from Mount St. Augustine volcano, Alaska. Science, 236(4807): 1442-1447.

Kishi, T. and Saeki, H., 1966. The shoaling, breaking and runup of the solitary wave on impermeable rough slopes Proceedings of the International Conference on Coastal Engineering, Tokyo, Japan, pp. 322-348.

Koch, T., 1989. Bewegung einer Granulatlawine entlang einer gekrümmten Bahn. Techn. Hochschule Darmstadt, Germany.

Koch, T., Greve, R. and Hutter, K., 1994. Unconfined flow of granular avalanches along a partly curved surface. II. Experiments and numerical computations. Proceedings of the Royal Society of London. Series A: Mathematical and Physical Sciences, 445(1924): 415-435.

Körner, H.J., 1976. Reichweite und Geschwindigkeit von Bergstürzen und Fliesschneelawinen. Rock Mechanics, 8(3): 225-256.

Kranzer, H.C. and Keller, J.B., 1959. Water waves produced by explosions. Journal of applied physics, 30(3): 398-407.

Laitone, E.V., 1960. The second approximation to cnoidal and solitary waves. Journal of Fluid Mechanics, 9(03): 430-444.

Lamb, H., 1932. Hydrodynamics 6th ed., Dover, New York.

Lautenbacher, C.C., 1970. Gravity wave refraction by islands. Journal of Fluid Mechanics, 41(03): 655-672.

Law, L. and Brebner, A., 1968. On water waves generated by landslides, Proceeding of the 3rd Australasian Conference on Hydraulics and Fluid Mechanics. Institution of Engineers Sydney, pp. 155-159.

Lawrence, M.S., Roberts, N.J. and Clague, J.J., 2013. The 2007 Chehalis Lake landslide, British Columbia: A landslide-generated surge wave (tsunami) with implications for dam safety, GéoMontréal 2013, Montréal, CAN.

Lighthill, J., 2001. Waves in Fluids. Cambridge University Press, Cambridge, U.K.

Liu, P.L.-F., Cho, Y.-S., Briggs, M.J., Kanoglu, U. and Synolakis, C.E., 1995. Runup of solitary waves on a circular island. Journal of Fluid Mechanics, 302: 259-286.

Liu, P.L.-F., Wu, T., Raichlen, F., Synolakis, C. and Borrero, J., 2005. Runup and rundown generated by three-dimensional sliding masses. Journal of Fluid Mechanics, 536(1): 107-144.

Liu, P.L.-F., Yeh, H., Lin, P., Chang, K. and Cho, Y.S., 1998. Generation and evolution of edge-wave packets. Physics of Fluids, 10: 1635-1657.

Liu, P.L.-F. and Yeh, H.H., 1996. The generation of edge waves by a wave-maker. Physics of Fluids, 8(8): 2060-2065.

Longuet-Higgins, M.S., 1967. On the trapping of wave energy round islands. Journal of Fluid Mechanics, 29(04): 781-821.

Løvholt, F., Pedersen, G. and Gisler, G., 2008. Oceanic propagation of a potential tsunami from the La Palma Island. Journal of Geophysical Research: Oceans 113(C09026).

Lynett, P. and Liu, P.L.-F., 2002. A numerical study of submarine-landslide-generated waves and run-up. Proceedings of the Royal Society of London. Series A: Mathematical, Physical and Engineering Sciences, 458(2028): 2885-2910.

Lynett, P. and Liu, P.L.-F., 2005. A numerical study of the run-up generated by three-dimensional landslides. Journal of Geophysical Research, 110(C3): C03006.

Ma, G.F., Shi, F.Y. and Kirby, J.T., 2012. Shock-capturing non-hydrostatic model for fully dispersive surface wave processes. Ocean Modelling, 43-44: 22-35.

Mader, C.L., 1988. Numerical modeling of water waves, University of California press, Berkeley.

Mader, C.L., 1999. Modeling of the 1958 Lituya Bay mega-tsunami. Science of Tsunami Hazards, 17(2): 57-67.

Mader, C.L. and Gittings, M.L., 2002. Modeling the 1958 Lituya Bay mega-tsunami, II. Science of Tsunami Hazards, 20(5): 241-250.

Mader, C.L. and Gittings, M.L., 2006. Numerical model for the Krakatoa hydrovolcanic explosion and tsunami. Science of Tsunami Hazards, 24(3): 174.

Madsen, O.S., 1971. On the generation of long waves. Journal of Geophysical Research, 76(36): 8672-8683.

Madsen, P.A. and Schäffer, H.A., 2010. Analytical solutions for tsunami runup on a plane beach: single waves, N-waves and transient waves. Journal of Fluid Mechanics, 645: 27-57.

Mazzanti, P. and Bozzano, F., 2011. Revisiting the February 6th 1783 Scilla (Calabria, Italy) landslide and tsunami by numerical simulation. Marine Geophysical Research, 32(1-2): 273-286.

McCowan, J., 1894. On the highest wave of permanent type. Philosophical Magazine Series 5, 38(233): 351-358.

McEwen, A.S., 1989. Mobility of large rock avalanches: Evidence from Valles Marineris, Mars. Geology, 17(12): 1111-1114.

McHugh, C.M., Seeber, L., Braudy, N., Cormier, M.-H., Davis, M.B., Diebold, J.B., Dieudonne, N., Douilly, R., Gulick, S.P. and Hornbach, M.J., 2011. Offshore sedimentary effects of the 12 January 2010 Haiti earthquake. Geology, 39(8): 723-726.

Melosh, H., 1986. The physics of very large landslides. Acta Mechanica, 64(1): 89-99.

Miller, D.J., 1960. Giant waves in Lituya Bay, Alaska. Geological Survey Professional Paper, 354-C.

Miller, R.L., 1970. Prediction curves for waves near the source of an impulse, Proceedings of the 12th Coastal Engineering, ASCE, Washington, D.C., pp. 609-624.

Miller, R.L. and White, R.V., 1966. A single-impulse system for generating solitary, undulating surge, and gravity shock waves in the laboratory, Dept. Geophys., Univ. Chicago, Ill.

Mohammed, F., 2010. Physical modeling of tsunamis generated by three-dimensional deformable granular landslides. Ph.D. Thesis, Georgia Institute of Technology, Atlanta, GA, USA.

Mohammed, F. and Fritz, H.M., 2012. Physical modeling of tsunamis generated by three-dimensional deformable granular landslides. Journal of Geophysical Research: Oceans, 117(C11015).

Mohammed, F. and Fritz, H.M., 2013. Correction to "Physical modeling of tsunamis generated by three-dimensional deformable granular landslides". Journal of Geophysical Research: Oceans, 118(6): 3221-3221.

Monaghan, J. and Kos, A., 2000. Scott Russell's wave generator. Physics of Fluids, 12(3): 622-630.

Monaghan, J.J. and Kos, A., 1999. Solitary waves on a Cretan beach. Journal of Waterway, Port, Coastal, and Ocean Engineering, 125(3): 145-155.

Montagna, F., Bellotti, G. and Di Risio, M., 2011. 3D numerical modeling of landslide-generated tsunamis around a conical island. Natural hazards, 58(1): 591-608.

Moore, J.G., Clague, D.A., Holcomb, R.T., Lipman, P.W., Normark, W.R. and Torresan, M.E., 1989. Prodigious submarine landslides on the Hawaiian Ridge. Journal of Geophysical Research: Solid Earth, 94(B12): 17465-17484.

Müller, D., 1995. Auflaufen und Überschwappen von Impulswellen an Talsperren. In: D. Vischer (Editor), *VAW-Mitteilung*. Versuchsanstalt für Wasserbau, Hydrologie und Glaziologie. ETH Zürich.

Müller, L., 1964. the rock slide in the vajont valley. Rock Mechanism Engineering Geology, 2(3-4): 148-212.

Najafi-Jilani, A. and Ataie-Ashtiani, B., 2008. Estimation of near-field characteristics of tsunami generation by submarine landslide. Ocean Engineering, 35(5): 545-557.

Noda, E., 1970. Water waves generated by landslides. Journal of the Waterways, Harbors and Coastal Engineering Division, 96(4): 835-855.

Ogawa, T., 1924. Notes on the Volcanic and Seismic Phenomena in the Volcanic District of Shimabara: With a Report on the Earthquake of December 8th, 1922.

Okal, E.A., Fryer, G.J., Borrero, J.C. and Ruscher, C., 2002. The landslide and local tsunami of 13 september 1999 on Fatu Hiva (Marquesas Islands; French Polynesia). Bulletin de la Société géologique de France, 173(4): 359-367.

Özeren, M.S. and Postacioglu, N., 2012. Nonlinear landslide tsunami run-up. Journal of Fluid Mechanics, 691: 440-460.

Panizzo, A., Bellotti, G. and De Girolamo, P., 2002. Application of wavelet transform analysis to landslide generated waves. Coastal Engineering, 44(4): 321-338.

Panizzo, A., De Girolamo, P. and Petaccia, A., 2005. Forecasting impulse waves generated by subaerial landslides. Journal of Geophysical Research, 110(C12): C12025.

Plafker, G. and Eyzaguirre, V., 1979. Rock avalanche and wave at Chungar, Peru, Rockslides and avalanches. Developments in Geotechnical Engineering. Elsevier, Amsterdam, Netherlands, pp. 269-279.

Plüss, C., 1987. Experiments on granular landslides. (Diplomarbeit. Abt X, Eidg. Techn. Hochschule, Zürich).

Pudasaini, S.P., Wang, Y., Sheng, L.-T., Hsiau, S.-S., Hutter, K. and Katzenbach, R., 2008. Avalanching granular flows down curved and twisted channels: Theoretical and experimental results. Physics of Fluids, 20(7): 073302.

Quecedo, M., Pastor, M. and Herreros, M.I., 2004. Numerical modeling of impulse waves gnerated by fast landslides. International Journal for Numerical Methods in Engineering, 59: 1633-1656.

Raney, D.C. and Butler, H.L., 1975. A numerical model for predicting the effects of landslide generated water waves, U.S. Army Corps of Engineers Waterways Experiment Station, Springfield, VA.

Renzi, E. and Sammarco, P., 2010. Landslide tsunamis propagating around a conical island. Journal of Fluid Mechanics, 650: 251-285.

Renzi, E. and Sammarco, P., 2012. The influence of landslide shape and continental shelf on landslide generated tsunamis along a plane beach. Natural Hazards and Earth System Sciences, 12(5): 1503-1520.

Roberts, N.J., McKillop, R.J., Lawrence, M.S., Psutka, J.F., Clague, J.J., Brideau, M.-A. and Ward, B.C., 2013. Impacts of the 2007 Landslide-Generated Tsunami in Chehalis Lake, Canada, Landslide Science and Practice. Springer, pp. 133-140.

Romano, A., Bellotti, G. and Di Risio, M., 2013. Wavenumber-frequency analysis of the landslide-generated tsunamis at a conical island. Coastal Engineering, 81: 32-43.

Russell, J.S., 1837. Report on the committee of waves, Report of the 7th Meeting of the British Association for the Advancement of Science, pp. 417-496.

Russell, J.S., 1844. Report on waves, Report of the 14th Meeting of the British Association for the Advancement of Science, pp. 311-390.

Rzadkiewicz, S.A., Mariotti, C. and Heinrich, P., 1997. Numerical simulation of submarine landslides and their hydraulic effects. Journal of Waterway, Port, Coastal, and Ocean Engineering, 123(4): 149-157.

Sælevik, G., Jensen, A. and Pedersen, G., 2009. Experimental investigation of impact generated tsunami; related to a potential rock slide, Western Norway. Coastal Engineering, 56(9): 897-906.

Sælevik, G., Jensen, A. and Pedersen, G., 2013. Runup of solitary waves on a straight and a composite beach. Coastal Engineering, 77: 40-48.

Sammarco, P. and Renzi, E., 2008. Landslide tsunamis propagating along a plane beach. Journal of Fluid Mechanics, 598: 107-120.

Sander, D., 1990. Weakly nonlinear unidirectional shallow water waves generated by a moving boundary. VAW-Mitteilung (105). Hydrologie und Glaziologie, ETH Zürich.

Satake, K., 2007. Volcanic origin of the 1741 Oshima-Oshima tsunami in the Japan Sea. Earth, Planets and Space, 59(5): 381.

Savage, S. and Hutter, K., 1989. The motion of a finite mass of granular material down a rough incline. Journal of Fluid Mechanics, 199(1): 177-215.

Savage, S. and Hutter, K., 1991. The dynamics of avalanches of granular materials from initiation to runout. Part I: Analysis. Acta Mechanica, 86(1): 201-223.

Scheidegger, A.E., 1973. On the prediction of the reach and velocity of catastrophic landslides. Rock Mechanics and Rock Engineering, 5(4): 231-236.

Schwaiger, H.F. and Higman, B., 2007. Lagrangian hydrocode simulations of the 1958 Lituya Bay tsunamigenic rockslide. Geochemistry Geophysics Geosystems, 8(7): Q07006.

Seo, S.-N. and Liu, P.L.-F., 2013. Edge waves generated by the landslide on a sloping beach. Coastal Engineering, 73: 133-150.

Sethian, J.A., 1996. Level set methods: evolving interfaces in geometry, fluid mechanics, computer vision and material science. Cambridge University Press., Cambridge.

Shreve, R.L., 1966. Sherman landslide, Alaska. Science, 154(3757): 1639-1643.

Shreve, R.L., 1968. The Blackhawk landslide, Geological Society of America, Special Paper: 108 (1-47), Boulder, CO.

Shusser, M. and Gharib, M., 2000. Energy and velocity of a forming vortex ring. Physics of Fluids, 12(3): 618-621.

Simkin, T. and Fiske, R.S., 1983. Krakatau, 1883--the volcanic eruption and its effects. Smithsonian Institute Press, Washington, D.C.

Slingerland, R. and Voight, B., 1982. Evaluating hazard of landslide-induced water waves. Journal of the Waterway Port Coastal and Ocean Division, 108(4): 504-512.

Slingerland, R.L. and Voight, B., 1979. Occurrences, properties, and predictive models of landslide-generated water waves. In: B. Voight (Editor), Rockslides and avalanches. Elsevier, Amsterdam.

Smith, R. and Sprinks, T., 1975. Scattering of surface waves by a conical island. Journal of Fluid Mechanics, 72(02): 373-384.

Stokes, G.G., 1846. Report on recent researches in hydrodynamics. Brit. Ass. Rep, 1: 1-20.

Sue, L.P., Nokes, R.I. and Davidson, M.J., 2011. Tsunami generation by submarine landslides: comparison of physical and numerical models. Environmental Fluid Mechanics, 11(2): 133-165.

Synolakis, C.E., 1987. The runup of solitary waves. Journal of Fluid Mechanics, 185: 523-545.

Synolakis, C.E., 1991. Generation of long waves in laboratory. Journal of Waterway, Port, Coastal, and Ocean Engineering, 116(2): 252-266.

Synolakis, C.E., Bardet, J.-P., Borrero, J.C., Davies, H.L., Okal, E.A., Silver, E.A., Sweet, S. and Tappin, D.R., 2002. The slump origin of the 1998 Papua New Guinea tsunami. Proceedings of the royal society of London. Series A. Mathematical and Physical Sciences, 458(2020): 763-789.

Synolakis, C.E., Deb, M.K. and Skjelbreia, J.E., 1988. The anomalous behavior of the run-up of cnoidal waves. Physics of Fluids, 31: 3-5.

Tinti, S. and Bortolucci, E., 2000. Energy of water waves induced by submarine landslides. Pure and Applied Geophysics, 157(3): 281-318.

Tinti, S., Chiocci, F.L., Zaniboni, F., Pagnoni, G. and Alteriis, G.D., 2011. Numerical simulation of the tsunami generated by a past catastrophic landslide on the volcanic island of Ischia, Italy. Marine Geophysical Research, 32(1-2): 287-297.

Tinti, S., Manucci, A., Pagnoni, G., Armigliato, A. and Zaniboni, F., 2005. The 30 December 2002 landslide-induced tsunamis in Stromboli: sequence of the events reconstructed from the eyewitness accounts. Natural Hazards and Earth System Science, 5(6): 763-775.

Tocher, D. and Miller, D.J., 1959. Field observations on effects of Alaska earthquake of 10 July 1958. Science, 129(3346): 394-395.

Townson, J. and Kaya, Y., 1988. Simulations of the waves in Lake Boten created by the Rissa landslide, Proceedings of the Institute of Civil Engineering, pp. 145-160.

Ursell, F., 1952. Edge waves on a sloping beach. Proceedings of the royal society of London. Series A. Mathematical and Physical Sciences, 214(1116): 79-97.

Ursell, F., Dean, R.G. and Yu, Y.S., 1960. Forced small-amplitude water waves: a comparison of theory and experiment. Journal of Fluid Mechanics, 7(01): 33-52.

Van Dorn, W.G., 1961. Some characteristics of surface gravity waves in the sea produced by nuclear explosions. Journal of Geophysical Research, 66(11): 3845-3862.

Villeneuve, M. and Savage, S.B., 1993. Nonlinear, dispersive, shallow-water waves developed by a moving bed. Journal of Hydraulic Research, 31(2): 249-266.

Voight, B., Glicken, H., Janda, R. and Douglass, P., 1981. Catastrophic rockslide avalanche of May 18. US Geologial Survey Professional Paper, 1250: 347-378.

Voight, B., Janda, R. and Douglass, P., 1983. Nature and mechanics of the Mount St Helens rockslide-avalanche of 18 May 1980. Geotechnique, 33(3): 243-273.

Walder, J.S., Watts, P., Sorensen, O.E. and Janssen, K., 2003. Tsunamis generated by subaerial mass flows. Journal of Geophysical Research, 108(B5): 2236.

Wang, Y., Liu, P.L.-F. and Mei, C.C., 2011. Solid landslide generated waves. Journal of Fluid Mechanics, 675(1): 529-539.

Ward, S.N., 2001. Landslide tsunami. Journal of Geophysical Research, 106(6): 11,201-11,215.

Ward, S.N. and Day, S., 2001. Cumbre Vieja volcano potential collapse and tsunami at La Palma, Canary Islands. Geophysical Research Letters, 28(17): 3397-3400.

Ward, S.N. and Day, S., 2003. Ritter Island Volcano-lateral collapse and the tsunami of 1888. Geophysical Journal International, 154(3): 891-902.

Ward, S.N. and Day, S., 2008. Tsunami balls: a granular approach to tsunami runup and inundation. Communications in Computational Physics, 3(1): 222-249.

Ward, S.N. and Day, S., 2010. The 1958 Lituya Bay landslide and tsunami - a tsunami ball approach. Journal of Earthquake and Tsunami, 4(4): 285-319.

Ward, S.N. and Day, S., 2011. The 1963 Landslide and flood at Vaiont Reservoir Italy. A tsunami ball simulation. Italian Journal of Geosciences, 130(1): 16-26.

Watt, S., Talling, P., Vardy, M., Heller, V., Hühnerbach, V., Urlaub, M., Sarkar, S., Masson, D., Henstock, T. and Minshull, T., 2012. Combinations of volcanic-flank and seafloor-sediment failure offshore Montserrat, and their implications for tsunami generation. Earth and Planetary Science Letters, 319(320): 228-240.

Watts, P., 1997. Water waves generated by underwater landslides. Ph.D. Thesis, California Institute of Technology, Pasadena, CA, USA.

Watts, P., 1998. Wavemaker curves for tsunamis generated by underwater landslides. Journal of Waterway, Port, Coastal, and Ocean Engineering, 124(3): 127-137.

Watts, P., 2000. Tsunami features of solid block underwater landslides. Journal of Waterway, Port, Coastal, and Ocean Engineering, 126(3): 144-152.

Watts, P., Grilli, S.T., Kirby, J.T., Fryer, G.J. and Tappin, D.R., 2003. Landslide tsunami case studies using a Boussinesq model and a fully nonlinear tsunami generation model. Natural Hazards and Earth System Science, 3(5): 391-402.

Weiss, R., Fritz, H.M. and Wünnemann, K., 2009. Hybrid modeling of the mega-tsunami runup in Lituya Bay after half a century. Geophysical Research Letters, 36(9): L09602.

Weiss, R. and Wünnemann, K., 2007. Understanding tsunami by landslides as the next challege for hazard, risk and mitigation: Insight from multi-material hydrocode modeling, Transactions of the American Geophysical Union, pp. Abstract S51C-06.

Whittaker, E.T. and Watson, G.N., 1927. A Course of Modern Analysis. Cambridge University Press., Cambridge, N.Y.

Wiegel, R.L., 1955. Laboratory studies of gravity waves generated by the movement of a submerged body. Transactions of the American Geophysical Union, 36(5): 759-774.

Wiegel, R.L., Noda, E.K., Kuba, E.M., Gee, D.M. and Tornberg, G.F., 1970. Water waves generated by landslides in reservoirs. Journal of the Waterways, Harbors and Coastal Engineering Division, 96(2): 307-333.

Williams, J.M., 1985. Tables of progressive gravity waves. Pitman Advanced Pub. Program, Boston, MA.

Wu, T.Y., 1981. Long waves in ocean and coastal waters. Journal of Engineering Mechanics Division, 107: 401-522.

Wünnemann, K., Collins, G.S. and Melosh, H.J., 2006. A strain-based porosity model for use in hydrocode simulations of impacts and implications for transient crater growth in porous targets. Icarus, 180(2): 514-527.

Yalin, M.S., 1971. Theory of hydraulic models. Macmillan, London.

Yeh, H., Liu, P.L.-F., Briggs, M. and Synolakis, C., 1994. Propagation and amplification of tsunamis at coastal boundaries. Nature, 372(6504): 353-355.

Yokoyama, I., 1981. A geophysical interpretation of the 1883 Krakatau eruption. Journal of volcanology and geothermal research, 9(4): 359-378.

Zweifel, A., 2004. Impulswellen: Effeckte der Rutschdichte und der Wassertiefe. Ph.D. Thesis, Eidgenössische Technischen Hochschule Zürich, Zürich, Switzerland, No. 15596.

Zweifel, A., Hager, W.H. and Minor, H.-E., 2006. Plane impulse waves in reservoirs. Journal of Waterway, Port, Coastal, and Ocean Engineering, 132(5): 358-368.

VITA

BRIAN C. McFALL

Brian McFall was born and raised in Jasper, Texas. He graduated from Jasper High School in 2001. Brian received a B.S. and M.S. in Civil Engineering from Texas A&M University-Kingsville, Kingsville, Texas in 2005 and 2008, respectively. Before attending the Georgia Institute of Technology to pursue a doctorate in Civil Engineering, Brian worked for five years as a project manager and commercial diver for a consulting engineering company in Corpus Christi, Texas. He is currently a registered commercial diver with the Association of Diving Contractors and a licensed professional engineer in the State of Texas.